Hydrogen Millimeter Recombination Lines as a Tracer of Extragalactic Star Formation Rates

Dissertation
zur
Erlangung des Doktorgrades (Dr. rer. nat.)
der
Mathematisch-Naturwissenschaftlichen Fakultät
der
Rheinischen Friedrich-Wilhelms-Universität Bonn

vorgelegt von
Toma Bădescu
aus
București, România

Bonn 2024

Angefertigt mit Genehmigung der Mathematisch-Naturwissenschaftlichen Fakultät der Rheinischen Friedrich-Wilhelms-Universität Bonn

Gutachter/Betreuer:	Prof. Dr. Frank Bertoldi
Gutachter:	Prof. Dr. Frank Bigiel
Tag der Promotion:	11.09.2025
Erscheinungsjahr:	2025

For my parents, who believed in me

”I’ll tell you this
No eternal reward will forgive us now
For wasting the dawn”

— *Stoned Immaculate*, Jim Morrison

Abstract

When studying the structure and evolution of distant galaxies, the total star formation rate (SFR) of a given galaxy is an important observable. It is related to the gas, dust, and stellar mass content of a galaxy, and is strongly related to the ultraviolet (UV) radiation field, which affects the physical and chemical state of the star-forming interstellar gas. The SFR can be inferred from several observational tracers, such as UV emission (from massive stars), far-infrared (FIR) emission (from dust heated by massive stars), radio synchrotron emission (from relativistic electrons accelerated in supernovae), or hydrogen recombination line emission (in ionized gas around massive stars, the so-called HII regions). All have their advantages and disadvantages. A promising SFR tracer that has not yet been extensively studied for distant galaxies is the millimeter-wavelength hydrogen recombination line (mm-RL) emission. In this work, I investigate how the physical conditions in HII regions affect the amplification and attenuation of mm-RL emission. We harvest the Atacama Large Millimeter-submillimeter Array (ALMA) data archive and use our own IRAM 30m telescope observations to assemble mm-RL detections towards nearby (within a few hundred Mpc) star-forming galaxies. Our ALMA archive sample consists of the 20 brightest infrared star-forming galaxies, while the IRAM 30m observations target six nearby star-forming galaxies with prior cm-wavelength RL detections. We detect mm RL emission from 9 galaxies in the ALMA sample, while no lines are detected in the IRAM 30m sample. We compare the implied SFR of these galaxies when derived from the mm-RL emission and from their FIR emission, and find a linear correlation that is consistent with measurements of individual massive star-forming regions in our Milky Way galaxy, stretching over eight orders of magnitude. We find that several sources show mm-RL emission suffering from maser amplification, and that maser amplification cannot be ruled out even for galactic sources. We evaluate the quality of mm-RL emission as a reliable SFR tracer and suggest that mm-RL emission, in combination with FIR emission, can be used to trace the recent star formation history.

Contents

CHAPTER 1

Introduction

Astrophysical observations not only reveal the history of our universe and our place in it, or the properties of astronomical objects, but are also a tool for developing or validating models in physics. For example, pulsar observations have been used to test the theory of relativity (Taylor et al., 1979; Ding et al., 2021; Kramer et al., 2021). Spectral line emission observations of the Sun or interstellar gas clouds have been used to perfect and develop quantum mechanical models of the atom (Heilbron, 2013; Hitomi Collaboration et al., 2018; Dufresne et al., 2023). The variation of the rotational velocities of stars, gas, and dust in galaxies as a function of distance from their center, revealed by the Doppler shift of their spectral line emission, were some of the first observations to reveal the presence of an unseen mass component in galaxies, also known as dark matter (DM) (Zwicky, 1933; Rubin & Ford, 1970; Ostriker et al., 1974). Observations of the distribution of galaxies and of the cosmic microwave background have led to the development of the current cosmological model in which DM dominates the mass of the Universe (Bondi, 1952; Bahcall et al., 1997; Eisenstein & Hu, 1998; Eisenstein et al., 2005; Weinberg et al., 2013; Planck Collaboration et al., 2020). Observations of these extreme environments, which cannot be replicated in laboratory experiments, have helped to develop, perfect, or confirm the validity of models used in physics. Observations of galaxies are important for a number of reasons. On spatial scales larger $1 \sim 3$ Mpc, the spatial distribution of galaxies and their basic properties, such as their mass, their stellar and gas content, can help constrain the parameters of cosmological models (Peebles, 1980; Landy & Szalay, 1993; Eisenstein et al., 2005; Cole et al., 2005; Tully et al., 2023). Galaxies are also the site of complex interactions between stars, radiation, dust, and gas (e.g. McKee & Ostriker, 2007; Osterbrock & Ferland, 2006; Draine, 2011). Thus, observations of galaxies present unique opportunities to test fundamental physics. The mass and luminosity of a galaxy depend on the number of stars it contains. The emission spectrum of a galaxy is influenced by the stellar mass and age distribution, and by the properties of the interstellar medium (ISM), such as the abundance and spatial distribution of gas and dust.

The star formation rate (SFR), the rate at which the total mass of all stars of a galaxy changes, also determines the rate at which energy and chemical elements (particularly metals, i.e., elements with atomic number $Z > 2$) are introduced into the ISM, as well as the rate at which supernova explosions (SNe) occur (e.g. McKee & Ostriker, 2007; Kennicutt & Evans, 2012; Kobayashi & Taylor, 2023). There is substantial evidence that, at least in some galaxies, star formation occurs in sporadic bursts (e.g. Ma et al., 2017; Faisst et al., 2019; Mehta et al., 2023). Thus, the star formation history (SFH) of a galaxy is also an important part of understanding its properties and evolution. For all these reasons,

the SFR is an important parameter for understanding galaxy evolution. It is therefore crucial to ensure that the methods used to measure and infer the SFR are accurate and as unbiased as possible.

Various observables, also known as tracers, can be used to infer the SFR of a galaxy. However, in the absence of direct knowledge of the true SFR, results from different tracers must be cross-checked using established physical principles to account for potential biases. Stellar radiation serves as a direct SFR tracer, since observing the light emitted by newly formed stars could, in principle, provide a direct estimate of the SFR. However, it is not straightforward to distinguish newborn stars from older stars, especially in the case of low- to intermediate-mass stars ($M \lesssim 3\,M_{\odot}$) that have lives longer than $\sim 0.5 \times 10^9$ yr. Fortunately, massive stars ($M \gtrsim 8\,M_{\odot}$) are comparatively short-lived ($\sim 10^7$ yr) and have very high luminosities ($L \sim 10^4 - 10^5\,L_{\odot}$), emitting mostly at UV wavelengths. Assuming a steady state of constant SFR, and a specific stellar mass distribution function at birth, known as an initial mass function (IMF), observations of the UV continuum from the total stellar population can be used to infer the SFR (e.g. Hao et al., 2011).

Indirect tracers of the SFR are components of stellar radiation that are processed by interstellar gas or dust. Just like the direct tracers, these indirect tracers are also sensitive to an assumption about the IMF, the temporal evolution of the stellar population, and the past evolution of the SFR, also known as the star formation history. A commonly used indirect tracer is the thermal, far-infrared continuum radiation emitted by interstellar dust, by grains that are heated by the UV radiation from nearby massive stars. (e.g. Calzetti et al., 2007; Kennicutt & Evans, 2012).

Indirect tracers of the SFR are components of stellar radiation that are processed by interstellar gas or dust. Like the direct tracers, these indirect tracers are sensitive to an assumption about the IMF, the time evolution of the stellar population, and the past evolution of the SFR, also known as the star formation history. A commonly used indirect tracer is the thermal far-infrared continuum radiation emitted by interstellar dust grains heated by UV radiation from nearby massive stars. (e.g. Calzetti et al., 2007; Kennicutt & Evans, 2012).

These established SFR tracers have shortcomings. Although UV continuum emission is a direct tracer of the SFR, UV light is easily absorbed by interstellar dust, so extinction corrections must be applied. Inferring the SFR from infrared dust emission also requires knowledge of the composition and spatial distribution of the dust, as well as an initial mass function to distinguish the dust emission from that of older, low-mass stars (e.g. Calzetti et al., 2007; Kennicutt & Evans, 2012). Another indirect tracer is the free continuum and line emission from ionized hydrogen gas around massive stars, such as the hydrogen recombination line (H-RL) emission, which includes hydrogen millimeter recombination lines (mm-RL).

When a hydrogen ion recombines with a free electron, the result is often an atom in an excited state, meaning that the now captured electron is in a higher energy state, corresponding to a high principal quantum number. The captured electron transitions to lower energy states in the newly formed atom. If unperturbed, the process continues until the lowest energy state, called the ground state, with a principal quantum number of $n = 1$ is reached. In ionized gas, electrons can be continuously released and recaptured, or atoms can be re-excited by photons or other electrons, leading to repeated recombination and de-excitation events (e.g. Osterbrock & Ferland, 2006; Draine, 2011).

In the absence of collisional processes, atomic de-excitation, i.e. transition from a higher to a lower energy state, can result in the emission of a photon, whose energy is equal to the energy difference between the two states. This recombination line radiation is denoted α for transitions between two adjacent principal quantum states, e.g. $n + 1 \rightarrow n$, and for hydrogen, e.g., H$n\alpha$. For historical reasons,

some H emission lines do not quite follow this notation: e.g., Lyα refers to H1α and Hα to H2α.

Hydrogen recombination lines, when emitted from ionized hydrogen surrounding massive stars, are proportional, among other things, to the amount of ionizing radiation emitted by these massive stars, and can thus be used to trace the SFR.

The intensity of hydrogen recombination line emission from ionized gas surrounding massive stars depends on the total ionizing photon emission from the stars, i.e. photons with energy larger 13.6 eV. Since the abundance of massive stars that emit such high-energy radiation depends on the star formation rate at timescales longer than about 10 million years, H recombination lines are good tracers of the SFR.

Interstellar dust, however, preferentially absorbs shorter wavelength electromagnetic radiation, such as optical or UV radiation, but does not affect far-infrared, millimeter-wavelength, or radio emission. This makes optical recombination lines, such as Hα, potentially problematic SFR tracers in places where dust is highly abundant. However, millimeter hydrogen recombination lines are not absorbed by dust, and could prove an accurate SFR tracer (Gordon & Sorochenko, 2002). Thus far, their relative faintness when compared to the optical lines, as line intensity decreases roughly as $\sim 1/n^6$, where n is the principal quantum number, has prevented their extensive study even in nearby extragalactic star-forming regions (Gordon & Sorochenko, 2002). The development of much more sensitive millimeter wave observatories, over the past decade, such as the Atacama Millimeter-submillimeter Array (ALMA), offers the possibility to better study extragalactic mm-RL emission (e.g. Bendo et al., 2015, 2016).

The absorption of radiation by interstellar dust is strongly wavelength-dependent, where UV radiation is much stronger affected than optical than infrared radiation. In typical star-forming environments dust can significantly attenuate UV and optical H-RL emission, whereas in the near- and far-infrared this is less important, and at mm- and radio-wavelengths, absorption is a negligible effect. This makes optical recombination lines, such as Hα, potentially problematic SFR tracers that rely on extinction corrections, and mm and radio lines are potentially much better SFR tracers (Gordon & Sorochenko, 2002). Although the H-RL intensities decrease strongly, $\sim n^{-6}$, with higher quantum number, n, they could be observed at radio wavelengths already in the 1960s towards galactic massive star-forming regions ((Gordon & Sorochenko, 2002)). At mm wavelengths, the insufficient telescope sensitivity made observations of extragalactic sources sparse until the Atacama Millimeter-submillimeter Array (ALMA) allowed high-resolution, sensitive observations that now allow for a systematic study of mm-RL emission as SFR tracers over large star-forming regions and even entire galaxies (e.g. Bendo et al., 2015, 2016).

In this thesis we analyze the properties of hydrogen mm-RL, their reliability as SFR tracers, their possible use in studying the star formation history (SFH) of galaxies, and their possible application in determining the electron temperature and density of the ionized gas in massive star-forming regions. In the following sections of this chapter, we provide some background that is relevant to our work, concerning the properties of galaxies, star formation, and the star formation rate tracers. In Chapter 1.5 we present the motivation for our work and in Chapter 2 we present the observational data we use and the analysis method we apply. In Chapter 3 we revisit the theory of mm-RL emission and the use of mm-RL emission as a SFR tracer. We also perform an in-depth analysis of how the properties of the ionized gas affect mm-RL emission. We present our main results in Chapter 4, which include a comparison between the SFR obtained from mm-RL observations with that obtained from other tracers, as well as the possible use of mm-RL emission as a probe of the SFH of galaxies. In Chapter 5 we discuss possible sources of uncertainty affecting mm-RL and other SFR tracers, and provide an

outlook assessing the prospects for future ALMA observations of mm-RL. In Chapter 6 we summarize our results and present our conclusions.

1.1 Constituents of galaxies

The Milky Way galaxy has a total mass $M_{\rm MW} = 1.3 \sim 1.5 \times 10^{12}\, M_\odot$ (McMillan, 2011; Watkins et al., 2019). Excluding DM, stars and the ISM are the main constituents of a galaxy. The stellar mass of the Milky Way is estimated to be $M_* = 4.5 \sim 6.5 \times 10^{10}\, M_\odot$. The mass of the ISM in our galaxy is $\sim$ 10% that of the stellar mass (Draine, 2011). This is similar to what is found in local giant spiral galaxies, where the ISM mass is 7-10% of their stellar mass (Leroy et al., 2008; Saintonge et al., 2011). The ISM is defined as everything present between the stars, i.e. gas, dust, cosmic rays, and occupies most of the volume inside a galaxy, and also influences properties of the stellar population. A special set of conditions are required in the ISM for star formation to take place (see Sec. 1.2). If these conditions are met, the cold gas clouds in the ISM collapse under their own gravity, forming stars in their cores (McKee & Ostriker, 2007). The chemical composition of these initial gas cloud influences the properties and the future evolution of the newly born star. The properties of the ISM and those of the stellar population, such as the stellar mass distribution and star formation rates, are therefore mutually linked (e.g. McKee & Ostriker, 2007; Kobayashi & Taylor, 2023). Understanding the composition and the properties of these constituents is thus crucial in the study of the physical processes in galaxies and their evolution.

1.1.1 Stars

Determining the SFR also requires an understanding of stellar structure and evolution, since many SFR tracers rely on direct of stellar radiation and its effects on the ISM. In this section we provide a brief overview of the properties of stars and stellar populations. Mass is one of the most important characteristics of stars, as it determines their luminosity, surface temperature, and how long they live.

A Hertzsprung-Russel (HR) diagram shows the observed number of stars as a function of their luminosity and surface temperature (Hertzsprung, 1905; Russell, 1919). For the majority of their lives, stars are in hydrostatic equilibrium, fusing hydrogen into helium in their cores (e.g. Hansen & Kawaler, 1994; Nomoto et al., 2013). Stars spend most of their lives in this stage of their lives and are called main sequence stars, located on a diagonal band in the HR diagram, as shown in Figure 1.1. More than 90% of observed stars are on the main sequence. Their luminosity depends on their mass, approximately as $L \propto M^{3.5}$ (e.g. Popper, 1980; Hansen & Kawaler, 1994; Wang & Zhong, 2018). To first order, especially at non-FUV wavelengths, the stellar spectrum can be approximated to first order as a black body spectrum. The higher the surface temperature of a star is, the shorter the wavelength of the peak of their emission spectrum, leading to more massive stars being "bluer" while less massive stars being "redder" (e.g. Zeilik & Gregory, 1998).

Under the Harvard Classification System, stars are classified according to their emission spectrum. Using this classification, O-type stars are the "bluest", making them also the hottest and most massive, with surface temperatures above 30000 K and masses $\gtrsim 15\, M_\odot$. The black body emission from these O-type stars having these very high surface temperatures contains a significant proportion of short wavelength photons, mostly having UV wavelengths or shorter (e.g. Hansen & Kawaler, 1994; Martins et al., 2005). Stars with masses below those of the G-type stars similar to the Sun have "redder" colors

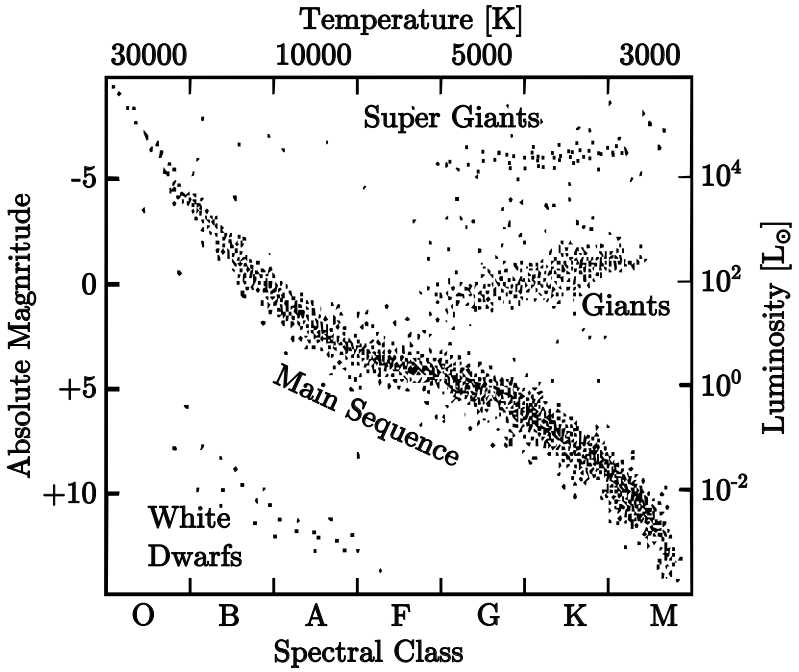

Figure 1.1: Typical HR diagram (Hertzsprung, 1905; Russell, 1919), showing the distribution of luminosity as a function of temperature of stars in a galaxy. The bottom axis indicates the stellar types based on the Harvard Classification System. Figure adapted adapted from Colaboration (2015), part of the CHANDRA collaboration (Weisskopf et al., 2000).

and their spectra peak towards the long wavelength end of the optical spectrum.

The lifetime of a star is a highly non-linear function of its mass, with the lifetime decreasing significantly as the mass of the star increases.. The luminous massive stars lose energy faster than less massive stars. The energy loss causes the star to contract due to gravity and leads to an increase in its average temperature, according to the virial theorem.The increase of the core temperature leads to an increase of the fusion reaction rate (Nomoto et al., 2013). Thus, more massive stars convert their hydrogen reserves into helium much faster than less massive ones (e.g. Hansen & Kawaler, 1994; Nomoto et al., 2013). This can be seen in Table 1.1, where O-type stars have lives shorter than ~ 10 Myr, in contrast to less massive stars. As hydrogen is depleted by nuclear fusion, stars approach the end of their lives and exit the phase known as the main sequence (e.g. Nomoto et al., 2013). When the hydrogen fusion ends, the stars contract under gravity, leading to an increase in temperature (e.g. Hansen & Kawaler, 1994; Zeilik & Gregory, 1998). If the mass of the star is high enough, fusion of heavier elements will follow (e.g. Hansen & Kawaler, 1994; Nomoto et al., 2013). Stars with masses below $\sim 8\,M_\odot$ eventually reach a stage where further contraction will not generate the temperatures necessary for fusion to proceed, and a hot dense core will form instead (Nomoto et al., 2013). Fusion of hydrogen or helium then proceeds in a shell surrounding the hot core, expanding the layers of the star above it, resulting in a large-diameter object with a lower surface temperature, a red giant star. The star loses material from its outer layer in strong stellar winds and outflows, leaving its core as a hot, dense object known as a white dwarf (Zeilik & Gregory, 1998; McKee & Ostriker, 1977; Anderson et al., 2016; Péroux & Howk, 2020).

Stellar Type	Mass Range[ab]	Luminosity[ab]	Surface Temperature[abc]	Life Span[d]
	$[M_\odot]$	$\log [L/L_\odot]$	[K]	
O	≥ 15.6	≥ 4.68	≥ 30000	$\lesssim$ 10Myr
B	$\sim 2.3 - 15.6$	$4.5 \sim 1.6$	11000-29000	$\sim$ 0.015 -1.2 Gyr
A	$\sim 1.5 - 2.3$	$0.7 \sim 1.5$	7400-10000	~1.5-3.6 Gyr
F	$\sim 1.04 - 1.5$	$0.17 \sim 0.6$	5900-7400	~10-1.5 Gyr
G	$\sim 0.8 - 1.04$	$-0.22 \sim 0.17$	4800-5900	~10-17 Gyr
K	$\sim 0.5 - 0.8$	$-1.1 \sim -0.23$	3900 - 4800	≥17 Gyr
M	≤ 0.08	≤ -1.1	≤ 3900	≥17 Gyr

Table 1.1: Properties of stellar types in the Harvard Classification System. Stars with higher mass tend to have higher luminosities and temperatures, and shorter lives. [a](Martins et al., 2005), [b] (Habets & Heintze, 1981), [c](Zeilik & Gregory, 1998), [d](Hansen & Kawaler, 1994)

For stars with masses above $\sim 8\,M_\odot$, fusing ever heavier elements is not enough to prevent their eventual collapse under their own gravity (Nomoto et al., 2013). When this happens, they produce a supernova explosion (SN), releasing a kinetic energy of $\sim 10^{51}$ erg and injecting material, including heavier elements, into the ISM. After the supernova explosion, a compact object is left behind, in the form of a neutron star or black hole.

Thus, not only are the most massive stars the brightest, and thus easier to detect, but they can also significantly influence their surroundings, i.e. the ISM. Furthermore, assuming they form at a steady rate, their short lives help keep their overall number in a galaxy proportional to their formation rate, as a steady state can be reached where old massive stars die at the same rate as new ones are formed. This means that determining the number of massive stars in a galaxy or region, can be used to determine the overall star formation rate, provided that the mass distribution of stars on the main sequence is known (e.g. Calzetti et al., 2007; Kennicutt & Evans, 2012). This distribution of stellar masses, called the initial mass function (IMF), is the empirical mass distribution of stars that enter the main sequence, i.e., begin hydrogen burning. The IMF describes the relative abundance of stars of different masses. It would be possible, after determining the number of stars of a certain mass in a galaxy, to use the IMF and the SFH to determine the mass of all the stars in a galaxy or region. Thus, the IMF, together with the SFH, is essential for measuring stellar masses or the star formation rate when only a part of the stellar population can be observed.

The first studies of the IMF were carried out for stars with masses $M > 1\,M_\odot$, which found it has the form of a powerlaw (Salpeter, 1955):

$$\frac{dN}{dM} \propto M^{-\alpha}, \tag{1.1}$$

where dN is the total number of stars in the mass range dM, and $\alpha = 2.35$ (Salpeter, 1955). With the Salpeter IMF, using $n(M) = dN/dM = \xi_0\, M^{-\alpha}$, with ξ_0 being a constant depending on the local stellar density, for every $M = 15 M_\odot$ star, there would be $\sim$ 580 stars with the mass of our Sun. Combining the mass-luminosity relation with the IMF, one finds that, although much less abundant, massive stars dominate the luminosity output of a stellar population. Similarly, due to their high relative numbers, low mass stars dominate by mass. More recent studies of the IMF have revealed its shape also for the lower mass stars (Kroupa, 2001; Chabrier, 2003). In this work we use the Kroupa

IMF, which has the form of a broken powerlaw:

$$\frac{dN}{dM} \propto M^{-\alpha} \qquad \text{where} \begin{cases} \alpha = 0.3 \pm 0.7, & 0.01 \leq M/M_{\odot} < 0.08 \\ \alpha = 1.3 \pm 0.5, & 0.08 \leq M/M_{\odot} < 0.5 \\ \alpha = 2.3 \pm 0.3, & 0.5 \leq M/M_{\odot} < 1 \\ \alpha = 2.3 \pm 0.7, & 1 \leq M/M_{\odot}. \end{cases} \tag{1.2}$$

The uncertainties of the IMF are highest at the low and high mass ends. This is because the low mass stars are faint, thus difficult to observe, while high mass stars are rare, and thus suffer from the effects low number statistics. Furthermore, these numbers are also sensitive to the star formation history. Because low mass stars have significantly longer lives than high mass stars, their relative abundance increases over time, as star formation takes place in a galaxy, meaning the present day stellar mass distribution is also dependent on the SFH. For all these reasons, small uncertainties in the number of high mass stars, the SFH, or the slope of the IMF, can introduce large uncertainties in the calculated SFR.

1.1.2 The interstellar medium

As mentioned earlier, the ISM fills the space between the stars and consists of interstellar gas and dust, cosmic rays, magnetic fields, electromagnetic radiation, as well as dark matter and gravitational fields. In this section we provide a brief overview of its most important components, namely interstellar gas and its phases, molecular clouds, and interstellar dust.

The hydrogen and helium nuclei in the Universe were created a few minutes after the Big Bang, with relative abundances of 75% and 25% respectively, along with trace amounts of lithium (e.g. Steigman, 2007; Patrignani et al., 2016; Coc & Vangioni, 2017). In the Milky Way, the relative abundance of helium to hydrogen by mass is $M_{\rm He}/M_{\rm H} \simeq 38\%$, while its relative abundance in terms of particle numbers is $N_{\rm He}/N_{\rm H} \simeq 10\%$. Elements heavier than helium have a relative abundance by mass, with respect to hydrogen, of $M_{\rm Z>2}/M_{\rm H} \simeq 2\%$ (Asplund et al., 2009; Draine, 2011). The ratio of gas mass to the total mass of a present day galaxy ($f_{\rm gas} = M_{\rm gas}/M_{\rm tot}$), also known as the gas fraction, is in the range $f_{\rm gas} \sim 0.1 - 0.2$, while for galaxies in the earlier Universe, e.g. at redshift z$\gtrsim$2, it has values of $f_{\rm gas} \sim 0.5 - 0.8$ (Magdis et al., 2012; Tacconi et al., 2018, 2020; Wang et al., 2022). A descending trend in the gas mass of a galaxies with increasing stellar mass is observed as well, with $f_{\rm gas} \propto M_{*}^{-0.5}$ (Magdis et al., 2012).

The gas in the ISM can be modeled as having multiple components of different temperatures or ionization states, coexisting in pressure equilibrium, known as phases. Field et al. (1969) proposed a two phase model of the ISM, consisting of a warm medium (WM) and a cold neutral medium (CNM). The warm gas phase at $T = 10^4$ K, fills most of the interstellar space, and the colder component at $T \lesssim 300$ K, exists in the form of interstellar clouds of gas. In this model the gas is heated by collisions with cosmic rays, and is cooled by collisional excitation of H and He, and [CII] emission. A third phase of the ISM, consisting of very hot gas, at $T \gtrsim 10^{5.6}$ K, with a very low density $n \lesssim 10^{-2.5}$ cm^{-3}, known as the hot interstellar medium (HIM) was introduced by McKee & Ostriker (1977) with their three-phase model of the ISM. In this model, the HIM is the result of super nova explosions shock heating interstellar gas, and it is this phase that fills most of the interstellar space, having a filling factor of $f_V = 0.7 - 0.8$. Cold neutral clouds, with temperatures of $T \sim 10^{1-2}$ K are embedded in the HIM,

surrounded by the coronae making up the warm medium. The warm medium is modeled as a volume of ionized gas at $T \sim 8000\,\mathrm{K}$, larger than the neutral clouds, with $f_V \sim 0.2$. McKee & Ostriker (1977) further made a distinction between the inner and outer parts of this volume of warm gas surrounding neutral clouds. They designated the weakly ionized inner region, closer to the neutral cloud, having a ionization fraction of ~ 0.1, as the warm neutral medium (WNM), and the outer region, with having a ionization fraction of ~ 0.7, as the warm ionized medium (WIM). The ionization states of the WIM and WNM are maintained by hot B stars, and X-rays from super nova remnants, respectively. In this model, the shock heated gas cools radiatively, while the evaporating cold clouds are replenished by the dense gas shells around super nova remnants (McKee & Ostriker, 1977).

More recent studies of the inner 20 kpc of the Milky Way place the relative mass abundances of ionized, atomic, and molecular hydrogen, at $\sim 23\%$, $\sim 60\%$, and $\sim 17\%$, respectively (Dame et al., 2001; Heiles & Troland, 2003; Armentrout et al., 2018; Saintonge et al., 2011). In terms of volume, the ionized gas occupies the largest share of the volume in the galactic disk, with $f_V \simeq 0.5 - 0.6$, followed by neutral gas with $f_V \simeq 0.4$, the rest being taken up by H_2 with $f_V \simeq 0.001$ (Churchwell, 2002; Osterbrock & Ferland, 2006).

The three phase model does not take into account ionized regions around massive stars or molecular clouds, since neither are in pressure equilibrium with the other phases of the ISM (McKee & Ostriker, 1977).

The ionized regions around massive stars, also known as HII regions, have $T \approx 10^4\,\mathrm{K}$, with a wide range of densities of $n_\mathrm{H} \simeq 10^2 - 10^7\,\mathrm{cm}^{-3}$ and $f_V \sim 0.1$. While the HIM is heated by shock-waves from SN, and ionized by collisions with other particles, these HII regions are heated by electrons originating from atoms ionized by energetic photons from massive stars (Draine, 2011; Osterbrock & Ferland, 2006; Luisi et al., 2020). These regions are discussed in mode detail in Sec. 1.3.2, as they can provide a way to measure the SFR (Kennicutt et al., 1989; Thilker et al., 2000; Lawton et al., 2010).

While not present in the three phase model of McKee & Ostriker (1977), the molecular medium is also considered a distinct phase of the ISM (e.g. Draine, 2011). The molecular medium has a clumpy and fragmented structure, consisting of molecular clouds, mostly containing H_2 gas. Through a process called self-shielding, molecular hydrogen in the outer layers of the clouds shields their interior from interstellar radiation that would otherwise quickly dissociate the H_2 molecules and lead to cloud evaporation. The temperature and density of molecular clouds are in the range of $T = 10 - 15\,\mathrm{K}$ and $n_\mathrm{H} \sim 10^2 \sim 10^6\,\mathrm{cm}^{-3}$, respectively. Clouds having masses of $10^3 - 10^{5.5}\,M_\odot$ are known as giant molecular clouds (GMC). The gravitational collapse of overdense regions inside molecular clouds leads to star formation. These density peaks have masses $M = 0.3 - 500\,M_\odot$ and densities $n = 10^5 - 10^6\,\mathrm{cm}^{-3}$ (Draine, 2011; Beltrán et al., 2006; Seale et al., 2012). The exact mechanism that governs cloud formation from the neutral medium is the subject of ongoing research. The main avenue for the formation of the H^2 molecule in galaxies is through dust grain catalysis, a process where two H atoms react to to form an H_2 molecule on the surface of an interstellar dust grain. This H_2 molecule, which forms in an excited state, is ejected from the grain surface by the energy released when it transitions to the ground state (Gould & Salpeter, 1963; Hollenbach & Salpeter, 1971; Draine, 2011). The lifetime of molecular clouds is also uncertain, with studies inferring lifetimes of $10 \sim 100\,\mathrm{Myr}$. It is not yet clear if the feedback from star formation, in the form of stellar winds and photoionization from young massive stars, or if the subsequent SN explosions play a main role in dispersing these clouds and possibly halting further star formation (e.g. Chevance et al., 2020, and references therein).

In the Milky Way, the total mass of interstellar dust constitutes almost one percent of the total gas

mass, with $M_{\rm dust}/M_{\rm gas} \simeq 0.0083$. (Purcell, 1969; Kim & Martin, 1996; Hirashita, 1999) Interstellar dust grains are mainly composed of C, O, Mg, Si, S, and Fe, ordered by mass abundance. The observed spectral features of interstellar dust clouds reveal the existence two main types of dust grains: carbonaceous and amorphous silicates. Most carbonaceous dust grains consist sheets of carbon atoms organized into a hexagonal structure, with hydrogen atoms at their edges called polycyclic aromatic hydrocarbons (PAH). Examples of PAHs include large molecules such as coronene ($C_{24}H_{12}$), antrhacene ($C_{24}H_{10}$), and hexabenzocoronene ($C_{42}H_{18}$). The strength of the features observed in the emission spectrum of PAHs indicates that approximately $10-15\%$ of interstellar carbon is present in these molecules (Joblin & Tielens, 2011). Carbonaceous dust grains inside dark molecular clouds can also acquire an ice mantle mantle, which is revealed by the emission features of H_2O, CO_2, NH_3, and other molecules (Draine & Li, 2007a; Asplund et al., 2009; Draine, 2011). Silicate grains are generally larger than carbonaceous grains. They are composed of materials containing Si-O bonds, such as pyroxene (Mg_xSiO_3 or $Fe_{1-x}SiO_3$) and olivine (Mg_2SiO_4 or Fe_2SiO_4), are mostly amorphous, with only $\sim 2-5\%$ of interstellar Si contained in grains having a crystalline structure (Li & Draine, 2001; Kemper et al., 2005; Draine, 2011). The cores of dust grains form in the outflows, novae or in SN explosions. Asymptotic giant branch (AGB) stars with $M = 0.5-8\,M_{\odot}$, have a low surface temperature and exhibit strong winds, ejecting a significant amounts of material into the ISM (Lattanzio & Forestini, 1999; Boulangier et al., 2019). Due to these outflows, these stars are highly effective interstellar dust progenitors (Johnson et al., 1993; Gail, 2009; Kochanek, 2011; Tielens, 2022).

Observational data are used to develop interstellar dust models, which describe the overall size, shape, and relative chemical abundance distribution of dust grains. The most successful models so far take into account the two main types of grains described above (Draine, 2011). One of the earliest dust models, known as the MRN model (Mathis et al., 1977), did not incorporate PAHs, and proposed a powerlaw distribution of dust grain sizes, of the form $dn/da \propto a^{-3.5}$. Later models incorporate silicates and PAHs, as well as graphite grains. These models, such as WD01 (Weingartner & Draine, 2001), ZDA04 (Zubko et al., 2004), DL07 (Draine & Li, 2007a), and DFA09 (Draine & Fraisse, 2009), assign various size distributions to the carbon and silicon containing grains, and some also incorporate non-spherical grains in order to explain the polarization of dust emission (Draine & Fraisse, 2009; Draine, 2011). In the WD01 and ZDA04 models, the half-mass grain radii, i.e. the radii that divide the mass distribution of the grains into two equal parts, are $\sim 0.12\,\mu$m and $\sim 0.07\,\mu$m for carbonaceous and silicate grains, respectively. In the DFA09 model, the half-mass radii for carbonaceous and silicate grains are $\sim 0.04\,\mu$m and $\sim 0.14\,\mu$m, respectively. Nevertheless, all of these models agree that the relative number density of grains diminishes significantly as their radius increases. Consequently, the total surface area of grains is dominated by small grains, while large grains constitute the majority of the mass. Developing a unified model is not straightforward because a dust model has to explain observed spectral features and agree with the observed abundance of chemical elements in the other phases of the ISM. At the same time, multiple distributions of the size, shape, and composition of dust grains grains that can exhibit similar emission features. (Draine, 2011; Mathis et al., 1977; Zubko et al., 2004; Weingartner & Draine, 2001; Draine & Li, 2007a; Draine & Fraisse, 2009)

Interstellar dust interacts with the interstellar radiation field, by preferentially absorbing short wavelength radiation, including UV photons emitted by massive stars. This process heats the dust, and cools radiatively emitting infrared radiation. The dust emission and its use as a SFR tracer is discussed in more detail in Section 1.3.2.

1.2 The star formation process

Star formation is a complex process in which dense regions within molecular clouds in interstellar space collapse under their own gravity, eventually initiating nuclear fusion in their cores. Due to the fact that massive stars evolve rapidly and make up about 1% of the stellar population by number, direct observations of the complete process of massive star formation are difficult to obtain. As a result, massive star formation is less well understood than low-mass star formation (e.g. Rosen & Krumholz, 2020, and references therein). In this section, we give a an outline of the star formation process, with a focus on high-mass star formation.

Massive star formation takes place in gravitationally bound dense and cold molecular clouds, containing turbulent and magnetized gas with $n = 10^4 - 10^6\,\mathrm{cm}$ and $T \sim 10\,\mathrm{K}$. These clouds are also known as star-forming clumps. The gravitational collapse of these clouds is the first stage in the star formation process. For this collapse to take place, the mass of the cloud has to be above a critical value in order to overcome their internal pressure. At later stages of massive star formation, the infalling material also has to overcome intense radiation pressure from the emerging protostar. However, the details of this sequence of events is not firmly established. Presently, the main theories describing massive star formation are the Core Accretion and the Competitive Accretion models (e.g. Motte et al., 2018, and references therein). In the Core Accretion framework, the process begins with the collapse of gravitationally bound cores of gas within a dense star-forming cloud, where turbulence and magnetic fields play an important role. The collapse of each core, mediated by an accretion disk, eventually gives birth to one or several massive stars. In Competitive Accretion, the star-forming cloud undergoes a global free-fall collapse. The chaotic collapse and fragmentation of this cloud leads to the formation of multiple stars, that competitively accrete material from their surroundings. In this framework, each newly formed massive star is surrounded by multiple low-mass stars (e.g. Motte et al., 2018, and references therein).

A key feature Core Accretion model is the collapse of a gravitationally bound cloud that eventually forms one or a few massive stars. A molecular cloud with a mass above a critical value becomes unstable against gravitational collapse. Historically, the first calculations of this critical mass were made by Jeans (1928). They considered a sphere of gas in hydrostatic equilibrium, and ignored angular momentum, magnetic fields, turbulence, or external pressure. In this framework a cloud is stable if the timescale on which the gas responds to a perturbation is shorter than the free-fall timescale of its collapse. Jeans (1928) considered that information about a perturbation, e.g. in density or pressure, propagates through a gas at the speed of sound in that gas, c_s. For a cloud of size R, this timescale also known as the sound crossing timescale, is $t_\mathrm{s} = R/c_\mathrm{s}$. The timescale for the collapse of the gas cloud was taken by Jeans (1928) to be its free-fall time, $t_\mathrm{ff} = (3\pi)^{1/2}(32G\rho)^{-1/2}$, where $\rho = 3M/(4\pi R^3)$ is the density of the gas cloud. The cloud is stable against collapse if $t_\mathrm{ff} \geq t_\mathrm{s}$. Otherwise, the gas does not have time to react to contraction under free-fall conditions, and it will continue to collapse before it can reach hydrostatic equilibrium. When $t_\mathrm{ff} = t_\mathrm{s}$, the cloud reaches the critical mass and radius, in this model known as the Jeans mass and the Jeans radius M_J and $R = R_\mathrm{J}$, respectively:

$$M_\mathrm{J} = \frac{4\pi}{3}\rho\left(\frac{R_\mathrm{J}}{2}\right)^3 = \frac{4\pi}{3}\rho^{-1/2}\left(\frac{3\pi c_s^2}{16G}\right)^{3/2}. \tag{1.3}$$

Despite its simplifying assumptions, this calculation proves to be a good approximation, as using the

observed values for molecular clouds, equation 1.3 yields a Jeans mass of the order of a few solar masses. A similar approach used the virial theorem, where a gas is unstable under collapse if the change in gravitational potential energy due to contraction is greater than the change in thermal energy of the gas, due to the work done on it to compress it. Accounting for the pressure exerted by the medium surrounding the gas cloud, as well as for its non uniform radial density profile, Bonnor (1956) calculate a critical mass, the Bonnor-Ebert mass, that is close to the Jeans mass, $M_{\rm BE} \sim 1.18 M_{\rm J}$.

The main limitation of these two different approaches is that they did not take into account the presence of turbulence, magnetic fields or the angular momentum of the initial gas cloud. In the Core Accretion framework, turbulence and magnetic fields play a key role in maintaining the internal pressure of the cloud. Because of the high conductivity inside an astrophysical plasma, the magnetic field lines follow its motion, in a phenomenon called flux freezing. This means that when a gas cloud or core containing charged particles collapses, the magnetic field lines are compressed, increasing the energy density of the magnetic field. Without a means of escape, magnetic fields could thus prevent the gravitational collapse of a core (e.g. Mouschovias, 1987; Crutcher, 2005; McKee & Ostriker, 2007). However, although the magnetic field lines follow the motion of the plasma, the charged particles of the plasma can move independently of the other neutral particles in the cloud (e.g. Zweibel, 2002; McKee & Ostriker, 2007; Draine, 2011). One proposed solution to this problem is ambipolar diffusion. As the cloud collapses, compressing the magnetic field, the charged particles escape from the cloud in directions perpendicular to the field lines, allowing the magnetic field to also escape from the cloud without stopping its collapse.(e.g. Mouschovias, 1987; Zweibel, 2002; Heitsch et al., 2004; McKee & Ostriker, 2007; Dall'Olio et al., 2019). Turbulence also causes magnetic field lines to reconnect, reducing the ambipolar diffusion timescale by removing magnetic flux from the cloud.

The collapse of a rotating cloud stops at a critical radius, $R_{\rm crit}$, if the rotational kinetic energy overcomes the absolute value of the gravitational potential energy (Sakai et al., 2017; Csengeri et al., 2018). This radius depends on the initial ratio of the angular momentum to the mass of the core, J/M, also known as the specific angular momentum. Observations of our Galaxy show that a typical core with a diameter of 1 pc would have a specific angular momentum of $J/M \sim 3 \times 10^{21} {\rm cm}^2\ {\rm s}^{-1}$ (Draine, 2011). This would correspond to a critical radius of $R_{\rm crit} \simeq 0.1$ pc, meaning that the collapse of such a rotating cloud would stop before a protostar is formed. Two mechanisms have been proposed to explain how the collapse would proceed under these conditions, dissipating the rotational kinetic energy from the core: gravitational and magnetic torques. In the gravitational torque mechanism, energy is dissipated from the core due to gravitational instabilities caused by non-axis-symmetric density distributions in the cloud (e.g. Jappsen & Klessen, 2004; McKee & Ostriker, 2007; Zhao et al., 2020; Chen et al., 2021). Magnetic torque is a mechanism by which the magnetic field dissipates angular momentum. Due to flux freezing, the rotation of the disk bends the magnetic field lines, and this in turn opposes the rotation (Mouschovias, 1987; Allen et al., 2003; Maury et al., 2018). The current limitations of the Core Accretion model are twofold: firstly, to provide an explanation for the observations of some massive stars in the absence of accretion disks; and secondly, to elucidate the mechanism preventing the collapsing cloud from fragmenting into smaller clumps (e.g. Motte et al., 2018, and references therein).

In the Competitive Accretion model, multiple protostars form in a proto-cluster and accrete mass competitively from their parent cloud, the end result being the formation of multiple stars of varying masses. This is in contrast to the Core Accretion model, where each star forms from a denser core inside the parent cloud. The mass accretion rate for a proto-star in this framework depends on the relative velocity of the proto-star with respect to the gas cloud. In this model, the most massive stars

form at the center of the proto-cluster. The infalling gas from the parent cloud maintains the accretion rate onto the proto-stars and density of their surrounding medium. The average accretion rate in the Competitive Accretion model, for a single star massive star $M \sim 50\,M_{\odot}$ is the order of $5 \times 10^{-5}\,M_{\odot}$, much lower than in the Core Accretion model. This low accretion rate poses a challenge for the Competitive Accretion model, which together with stellar feedback and turbulence, would prevent the formation of massive stars. A key prediction of the Competitive Accretion models is the presence small, randomly oriented, accretion disks, and the clustered formation of stars having various masses. The process of forming multiple stars would provide an explanation for the origin of the observed IMF. This is in contrast with the Core Accretion model, which assumes a close correspondence between the pre-stellar core mass function and the stellar IMF. (e.g. Motte et al., 2018, and references therein).

In both Core Accretion and Competitive Accretion models the collapsing material eventually forms disks around proto-stars, due to the conservation of angular momentum. The proto-star accretes matter from its disk, known as a proto-stellar disk (e.g. Black & Bodenheimer, 1975; Yorke & Bodenheimer, 1999; Zinnecker & Yorke, 2007; Turner et al., 2014). Submillimeter and millimeter continuum observations reveal some of the properties of these disks. They have diameters of $100 \sim 1000$ AU Andrews & Williams (2007); Kitamura et al. (2002); Yen et al. (2014); Louvet et al. (2016); Plambeck & Wright (2016). The disk and protostar appear enshrouded in a dusty envelope during the initial stages of accretion, with $T \sim 30 - 100$ K (Zhang et al., 2014; van 't Hoff et al., 2018). As the protostar forms, the temperature of the gas and dust in the central regions reaches $500 \sim 3000$ K (Zinnecker & Yorke, 2007; Plambeck & Wright, 2016; Tanaka et al., 2020; Lu et al., 2022; Maud et al., 2019; Liu et al., 2020b). The temperature of the dust outside this region remains at ~ 100 K (Chen et al., 2016; Liu et al., 2020b).

As the protostar continues to accrete material and increase in mass, nuclear fusion begins in its core. Massive protostars begin hydrogen fusion, entering the main sequence, earlier than their low mass counterparts, while still accreting material (e.g. Palla & Stahler, 1993; Zinnecker & Yorke, 2007). If the strong radiation from the young massive stars mass would prevent further infall of material, their mass would not exceed $\sim 40\,M_{\odot}$ (Kahn, 1974; Wolfire & Cassinelli, 1987; Krumholz et al., 2005; Tanaka et al., 2017). The existence of higher mass stars indicates that the accumulation of material has to continue even after these massive stars enter the main sequence, despite the strong radiation pressure. Theoretical models and simulations have shown that this accumulation of material can be facilitated through disk mediated accretion, where accretion from a protostellar disk close to the massive star is possible because dust in the inner parts of the disk provides shielding from the intense radiation around the stellar equator(Nakano, 1989; Yorke & Sonnhalter, 2002; Krumholz & Matzner, 2009; Kölligan & Kuiper, 2018). Towards the poles, and away from the disk, the radiation pressure from the star blows any infalling material away, and the radiation from the star escapes into the ISM, while creating outflows of ionized or molecular gas (Krumholz et al., 2005; Kuiper et al., 2011; Rosen et al., 2016). Disks and outflows around several young massive stars have also been detected by high resolution interferometric observations (e.g. Hirota et al., 2014; Purser et al., 2016; Chen et al., 2016; Cesaroni et al., 2017; Csengeri et al., 2018; Maud et al., 2019; Guzmán et al., 2020; Moscadelli et al., 2021; Williams et al., 2022; Zhang et al., 2022b).

In the final stage of star formation, the stellar wind radiation from the newly born massive star begins to destroy the proto-stellar disk and to ionize the hydrogen gas in its surroundings (McKee & Ostriker, 2007; Maud et al., 2018; Liu et al., 2020a; van Terwisga & Hacar, 2023; Miyawaki et al., 2023; Zhang et al., 2022b). The timescales over which disks are destroyed appears to be very short, of the order of 10^5 yr (Clarke et al., 2001; Alexander et al., 2006a,b; McKee & Ostriker, 2007; Sabatini

et al., 2021). The HII regions formed around the newly born star can be ultra-compact, with diameters $d \sim 0.01 - 0.1$ pc, these can then expand, pushing material outwards and clearing the molecular cloud (Zinnecker & Yorke, 2007; Hoare et al., 2007; Liu et al., 2017, 2020a; Miyawaki et al., 2023).

1.3 Measuring the star formation rate

Apart from extragalactic high energy particles (e.g. Pierre Auger Collaboration et al., 2017), or gravitational waves (e.g. Abbott et al., 2016, 2020) the vast majority of extragalactic observations rely on detecting the electromagnetic radiation. The main constituents of a galaxy, presented in section 1.1, interact with each other and mutually influence their properties and evolution. As already mentioned, massive stars inject large quantities of energy and matter into the ISM (e.g. McKee & Ostriker, 1977; Larson, 1974; Karpov et al., 2020). Their radiation can ionize atoms and molecules, heat gas and dust, and even destroy dust particles (e.g. Lequeux, 2005). Stellar winds and SNe enrich the ISM with metals (e.g. McKee & Ostriker, 1977; Anderson et al., 2016; Péroux & Howk, 2020; Kobayashi & Taylor, 2023), which in turn influence the evolution of the ISM and subsequent star formation (e.g. Dwek, 1998; Asplund et al., 2006; Herbst & van Dishoeck, 2009; Scoville et al., 2013). The radiation emitted by a galaxy is the result of the combined action of all these components and processes. The relative intensity of the radiation emitted by each component can be used to infer their properties. In order to correctly identify the emission associated with star formation and disentangle it from that originating from other processes, a thorough understanding of the spectral energy distribution (SED) of a galaxy is required. This section introduces the global SED of a star-forming galaxy and the most important tracers used to measure the SFR.

1.3.1 The SED of star-forming galaxies

In Figure 1.2, adapted from Galliano & Alloin (2008) and Galliano (2022), we present the SED of a star-forming galaxy, which shows the relative power per unit frequency of electromagnetic radiation from a galaxy as a function of frequency, where several components that contribute to the emission are highlighted.

The SED of a young stellar population that follows a standard IMF, e.g. Kroupa (2001), peaks at FUV wavelengths, as it is dominated by massive stars with temperatures above ~ 15000 K (e.g. O'Connell, 1999; Conroy, 2013; Leitherer et al., 2014). The SED of massive stars is shown with a cyan line in Fig. 1.2. The continuum emission at wavelengths shorter than 912 Å, also known as the Lyman continuum (LyC), originates mostly from O type stars (e.g. Martins et al., 2005), and would be a direct tracer of massive star formation over timescales shorter than ~ 10 Myr (e.g. Calzetti et al., 2005; Salim et al., 2007). These photons, however, are absorbed not only by dust but also by hydrogen atoms (see Sec. 1.3.2) present in galaxies, meaning only a very low fraction of LyC photons could potentially escape their host galaxies (e.g. Heckman et al., 2011). The prime candidates for galaxies that leak LyC photons are thought to be compact, low mass, star-forming galaxies (Cardamone et al., 2009; Izotov et al., 2011; Jaskot & Oey, 2013; Duncan & Conselice, 2015; Chisholm et al., 2017). These are more prevalent at high redshifts (Razoumov & Sommer-Larsen, 2010; Yajima et al., 2011; Zackrisson et al., 2011, 2013; Ma et al., 2020), where galaxies tend to have more massive low metallicity stars (Schaerer, 2003; Johnson et al., 2009; Zackrisson et al., 2011; Conroy & van Dokkum, 2012), as well as higher SFR (e.g. Madau & Dickinson, 2014), than their low redshift counterparts.

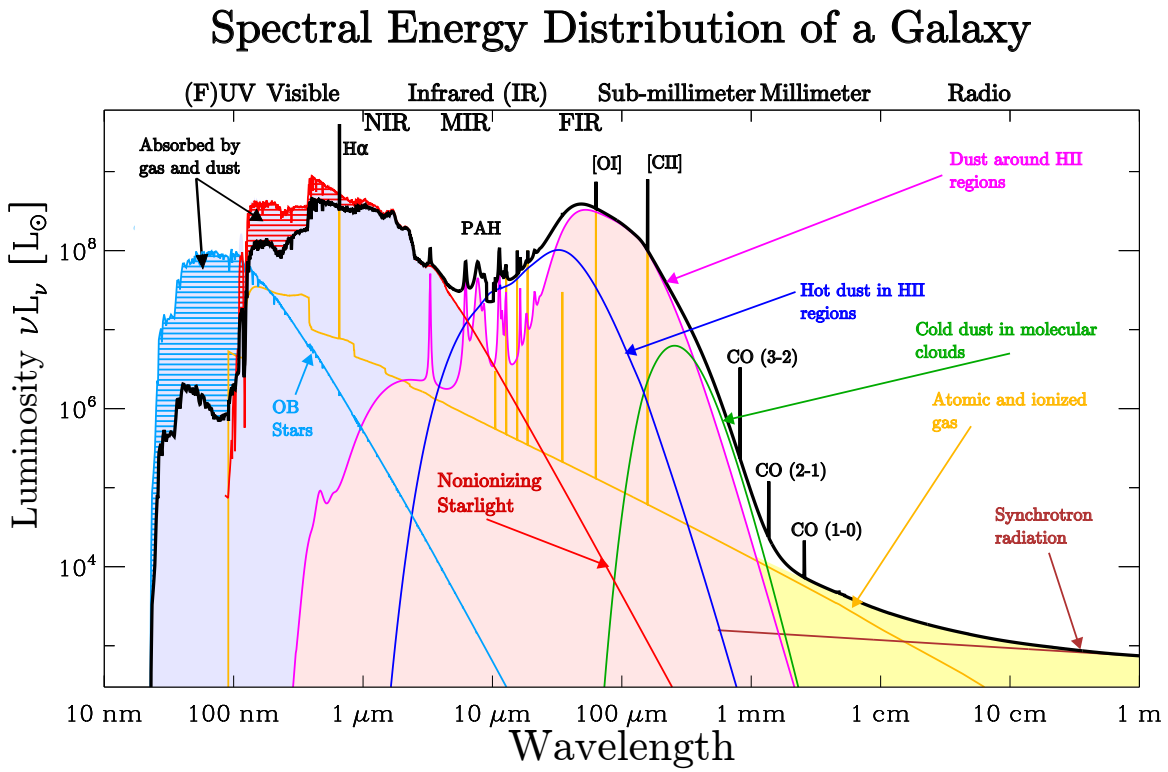

Figure 1.2: An SED of a local star-forming galaxy, adapted from Galliano (2022). The spectrum is composed of contributions from various sources. Hot stars, of type O or B, emit large amounts of radiation at short wavelengths. This is absorbed by gas and dust, which results in a reduction in the expected emission at those wavelengths, indicated by the hatched pattern. The resulting plasma, excited atoms and molecules, and the heated dust, cool radiatively by emitting continuum and line emission. The intensity of each component depends on its various properties, e.g. the overall mass of stars, gas, and dust, the temperature and density of various phases of the ISM, the age of the stellar population, etc. Using physical models and observations at multiple wavelengths reveals the contribution of each component to the SED of a galaxy and their properties.

Nevertheless, only a limited number of LyC leaking star-forming galaxies have been detected at high redshift (Shapley et al., 2006; Iwata et al., 2009; Siana et al., 2010; Nestor et al., 2013; Grazian et al., 2016, 2017; de Barros et al., 2016), in part due to the increasing opacity of the IGM to LyC photons at these epochs (e.g. Haardt & Madau, 2012; Inoue et al., 2014). The few star-forming galaxies that leak LyC photons detected at low redshift have wide range of LyC escape fractions, with values of $1 \sim 15\%$ (Bergvall et al., 2006; Leitet et al., 2011, 2013; Borthakur et al., 2014; Leitherer et al., 2016; Izotov et al., 2016b,a).

The shape of the stellar SED is influenced by its SFH, the usual scenarios considered are steady state star formation, where the SFR is constant over time or instantaneous, where the star formation takes place in a short burst. In the instantaneous case, the peak of the SED shifts to longer wavelengths following the initial burst because the contribution from massive stars diminishes as they die out (Fioc & Rocca-Volmerange, 1997; Leitherer et al., 1999; Robert et al., 2003; González Delgado et al., 2005), and after ~ 1000 Myr, the stellar SED peaks in the NIR (e.g. Fioc & Rocca-Volmerange, 1997). For steady state SFR the SED of the stellar population peaks in the UV range even if the star formation

has been ongoing for 500 ∼ 1000 $M_\odot$ yr^{-1} (e.g. Leitherer et al., 1999), however, a significant number of lower mass stars are created in this time frame, which can contribute significantly to NIR segments of the SED (Fioc & Rocca-Volmerange, 1997; Leitherer et al., 2014). The SED of the non-ionizing radiation from lower mass stars is shown as the red line in figure 1.2. Thus, in principle, for a star-forming galaxy, the emission from its stellar population at UV wavelengths can be used to infer its SFR, the NIR emission can be used to infer its stellar mass, while the ratio of the UV to NIR emission is modulated by its SFH. However, the use of these indicators is complicated by the attenuation of starlight by dust and gas. A substantial part of the energy radiated by stars does not escape the galaxy directly and is instead transferred into the ISM (e.g. Lequeux, 2005; Draine, 2011; Kobayashi & Taylor, 2023). This is particularly significant for radiation from massive stars, as dust preferentially absorbs shorter wavelength radiation (see Sec. 1.1.2), while hydrogen gas readily absorbs absorbs ionizing radiation (see Sec. 1.3.2).

The ISM reradiates this energy at longer wavelengths, usually from MIR to radio (e.g. Draine, 2011; Galliano & Alloin, 2008; Galliano, 2022). The continuum emission from gas (yellow line in Fig. 1.2) covers a wide range of wavelengths from UV to radio. It is, however, usually fainter than the other SED components at submm or shorter wavelengths. It starts dominate the SED at millimeter or longer wavelengths, corresponding to frequencies below ∼ 100 GHz, in the form free-free emission (Condon, 1992; Osterbrock & Ferland, 2006; Wille, 1991; Klein & Fletcher, 2015). At frequencies below ∼ 10GHz, synchrotron emission, caused by electrons interacting with the magnetic fields, dominates the SED (ochre line in Fig. 1.2) (e.g. Klein & Emerson, 1981; Klein, 1988; Gioia et al., 1982). The SN occurring in star-forming galaxies inject high energy electrons in the ISM, and these gyrate along the magnetic field lines, producing synchrotron emission. The synchrotron spectrum is usually modelled as a powerlaw in frequency, observed spectral indices lying in the range $\alpha = 0.4 \sim 1.1$ (e.g. Klein, 1988; Duric et al., 1988; Marvil et al., 2015; Tabatabaei et al., 2017). A break occurs close around a few ∼ GHz, where the spectrum flattens out towards lower frequencies due to absorption (e.g. Hummel, 1991; Wardziński & Zdziarski, 2000; Klein et al., 2018). Line emission from gas can also have intensities well above the continuum level, and some lines, such as the Hα or CO lines shown in Fig. 1.2, are widely used to diagnose the conditions in the ISM (see e.g. Sec. 1.3.2). Emission from CO and other molecular lines, such as HCN, can be used to measure the molecular, and the dense gas masses in a galaxy. Observations revealed that the total luminosity of the HCN line of galaxies, which traces dense gas in GMCs, correlates linearly to its FIR luminosity, and can used to study the star formation efficiency (e.g. Gao & Solomon, 2004; Bigiel et al., 2015; Evans et al., 2020).

The continuum emission from dust heated by massive stars covers wavelengths from MIR to submm (blue, magenta, and green lines in Fig. 1.2). The exact boundaries of the wavelength bands constituting the infrared spectrum vary in the literature, and are somewhat arbitrary, however, a rough definition can be made where NIR, MIR, and FIR correspond to wavelengths in the ranges of $0.8 - 3.5\,\mu$m, $3.5 - 25\,\mu$m, and above 25μm, respectively. Approximately a third of the power radiated by dust is at wavelengths $\lambda \lesssim 50\,\mu m$ (Draine, 2011). Dust emission at IR wavelengths shorter than ∼ 20 μm is mainly the result of emission from hot dust grains having temperatures of ∼ 150 K, or of single photon emission from stochastically heated grains (Calzetti, 2013). The emission spectrum of grains with sizes $\gtrsim 50$ Å heated by a strong radiation field can be approximated by that of a modified black body. Smaller grains, are stochastically heated (Draine, 2011). These small grains have a small heat capacity and cool quickly between photon absorption events (Draine & Li, 2007b) with their temperature varying stochastically, and thus are considered to have a distribution of temperatures (Draine & Li, 2007b; Draine, 2011). At MIR wavelengths, dust emission exhibits spectral emission features due to

vibrational transitions in PAHs (Draine, 2011). The emission features appear as broad emission lines, the strongest of which are centered on the 3.3, 6.2, 7.7, 8.6, 11.3, and 12.7 μm wavelengths, and are seen in Figure 1.2. The FIR dust emission at wavelengths between $20 - 60\,\mu$m is mainly due to large dust grains at temperatures of ~ 50 K (Calzetti, 2013). At these wavelengths dust emission heated by stellar radiation is usually the main component of the SED, while colder dust in molecular clouds dominates the emission at submm and mm wavelengths (see Sec. 1.1.2). The overall shape of the dust SED depends on several factors, such as grain size distribution and chemistry, as well as the stellar radiation field (e.g. Draine & Li, 2007a), meaning dust emission can also be used to trace the SFR (see Sec. 1.3.2).

1.3.2 The star formation rate tracers

Star formation rate tracers usually refer to observable quantities, in the form electromagnetic radiation, that can be used to infer the rate at which stars form. Establishing whether an observable is a reliable SFR tracer often involves comparing it with other, already established tracers. In this section we present several well known SFR tracers, along with their advantages and disadvantages, which are used later in this work.

Due to the high luminosity and short lives of massive O-type stars, many tracers of extragalactic SFR rely either on direct radiation from massive stars, or on the radiation from the ISM affected by the emission of massive stars. These tracers ultimately rely on obtaining an estimate of the photon flux from the young massive stars in the star-forming region. This photon flux together with stellar evolution models is used to obtain the number of young stars in the star-forming region. Using an IMF, the SFR is inferred from the number of young stars. The observed quantity which corresponds to these tracers is thus proportional to the SFR. All the assumptions about the stellar population, the IMF, the SFH, or the ISM, influence the value of the proportionality factor between a specific observable and the SFR. The relation between the SFR and a specific tracer has the logarithmic form (Kennicutt & Evans, 2012):

$$\log\left[\frac{\mathrm{SFR_i}}{M_\odot\,\mathrm{yr}^{-1}}\right] = C_\mathrm{i} + \log\left[\frac{L_\mathrm{i}}{\mathrm{erg\,s}^{-1}}\right], \tag{1.4}$$

where C_i is the calibration constant, or proportionality factor, for tracer i, and L_i is the luminosity of the electromagnetic radiation associated with the tracer i. Depending on the type of tracer, L_i represents either a total luminosity, having units of power, $\mathrm{erg\,s}^{-1}$, or a specific luminosity, having units of power spectral density, $\mathrm{erg\,s}^{-1}\,\mathrm{Hz}^{-1}$.

Stellar emission

Because it relies on stellar radiation, observations of stellar light at UV wavelengths or shorter, is one of the more direct methods of determining the SFR, as it does not rely on the ISM to reprocess stellar emission (e.g. Kennicutt, 1998; Calzetti, 2013). Ultraviolet emission from galaxies, in the range of 1000~3800 Å is mostly emitted by young massive stars of types O to B8 (e.g. Martins et al., 2005; Calzetti, 2013). Thus, the UV flux can be used to determine the number of these massive stars in a galaxy. This number, used together with stellar population models, and assuming an IMF, can be converted into a SFR (e.g. Kennicutt & Evans, 2012). For a conventional IMF (e.g. Kroupa, 2001), the contribution to the UV continuum from the relatively more numerous B8 type stars, having

lifetimes of $\sim$ 300 Myr, can be comparable to that of the much brighter O type stars, with lifetimes of $\sim$ 10 Myr (Calzetti, 2013). Thus, despite the average age of the stellar population responsible for the UV emission being $\sim$ 10 Myr, the average age of stars contributing to $\sim$ 90% of the UV emission is $\sim$ 100 Myr (Kennicutt & Evans, 2012). This means that the total UV emission traces the SFR averaged over the past $\sim$ 100 Myr (Calzetti, 2013; Leitherer et al., 1999; Kennicutt, 1998; Kennicutt & Evans, 2012), with shorter wavelength UV fluxes tracing SFR over shorter timescales (e.g. Leitherer et al., 1999; Kennicutt & Evans, 2012). Thus, when using the UV flux as a SFR tracer, the SFH has to be taken into account (e.g. Calzetti, 2013). Because the lifetime of massive O-type stars is comparable to the timescale needed for young star to clear its surroundings of dust and molecular gas leftover from its formation, dust is likely to be present at the sites of massive star formation (e.g. Wang & Heckman, 1996; Calzetti, 2001; Calzetti et al., 2007), and significantly attenuate the UV emission (see Sec. 1.1.2). Thus, dust extinction constitutes one of the main disadvantages of this SFR tracer. Another shortcoming is that due to the atmosphere of the Earth, observations of the UV continuum emission in the local Universe have to be performed by space telescopes (e.g. Salim et al., 2007). In this work the conversion from $L_{\rm FUV}$ to $\rm SFR_{UV}$ is done following Hao et al. (2011); Kennicutt & Evans (2012):

$$\log\left[\frac{\rm SFR_{UV}}{\rm M_\odot\ yr^{-1}}\right] = -43.35 + \log\left[\frac{L_{\rm FUV}}{\rm erg\,s^{-1}\,\mathring{A}^{-1}}\right] \tag{1.5}$$

which was calibrated using data from the Galaxy Evolution Explorer (GALEX) space telescope (Martin et al., 2005) at $\sim$ 150 nm.

Emission from ionized gas

Around 36% of the emission from O-type stars with a surface temperature of $T \simeq 35000$ K is composed of photons with energies $E_\nu \geq 13.6$ eV (Martins et al., 2005). These photons ionize the hydrogen around the star, creating an HII region. The simplest model for this HII region was first developed by Strömgren (1939). In their model, the ionization rate of hydrogen by stellar radiation is balanced by the recombination rate of hydrogen ions and electrons, inside a spherical region around the star – the so-called Strömgren sphere. At equilibrium, the relation between the ionization and recombination rates is:

$$Q_{\rm H} = V\alpha_{\rm B} n_{\rm e} n_{\rm H^+}, \tag{1.6}$$

where $Q_{\rm H}$ is the stellar photon flux that can ionize H, $V = 4/3\pi R^3$ is the volume of the HII region with radius R, $\alpha_{\rm B}$ is the case B recombination rate, $n_{\rm H^+}$ is the proton density, and n_e is the electron density. Case A and Case B recombination refer to the two possible hydrogen to electron recombination scenarios, in the cases when the gas is optically thin and optically thick to ionizing radiation, respectively. In case A recombination, a transitions to the ground state of hydrogen, i.e. the Lyα line emission, emit photons that can escape the gas. In case B recombination, the gas is optically thick to ionizing radiation, and photons emitted by a hydrogen atom transitioning to the ground state quickly excite a nearby atom out of the ground state. This type of scattering takes place many times before the photon can escape the gas. For the typical HII regions with densities $n_e \gtrsim 10^3$ cm^{-3}, case

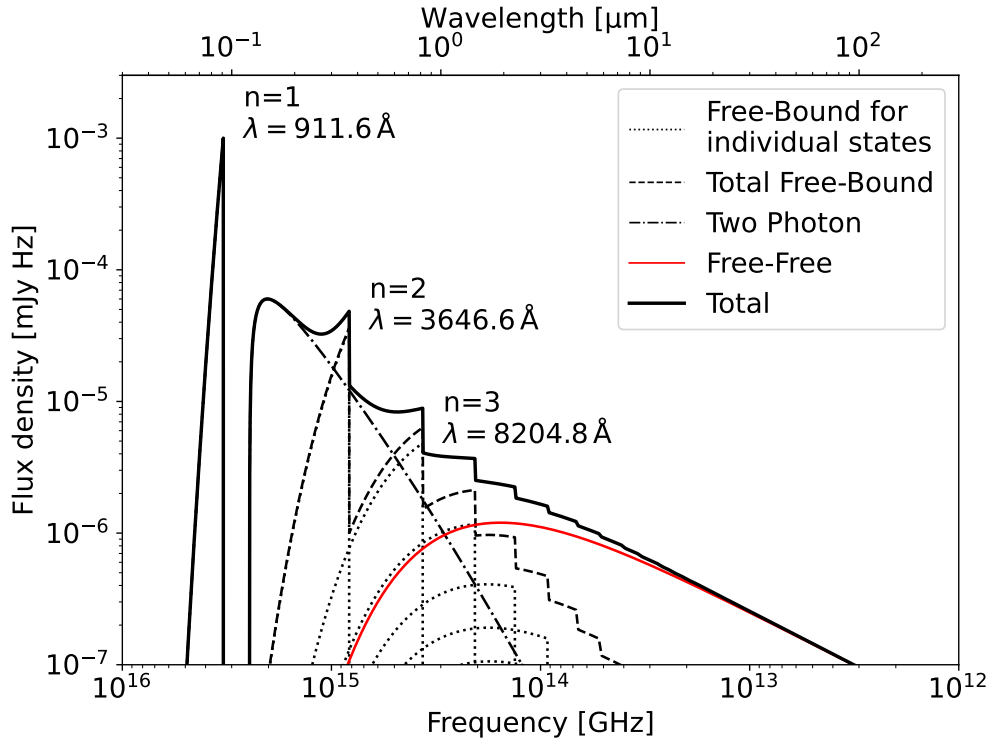

Figure 1.3: The emission of ionized hydrogen gas, at a temperature $T =\sim 8000\,\mathrm{K}$ and density $n_e = 1000\,\mathrm{cm}^{-3}$, adapted from Draine (2011), and also using values from Seaton (1959); Nussbaumer & Schmutz (1984); Osterbrock & Ferland (2006); Nahar (2021). The free-free, free-bound, and two-photon contributions to the overall spectrum are shown. The absolute value of the units on the vertical axis is arbitrary.

B recombination is considered (Draine, 2011). The radius of a Strömgren sphere is:

$$R = \left(\frac{3Q_{\mathrm{H}}}{4\pi n_{\mathrm{e}}^2 \alpha_{\mathrm{B}}} \right)^{1/3}, \tag{1.7}$$

where we consider a fully ionized plasma with $n_e = n_{\mathrm{H}}$. The strongest influence on the radius of a Strömgren sphere is given by its electron density. For an O-type star with $Q_H = 10^{49}\,\mathrm{s}^{-1}$, an electron temperature $T_e = 10000\,\mathrm{K}$ and a low density of $n_{\mathrm{e}} = 100\,\mathrm{cm}^{-3}$, the radius of the sphere is $R \approx 3.16\,\mathrm{pc}$. Keeping the same conditions, but increasing the hydrogen density to a value of $10^5\mathrm{cm}^{-3}$, the radius becomes $R \sim 0.03\,\mathrm{pc}$. Photons with energies above $\sim 24.6\,\mathrm{eV}$ can ionize He^+ ions. In general, He is doubly ionized only in a small sphere surrounding the massive star (Osterbrock & Ferland, 2006). There are however conditions in which all the He inside a Strömgren sphere is ionized. For this to take place, the photon flux that can ionize He^+, Q_{He^+}, has to be significantly higher than Q_{H}. This happens for values of $Q_{\mathrm{He}^+}/Q_{\mathrm{H}} \geq 0.18$ (Draine, 2011), which correspond to stars with masses above $\sim 35\,M_\odot$ (Martins et al., 2005).

The ionized gas in HII regions cools, i.e. loses energy, by emitting radiation through several mechanisms. In the case of HII regions around massive stars, with densities $n_e \sim 10^3\mathrm{cm}^{-3}$, this emission is caused by the so-called free-free and free-bound processes. The spectrum emitted can

be seen in Figure 1.2, and in more detail in Figure 1.3. Free-bound emission occurs when a free electron recombines with a hydrogen ion, ending up in a bound state. The energy of the bound state is quantized, and, together with the ionization cross-section, it varies with the principal quantum number of the state like $E_n \propto 1/n^2$ (e.g. Seaton, 1959; Nahar, 2021). Due to this, the free-bound spectrum has a "ladder"-like appearance (Osterbrock & Ferland, 2006). The direct $2s \rightarrow 1s$ transition of the hydrogen atom is strongly forbidden, so this transition occurs through an intermediary virtual state, with two photons being emitted, resulting in a continuous emission spectrum (Nussbaumer & Schmutz, 1984). This type of transition is slow, and collisions with other particles in the ISM can depopulate the $2s$ level before it takes place (Osterbrock & Ferland, 2006). This is why two photon emission is suppressed in HII regions with $n_e \gtrsim 1000\,\mathrm{cm}^{-3}$ (e.g. Draine, 2011; Osterbrock & Ferland, 2006). This free-bound and two-photon spectrum from HII regions peaks at visible wavelengths, of $100 \sim 300\,\mathring{\mathrm{A}}$, while being significantly dimmer than stellar emission, as can be seen in Fig. 1.2. Free-free emission occurs when a free electron scatters off of an ion in a plasma without recombining, ending up in a free state after the interaction. A brehmsstrahlung photon is emitted during this interaction, and the free-free continuum spectrum is a continuous function of frequency (Osterbrock & Ferland, 2006). Because free-free emission occurs when electrons interact with ions, the intensity of the emitted radiation is proportional to the product between number densities of ions and electrons, n_i and n_e, respectively. The emitted power per unit volume can be written as (e.g. Draine, 2011):

$$\Lambda \propto n_e n_\mathrm{i} \times T^{0.5} \tag{1.8}$$

Integrating this quantity along the line of sight yields a power emitted per surface area, proportional to the emission measure $\mathrm{EM} = \int n_e n_\mathrm{i} ds$. Because the volume of ionized gas depends on the ionizing photon flux, and thus on the mass of the massive star, the strength of the free-free emission can be used to infer the number of massive stars, and thus the SFR. The free-free emission dominates the SED of a galaxy at frequencies of 30-100 GHz, (Condon, 1992; Osterbrock & Ferland, 2006; Galliano, 2022) which is also shown in Fig. 1.2. At these frequencies, the emission is unaffected by interstellar dust. The free-free emission and its use in measuring the SFR are discussed in more detail in section 3.

Hydrogen recombination lines are emitted in HII regions when, after recombination with a proton, the electron in the hydrogen atom undergoes a transition from a higher energy state to a lower energy state, emitting a photon. The nα recombination lines are caused by $n+1 \rightarrow n$ transitions, where $n+1$ and n are the principal quantum numbers of the two states. The energy of the emitted photon is equal to the difference in the energies corresponding to the two states. To a first approximation, the energy of state n in a hydrogen atom is $E_n \propto I_\mathrm{H}/n^2$, where $I_\mathrm{H} = 13.6\,\mathrm{eV}$ is the ionization energy of hydrogen. To first order, the intensity of a H-RL, is also proportional with the EM, meaning H-RLs can be used to measure the ionizing photon flux, and thus the SFR. Some hydrogen recombination lines have wavelengths in the optical regime, such as the Hα at $6564.6\,\mathring{\mathrm{A}}$, shown in Fig. 1.2, and have been used to extensively to measure SFR (Kennicutt & Evans, 2012). The Hα tracer is thus well calibrated, having the form (Murphy et al., 2011; Kennicutt & Evans, 2012)

$$\log\left[\frac{\mathrm{SFR}_{\mathrm{H}\alpha}}{\mathrm{M}_\odot\,\mathrm{yr}^{-1}}\right] = -41.27 + \log\left[\frac{L_{\mathrm{H}\alpha}}{\mathrm{erg\,s}^{-1}}\right], \tag{1.9}$$

while the more general form for Hnα lines, at mm and submm wavelengths, is presented in Chapter 3. The value of $C_{\mathrm{H}\alpha}$ in Eq. 1.9 varies by less than 15% for electron temperatures in the range

$T_e = 5000 - 20000\,\mathrm{K}$ and less than 1% for electron densities in the range $n_e = 10^2 - 10^6\,\mathrm{cm}^{-3}$ (Osterbrock & Ferland, 2006; Calzetti, 2013). Thus, the Hα line luminosity can be robust SFR tracer for a wide range of conditions present in the ISM.

The Hα line, however, as well as the other hydrogen recombination lines having UV or optical wavelengths, are attenuated by dust (Kennicutt & Evans, 2012). A model of the dust and multiple line observation are therefore needed to infer the amount of attenuation and the true line luminosity (Buat, 2002; Kennicutt & Evans, 2012; Vale Asari et al., 2020). A way to overcome this problem would be to use long wavelength H-RLs, e.g., cm-RL or mm-RL, which are not attenuated by dust. A shortcoming of using longer wavelength H-RLs is the influence that the often unknown electron temperature and density in an HII region have on the intensities of these lines. Unlike optical H-RLs, the intensity of mm-RL can vary by more than a factor ~ 2 between $\sim 5000\,\mathrm{K}$ and $\sim 20000\,\mathrm{K}$ ((e.g. Gordon & Sorochenko, 2002; Calzetti, 2013) as well as Chp. 3). The temperature can however be estimated from the ratio between the intensities of the mm-RL and the continuum free-free emission ((e.g. Gordon & Sorochenko, 2002; Bendo et al., 2015) as well as Sec. 3.4). Another potential disadvantage of long wavelength RL is their intrinsic faintness (Gordon & Sorochenko, 2002; Calzetti, 2013). The overall intensity of recombination lines is roughly proportional to the inverse square of their frequency, making extragalactic observations difficult (Gordon & Sorochenko, 2002). Finally, unlike their short wavelength counterparts, H-RL emission at centimeter wavelengths can be affected by maser amplification, although how important the maser effect is at millimeter wavelengths is not yet clear (Gordon & Sorochenko, 2002). The properties of mm-RL, the influence of the electron density and temperature on their intensities, their relationship to the SFR and their potential use as a diagnostic for the state of ionized gas in SFR regions are rederived and studied in more detail in Chapter 3.

The timescale for the formation or destruction of a HII region around a massive star is of the order $\tau \approx 1.1 \times 10^5 / n_\mathrm{H}\,\mathrm{yr}$, where n_H is the hydrogen density in units of cm^{-3} (Sabatini et al., 2021). For densities typical of HII regions around young massive stars, $n_\mathrm{H} \gtrsim \sim 10\,\mathrm{cm}^{-3}$, this timescale is much shorter than the main sequence lifetime of massive O-type stars. The ionizing photon flux, and thus the emission from ionized gas, decreases by several orders of magnitude between ~ 5 and $\sim 10\,\mathrm{Myr}$ after an instantaneous burst of star formation (e.g. Leitherer et al., 1999; Robert et al., 2003; Calzetti, 2013). Thus, emission from ionized gas traces SFR averaged over the past $\sim 10\,\mathrm{Myr}$ (e.g. Leitherer et al., 1999; Kennicutt & Evans, 2012), making free-free and H-RL emission instantaneous tracers of SFR.

Emission from interstellar dust

Interstellar dust attenuates light through absorption and scattering, a phenomenon also called extinction (e.g. Draine, 2011). The wavelength dependence of extinction is shown in figure 1.4. Several broad absorption features in the dust extinction curve, of which the one at 2175 Å is shown, are due to carbon, Si-O, and O-Si-O bonds in the dust grains (Draine, 2011). Although the exact shape of the extinction curve depends on the on the chemical and physical properties of the grains and their size distribution, the overall trend with wavelength remains similar, extinction is stronger towards shorter wavelengths. This implies that dust would preferentially interact with the short wavelength, e.g. UV, light from young massive stars, providing the first clue that dust emission could be used as a SFR tracer (e.g. Calzetti, 2013; Kennicutt & Evans, 2012). The amount of dust along the direction of light propagation, i.e. the dust column density, also determines the level of attenuation, and thus the amount of extinction.

Dust grains are radiatively heated, mainly by stars (e.g. Draine & Li, 2007a; Draine, 2011), while

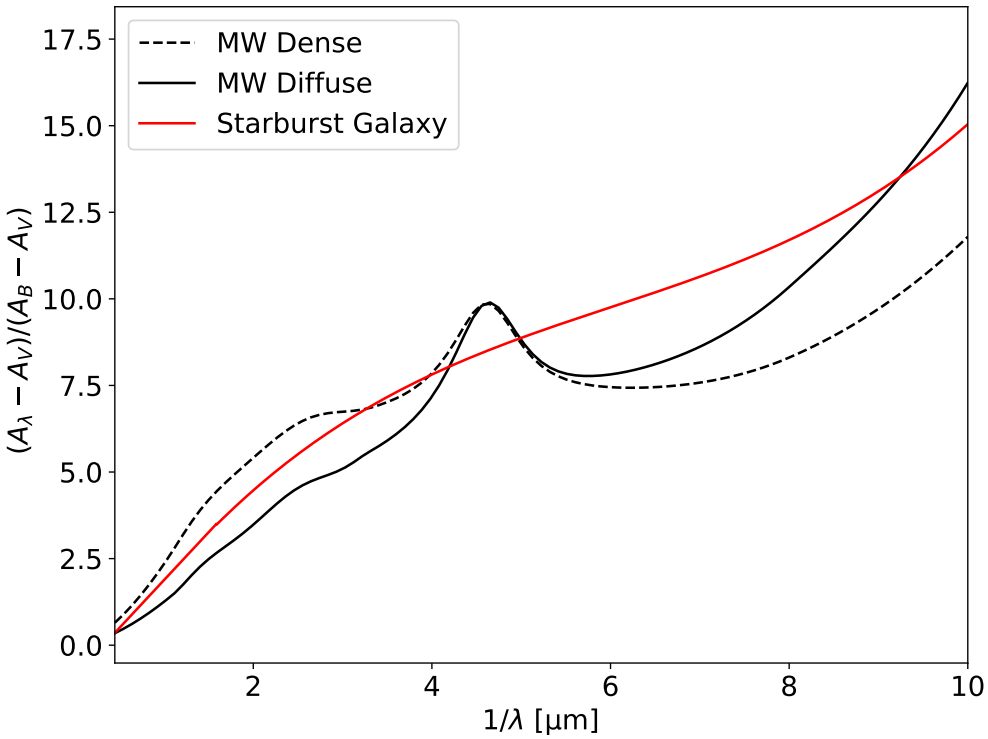

Figure 1.4: Average dust extinction curves, characterizing the attenuation of light at a given wavelength λ. The extinction at a given wavelength, A_λ, is expressed in magnitudes. The different curves correspond to different directions inside the Milky Way, and to the average extinction in starburst galaxies, where intense star formation takes place. Light at shorter wavelengths is preferentially attenuated. The spectral feature at 2175 Å, due to carbon grains, is visible in the MW extinction curves.The data for the MW curves is taken from Gordon et al. (2003), while the data for the starburst galaxy is from Calzetti et al. (2000).

collisional heating, where dust is heated by the collisions with the surrounding gas particles, becomes important only inside dark molecular clouds, at high gas and low UV photon densities (Draine, 2011). Interstellar dust cools radiatively, emitting photons at infrared wavelengths (Draine, 2011). In thermal equilibrium, when dust heating and cooling rates are equal, the power radiated by dust equals the power it absorbs from stars. The total infrared luminosity, $L_{\rm TIR}$, represents the total power radiated in the infrared by a galaxy, conventionally measured in the $8 - 1000\,\mu$m wavelength range (e.g. Murphy et al., 2011). Dust absorbs $\sim 33\%$ of the starlight in the Milky Way (Draine, 2011), similar to other late-type galaxies, where dust absorbs $5-25\%$ of the stellar radiation (Paspaliaris et al., 2021). In dusty galaxies undergoing intense star formation, such as (ultra) luminous infrared galaxies, or (U)LIRGs, dust absorbs $\sim 80\%$ of the stellar radiation (Paspaliaris et al., 2021), and the FIR luminosity of these galaxies exceeds those at other wavelengths (e.g. Sanders et al., 2003; Piqueras López et al., 2013; Kennicutt & Evans, 2012; Lonsdale et al., 2006). Furthermore, $\sim 92\%$ of the radiation from young massive stars contributes to the dust heating in (U)LIRGS (Paspaliaris et al., 2021), meaning that their infrared luminosities are a good indicator of their overall SFR.

The power emitted in the infrared by a dust grain with temperature T at frequency ν, can be approximated as $P(\nu) = 4\pi C_{\rm abs}(\nu) B_\nu(T)$, (Li & Draine, 2001), where $C_{\rm abs}(\nu)$ is frequency dependent

absorption cross-section of the grain, and B_ν is the Planck function. In the simplest models, the absorption cross-section depends on frequency as a powerlaw, with $C_{\rm abs} \propto \nu^\beta$, for low energy photons with wavelengths larger than the grain diameter (e.g. Draine & Lee, 1984; Li & Draine, 2001; Draine, 2011). Emission from grains with often unknown size, temperature, and shape distributions, having various chemical compositions, contribute to the infrared luminosity of a galaxy, $L_{\rm TIR}$, which makes a theoretical formulation of dust emission challenging. Nevertheless, observations have revealed that it is often appropriate to model the FIR SED of a galaxy as a modified black body function,

$$f_\nu(T_{\rm dust}) \propto B_\nu(T_{\rm dust})\nu^\beta, \tag{1.10}$$

where f_ν is flux density, β is the dust thermal emissivity spectral index (e.g. Calzetti et al., 2000; Dunne et al., 2000; Dunne & Eales, 2001; Franceschini, 2000). This model makes several simplifying assumptions, one of them being that the dust can be characterized by a single temperature, $T_{\rm dust}$, and that the emission is optically thin. More complicated models can include multiple temperature components, which correspond to a hot and a cold dust grain population, respectively, multiple grain populations, having different size distributions (e.g. Draine & Li, 2007a), and multiple spectral indices to correct for optical depth effects towards MIR wavelengths, or corrections for optically thick emission (e.g. Blain et al., 2003; Casey, 2012).

Integrating over the infrared SED of a galaxy, that was fit to the observed dust emission, yields the total infrared flux of the galaxy, which together with the distance, gives its total infrared luminosity, $L_{\rm TIR}$. Because $L_{\rm TIR}$ is equal to the power absorbed by dust at shorter wavelengths, which in star-forming galaxies is dominated by the UV flux from massive stars, measuring $L_{\rm TIR}$ is an indirect measurement of the obscured UV luminosity, $L_{\rm UV}$. If all of the UV light in a galaxy is absorbed by the dust, $L_{\rm TIR}$ can provide a complete measure of its SFR. Thus, the total infrared luminosity $L_{\rm TIR}$ can be a robust SFR tracer, provided the dust SED, thus the total infrared flux, can be determined. The relation used in this work is (Murphy et al., 2011)

$$\log\left[\frac{\rm SFR_{TIR}}{\rm M_\odot\,yr^{-1}}\right] = -43.41 + \log\left[\frac{L_{\rm TIR}}{\rm erg\,s^{-1}}\right]. \tag{1.11}$$

Because dust is mainly heated by non-ionizing UV radiation, $L_{\rm TIR}$ traces SFR averaged over timescales of $\sim 100\,M_\odot\,{\rm yr}^{-1}$, similar to those of the SFR tracer based on $L_{\rm UV}$ (see Sec. 1.3.2). Empirical relations have been developed that link $L_{\rm TIR}$ to the luminosity in one or a few IR bands, e.g. the $L_{24\,\mu\rm m}$ (e.g. Calzetti et al., 2007). Ideally, however, an accurate determination of $L_{\rm TIR}$ requires multiple observations in the $\sim 8 - 1000\,\mu$m wavelength range, that also sample the peak of the dust emission in the $40 - 100\,\mu$m wavelength range. This is one of the disadvantages of this tracer, as these observations are not always available. Another disadvantage of using $L_{\rm TIR}$ as a SFR tracer is that it does not account for the stellar radiation that is not absorbed by dust, however, this effect is not important in the case of starbursts and other dusty galaxies where intense star formation takes place (Calzetti, 2013; Kennicutt & Evans, 2012). Nevertheless, this problem can be mitigated by complementing infrared observations with those at shorter, e.g. UV, wavelengths (Murphy et al., 2011). The contribution to the of older stars with ages above $100 - 200$ Myr to the dust heating can also be significant, and can potentially lead to an overestimation of the SFR. However, this effect is not significant in actively star-forming galaxies or regions (Kennicutt & Evans, 2012), such as those studied in this work. Thus, the conversion of $L_{\rm TIR}$ to SFR is affected by assumptions regarding the

SFH and the IMF of the stellar populations. In this work we assume a Kroupa (2002) IMF for stellar masses in the range $0.1 - 100\,M_{\odot}$, and a constant star formation over the past 100 Myr.

1.4 A brief overview of star-forming galaxies

Optical observations of local galaxies reveal a bimodal distribution of their colors, corresponding to two broad categories: blue star-forming disk galaxies and the so-called passive, "red and dead" elliptical galaxies, where almost no star formation is taking place (Strateva et al., 2001; Balogh et al., 2004; Baldry et al., 2004; Gabor et al., 2010). The star-forming galaxies are usually encountered in field regions, while the ellipticals reside mostly in galaxy clusters (e.g. Balogh et al., 2004; Gabor et al., 2010; Weinmann et al., 2009; Baldry et al., 2006). More distant galaxies, up to redshift $z \simeq 2$, have also been found to follow this bimodal distribution (e.g. Brammer et al., 2009; Taylor et al., 2009; Weiner et al., 2005; Willmer et al., 2006).

star-forming galaxies show a correlation between their stellar mass, M_*, and their SFR, known as the main sequence of star-forming galaxies (Brinchmann et al., 2004; Daddi et al., 2007; Noeske et al., 2007; Caputi et al., 2006). This relation between the SFR and M_* of star-forming galaxies has the form of a powerlaw, SFR $\propto M_*^{\alpha}$. It is valid for the local as well as the early Universe (Daddi et al., 2007; Elbaz et al., 2007; Rodighiero et al., 2011; Schreiber et al., 2015; Popesso et al., 2019), its index α and its scatter remaining roughly constant over cosmic time (Daddi et al., 2007; Elbaz et al., 2007; Speagle et al., 2014; Ilbert et al., 2015; Schreiber et al., 2015). This indicates that the same mechanism could regulate galaxy evolution across a wide range of masses (Noeske et al., 2007), and that most of the stellar mass is the result of steady state SFR (Mancuso et al., 2016). Passive galaxies are located well below this main sequence. Starburst galaxies or regions, are located above the main sequence, and have SFR orders of magnitude larger than the main sequence values for their stellar mass (e.g. Lee et al., 2017; Rodighiero et al., 2011; Muxlow et al., 2006; Elbaz et al., 2018). The periods of high SFR associated with starbursts have a duration of the order of $10 \sim 200$ Myr, a fraction of the life of a galaxy (Thornley et al., 2000; Di Matteo et al., 2008; McQuinn et al., 2009; Wilkinson et al., 2018; McQuinn et al., 2018). Nevertheless, starburst episodes are estimated to have contributed $\sim 10\%$ of the stellar mass of present day galaxies with $10^{10}\,M_{\odot} \leq 10^{11.5}\,M_{\odot}$ (Lamastra et al., 2013).

As presented in Sec. 1.2, molecular gas is needed for star formation, a fact that is reflected in the observed correlation between the gas and the star formation rate surface density of a galaxy known as the Kennicutt-Schmidt law (Schmidt, 1959; Kennicutt, 1998). Thus, a rough picture of galaxy evolution emerges: the stellar mass of galaxies increases as the molecular gas is converted into stars; galaxies accrete gas from the intergalactic medium (Kereš et al., 2005; Birnboim & Dekel, 2003; Dekel et al., 2009; Faucher-Giguère et al., 2009; van de Voort et al., 2011; Joung et al., 2012), allowing star formation, and thus mass growth, to continue over extended periods of time without the gas being depleted; once the gas is depleted, the star formation ends. The sporadic increase in SFR, revealed by the presence of starburst galaxies, is thought to be caused either by galaxy mergers (e.g. Mihos & Hernquist, 1996; Daddi et al., 2007; Elbaz et al., 2007; Lamastra et al., 2013; Calabrò et al., 2019), stellar driven gravitational instabilities (e.g. Inoue et al., 2016; Romeo & Fathi, 2016; Tadaki et al., 2018), or simply galaxies with a very large initial gas reservoir (Scoville et al., 2014, 2017; Genzel et al., 2015).

Due to dust being a byproduct of stellar evolution, and due to its association with cold molecular gas, galaxies where intense star formation has been ongoing for extended periods of time are likely to

contain large amounts of dust and be strong infrared emitters (see Sec. 1.3.2). Galaxies with infrared luminosities above $10^{11}\,L_{\odot}$, known as luminous infrared galaxies (LIRGS) (Sanders & Mirabel, 1996), were first discovered with the Infrared Astronomical Satellite (IRAS) space telescope (Soifer et al., 1984). Further observations established the ultra, hyper, and extremely infrared luminous galaxies (ULIRG, HyLIRG, and ELIRG), with infrared luminosities exceeding $10^{12}\,L_{\odot}$ (Houck et al., 1985), $10^{13}\,L_{\odot}$ (Rowan-Robinson et al., 1991), and $10^{14}\,L_{\odot}$ (Tsai et al., 2015), respectively. The defining characteristic of these galaxies is their infrared luminosity caused by thermal emission from dust which exceeds that of all other wavelengths combined (e.g. Lonsdale et al., 2006). Arp220 is an archetypal ULIRG and starburst galaxy, with an infrared luminosity of $\sim 2\times10^{12}\,L_{\odot}$ corresponding to a SFR$\sim 200\,M_{\odot}\,\mathrm{yr}^{-1}$ (e.g. Anantharamaiah et al., 2000; Sanders et al., 2003). Using infrared space telescopes, such as Spitzer or Herschel (Werner et al., 2004; Pilbratt et al., 2010), these infrared galaxies are easily detected (e.g. Armus, 2014; Rosenberg et al., 2015; Rawle et al., 2016; Chu et al., 2017a). Because dust severely attenuates UV emission, their bright FIR emission of these (U)LIRGS alone could be used to measure their SFR. This SFR value based a well established tracer can then be compared with the SFR derived from a tracer which is not affected by dust, like mm-RL. Furthermore, their high SFR increases the likelihood of detecting the faint mm-RL emission. Thus, dusty star-forming galaxies, such as (U)LIRGS, are ideal targets for testing the reliability of using mm-RL as SFR tracers.

Although most of the infrared emission of local (U)LIRGs is due to intense star formation, the more luminous infrared galaxies can also host an active galactic nucleus (Downes & Solomon, 1998; Gao & Solomon, 2004; Veilleux, 2006, 2008; Veilleux et al., 2009). Galaxies with active galactic nuclei (AGN), exhibit strong emissions at X-Ray, UV, infrared, and radio wavelengths, from a compact region in their nucleus (e.g. Alloin et al., 1995; Edelson & Malkan, 1986; Elvis et al., 1978; Hewitt & Burbidge, 1993; Shields, 1990; Antonucci, 1993; Netzer, 2015). The source of these emissions is a super massive black hole (SMBH) fed by an accretion disk surrounded by a dust torus (e.g. Antonucci, 1993; Urry & Padovani, 1995; Netzer, 2015). The strong X-Ray and UV emission from the accretion disk heats the dust torus (e.g. Barvainis, 1987; Calderone et al., 2012), and the radiation from both can contaminate the ionized gas and dust emission SFR tracers. Thus, the presence of an AGN in a galaxy has to be taken into account when measuring the SFR.

1.5 Motivation

Although a variety of SFR tracers have been established and used to study galaxy evolution over cosmic time, each of these tracers has some drawbacks due to the physical interactions between different components of a galaxy. In particular, the well-established SFR tracers, such as the Hα line emission from ionized gas and the UV stellar continuum, cannot be used alone in the presence of interstellar dust to account for all the SFR in a galaxy. The inclusion of tracers that are sensitive to the dust-obscured star formation, such as far-infrared emission, is then required to obtain the total SFR. Tracers based on dust emission, however, require information about the dust content of a galaxy as well as its properties (e.g. Draine & Li, 2007a). Instead of the complex combination of UV/optical and IR-based SFR tracers, one could consider direct tracers that are unaffected by obscuration, such as free-free and radio H-RL emission. Free-free emission is difficult to disentangle from the underlying dust and synchrotron emission, leaving radio H-RL as a potential tracer unaffected by the presence of dust. Among radio H-RL, mm-RL have an advantage over the longer wavelength cm-RL in that they

are less affected by stimulated emission and could also be used to determine the properties of HII regions (e.g. Gordon & Sorochenko, 2002; Zhu et al., 2019). So far, extragalactic mm-RL observations have been hampered by the fact that these lines are intrinsically faint (e.g. Gordon & Sorochenko, 2002; Bendo et al., 2017). Developments in radio telescope technology that began in the last decade and will continue into the future can now help overcome this problem.

To overcome the faint nature of mm-RL, the first observations targeted galactic regions, such as the Omega or Orion regions, and were used to measure their electron temperatures, finding values of $T_e \sim 7000$ K (Sorochenko et al., 1969; Sorochenko & Berulis, 1969; Waltman et al., 1973; Wilson & Pauls, 1984). Further galactic surveys of mm- and cm-RL found the electron temperatures of HII to be in the range of $\sim 3000 - 8000$ K (Gordon, 1989; Lockman, 1989; Quireza et al., 2006a; Law et al., 2009), and established the existence of a temperature gradient with distance from the galactic center (e.g. Quireza et al., 2006b). Recent mm-RL surveys of HII regions associated with massive star-forming clumps in our Galaxy found no evidence for maser amplification, determined their electron density at $n_e \sim 10^4 - 10^5$, and found that most of these regions are compact, with diameters of $0.01 - 0.1$ pc (Kim et al., 2017, 2018). Another survey of 146 massive galactic star-forming regions found a correlation between their H40α line luminosity and the SFR derived from their bolometric luminosity for SFR $> 5 \times 10^{-6}\,M_\odot\,yr^{-1}$ (Zhang et al., 2022a). This suggests that for our Galaxy, mm-RL trace massive star formation and are a good SFR indicator (Zhang et al., 2022a).

Early observations of extragalactic radio H-RL targeted nearby galaxies at centimeter or decimeter wavelengths, corresponding to frequencies between 1.4 and 14 GHz (Gordon & Sorochenko, 2002). The first dm- and cm-RLs were detected in nearby, bright, star-forming galaxies such as M82 and NGC253. The H85α, H102α, H110α, and H166α lines were detected in M82, a prototypical star-forming galaxy, and their comparison shows that maser amplification contributes more than 70% of their intensity, increasing with wavelength (Bell & Seaquist, 1978; Shaver et al., 1977, 1978). Similarly, the H92α, H102α, H110α, and H166α lines have been detected in the star-forming galaxy NGC253 (Anantharamaiah & Goss, 1990; Seaquist & Bell, 1977). The H92α at 8.3 GHz has been detected in several other nearby, usually star-forming galaxies, such as NGC0660, NGC1365, NGC2146, NGC3628, NGC3690, IC694, M83, and Arp220 (Phookun et al., 1998; Puxley et al., 1991; Anantharamaiah et al., 1993; Zhao et al., 1996, 1997; Anantharamaiah et al., 2000). These early extragalactic detections were modeled as arising from collections of HII regions with diameters $\sim 0.2 - 5$ pc, electron densities $n_e = 10^3 - 10^5$ cm^{-3}, and temperatures $T_e = 5000 - 10000$ K (Phookun et al., 1998; Anantharamaiah et al., 1993; Gordon & Sorochenko, 2002).

Early extragalactic mm-RL detections with single dish telescopes were made only in a few nearby star-forming galaxies, such as NGC253 (Puxley et al., 1997; Martín et al., 2006), Arp220 (Anantharamaiah et al., 2000), M82 (Puxley et al., 1989; Seaquist et al., 1994, 1996) and M83 (Puxley et al., 1991). These observations showed that two components, a dense ionized gas component ($n_e \gtrsim 10^5$ cm^{-3}) with a low filling factor in the form of compact HII regions and a diffuse component ($n_e = 1 \sim 100$ cm^{-3}) with a high filling factor, are needed to explain the intensities of the mm-RL together with those of the cm-RL. No clear evidence for maser amplification or optically thick mm-RL emission was found for most of the observed lines. By comparing the mm-RL intensities with those of lines at shorter wavelengths, such as Brγ, it was found that the dust extinction in NGC253 is also significant at IR wavelengths, with $A_V = 35 \sim 80$(Puxley et al., 1997). After the commissioning of the ALMA telescope, the number of extragalactic mm-RL detections increased. Millimeter recombination lines have been detected in NGC253 (Bendo et al., 2015; Báez-Rubio et al., 2018), NGC4945 (Bendo et al., 2016), NGC3256 (Michiyama et al., 2020), and NGC5253 (Bendo et al., 2017). Compared

to single-dish observations, these high-resolution ALMA studies reveal the spatial distribution of electron temperatures in these extragalactic star-forming regions. Despite probing different spatial scales and regions with different star-forming activities, their electron temperatures were found to be in good agreement with each other, with values of $\sim 3000 - 7000$ K, and the SFR derived from mm-RL is in general agreement with that derived from other tracers. Thus far, these ALMA observations of galactic and extragalactic star-forming regions have shown mm-RL to be a promising SFR tracer.

Despite the encouraging initial results that mm-RL are a reliable tracer of galactic and extragalactic SFR, it remains unclear to what extent extragalactic mm-RL are affected by maser amplification. Observations of H41α and H30α mm-RL from M82 showed no evidence of line amplification (Seaquist et al., 1994). However, the intensity of the H27α line in M82 was found to be much larger than expected, indicating that maser amplification is occurring (Seaquist et al., 1996). The values of the relative intensities of different mm-RLs observed in other galaxies also suggested that line amplification might be taking place, but a definitive picture could not be established (Zhao et al., 1996; Phookun et al., 1998; Anantharamaiah et al., 2000). More recently, using sub-arcsecond resolution ALMA observations of the H30α and H26α lines, Báez-Rubio et al. (2018) report the detection of a hydrogen recombination line maser in the very center of NGC253. All these results suggest that conditions leading to mm-RL maser amplification can be found in extragalactic sources, which warrants a closer study of this phenomenon.

The overall picture provided by these mm-RL studies is limited by the low number statistics and the relatively poor sampling of different star-forming environments. In addition, non-detections of mm-RLs have rarely been reported, raising the possibility that we have a biased sample of detected regions. To test the reliability of mm-RLs as SFR tracers in a variety of different star-forming environments. For this reason, and to overcome the challenges associated with observing mm-RLs, we first rederive some of the equations that describe mm-RL emission, transfer, and relation to the SFR. Using these equations, we perform new calculations to determine the conditions for optically thick emission, line amplification, and attenuation of mm-RL. We use our own observations of six nearby star-forming galaxies, and also use existing ALMA archival data of another twenty nearby star-forming galaxies, to build a catalog of mm-RL detections. The SFRs of the galaxies are then calculated from the mm-RL intensity, the free-free continuum, and compared with the SFR derived from the infrared luminosity. We also estimate the capabilities of ALMA to observe mm-RL in star-forming extragalactic regions.

CHAPTER 2

Data and Methods

The most straightforward way to test the reliability of mm-RL as a SFR tracer for extragalactic sources is to compare their SFR obtained from mm-RL observations with their known SFR derived using other established tracers. For a robust calibration, ideally a large sample consisting of star-forming galaxies covering a wide range of SFR is required. Because of the difficulties associated with mm-RL observations, i.e. their faintness, successful mm-RL detections require ample observing time, which is not always available. In order to increase the sample size, we performed our own mm-RL observations and also mined the ALMA archive in search of mm-RL detections. By combining the ALMA archival data with other existing continuum observations between 1.4 and ~ 450 GHz, which include VLA and ATCA data, we fit the radio to submm SED to also extract the free-free continuum flux emitted by the regions where mm-RLs are detected. The SFR is calculated from the mm-RL data as well as from the dust TIR emission. For a meaningful comparison, we calculated the $L_{\rm TIR}$ corresponding only to the regions covered by the mm-RL observations, or exhibiting mm-RL emission. The value of $L_{\rm TIR}$ was obtained by integrating over the FIR SED of the observed regions. The SEDs were determined by fitting models to, where available, MIR, FIR, and submm fluxes extracted from archival data from Spitzer, Herschel, APEX, and ALMA. In some cases fitting SED models to incomplete FIR data was required, containing upper limits instead of complete measurements. For these cases, we developed an algorithm using Bayesian methods together with the`emcee` python package (Foreman-Mackey et al., 2013) to fit SED models to data containing upper limits.

2.1 Data

2.1.1 Single dish and interferometric radio telescopes

Radio telescopes detect electromagnetic waves from astronomical sources, having wavelengths ranging from submillimeter to several meters, corresponding to frequencies of a few hundred GHz to a few tens of MHz. The power of the electromagnetic waves of a given frequency arriving from the observed source and collected by the antenna of the telescope is:

$$P_\nu \propto A_{\rm eff} \times F_\nu, \tag{2.1}$$

where $A_{\rm eff}$ is the effective collecting area of the antenna, and F_ν is the flux density of the source, with units of power, per unit area per unit frequency. A customary unit for flux density in radio astronomy

is the Jansky, where $1\,\mathrm{Jy} = 10^{-23}\,\mathrm{erg\,s^{-1}\,Hz^{-1}\,cm^{-2}}$. Using the Raileigh-Jeans approximation of Planck's law, P_ν can be expressed as a function of temperature, leading to:

$$F_\nu = \frac{2k_\mathrm{B}}{A_\mathrm{eff}} T_\mathrm{A}, \tag{2.2}$$

where T_A is the so-called antenna temperature and k_B is Boltzmann's constant. The actual quantity that is measured at the telescope is the T_A, which then can be used to determine flux density of the source. This is usually done through multiplication by the sensitivity factor $(2k_\mathrm{B}/A_\mathrm{eff})$, having units of Jy/K, that depends on the properties of each telescope. Single dish telescopes have a spatial angular resolution $\theta \propto \lambda/D$, where λ is the observing wavelength and D is the antenna diameter. This resolution is the result of the sensitivity of the receiving antenna being at maximum towards the direction of the antenna axis, and becoming lower for off axis directions. The sensitivity profile of a single dish telescope, which can be expressed as the fraction of power received as a function of this off axis angle, is also known as the telescope beam. In practice, the resolution is expressed as the full-width half maximum (FWHM) of the beam, or the half-power beam width (HPBW). These quantities represent the angle where the power received by an antenna has dropped to half its maximum value. For a uniformly illuminated dish with diameter D, observing at a wavelength λ, we have:

$$\mathrm{HPBW} \simeq 70^\circ \times \frac{\lambda}{D}. \tag{2.3}$$

The IRAM 30m telescope, located in the Sierra Nevada mountains of Spain, is one of the largest and most sensitive single-dish radio telescopes at millimeter wavelengths. It has a 30m diameter main dish. The telescope is equipped with several heterodyne receivers covering frequencies from 70 to 365 GHz (Carter et al., 2012), as well as a continuum camera that operates at submillimeter wavelengths (Adam et al., 2018). Its HPBW varies from 9.5" to 28.5" for frequencies ranging from 260 to 86 GHz (Mauersberger, 2003). Its high-altitude location and stable atmospheric conditions enhance its observing efficiency and allow it to operate at submm wavelengths.

Radio interferometers, instead, use multiple antennas to increase the resolution and sensitivity of observations. Radio interferometers record the correlation, i.e. interference, between the electromagnetic radiation detected by each pair of antennas in the array. Due to the geometry of a radio interferometer, there is a time delay between the arrival times of the electromagnetic wave reaching any pair of antennas. The time delay introduces a phase difference between the signals detected by the two antennas, which determines their degree of correlation. The correlated signal is zero when the two signals are completely out of phase and proportional to their amplitude when the signal are in phase. The correlated signal is thus a periodic function of the orientation angle of the arriving emission. The period of this function depends on the ratio between the observing wavelength, λ, and the distance between the antennas known as the baseline, D_B. Thus, any two antennas can only detect signals that are distributed over angular scales having a size $\theta \lesssim \lambda/D_\mathrm{B}$, effectively sampling a point in the Fourier transform of the brightness distribution of the sky, called the Fourier plane. The maximum recoverable scale that can be detected depends on the shortest baseline, while the maximum achievable resolution is given by the longest baseline. The resulting data collected from each antenna pair is called the visibility, and is a sparse sample of the Fourier plane. The visibility is a complex

function and has the form:

$$V(u,v) = \int \int B(\xi,\eta) \cdot e^{-i2\pi(u\xi+v\eta)} d\xi d\eta, \tag{2.4}$$

where u and v are the coordinates of the sample in the Fourier plane, and $B(\xi,\eta)$ is the sky brightness on the sky given by the direction cosines ξ and η. To obtain the original brightness distribution of the source, the inverse Fourier transform is performed on this visibility function. Because the visibility does not cover all of the Fourier plane, the resulting image exhibits artifacts stemming from the missing information and is also known as the dirty image. Through a process called deconvolution, or cleaning, the dirty image is processed to obtain an image that is closer to the true sky brightness distribution. Several algorithms exist to perform this task, such as CLEAN (Högbom, 1974), Clark (Clark, 1980), CS Clark (Schwab, 1984) etc.

The ALMA telescope is a radio interferometer in the Chilean Atacama desert, consisting of two independent arrays of antennas: fifty 12 m antennas constitute the main array and sixteen 7 m antennas constitute the ALMA Compact Array (ACA) (Remijan et al., 2019). ALMA can perform observations in multiple frequency bands, from ~ 35 GHz to ~ 950 GHz (Remijan et al., 2019). Its antennas can change positions, resulting in different array configuration that determine its angular resolution. The typical angular resolution of ALMA at 80 ~ 350 GHz ranges from ~ 1" to ~ 0.1" (Remijan et al., 2019). The maximum achieved resolution is, however, of the order of ~ 0.005" (Asaki et al., 2023). Its large combined collecting area of 6600 m^2 and its high altitude location in a dry area make ALMA the most sensitive millimeter and submillimeter telescope in the world. Its unprecedented sensitivity make it an ideal choice for the observation of faint mm-RL lines.

2.1.2 Our ALMA archival sample

Millimeter recombination lines can be detected by ALMA in nearby galaxies (e.g. Bendo et al., 2015, 2016, 2017; Michiyama et al., 2020). However, because of the time requirements for a successful detection, mm-RL they have only been the subject of a handful of dedicated ALMA observations (e.g. Scoville et al., 2013). Nevertheless, the frequencies of some mm-RL are close to those of other prominently observed lines, e.g., the H40α and CS(2-1) lines at 99.02 GHz and 97.98 GHz, respectively, or the H30α and CO(2-1) lines at 231.9 GHz and 231.5 GHz, respectively. Typical ALMA observations have a total bandwidth of ~ 8 GHz, so it is likely that observations targeting one of those molecular lines also cover recombination line emission. We thus used the extensive and ever growing ALMA archive to look for mm-RL detections. The ALMA archival sample was constructed by mining the ALMA archive for observations of the brightest infrared galaxies in the IRAS revised bright galaxy sample (Sanders et al., 2004), as they have the highest SFR in the local Universe (Sanders et al., 2004). From this sample, we selected the 20 brightest galaxies at 100μm that have at least one mm-RL frequency band covered by ALMA archival observations available to the public prior to the year 2020. The names of these 20 IR-bright galaxies, the corresponding ALMA project containing the observations, as well as mm-RL transition covered by these observations are given in Table 2.1. Where multiple archival data cover the same line, the most sensitive observations are used, with the exception of NGC3256, where multiple datasets of similar sensitivities were combined in order to increase the signal-to-noise of the mm-RL detection.

The ALMA archive provides for each project the raw data and the scripts to run its calibration. It also contains science-ready cleaned data cubes, however, these do not always cover the full frequency

range recorded in the raw data, covering instead only the frequencies requested in the project. In case the science-ready data cubes already covered the frequencies of the mm-RLs, we simply use those. Otherwise, we re-run the calibration and imaging using the scripts provided by the archive to produce cubes that cover the whole originally observed frequency bandwidth, which includes the mm-RL frequencies, using the Common Astronomy Software Applications (CASA) package (McMullin et al., 2007). These clean cubes were obtained setting using natural weighting and the the Clark cleaning algorithm (Clark, 1980) in CASA. The cleaning mode was set to "interactive", the cleaning mask covered any observable line emission, and setting the cleaning threshold was set to automatic. Each clean data cube was then visually inspected for mm-RL emission, and mm-RL spectra were extracted from apertures surrounding the mm-RL emission. Where multiple mm-RL were detected, one common aperture was defined to encompass the emission of all the different line transitions. In the case of a non-detection, spectra were extracted from regions where the continuum emission at the mm-RL frequency was more than three times above the background rms level.

Table 2.1: The galaxy sample and their ALMA projects

Target	Distance [Mpc]	Line	Sensitivity per 100 km s^{-1} channel [mJy beam^{-1}]	Project
NGC4945	3.8	H30α	0.35	2016.1.01279.S
		H40α	1.54	2018.1.01236.S
		H42$\alpha^{\dagger}$	1.54	2018.1.01236.S
		H42$\alpha^{\dagger}$	0.22	2012.1.00912.S
NGC253	3.2	H26α	0.37	2013.1.00735.S
		H27α	1.89	2017.1.00161.L
		H30α	1.21	2017.1.00161.L
		H33α	0.15	2017.1.00028.S
		H34α	1.35	2017.1.00161.L
		H40α	0.12	2017.1.00161.L
M83	6.5	H40α	0.18	2015.1.01177.S
		H41α	0.15	2016.1.00164.S
NGC5128	3.8	H40α	0.15	2017.1.00005.S
NGC1068	10.6	H40α	0.22	2013.1.00055.S
		H42α	0.37	2015.1.00960.S
NGC0055	1.9	H40α	0.12	2015.1.00944.S
NGC1365	16.6	H30α	4.14	2013.1.01161.S
NGC1808	9.3	H40α	0.15	2016.1.00562.S
		H42α	0.15	2016.1.00562.S
NGC3627	9.6	H30α	2.24	2015.1.00956.S
NGC2903	8.0	H40α	2.97	2017.1.00230.S
Arp220	78.7	H40α	0.12	2017.1.00042.S
NGC3256	40.3	H30α	0.28	2015.1.00902.S
		H40α	0.22	2015.1.00412.S

Target	Distance	Line	Sensitivity per 100 km s^{-1} channel	Project
	[Mpc]		[mJy beam^{-1}]	
			0.15	2016.1.00965.S
			0.15	2015.1.00993.S
		H41α	0.22	2015.1.00412.S
			0.25	2016.1.00965.S
		H42α	0.15	2015.1.00993.S
NGC3628	9.8	H30α	0.18	2013.1.00087.S
NGC1097	24.1	H40α	0.28	2011.0.00108.S
NGC6822	0.5	H40α	0.22	2016.1.01296.S
NGC4038/9	21.0	H30α	0.12	2016.1.00924.S
NGC7582	21.2	H30α	0.15	2016.1.00254.S
NGC5253	3.6	H30α	0.28	2013.1.00210.S
NGC4418	32.5	H40α	0.15	2016.1.00387.S
NGC1614	69.1	H30α	0.15	2017.1.00255.S

Table 2.1: The first column lists the name of the galaxies, the second column shows the distance, the third column shows transition that was covered by the ALMA bands, the third column lists the spectral RMS of the observations as listed in the ALMA archive, and the last column shows the ALMA archive project code.

For each of the NGC253, NGC4945, NGC3256, NGC1808, and M83 galaxies multiple mm-RL were recovered from the archival data. Single mm-RL line detections are recovered from each of the NGC5253, NGC3627, NGC3628, and Arp220 galaxies. In appendix A we also show the continuum maps at the detected mm-RL frequencies as well as the spectra of the detected lines. In the following subsections, we provide a short description of each of these galaxies and details on the mm-RL detections. †: This line is potentially contaminate by molecular emission.

NGC4945

NGC4945 is a nearby, nearly edge-on, spiral (de Vaucouleurs et al., 1991a) starburst galaxy. While host to a deeply obscured active galactic nucleus (AGN), star formation is the major power source for exciting the hot ionized gas (Done et al., 1996; Marconi et al., 2000; Spoon et al., 2000, 2003; Pérez-Beaupuits et al., 2011). Three different recombination lines, H30α, H40α, and H42α, are detected from in the nuclear region of this galaxy (Figure 2.1). The H42α line is detected with ALMA's 7m Atacama Compact Array (ACA) and with the 12m main ALMA array. These two datasets have very different spatial resolutions. The H42α line is marginally resolved with the ACA at a resolution of 18.″8 while it is clearly resolved by the 12m array with a resolution of 2.″65. Nevertheless, the H42α line intensities measured in the 7m and 12m array data from matched apertures (see Figure 2.1) are fully consistent within 1σ. This suggests that there is no large scale emission filtered out in the 12m array observations and that the line emission originates from a region of $\sim$ 250 pc. We note that Bendo et al. (2016) also reported the H42α 12m array detection in NGC4945.

In a molecular line survey of NGC4945, using ALMA, Henkel et al. (2018) report the detection of a Cyclopropenylidene transition (c-C_3H_2, $J = 2_{12} \rightarrow 1_{10}$) with a rest frequency of 85.338 GHz. Another transition line of this molecule, with $J = 4_{32} \rightarrow 4_{23}$, has a rest frequency of 85.656 GHz,

overlapping with the H42α line at 85.688 GHz. The integrated line flux recovered by Henkel et al. (2018) for c-C_3H_2, $J = 2_{12} \rightarrow 1_{10}$ is 21.4 ± 0.7 Jy km s^{-1}. Using the eXtended CASA Line Analysis Software Suite (XCLASS, Möller et al., 2017) we model the relative intensities of the $J = 2_{12} \rightarrow 1_{10}$ and $J = 4_{32} \rightarrow 4_{23}$ molecular transitions for temperatures of $20 - 110$ K and column densities of N(c $-$ C_3H_2)=$10^8 - 10^{16}$ cm^{-2}. We find that the intensity of the $J = 4_{32} \rightarrow 4_{23}$ transition is 40% to 80% that of the $J = 2_{12} \rightarrow 1_{10}$. This implies that a significant part of the H42α line flux of 13.2 ± 0.3 Jy km s^{-1} is contaminated by the $J = 4_{32} \rightarrow 4_{23}$ emission of c-C_3H_2. Therefore, we do not use the H42α line in our analysis.

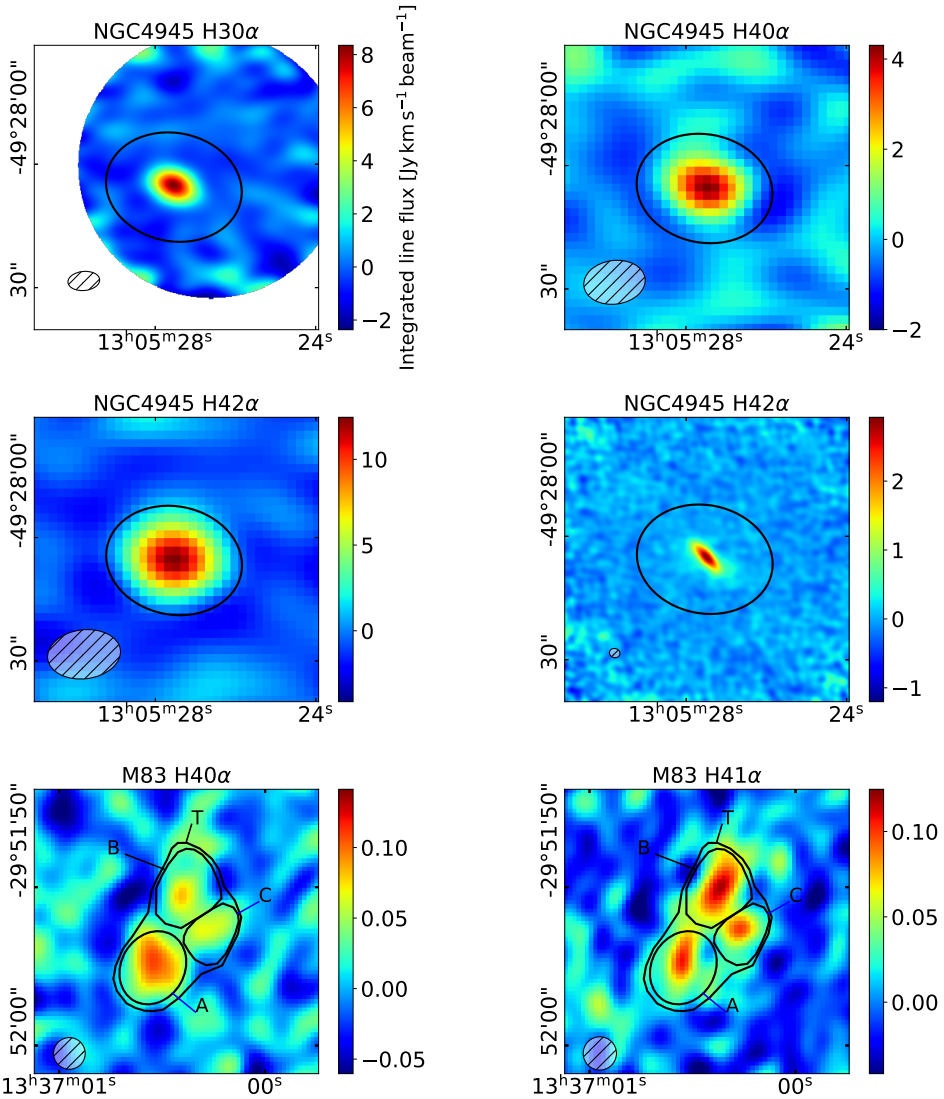

Figure 2.1: Moment zero maps of mm-RL detected in NGC4945 and M83. In NGC4945, three lines were detected with the ALMA compact array (top panels) while H42α was also detected with the ALMA main array (bottom left panel). The aperture used to extract the integrated line flux is outlined in black. The telescope beam is shown in the lower left corner of each panel.

NGC253

NGC253 is a nearly edge-on, barred spiral (de Vaucouleurs et al., 1991a) galaxy. It has a nuclear starburst, as suggested by intense IR emission (Strickland et al., 2004) and the presence of high density gas, photo dissociation regions, and shocked gas in the inner part of its nucleus (Martín et al., 2006; Meier et al., 2015). We recover several millimeter and submillimeter recombination line detections from the nucleus of NGC253. The H27α, H30α and H34α line detections are made with the ACA at resolutions of $3\farcs8$, $5\farcs6$, and $7\farcs6$, respectively. The H26α, H33α and H40α line detections are made with the 12m ALMA main array at a resolution of $1\farcs65$, $1\farcs1$, and $2\farcs4$, respectively. As seen in Figure 2.2, the line emission is well resolved in the 12m main array data and barely resolved in the 7m ACA data. Even so, the line fluxes of the neighboring H33α and H34α transitions, which are detected with the high, respectively low resolution arrays, are consistent with each other. This suggests there is no outresolved flux in the high resolution 12m main array ALMA data. The H40α line is detected by Bendo et al. (2015), who report an integrated line flux for the whole nucleus in agreement with our measurement.

M83

M83 is a nearly face-on, barred spiral galaxy (de Vaucouleurs et al., 1991a), with a circumnuclear ring and a starbursting nucleus (Turner et al., 1987; Turner & Ho, 1994). Detailed ALMA observations reveal the presence of dense and shocked gas in the nucleus, and that star formation occurs mainly at the intersection between the bar and the circumnuclear ring (Harada et al., 2019). The H40α and H41α are detected at a resolution of ~ 2 arcsec in three regions of M83's nucleus, named here A, B, and C, shown in Figure 2.1 – bottom middle and right panels. The H41α line detection in region C presented a second peak in the spectrum which we interpret as contamination by molecular line emission, and was not used in our work. The detection of the H41α line is mentioned in Harada et al. (2019), who use it to pinpoint the active star-forming region in this galaxy, without providing a flux measurement.

NGC1808

NGC1808 is a nearby, nearly face-on, barred spiral (de Vaucouleurs et al., 1991a) starbursting galaxy. Star formation coexists with a faint AGN and prominent dust lanes are present in the disk (Veron-Cetty & Veron, 1985; Awaki et al., 1996). In the central region, star formation activity is present in a circumnuclear ring (Sérsic & Pastoriza, 1965, 1967; Pastoriza, 1967) as well as in young embedded starclusters visible in mid infrared and radio continuum emission (Galliano et al., 2005; Galliano & Alloin, 2008). ALMA observations reveal a rich chemistry, the presence of a dusty torus, and shocked gas and free electrons as a result of SNe and HII regions (Salak et al., 2017). The H40α and H42α lines are detected in the central starburst of NGC1808, at a resolution of $3\farcs5$ (Figure 2.3). The two lines seem to originate from distinct regions, which do not overlap.

NGC3627

NGC3627 is a nearly face on, barred spiral galaxy (de Vaucouleurs et al., 1991a) with a Seyfert 2 nucleus (Ho et al., 1997; Peng et al., 1998). Intense star formation activity at the interface between the bar and the inner parts of the spiral arms is revealed by Hα emission (Smith et al., 1994; Sheth et al.,

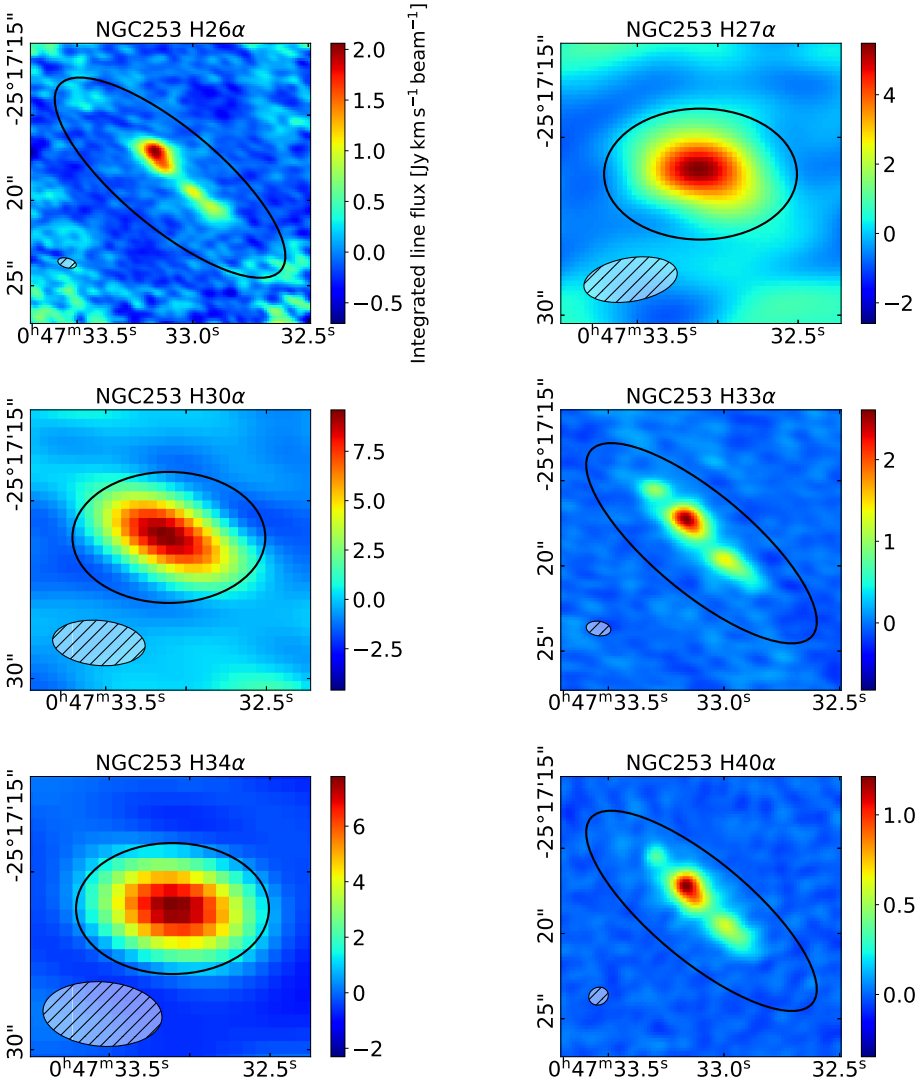

Figure 2.2: ALMA moment zero maps of the mm-RL detected in NGC253. The H27α, H30α, and H34α lines were detected with the ACA and are shown in the top, top right, and bottom middle panel, respectively. The H26α, H33α and H40α lines were detected with the ALMA main array and are shown in the top left, bottom left and bottom right panels, respectively. The aperture used to extract the fluxes of all the lines is outlined in black. The telescope beam is shown in the lower left corner of each panel.

2002a) as well as by free-free emission (Paladino et al., 2008; Murphy et al., 2015). The H30α line is detected in two compact regions in the southern inter-arm region of NGC3627, at a resolution of 0.″75, shown in Figure 2.4. In this region, Murphy et al. (2015) reported the presence of dense gas as traced by HCN and HCO^+ emission. Unfortunately, until now, there are no ALMA archival data covering a mm-RL frequency for the bar or nucleus regions of NGC3627.

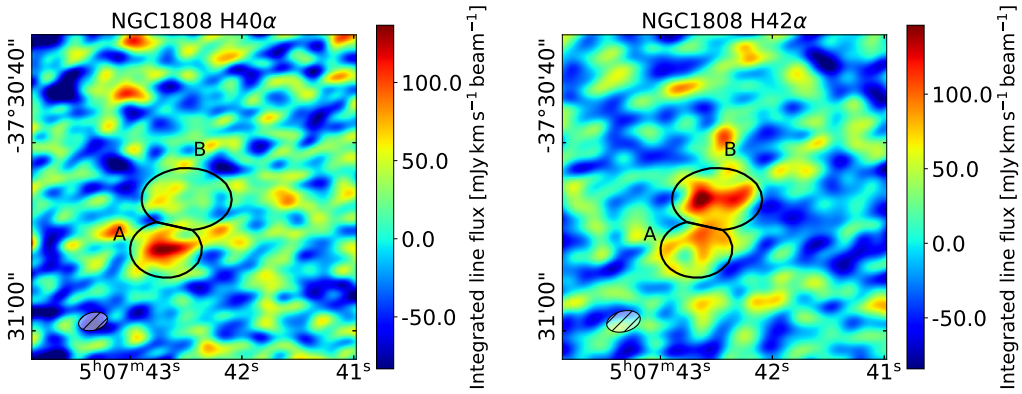

Figure 2.3: ALMA moment zero maps of the H40α and H42α lines in NGC1808. These two lines do not appear to be emitted from the same region. The apertures used to extract the integrated line flux are outlined in black. The telescope beam is shown in the lower left corner of each panel.

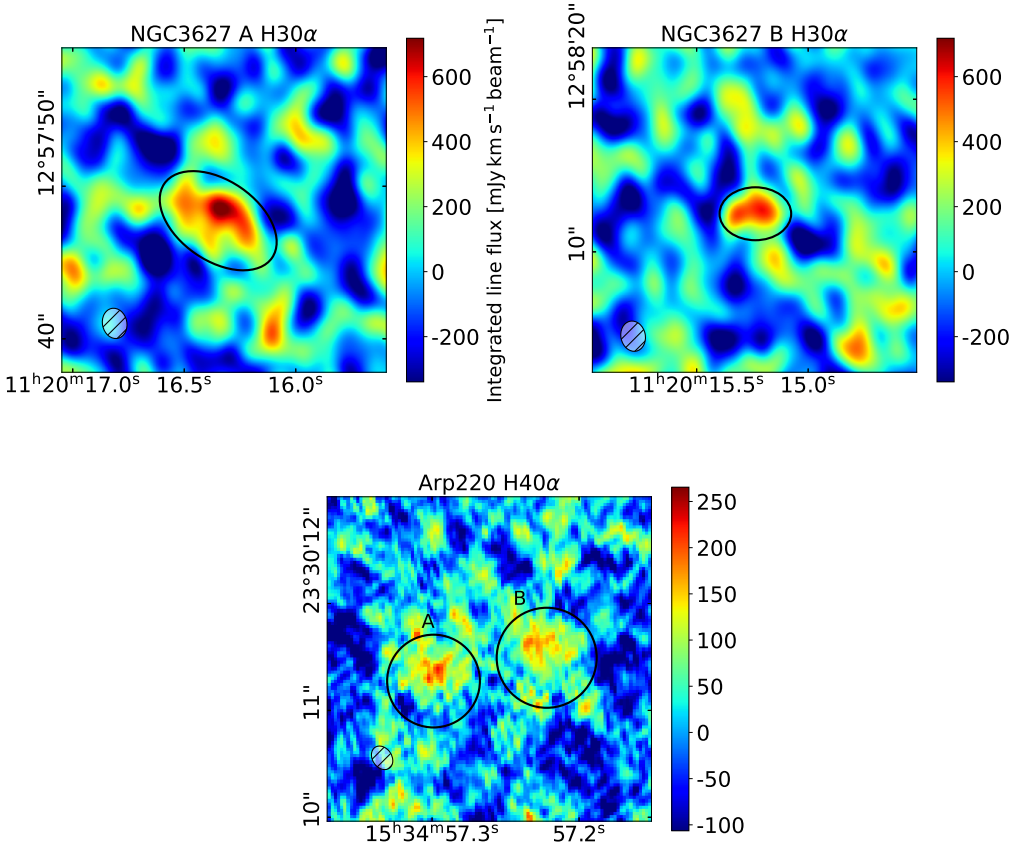

Figure 2.4: ALMA moment zero maps of the RL emission from NGC3627 and Arp220. The apertures used to extract the integrated line flux are outlined in black. The telescope beam is shown in the lower left corner of each panel.

Arp220

Arp220 is a peculiar (de Vaucouleurs et al., 1991a), ultraluminous infrared galaxy (Sanders et al., 2003) that is apparently the product of the merger of two gas-rich galaxies (Sanders & Mirabel, 1996). It contains two nuclei surrounded by ~ 200 pc-sized molecular disks that strongly obscure the nuclear regions (Sakamoto et al., 1999). It remains unclear to what extent the embedded AGN contribute to the total infrared emission, althould the far-IR appears dominated by the starburst (Wilson et al., 2014; Tunnard et al., 2015; Barcos-Muñoz et al., 2015; Scoville et al., 2015). We detect the H40α line in both nuclei from high resolution ALMA data ($0\farcs09$, Figure 2.4–right panel).

Anantharamaiah et al. (2000) report the detection of H31α, H40α, and H42α emission in IRAM 30m single dish, (15 to 25 arcsec resolution) with observations covering both nuclei. Anantharamaiah et al. (2000) report a H40α line flux of 12.2 ± 1.6 Jy km s^{-1} for the center of Arp220, almost a factor ten higher than our own integration measured within $\sim 0\farcs44$ apertures centered on the line peak emission of each nuclei. They report a continuum flux density of 61 ± 10 mJy at the H40α (99GHz) line frequency, almost a factor two higher than the total value of 35.01 ± 0.02 mJy we detect using the same $\sim 0\farcs44$ apertures.

To test whether the interferometric observations outresolve any large scale emission, we compare high resolution continuum ALMA data with various interferometric and single dish observations of Arp220. Downes & Solomon (1998) use the PdBI interferometer at a resolution of $1\farcs8 \times 1\farcs8$, to recover a total flux density of 41 ± 8 mJy at 114 GHz, in agreement with our values. At 347 GHz, Scoville et al. (2015) report a continuum flux density of 490 ± 2 mJy for the nucleus, within a $1\farcs8$ diameter aperture, using ALMA data at $\sim 0\farcs5$ resolution . Using the same aperture size with a high resolution ($0\farcs13 \times 0\farcs19$) ALMA dataset at the same frequency, we find a continuum flux density of 580 ± 15 mJy, somewhat higher than the Scoville et al. (2015) values. Increasing the aperture to 3 arcsec, we recover a flux density of 708 ± 71 mJy. This is comparable to the results of SMA interferometer observations by Sakamoto et al. (2008), who find 720-780 mJy at 345 GHz within a 3 arcsec aperture at resolutions of $0\farcs5$ and $0\farcs23$, and with single dish 350 GHz measurements that find a continuum flux density of 730-830 mJy (Seiffert et al., 2007; Klaas et al., 2001; Dunne & Eales, 2001; Lisenfeld et al., 2000). We conclude that most of the continuum emission originates from the two compact nuclei and that ALMA does not outresolve large scale emission. Thus, the H40α integrated line flux discrepancy between the ALMA observations used in this work and the values of Anantharamaiah et al. (2000) may be caused by possible calibration errors of the IRAM 1996 data, or by molecular line contamination at larger scales. In an SMA line survey of Arp220, Martín et al. (2011) identify the H31α line detection of Anantharamaiah et al. (2000) as HC_3N emission and argue that the reported H40α and H42α lines may be contaminated by molecular emission as well.

NGC3256

NGC3256 is a peculiar, luminous infrared galaxy (Sanders et al., 2003) and a late-stage merger system evidenced by its prominent tidal tails (Schweizer, 1986; Zenner & Lenzen, 1993; Norris & Forbes, 1995; English et al., 2003). Strong absorption features from massive stars indicate the presence of a powerful starburst in its central region (Doyon et al., 1994; Lípari et al., 2000). Radio and infrared images reveal the presence of a double nucleus (Norris & Forbes, 1995; Kotilainen et al., 1996). While the northern nucleus is thought to be a pure starburst, there is still debate about the presence of an AGN in the southern nucleus (Kotilainen et al., 1996; Sakamoto et al., 2014). ALMA observations reveal

the presence of molecular disks and outflows around both nuclei (Sakamoto et al., 2014). The H30α, H40α, H41α, and H42α lines are detected in NGC3256, and are shown in Figure 2.5. For the H40α and H41α lines, multiple ALMA datasets were combined in order to increase the signal-to-noise of the detected lines. These corresponding datasets are shown in Table 2.1. We denote the northern and southern nuclei of NGC3256 as regions A and B, respectively. The H40α, H41α, and H42α lines detected in the two nuclei are almost unresolved, at resolutions of $1\farcs15$, $1\farcs45$, $2\farcs1$, respectively. The H30α line emission is detected in a dataset with a resolution of $1\farcs$. This emission is confined to an area slighlty offset from the center of region B, which we denote region B*. Since the H40α, H41α, and H42α line emission in region B is unresolved, it is possible these lines have a common origin with the H30α line emission in region B*. Thus, when comparing line intensities and SFR, we will treat the H30α line emission from region B* as originating from region B. Michiyama et al. (2020) detected the H40α and H42α lines using ALMA. They report the line intensity of the H40α line in their work, which is in agreement with our own values.

NGC3628

NGC3628 is an edge on (Tully et al., 1988) starbursting luminous infrared galaxy (Sanders et al., 2003). The circumnuclear starburst is revealed by radio continuum observations (Condon et al., 1982). The H30α line is detected towards the nucleus of NGC3628 at a resolution of $1\farcs0$, (Figure 2.5–middle bottom panel). The nuclear emission is resolved into two close components. Observations of the H92α line from this galaxy also reveal the two component nature of its nucleus (Anantharamaiah et al., 1993).

NGC5253

NGC5253 is a peculiar (de Vaucouleurs et al., 1991a) luminous infrared galaxy (Sanders et al., 2003) with a young starbursting nucleus. The youth of the starburst in NGC5253 is supported by the absence of synchrotron emission from SNe (Beck et al., 1996) and the presence of Wolf-Rayet stars (Campbell et al., 1986; Kobulnicky et al., 1997; Schaerer et al., 1997; López-Sánchez et al., 2007; Monreal-Ibero et al., 2010; Westmoquette et al., 2013), which place an upper limit of $\sim 3-4$ Myr on the age of the starburst. The H30α line is detected in the nucleus of NGC5253 (Figure 2.5–botom right panel), and is unresolved at a resolution of $0\farcs22$. Using the same dataset, Bendo et al. (2017) also reported the detection of the H30α mm-RL in NGC5253, and their results are in agreement with ours.

Upper limits on mm-RL emission

Only 9 out of the 20 brightest IR galaxies in the nearby universe with adequate ALMA coverage yield robust mm-RL detections. To obtain upper limits of RL fluxes, we extract spectra from apertures that surround the continuum emission. When defining these apertures, only continuum emission at a level three times above the background per-pixel rms was considered. When calculating the mm-RL integrated line flux upper limits, a conservative mm-RL width of 200 km s^{-1} was chosen based on the values of the other mm-RL detections. The 1σ uncertainty in the mm-RL integrated line flux is defined as $1\sigma = \mathrm{RMS}\Delta v \times \sqrt{200/\Delta v}$, where Δv is the spectral channel width in km s^{-1}, and RMS is the per-channel rms in Jy. The upper limit of the integrated mm-RL flux is taken as 3σ. These upper limits are shown alongside our detections in Table 4.2, and will be used in Section 4.2.1 where the SFR is calculated based on the mm-RL intensities.

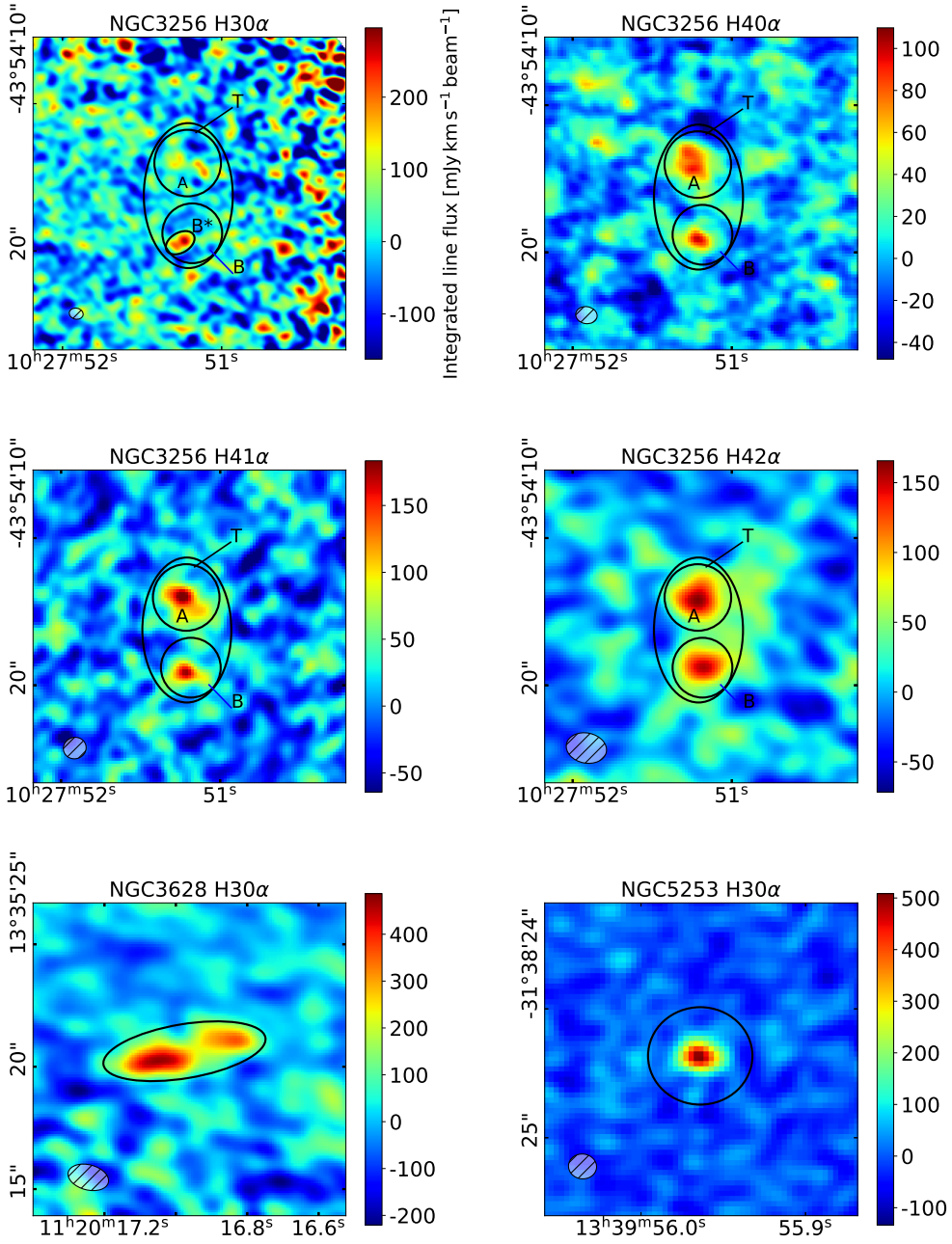

Figure 2.5: ALMA moment zero maps of the RL emission in NGC3256, NGC3628, and NGC5253. For NGC3256, the H30α line is detected in a small region in area B, which we denote B* on the map. The apertures used to extract the integrated line flux are outlined in black. The telescope beam is shown in the lower left corner of each panel.

Galaxy	H42α			H40α		
	$T_{\rm rms}$ [mK]	δv [km s^{-1}]	$f_{\rm rms}$ [mJy beam^{-1}]	$T_{\rm rms}$ [mK]	δv [km s^{-1}]	$f_{\rm rms}$ [mJy beam^{-1}]
NGC 0660	0.24	44	1.44	0.26	38	1.56
NGC 1614	0.34	44	2.04	0.36	38	2.16
NGC 2903	0.66	44	3.96	0.24	38	1.44
IC694	–	–	–	0.35	38	2.10
NGC 4102	–	–	–	0.35	75	2.10
NGC 4418	0.38	45	2.28	0.39	49	2.34

Table 2.2: Details of the observations. The first column shows the observed galaxy. The table is split into two sections which show the results of the H42α and H40α observations at 85.68 GHz and 99.02 GHz, respectively. The first column in each section show the sensitivity of the observations, the second column shows the spectral resolution, i.e. the bin-width of the spectrum, and the last column shows the sensitivity in units of Jansky.

2.1.3 Our IRAM 30m observational sample

We complete the ALMA sample with our own single-dish observations IRAM 30m observations. In addition to increasing the number statistics of mm-RL detections, these observations also probe larger spatial scales, thus allowing for a possible comparison of global and in-situ extragalactic SFR. The selected targets were NGC0660, NGC1614, NGC2903, IC694, NGC4102, and NGC4418, six nearby bright infrared galaxies, having high infrared luminosities of $L_{IR}/L_{\odot} > 10^1 1$, i.e., (U)LIRGS (Mirabel, 2002; Sanders & Mirabel, 1996; Sanders et al., 2003; Lonsdale et al., 2006), where mm-RL had not been previously observed or detected. The observations were carried out on 13-15 June 2015, 21-22 May and 3-4 July, 2016. The project codes for the three observing runs were 069-15, 181-15, and 055-16. The observations targeted the H40α and H42α mm-RL at 86.5 and 99.03 GHz, respectively, using the EMIR receiver with the FTS backend (Carter et al., 2012). The observing mode used was ON-OFF, using "wobbler" switching. In this observing mode, the secondary mirror is moved in order to observe the flux of nearby "OFF" position, away from the target galaxy, for calibration, without having to steer the main dish. The OFF positions used here were at a distance of 240" from the observed target in azimuth. We used relative coordinates in azimuth for the OFF positions in order to have the same optical depth through the atmosphere as for the ON position, and to not introduce any bias in the calibration due to a possible source at the OFF position, as the area of the sky under the OFF position changes due to the diurnal motion. At the frequencies of the H42α and H40α lines, the HPBW of the telescope has a size of 27" and 25", respectively. No mm-RL were detected in any of the observed galaxies, and upper limits were placed on the integrated line fluxes instead. Table 2.2 shows the sensitivity of the IRAM observations for each galaxy. These sensitivities are the per channel RMS of the IRAM spectra, excluding channels where line emission was observed, and are given in units of brightness temperature per beam, all having values of a fraction of 1 mK beam^{-1}. Assuming a beam filling factor of 1, we multiply the sensitivity values with the IRAM telescope efficiency factor, to convert them to units of mJy beam^{-1}. For the IRAM30m telescope, using the EMIR receiver, at the frequencies of the H42α and H40α lines, this factor is S/T 6 K Jy^{-1}. In the following sections we provide a more details about the observed targets targets.

NGC0660

This is a starburst, luminous infrared Sa galaxy, at a distance of 8.2 Mpc, exhibiting a polar ring (Goulding & Alexander, 2009). Its disk contains a high concentration of molecular gas, up to an order of magnitude larger than its ring (van Driel et al., 1995). The emission from the nuclear region of the galaxy appears to be due to star formation activity, with no AGN activity detected so far (Argo et al., 2015; Smirnova et al., 2017). Prior recombination line observations have detected the H92α line, and revealed an offset between the dynamical center of the galaxy and its radio continuum emitting core (Phookun et al., 1998). We target this galaxy with the IRAM30m telescope to observe millimeter recombination lines from its nuclear star-forming regions. The telescope was centered on coordinates of the prior cm-RL line detection by Phookun et al. (1998): 01 : 43 : 02.29 13 : 38 : 44.6 . The upper and lower side-bands were set up to cover the H42α and H40α lines at 85.688 GHz and 99.022 GHz respectively. The total integration time on NGC0660 is 21.5 hours, reaching a sensitivitiy of 0.24 mK and 0.26 mK at spectral resolutions of 44 km s^{-1} and 38 km s^{-1}, at the H42α and H40α line frequencies, respectively. No mm-RL lines were detected, and the 3-sigma upper limits on the integrated line flux of the H42α and H40α lines are $F_{40} = 1.2 \times 10^{-18}$ erg s^{-1} cm^{-2} and $F_{42} = 1.1 \times 10^{-18}$ erg s^{-1} cm^{-2}, respectively, where we integrated over a 200 km s^{-1} velocity range, centered on the respective line frequency.

NGC1614

NGC1614 is a barred spiral peculiar (SB(c)pec) galaxy (de Vaucouleurs et al., 1991b) that has a starbursting nucleus (Balzano, 1983). It is a LIRG (Sanders et al., 2003), at a distance of 67.8 Mpc (Armus et al., 2009). The central region of this galaxy shows no evidence of an AGN (Herrero-Illana et al., 2017), implying that the infrared and radio emission is purely originating from the star formation activity. Indeed, the central starburst ring with a prominent bar is revealed with multi-wavelength observations, from radio to infrared (Herrero-Illana et al., 2014; Olsson et al., 2010; Xu et al., 2015). Molecular observations indicate a high rate inflow of molecular gas onto the starbursting nucleus, suggesting that the star-forming nucleus is still growing by accumulating gas after a minor merger (Väisänen et al., 2012; König et al., 2016). We observed this galaxy with the IRAM30m telescope, project 181-15. The EMIR receiver was used with the lower and upper sidebands covering the H42α and H40α line frequencies. The beam was centered on 04 : 33 : 59.96 − 08 : 34 : 44.3, having a FWHM of 25" for this frequency range. The integration time was 5.5 hours, reaching sensitivities of 0.34 mK and 0.36 mK at a spectral resolutions of 43 km s^{-1} and 38 km s^{-1} at the H42α and H40α line frequencies, respectively. The upper limits on the integrated line flux at the 3-sigma level are $F_{40} = 1.3 \times 10^{-19}$ erg s^{-1} cm^{-2} and $F_{42} = 1.2 \times 10^{-19}$ erg s^{-1} cm^{-2} for the H40α and H42α lines, respectively, considering linewidths having a FWHM=200 km s^{-1}.

NGC2903

This is an intermediate spiral galaxy with a weak ring (SAB(rs)bc) (de Vaucouleurs et al., 1991b) with a straburst in its nucleus and no AGN (Yukita et al., 2012), at a distance of 8.9 Mpc (Popping et al., 2010). The morphology of the starburst region is ring-like, with a radius of 625 pc, revealed by near infrared Paα HST observations (Alonso-Herrero et al., 2001a), with X-ray observations showing a similar size 650 pc (Yukita et al., 2012). The Hα emission, when cross-correlated with CO(1-0) emission, shows that the star formation activity in the bar of this galaxy is offset towards the leading

side of the molecular emission (Sheth et al., 2002b). We observe the central region of NGC2903 with the IRAM30m telescope, projects 069-15 and 055-16, covering the H40α and H42α lines. The integration time was 2.8 hours for the H42α line and 8.2 hours for the H40α line. No mm-RL lines were detected. The sensitivity of the observations is 0.66 mK and 0.24 mK, at spectral resolutions of 44 km s^{-1} and 38 km s^{-1}, at the H42α and H40α line frequencies, respectively. The upper limits on the integrated line flux of the two lines, at the 3-sigma level, are $F_{40} = 1.4 \times 10^{-18}$ erg s^{-1} cm^{-2} and $F_{42} = 2.7 \times 10^{-18}$ erg s^{-1} cm^{-2}, considering linewidths having a FWHM=200 km s^{-1}.

IC694

The Arp299 consists of a pair of colliding galaxies IC694 and NGC3690. IC694 is a peculiar spiral galaxy (S pec) (Sandage & Tammann, 1981) at a distance of 50.7 Mpc (Armus et al., 2009). The two interacting galaxies are the site of intense star formation, with IC694 being classified as a LIRG (Sanders et al., 2003). Initial infrared observations of IC694 did not detect an AGN, and revealed a starburst that is not tightly concentrated in the nucleus, with an extremely strong dust extinction (Alonso-Herrero et al., 2000). The overall star formation activity in Arp299 is believed to have been ongoing for at least 15 Myr due to the collision of its two component galaxies (Alonso-Herrero et al., 2000). Subsequent X-Ray and MIR observations did not find evidence for the presence of an AGN in IC694 (Della Ceca et al., 2002; Ballo et al., 2004; Alonso-Herrero et al., 2009). Previous radio observations of IC694 by Zhao et al. (1997), at a frequency of 8.3 GHz, detected H92α line emission in its nucleus, and constrain the electron density and temperature of the ionized gas to $5 \times 10^2 - 10^4$ cm^{-3} and 5000 K respectively. We observe the H40α line at 99.02 GHz with the IRAM-30m telescope, with an integration time of 4.6 hours, reaching a sensitivity of 0.35 mK in 38 km s^{-1} velocity bins. The observations consist of a single pointing centered on 11 : 28 : 33.70 58 : 33 : 46.4. The upper limit on the integrated line flux of the H40α line, at the 3-sigma level, is $F_{40} = 1.4 \times 10^{-18}$ erg s^{-1} cm^{-2}, considering a linewidth having a FWHM=200 km s^{-1}..

NGC4102

NGC4102 is an intermediate barred spiral galaxy, of type SAB(s)b (de Vaucouleurs et al., 1991b), located at a distance of 17 Mpc (Willick et al., 1997; Tully et al., 2008). The nucleus is host to a starburst, having an optical spectrum similar to that of an HII region (Ho et al., 1997), and also contains a low luminosity AGN, revealed by X-Ray observations (González-Martín et al., 2011). Observations of the [NeII] line show that the intense star formation activity is confined inside a 300 pc ring around the nucleus (Beck et al., 2010). We observed this galaxy with the IRAM 30m telescope, covering the H40α line emission at 99.02 GHz, for an integration time of 1.8 hours. The observations consist of a single pointing centered on 12 : 06 : 23.00 52 : 42 : 39.1. The observation reaches a sensitivity of 0.35 mK for 75km s^{-1} velocity bins. The H40α line was not detected. The 3-sigma upper limit of the integrated line flux is $F_{40} = 1.8 \times 10^{-18}$ erg s^{-1} cm^{-2}, considering a H40α line with FWHM=200 km s^{-1}.

NGC4418

NGC4418 is a LIRG (Sanders et al., 2003), with the morphology of an intermediate barred spiral galaxy with an outer pseudo-ring, of type (R')SAB(s)a (de Vaucouleurs et al., 1991b), at a distance

of 34 Mpc (Sakamoto et al., 2013). Infrared and CO line observations of its nucleus reveal the presence of molecular gas concentration having the size of 100 pc, containing an infrared bright hot dusty core with a size of 20 pc which is responsible for most of the IR luminosity of the galaxy (Sakamoto et al., 2013). Together with the CO line peak surface brightness of 90 K (Sakamoto et al., 2013), and the strong silicate absorption features (Spoon et al., 2007), these observations suggest a heavily dust obscured AGN is present in the nucleus of this galaxy (Sakamoto et al., 2013). A spectral line survey in the 0.4~1.4 mm wavelength range, which detected molecular lines with excitation temperatures above 100 K in absorption against the bright, compact, nucleus, confirms the presence of an AGN (Sakamoto et al., 2021). We observed the nucleus of this galaxy with the IRAM30m telescope, using the EMIR receiver, covering the H40α and H42α line frequencies, for a final integration time of 6.8 and 5.2 hours, respectively. The observations consist of a single pointing centered on 12 : 26 : 54.57 − 00 : 52 : 39.8. The observations at the frequencies of the two lines have sensitivities of 0.38 mK and 0.39 mK at spectral resolutions of 45 km s^{-1} and 49 km s^{-1}, respectively. The two mm-RL were not detected, The 3-sigma upper limits on the integrated line fluxes are $F_{40} = 1.5 \times 10^{-18}$ erg s^{-1} cm^{-2} and $F_{42} = 1.9 \times 10^{-18}$ erg s^{-1} cm^{-2}, considering lines with FWHM=200 km s^{-1}.

Submillimeter, far-infrared, and mid-infrared archival data

Archival data is used to calculate the $L_{\rm FIR}$ and the FIR derived SFR for the observed regions in this sample. We use available archive data from the Wide-field Infrared Survey Explorer (WISE) (Wright et al., 2010) telescope, the Multiband Imaging Photometer (MIPS) instrument (Rieke et al., 2004) onboard the Spitzer (Werner et al., 2004) space telescope, the Photodetector Array Camera and Spectrometer (PACS) (Poglitsch et al., 2010) and the Spectral and Photometric Imaging REceiver (SPIRE) (Griffin et al., 2010) instruments onboard the Herschel (Pilbratt et al., 2010) space telescope, and the Submillimetre Common-User Bolometer Array (SCUBA) 1 and 2 instruments (Holland et al., 1999, 2013) at the James Clerk Maxwell Telescope (JCMT). In table 2.3 we show which instrument was used to collect the data for each galaxy in this sample. For some of the galaxies, no archival data was available covering the peak of the dust emission at resolutions better than or comparable to our IRAM observations. In those cases, measurements using data from telescopes with lower resolutions than the IRAM observations are used, and their values are taken as upper limits.

The flux from each image was extracted using the photutils package in astropy. The flux at each wavelength was extracted from circular apertures with diameters of 25" and 27", centered on and corresponding to the H40α and H42α IRAM observations, respectively, which we refer to as measurement or signal apertures. The emission from the sky background was measured in circular apertures of at least the same size, away from the galaxy emission, which we will refer to as background apertures. We used this method instead of annular apertures centered on the observed regions in order to avoid possible extended emission from the galaxy outside the central circular aperture. The flux density in each band was calculated using the following formula:

$$F_{\rm band} = A_{\rm cor}\left(\sum_{i=1}^{N_s} s_i - \frac{1}{N_b}\sum_{i=1}^{N_b} b_i\right) \tag{2.5}$$

where N_s are the number of pixels in the measurement, or signal aperture, s_i is the flux density value of the i-th pixel in the measurement aperture, N_b is the number of pixels in the background aperture,

Galaxy	Frequency Band and Wavelength [μm]								
	MIR		FIR					sub-mm	
	11	24	70	100	160	250	350	450	850
NGC0660	a	b	e*	e*	e*	e*	f*	d	d
NGC1614	a	a,b	c	c	c	c	c	–	–
NGC2903	a	a,b	b	–	b*	–	g*	d	d
IC694	a	a	c	c	c	c	c	–	–
NGC4102	a	a	c	–	c	c	c	–	–
NGC4418	a	a	c	c	c	c	c	–	–

Table 2.3: Data used to determine the FIR luminosity. The letters correspond to a telescope. a = WISE at 12 μm or 22.2 μm, b = Spitzer - MIPS instrument, c = Herschel - PACS instrument for 70-160 μm and SPIRE for 250 and 350 μm, d = JCMT with the SCUBA1/2 instrument, e = ISO, f = IRTF, g = UKIRT; * = used as upper limits only

b_i is the flux density value in the i-th pixel in the background aperture, and $A_{\rm cor}$ is the aperture correction factor. The aperture correction factor compensates for the energy that is scattered outside of our selected aperture due to the optics of the telescope. We calculate this correction factor using the enclosed energy profiles provided by Aniano et al. (2011) for each instrument. The measurement error is calculated taking into account several sources of uncertainty, such as the instrument uncertainty, sky background uncertainty, and absolute calibration uncertainty. Where available, archive supplied uncertainty maps were also used to calculate the uncertainty. These are images that have the same shape and cover the exact same area of the sky as the data, with each of their pixel values corresponding to the measurement uncertainty at that location. The uncertainty corresponding to the background subtraction/photometry and instrumental effects has the following form:

$$\sigma_{\rm pht} = A_{\rm cor}\left(\sigma_{\rm bI}^2 \times \left(\frac{N_s^2}{N_b}\right) + \sum_{i=1}^{N_b}\sigma_{\rm iU}^2\right)^{0.5} \tag{2.6}$$

where $\sigma_{\rm bI}^2$ is the standard deviation of the data pixels in the background aperture, and $\sigma_{\rm iU}$ is the uncertainty value of the i-th pixel in the measurement aperture, taken from the uncertainty map. Converting the quantities measured by the instruments, e.g. voltages, to physical values, such as flux densities, introduces calibration uncertainties. These uncertainties can be caused by fluctuations of the parameters of the instruments, optics, and electronics, as well as the properties of the calibrator source. For absolute flux calibration, instruments compare the results of their measurements to results of the same instrument when observing at an astronomical or artificial object with known flux. The flux of astronomical sources can vary over time, which introduces flux calibration uncertainties. The flux calibration uncertainty, $\sigma_{\rm abs}$, is usually expressed as a percentage of the total measured flux. For our measurements, we adopt the following flux calibration uncertainties: 4.5% and 5.7% for WISE bands 3 and 4, respectively, (Jarrett et al., 2011), 10% for Spitzer MIPS (Instrument & Teams, 2011), 5.5% for Herschel PACS/SPIRE (Chu et al., 2017b), 25% and 20% for the 450 μm and 800 μm JCMT SCUBA bands, respectively (Stevens et al., 2005; Di Francesco et al., 2008), 14% and 6% for the 450 μm and 800 μm JCMT SCUBA2 bands, respectively (Mairs et al., 2021). Finally, the overall uncertainty is obtained from the sum in quadrature of the flux calibration error and the measurement/photometric

error:

$$\sigma_{\rm tot} = \left(\sigma_{\rm pht}^2 + \sigma_{\rm abs}^2 F_{\rm band}^2\right)^{0.5} \tag{2.7}$$

A color correction factor of which increases the measured flux by 10% is also introduced for the band 4 WISE observations, which necessary when observing sources colder than stellar objects, such as interstellar dust. The MIPS instrument, at 70 μm and 160 μm, has a nonlinear response for bright sources. As the source brightness increases past a certain threshold, the non-linear response of the instrument causes it to significantly underestimate the flux density. For MIPS 70 μm image data, we apply the following non-linearity correction, on pixels with values higher than 66 MJy sr^{-1} (Dale et al., 2009):

$$\frac{f_{\rm MIPS70}^{\rm cor}}{\rm MJy\ sr^{-1}} = 0.581 \times \left(\frac{f_{\rm MIPS70}}{\rm MJy\ sr^{-1}}\right)^{1.182}, \tag{2.8}$$

where $f_{\rm MIPS70}^{\rm cor}$ and $f_{\rm MIPS70}$ are the corrected and uncorrected pixel values, respectively, in units of MJy sr^{-1}. A similar correction is applied to MIPS 160 μm images, on pixels values exceeding 50 MJy sr^{-1} (Meixner et al., 2013):

$$\frac{f_{\rm MIPS160}^{\rm cor}}{\rm MJy\ sr^{-1}} = 0.624 \times \left(\frac{f_{\rm MIPS160}}{\rm MJy\ sr^{-1}}\right)^{1.11}, \tag{2.9}$$

where $f_{\rm MIPS160}^{\rm cor}$ and $f_{\rm MIPS160}$ are the corrected and uncorrected pixel values, respectively, in units of MJy sr^{-1}. In Tables 2.4 and 2.5 we show the photometry measurements corresponding to the 25" and 27" diameter apertures, respectively. The overall uncertainty is dominated by the calibration uncertainty, with the photometric uncertainty only contributing a few percent to the overall uncertainty, with the only exception being some of the SCUBA data.

For two galaxies in our sample, NGC0660 and NGC2903, no archival data were available covering the dust emission in the 70-350 μm wavelength range, at resolutions better or comparable to the IRAM observations. Nevertheless, having upper limits for flux densities inside this wavelength range is still be useful for fitting an SED to determine the $L_{\rm FIR}$ and SFR. In the case of NGC0660 we obtain these upper limits using flux density values taken from the literature, measured with the Infrared Space Observatory (ISO) and Infrared Telescope Facility (IRTF) at Mauna Kea. These ISO measurements were made at wavelengths of 57, 88, 122, 145, 158, 170 μm and have flux density values of 110.0(11.2), 106.3(10.6), 91.5(9.2), 92.0(9.2), 75.6(7.6) Jy respectively (Brauher et al., 2008). The 350 μm measurement was made with the IRTF (Chini et al., 1986). These flux densities represent the emission from the whole NGC0660 galaxy. In the case of NGC2903 we consider flux density values corresponding to measurements taken at 160 μm and 350 μm. For the 160μm flux density, we use a 39" diameter aperture on MIPS 160 μm data, centered on the IRAM observations. The diameter of this aperture corresponds to the FWHM of the MIPS instrument at the given wavelength. For the 350 μm flux density, we use the values from Eales et al. (1989) taken with the United Kingdom Infrared Telescope (UKIRT) on Mauna Kea. All of these measurements will be treated as upper limits, and also listed in Tables 2.4 and 2.5, except for the NGC0660 ISO values which are shown in this text instead, as they don't cover the same wavelength bands as the rest of the data in the sample.

Wavelength	NGC0660	NGC1614	NGC2903	IC694	NGC4102	NGC4418
[μm]	[Jy]	[Jy]	[Jy]	[Jy]	[Jy]	[Jy]
11	1.11(0.05)	0.965(0.047)	0.776(0.038)	1.19(0.06)	0.931(0.046)	0.765(0.037)
24	5.18(0.51)	5.60(0.33) 5.95(0.59)	2.15(0.13) 2.02(0.21)	10.1(0.6)	4.65(0.28)	5.95(0.35)
70	–	37.3(2.1)	9.05(0.91)	92.4(5.1)	58.2(3.2)	44.2(2.4)
100	–	34.8(1.9)	–	80.5(4.4)	–	35.1(1.9)
160	–	20.8(1.1)	57.1(5.8)[1]	45.0(2.4)	45.1(2.5)	18.7(1.1)
250	–	6.06(0.35)	–	12.4(0.8)	14.6(0.8)	5.90(0.32)
350	10.0(0.7)[2]	1.96(0.11)	6.5(2.1)[3]	4.11(0.27)	5.2(0.3)	2.25(0.13)
450	5.4(2.1)	–	1.37(0.34)	–	–	–
850	0.46(0.09)	–	0.144(0.013)	–	–	–

Table 2.4: Flux density from 25" diameter apertures centered on the IRAM H40α observations. For NGC0660, in the 50-250 μm range, ISO measurements from the literature are used as upper limits, corresponding to fluxes from the whole galaxy (see text). Also used as upper limits are the following flux density values, taken from: 1 = MIPS archival image data, corresponding to the flux density inside a 39" aperture (1×FWHM of MIPS at 160μm), 2 = IRTF data for the whole galaxy (Chini et al., 1986), 3 = UKIRT data for the whole galaxy (Eales et al., 1989).

Wavelength	NGC0660	NGC1614	NGC2903	IC694	NGC4102	NGC4418
[μm]	[Jy]	[Jy]	[Jy]	[Jy]	[Jy]	[Jy]
11	1.15(0.06)	0.984(0.048)	0.815(0.041)	1.28(0.06)	0.956(0.047)	0.782(0.038)
24	5.19(0.52)	5.63(0.33) 5.89(0.58)	2.19(0.13) 2.15(0.21)	10.4(0.6)	4.68(0.28)	5.98(0.36)
70	–	37.5(2.1)	10.4(1.1)	94.2(5.2)	58.7(3.2)	44.1(2.4)
100	–	35.6(1.9)	–	82.7(4.6)	–	35.2(1.9)
160	–	21.5(1.2)	57.1(5.8)[1]	47.0(2.6)	45.9(2.5)	18.8(1.1)
250	–	6.18(0.35)	–	13.0(0.8)	15.0(0.9)	5.95(0.33)
350	10.0(0.7)[2]	2.00(0.11)	6.5(2.1)[3]	4.29(0.28)	5.39(0.31)	2.24(0.12)
450	6.1(2.3)	–	1.48(0.37)	–	–	–
850	0.54(0.11)	–	0.158(0.014)	–	–	–

Table 2.5: Flux density from 27" diameter apertures centered on the IRAM H42α observations. For NGC0660, in the 50-250 μm range, ISO measurements from the literature are used as upper limits, corresponding to fluxes from the whole galaxy (see text). Also used as upper limits are the following flux density values, taken from: 1 = MIPS archival image data, corresponding to the flux density inside a 39" aperture (1×FWHM of MIPS at 160μm), 2 = IRTF data for the whole galaxy (Chini et al., 1986), 3 = UKIRT data for the whole galaxy (Eales et al., 1989).

2.1.4 Ultraviolet and far-ultraviolet data

Archival images in the far UV (FUV) band of the Galactic Evolution Explorer (GALEX) space telescope (Martin et al., 2005) are used to determine the UV luminosity (L_{UV}) of the mm-RL emitting regions in galaxies NGC5253, NGC1808, NGC253, Arp220, and M83. The GALEX FUV band has an effective wavelength of 1528 Å and covers the 1344-1786 Å wavelength range. No archival FUV data were available for NGC3256, and instead near UV (NUV) band images were used. The NUV band has an effective wavelength of 2271 Å and covers the 1771-2831 Å wavelength range. The FWHM of the GALEX PSF is 4.″3 and 5.″3 for the FUV and NUV bands respectively. The UV fluxes are extracted using aperture photometry on background subtracted archival images. The uncertainties introduced by possible variations in the sky background emission are calculated by measuring the flux in 100 randomly placed photometric apertures in the signal free area of the background subtracted images, identical in size and shape with the aperture used for photometry. The final uncertainty value also includes poissonian noise, sky and instrumental noise, as well as a 5% calibration uncertainty (Voyer et al., 2014).

Target	$L_{UV} \times 10^{36}$	$\sigma^{L_{UV}}_{sky} \times 10^{36}$	$\sigma^{L_{UV}}_{inst} \times 10^{36}$	$\sigma^{L_{UV}}_{Poi} \times 10^{36}$	$\sigma^{L_{UV}}_{tot} \times 10^{36}$
	[erg s^{-1} Å^{-1}]	[erg s^{-1} Å^{-1}]	[erg s^{-1} Å^{-1}]	[erg s^{-1} Å^{-1}]	[erg s^{-1} Å^{-1}]
NGC3256 T	448[a]	4.53	0.54	3.3	21
NGC5253 T	22	0.001	0.001	0.08	2
NGC1808 A	1.44	0.07	0.02	0.09	0.13
NGC1808 B	3.21	0.1	0.03	0.13	0.22
NGC253 7m	0.36	0.02	0.0	0.01	0.03
NGC253 12m	0.2	0.02	0.0	0.01	0.02
NGC3627 A	0.58	0.04	0.02	0.07	0.09
NGC3628	1.51	0.15	0.03	0.06	0.18
Arp220 T	896	61	51	73	115.44
M83 T	131	0.06	0.01	0.26	6

Table 2.6: UV luminosities of the mm-RL emitting regions. The first column shows the host galaxy and the aperture used. The second column shows the measured luminosity using aperture photometry. The third, fourth, and fifth columns show uncertainties introduced by the sky background, instrument and poissonian noise, respectively. The last column shows the total uncertainty, including the 5% uncertainty from flux calibration. [a] FUV data was not available and NUV fluxes were measured instead.

The UV fluxes have to be extracted from the same apertures used to extract the mm-RL fluxes, thus only apertures larger than the GALEX PSF can be used for UV photometry. In the case of Arp220 and NGC5253, the ALMA apertures are smaller than the GALEX PSF. For Arp220 this is not a problem, since the central region around the mm-RL emission is heavily obscured by dust, and a negligible FUV flux is detected. In the case of NGC5253, the GALEX FUV emission appears more extended than the submm continuum and mm-RL emitting regions, but the peaks of the FUV, mm-RL, and submm continuum emission spatially coincide. An aperture the size of the GALEX PSF, centered on the mm-RL emission peak, is used to extract the FUV flux. Thus, the FUV flux reported here for the mm-RL emitting region in NGC5253 should be considered an upper limit. The (F)UV luminosities, along with uncertainties, are shown in table 2.6.

2.2 Model fitting and incomplete datasets

This work relies heavily on fitting physical models to measured quantities. Models are sometimes represented by mathematical functions or families of functions, defined by a set of parameters, that map one set of physical quantities, the independent variables, to another set of physical quantities, the dependent variables. For example, an SED model can be represented by a function defined by parameters such as temperature and emission index, that maps frequency values to flux density values. For a black body, this function is simply the Planck function. The measured quantities are often expressed as a value, i.e. the result of a measurement, with an associated uncertainty. This reflects the imperfect knowledge about the result, stemming from the precision limit of the measuring device, or through the inherently stochastic properties of the system being studied. Thus, performing measurement can be thought of drawing samples from an underlying unknown distribution. The result usually represents the expected, or the most likely, measured value, while the uncertainty is a measure of its dispersion, representing a standard deviation, or a confidence interval. Taken together, these values give the rough outline of the unknown underlying probability distribution function. One of the most common ways to express uncertainties is to assume they are normally distributed, which, due to the central limit theorem, is often a reasonable assumption.

The aim of fitting a model to measurements is to find the model parameters that best explain the data. When a measurement is described using a probability density function, the likelihood of obtaining that measurement result given the values proposed by a model as a function of the parameter values can be calculated. Thus, in practice, finding the model parameters that best explain the data often involves the minimization of a cost function, or some form of likelihood maximization. Then, the best parameter values are those that maximize the likelihood of all the measurements, given the model predictions.

We define a datapoint as containing three values, the independent variable, the measurement, and its uncertainty. In the context of this work a datapoint can be represented by the frequency where the observations were performed, the measured flux density and the flux density uncertainty. A dataset is comprised of all the datapoints that are used in the fitting process. When fitting an SED to a dataset, it is best to have as many datapoints, i.e. measurements, in the frequency range of interest as possible. In certain situations datapoints are missing. Namely, for some galaxies in our sample, at certain wavelengths, no flux density measurements are available at the required resolution. Instead, the only flux density measurements available have a lower resolution, and thus contain flux from a larger patch of the galaxy than the rest of the measurements. Instead of performing the fit without including any datapoints at these frequencies, we include the information provided by the low resolution measurements in our fitting procedure. This is done by creating the so called incomplete datapoints. These datapoints contain the same type of information as a regular datapoint, however, during the fitting process, the uncertainty of this measured value affects the likelihood calculation of the fit only in one direction. For example, we fit a FIR SED model to measurements of the FIR fluxes extracted from a 25" diameter region centered on NGC2903. For the 160 μm wavelength, however, only a low resolution measurement, representing the total flux density of this galaxy, is available. During the fitting procedure, this measurement and its uncertainty, are used to decrease the likelihood of the fit only when the SED model yields fluxes above this measured value. This reflects our incomplete knowledge about the true value of the flux density in this 25" region at this wavelength, the only information available is that its value cannot be exceed that from the whole galaxy. This places an upper limit on the likely values of the model at this wavelength, and better constrains the uncertainties of the model parameters. We call the datasets containing these datapoints incomplete

datasets. The exact fitting procedure is described in more in the following sections.

2.2.1 A brief view of Bayesian inference

Central to Bayesian statistics, and to the methods used in this thesis, is the Bayesian interpretation of probability, as opposed to the more commonly used and familiar concept of frequentist probability. Consider an event, which may be the result of a statistical trial, whose probability of occurrence we wish to estimate. Bayesian probability quantifies the expectation or degree of belief that the event will occur, which can be based on all of our prior assumptions and knowledge about the event and trial conditions, as well as current measurements or results. Frequentist probability, on the other hand, is defined as the relative frequency of the event occurring after a large number of trials are repeated under identical conditions.

Bayes' theorem, which can be used to assign a probability value to a hypothesis or to the parameters of an explanatory model, has the following form

$$P(H|E) = \frac{P(E|H)P(H)}{P(E)} \tag{2.10}$$

where H is a hypothesis, E is the evidence, it represents our data set, e.g. results of some experiment or observation. $P(H|E)$ is the probability of H given the evidence E, also known as the posterior probability. P(E—H)$is the likelihood, or the probability of observing$E$if$H$were true.$ $P(H)$ is known as the prior probability, our prior knowledge of H, which quantifies how likely H was before E was observed. $P(E)$ is known as the model evidence or marginal likelihood. It represents the probability of the evidence, E, when factoring out our hypothesis, H. This term can also be written as:

$$P(E) = P(E|H)P(H) + P(E| \sim H)P(\sim H) = P(E \text{ and } H) + P(E \text{ and } \sim H) \tag{2.11}$$

meaning the probability of observing E when H is true plus the probability of observing the E when H is false. This parameter is usually difficult to calculate; however, since it does not depend on the hypothesis being tested, it can be ignored when we only want to compare the relative probabilities of different hypotheses in explaining the same data.

For a set of independent observational evidence or data $\mathbf{Y} = (y_1, y_2, ..., y_n)$, to which we fit a model that is parametrized by a k dimensional vector $\boldsymbol{\theta} = (\theta_1, \theta_2, ..., \theta_k)$, we use Bayes' theorem to write the posterior probability for the model parameters, given the data:

$$P(\boldsymbol{\theta}|\mathbf{Y}) = \frac{P(\mathbf{Y}|\boldsymbol{\theta})P(\boldsymbol{\theta})}{P(\mathbf{Y})} = \frac{P(\mathbf{Y}|\boldsymbol{\theta})P(\boldsymbol{\theta})}{\int (\mathbf{Y}|\boldsymbol{\theta})P(\boldsymbol{\theta})d\boldsymbol{\theta}} \propto P(\mathbf{Y}|\boldsymbol{\theta})P(\boldsymbol{\theta}) \propto \prod_{i=1}^{n} P(y_i, \boldsymbol{\theta})P(\boldsymbol{\theta}). \tag{2.12}$$

The Bayes Theorem can be used to assign a probability to the values of $\boldsymbol{\theta}$. Here, the prior probability, $P(\boldsymbol{\theta})$, governs the likelihood of $\boldsymbol{\theta}$ without taking the evidence into account, reflecting our knowledge about the most likely location of $\boldsymbol{\theta}$, in the parameter space, before making any observations.

2.2.2 Posterior probability and incomplete datasets

A fitting problem often arises when a model is needed for a set of measured or observed values $\mathbf{Y} = (Y_1, Y_2, ..., Y_n)$, the dependent variable. These measurements are connected to a set of values

$\mathbf{X} = (X_1, X_2, ..., X_n)$, the so-called independent variables. In this work, $\mathbf{Y}$ is the observed quantity such as the flux density or the integrated line flux, while $\mathbf{X}$ represents the frequencies where each measurement was performed. The model is represented by a function f, aiming to explain the measurement $\mathbf{Y}$ by providing estimates of it in the form of $\hat{\mathbf{Y}} = f(\boldsymbol{\theta}, \mathbf{X})$. The model could be, for example, a modified black body function, with the parameters making up the vector $\boldsymbol{\theta} = (\theta_1, \theta_2, ..., \theta_k)$ being the temperature, its emission index, and its normalization value. The uncertainties of the measurements, $\mathbf{Y}$, are given by $\boldsymbol{\sigma} = (\sigma_1, \sigma_2, ..., \sigma_n)$. These uncertainties usually represent the 68% confidence interval around the values of $\mathbf{Y}$.

The problem of finding the best parameters that fit a model to the data is then finding the values of $\boldsymbol{\theta}$ that maximize the posterior probability $P(\boldsymbol{\theta}|\mathbf{Y}, \boldsymbol{\sigma})$, where the uncertainties are taken into account. Maximizing the posterior probability in its original form, as a long series of products, can be computationally expensive. Taking advantage of the fact that if $\boldsymbol{\theta'}$ maximizes $P(\boldsymbol{\theta'}|\mathbf{Y}, \boldsymbol{\sigma})$ then it also maximizes $\log P(\boldsymbol{\theta'}|\mathbf{Y}, \boldsymbol{\sigma})$, we can write the posterior probability as a logarithm, which transforms the product into a sum and makes it easier to calculate:

$$\log\left[P(\boldsymbol{\theta}|\mathbf{Y}, \boldsymbol{\sigma})\right] \propto \log\left[P(\mathbf{Y}, \sigma|\boldsymbol{\theta}) + P(\boldsymbol{\theta})\right] \propto \sum_{i=1}^{n} \log\left[P(y_i, \sigma_i|\boldsymbol{\theta})\right] \log\left[P(\theta)\right]. \tag{2.13}$$

Since the uncertainties are assumed to be normally distributed, the likelihood, which is part of the right hand side of the above equation, can then be written as:

$$\log P(\mathbf{Y}, \boldsymbol{\sigma}|\boldsymbol{\theta}) = \sum_{\mathrm{i}=1}^{\mathrm{n}} \left(p_{\mathrm{i}}\right) = -\frac{1}{2}\left[\sum_{i=1}^{n} \frac{\left(\hat{Y}_{\mathrm{i}} - Y_{\mathrm{i}}\right)^2}{\sigma_{\mathrm{i}}^2} + \log\left(2\pi\sigma_{\mathrm{i}}^2\right)\right] \tag{2.14}$$

where $\hat{Y}_{\mathrm{i}} = f(\boldsymbol{\theta}, X_i)$ represents the model estimate for the ith measurement, from independent variable X_i (which in our case is usually a frequency value, i.e. ν_{i}). The number of measurements is denoted by n, while p_{i} is a probability density function that describes the probability distribution of $\hat{Y}_{\mathrm{i}}$, which has the form of a Gaussian distribution with mean Y_{i} and standard deviation σ_{i}.

When dealing with an incomplete data point j that is used as a limiting value during the fit, with a value of Y_{j} and an uncertainty of σ_j, we calculate the posterior probability using a modified probability function q_{j}. This function has to reflect our lack of knowledge about the exact value of the measurement and that the true value of the measurement can have any value between 0 and Y_{j}. The lower limit on zero is included because the data represents measurements of fluxes, which can only have positive values. The log-likelihood is now given by

$$\log P(\hat{\mathbf{Y}}, \boldsymbol{\sigma}|\boldsymbol{\theta}) = \sum_{\mathrm{i}=1}^{\mathrm{n}} \log\left(p_{\mathrm{i}}\right) + \sum_{\mathrm{j}=1}^{\mathrm{m}} \log\left(q_{\mathrm{j}}\right) \tag{2.15}$$

where m is the number of data points representing upper limits. We construct q_{j} to be zero for $\hat{Y}_{\mathrm{j}} < 0$, reflecting the nonexistence of negative flux. For $\hat{Y}_{\mathrm{j}}$ between 0 and Y_{i} it returns a constant value, reflecting the fact that the real value of the measured data could be anywhere in this region. For $\hat{Y}_{\mathrm{j}} > Y_{\mathrm{j}}$, p_{j} drops to zero like a gaussian with standard deviation σ_{j}, representing the ever decreasing likelihood

of the values above this upper limit. The complete form of q_j is then:

$$q_j = \begin{cases} 0, & \hat{Y}_j < 0 \\ C_1, & 0 \leq \hat{Y}_j \leq Y_j \\ \left(\frac{C_2}{\sigma_j\sqrt{2\pi}}\right) \exp\left[\frac{\left(\hat{Y}_j - Y_j\right)^2}{\sigma_j^2}\right], & Y_j < \hat{Y}_j \end{cases} \tag{2.16}$$

The constants C_1 and C_2 are determined by the conditions imposed on q by its continuity at $\hat{Y}_j = Y_j$, and by the fact that it needs to integrate to 1 as a probability density function, i.e. $\int_{-\infty}^{+\infty} q_j \, df = 1$. Solving for the values of C_1 and C_2, the probability density used to calculate the likelihood term in Bayes' theorem is:

$$\log q_j = \begin{cases} -\infty, & \hat{Y}_j < 0 \\ \log\left(\frac{2}{2Y_j + \sigma_j\sqrt{2\pi}}\right), & 0 \leq \hat{Y}_j \leq Y_j \\ \log\left(\frac{2}{2Y_j + \sigma_j\sqrt{2\pi}}\right) - 0.5\frac{\left(\hat{Y}_j - Y_i\right)^2}{\sigma_i^2}, & Y_j < \hat{Y}_j, \end{cases} \tag{2.17}$$

in logarithmic form. The posterior probability, for a data set containing n complete and m incomplete datapoints, can be written:

$$\log\left[P(\boldsymbol{\theta}|\mathbf{Y}, \boldsymbol{\sigma})\right] \propto \sum_{i=1}^{n} \log\left(p_i\right) + \sum_{j=1}^{m} \log\left(q_j\right) + \log\left[P(\boldsymbol{\theta})\right]. \tag{2.18}$$

The value of θ that maximizes the above probability yields the best fit parameters of our model.

2.2.3 Using `emcee` with incomplete datasets

When fitting a model that depends on a set of parameters to observational data, one is interested not only in finding the best values of $\boldsymbol{\theta} = (\theta_1, ..., \theta_k)$, but also in finding its probability distribution, $P(\boldsymbol{\theta}|\mathbf{Y})$. However, finding the properties of a probability density function, such as its expectation value, requires evaluating an integral of the form $E\left[\boldsymbol{\theta}|\mathrm{Y}\right] = \int \boldsymbol{\theta} P(\boldsymbol{\theta}|\mathbf{Y}) d\boldsymbol{\theta}$. Evaluating this integral can be computationally expensive even for moderately small values of k. However, if instead samples could be drawn from the distribution $P(\boldsymbol{\theta}|\mathbf{Y})$, the mean and variance of the resulting samples could be good estimators of the mean and variance of $P(\boldsymbol{\theta}|\mathbf{Y})$. In this paper we use the `emcee` (Foreman-Mackey et al., 2013) Python package to draw samples from the posterior distribution and determine the parameter values that maximize the posterior probability and their uncertainties.

The `emcee` package Foreman-Mackey et al. (2013), based on the work of Goodman & Weare (2010), is an affine invariant Markov chain Monte Carlo ensemble sampler. We use the `emcee` package in several places in this work, and although it is used to fit different models to different types of data, the overall method of implementation is the same. We construct the likelihood, $P(\hat{\mathbf{Y}}, \boldsymbol{\sigma}|\boldsymbol{\theta})$, and prior probability, $P(\boldsymbol{\theta})$, as `python` functions based on our models, and pass them along with our data set to `emcee` for fitting. The results consist of a sample of parameter values whose distribution approximates the posterior distribution well, $P(\boldsymbol{\theta}|\mathbf{Y})$. To achieve this, the `emcee` package initializes a number of

Markov chains that take values from the parameter space Goodman & Weare (2010); Foreman-Mackey et al. (2013). A Markov chain is a list of values, where the probability of each value depends only on the value reached in the previous step. At each iteration, a new candidate value is proposed for each chain, which is accepted at a rate that typically depends on the posterior probabilities of the original and candidate values. Since at each iteration the last values in each chain represent a position in parameter space, the trajectory that each chain follows can be thought of as a "walk" through parameter space. For this reason, in the `emcee` framework, these chains, at any given iteration, are also referred to as "walkers" moving through parameter space (Foreman-Mackey et al., 2013).

The posterior probability distribution from which we ultimately want to sample may be heavily skewed in one or more directions in parameter space. An MC walker that determines the distance to its next candidate position by sampling a Gaussian probability distribution function with a fixed standard deviation, σ, is inefficient in such cases. It would, on average, generate many candidates from low posterior probability regions of the parameter space, leading to many rejections, while relatively undersampling regions of higher probability, making the sampling inefficient (Goodman & Weare, 2010; Foreman-Mackey et al., 2013). The `emcee` package solves this problem by performing affine invariant sampling. Affine sampling adjusts the direction and distance to new candidate positions for the Metropolis-Hastings algorithm, making it suitable for sampling probability distributions with skewed shapes. This is done by considering the relative positions of the walkers in the ensemble at the current step in otder to calculate candidate positions for the next step. The two main methods of affine invariant sampling used in the `emcee` package are described below, although the latest version of `emcee` provides several more options. In a stretch move, the new candidate position for a walker is chosen by stretching the distance between the position of the current walker and another randomly chosen walker (Goodman & Weare, 2010; Foreman-Mackey et al., 2013). The "walk" move uses a subsample of walker positions to generate a new candidate position. In this method, the candidate position is obtained by perturbing the position of a walker by an amount equal to the covariance of the subsample Goodman & Weare (2010); Foreman-Mackey et al. (2013). These methods ensure that the multiple walkers spend most of their time in regions of parameter space that have a high probability of fitting the observed data, and that the sampled positions follow the underlying probability distribution (Goodman & Weare, 2010; Foreman-Mackey et al., 2013).

In our work we use the default setting of `emcee`, which implements the "stretch move". The direction of the stretch is co-linear with the distance between the current walker and another randomly chosen walker, and the size of the move, i.e. the amount of stretching, is proportional to the distance between the two walkers multiplied by a normalization factor. The normalization factor, Z, is drawn from a distribution $g(z)$ Foreman-Mackey et al. (2013). After a new candidate position is generated, it is accepted or rejected with a probability p_{accept}. This probability depends on the the posterior probabilities of the current and candidate positions, as well as normalization factor Z (Foreman-Mackey et al., 2013):

$$p_{\text{accept}}(\boldsymbol{\theta}_{\text{i+1}}) = \min\left(1, \varepsilon = Z^{N-1}\frac{P(\boldsymbol{\theta}_{\text{i+1}}|\mathbf{Y})}{P(\boldsymbol{\theta}_{\text{i}}|\mathbf{Y})}\right), \tag{2.19}$$

where N is the number of dimensions of the parameter space. The probability distribution function of Z is (Goodman & Weare, 2010):

$$g(z) = \begin{cases} \frac{1}{\sqrt{z}}, z \in \left[\frac{1}{2}, 2\right], \\ 0, \text{ otherwise.} \end{cases} \tag{2.20}$$

In our work, we use the default setting of `emcee`, which implements the "stretch move". The direction of the stretch is co-linear with the distance between the current walker and another randomly chosen walker, and the size of the move, i.e. the amount of stretching, is proportional to the distance between the two walkers multiplied by a normalization factor. The normalization factor Z is drawn from a distribution $g(z)$ Foreman-Mackey et al. (2013). After a new candidate position is generated, it is accepted or rejected with a probability p_{accept}. This probability depends on the posterior probabilities of the current and candidate positions as well as the normalization factor Z (Foreman-Mackey et al., 2013): If the new candidate position is "better" than the previous one, then $\varepsilon \gtrsim 1$, $p_{\text{accept}} = 1$ and the new candidate position is accepted. The walker moves to the new position and the value of $\boldsymbol{\theta_{i+1}}$ is added to the chain. If the new position is "worse", $\varepsilon < 1$ and $p_{\text{accept}} = \varepsilon$. In this case, the probability of accepting the new position decreases depending on how much lower its posterior probability is compared to the current one, but it is never zero. In case of rejection, the walker keeps its current position and the value of $\boldsymbol{\theta_i}$ is added to the chain. This type of sampling makes the walker navigate the parameter space towards regions of higher posterior probability. However, given the non-zero probability of choosing a new sample with a lower posterior probability P than the current one, the walkers do not get stuck in local minima Goodman & Weare (2010); Foreman-Mackey et al. (2013).

In this work, we supply the `emcee` package with our likelihood functions defined by the equation 2.14 when the dataset is complete, or by the equation 2.15 when the dataset is incomplete. The prior probability functions we use with the `emcee` package are usually flat, meaning that for a given volume of parameter space, V_θ, the prior probability of the parameters is equal to one, i.e., $P(\boldsymbol{\theta} \in V_\theta) = 1$, and their probability distribution function has a constant value over V_θ and is zero otherwise. The exact configuration used is presented for each use case.

CHAPTER 3

Revisiting the Theory of mm-RL Emission

Hydrogen recombination lines and the free-free continuum both provide measures of the massive star content of the observed region, and they thereby provide measures of the (massive) star formation rate. In external galaxies we lack the spatial resolution to constrain the physical structure of the observed region. To relate the observables to a SFR, some simplifying assumptions about density, temperature and the line-of-sight emission measure must therefore be made, which we describe in this section. In the following we derive the relation between the observables and the SFR in the optically thin limit, and then derive a correction factor accounting for radiative transfer effects.

3.1 The optically thin limit

For photoionized gas in an HII region, the line volume emissivity from a hydrogen recombination transition between high quantum number states $u \rightarrow n$ is proportional to the product between the number density of atoms in state u and the Einstein-A coefficient. In the optically thin limit, the H-RL luminosity of an HII region of volume V is the volume integral over the H-RL volume emissivity. Since the high-n level states of the hydrogen atoms in an HII region are mainly populated through recombination, the volume emissivity scales with the product $n_e n_p$, times an emission rate coefficient, the specific volume emissivity, $\epsilon_{un}(T_e, n_e)$, which was computed and tabulated as a function of T_e and n_e by Storey & Hummer (1995) (Fig. 3.2). The luminosity of the H-RL can be written as

$$L_{un} = \int_V n_e n_p \, \epsilon_{un}(T_e, n_e) \, \mathrm{d}V, \tag{3.1}$$

and similarly for the free-free continuum luminosity density,

$$L_{\nu\mathrm{ff}} = \int_V n_e n_i \, \epsilon_{\nu\mathrm{ff}}(T_e) \, \mathrm{d}V, \tag{3.2}$$

where $\epsilon_{\nu\mathrm{ff}}$ is the free-free specific volume emissivity (per Herz) for singly charged ions, and $n_i = n(\mathrm{H}^+) + n(\mathrm{He}^+)$ is the singly charged ion density, where $n_i = n_e$ when ignoring doubly ionized He. The specific line volume emissivity depends weakly on the electron density, $n_e = n(\mathrm{H}^+) + n(\mathrm{He}^+)$ (ignoring double-ionized He), and more strongly on the electron temperature, T_e (e.g. Storey & Hummer, 1995; Gordon & Sorochenko, 2002).

In the following only the bright H$n\alpha$ transitions, $n+1 \rightarrow n$, are considered, although other transitions can be treated in a similar way. The apparent line flux at some distance, D,

$$I_{\mathrm{n}\alpha} = \frac{L_{\mathrm{n}\alpha}}{4\pi D^2} = \frac{\overline{\epsilon}_{\mathrm{n}\alpha}\ \mathrm{EM_V}}{4\pi D^2}, \tag{3.3}$$

where

$$\mathrm{EM_V} = \int_V n_e n_p \,\mathrm{d}V \tag{3.4}$$

is the ionized hydrogen volume emission measure, and $\overline{\epsilon}_{\mathrm{n}\alpha}$ is the n_e^2 weighted mean of the specific volume emissivity, which depends on the temperature and density distribution within the HII region. Similarly, the observed free-free continuum flux density,

$$F_{\nu,\mathrm{ff}} = \frac{L_{\nu\mathrm{ff}}}{4\pi D^2} = \frac{\overline{\epsilon}_{\nu\mathrm{ff}}(\,\mathrm{EM_V} + \mathrm{EM_{HeII}})}{4\pi D^2}, \tag{3.5}$$

where $\mathrm{EM_{HeII}}$ is the ionized He volume emission measure and $\overline{\epsilon}_{\nu\mathrm{ff}}$ is the n_e^2-weighted mean of $\epsilon_{\nu\mathrm{ff}}$, which depends on the temperature distribution in the HII region. For the free-free emission the helium contribution must be considered properly. For this we consider uniformly dense Stromgren spheres (Draine, 2011) with a 10% He abundance by number, a Kroupa (2002) IMF for main sequence O-type stars up to 100 $M_\odot$, and the $h\nu \geq 13.6$ eV and $h\nu \geq 24.6$ eV EUV emission from Martins et al. (2005) as tabulated by Draine (2011). We consider the two limiting cases: (i) each star creates a separate HII region, (ii) all stars form one HII region, as considered by Scoville & Murchikova (2013). For theses extreme cases we find $\mathrm{EM_{HeII}}/\mathrm{EM_V} \approx 0.047$ and 0.043, respectively. The details on how these contributions were calculated are presented in Section 3.2 The contribution of singly ionized He to the free-free emission is therefore small. Note that this does not depend on the density or temperature structure of the HII regions. The relative contribution of doubly ionized He is of order 10^{-4} (Scoville & Murchikova, 2013), and may thus be neglected.

3.2 The contribution of HeII emission to the free-free continuum

Free-free continuum emission arises from ionized gas as brehmsstrahlung radiation, as electrons scatter off of ions. The ions are usually hydrogen nuclei, i.e., protons. However, in the ISM and in HII regions in particular, ionized Helium is also present. This can be singly or doubly ionized, i.e. H^+ or H^{++}. The contribution of helium to the overall continuum emission has to be taken into consideration when comparing hydrogen recombination line intensities with the free-free emission level. In the following we calculate what the helium contribution to the free-free continuum emission is, assuming two geometries for the HII regions. In the first configuration we assume no overlap between HII region around massive stars, while in the second configuration we assume that all the radiation from massive stars contribute to the formation of a single, giant, HII region. The EM of hydrogen inside of an HII region, modelled as a Stromgren sphere, depends on the ionizing photon flux Q_0 of the massive star at its center. These are photons with E> 13.6 eV, i.e. enough energy to ionize hydrogen. The EM of He^+ depends on the ionizing photon flux Q_1 of the massive stars, which consists of photons that can ionize helium, having energies E> 24.6 eV. The intensity of the fluxes and their ratio depend, to a first order approximation, on the mass of the star and its metallicity. We calculate Q_0 and Q_1 as a

function of stellar mass using the values given by Draine (2011) in Table 15.1, i.e., O-type stars of luminosity class V. The values of Q_0 and Q_1/Q_0 in Draine (2011) are given only up to a stellar mass of $50\,M_\odot$. To get ionizing fluxes for higher masses, we fit the Q_0 data with a powerlaw, as shown in figure 3.1. The powerlaw has the form $f_{Q_0}(m) = a + b \times m^c$. The parameters obtained from the fit are $a = (1.09 \pm 0.03) \times 10^{42}\,\mathrm{s}^{-1}$, $b = (8.3 \pm 1.1) \times 10^{45}\,\mathrm{s}^{-1}$, and $c = 2.12 \pm 0.03$. To obtain Q_1, we multiply Q_0 with an interpolation of the Q_1/Q_0 data from Draine (2011), shown in figure 3.1. In the case where $Q_1/Q_0 > 0.15$, helium is ionized throughout the HII region, thus, there is no need to calculate Q_1/Q_0 values for stellar masses higher than $m \approx 30\,M_\odot$. The total flux Q_0^{total} or Q_1^{total} from a population of stars is obtained by integrating over the product between the ionizing photon flux as a function of mass, $Q_0(m)$, and the IMF, $\xi(m)$, i.e.:

$$Q_0^{\mathrm{total}} = \int_{M_l}^{M_u} Q_0(m) \times \xi(m) dm, \tag{3.6}$$

where M_l and M_u are the lower and upper limits for the stellar masses considered. The EM_V of hydrogen and helium are obtained adapting Eq. 15.32 and 15.33 in Draine (2011), for a stellar mass m:

$$\begin{aligned} \mathrm{EM}_V^{\mathrm{He}^+}(m) &= \frac{(1-y)Q_1(m)}{\alpha_B(\mathrm{He}) + y\alpha_{1S}(\mathrm{He})} \\ \mathrm{EM}_V^{\mathrm{H}^+} &= \frac{Q_0(m) - Q_1(m) + yQ_1 + EM_{\mathrm{He}^+}\left[z\alpha_B(\mathrm{He}) + y\alpha_{1S}(\mathrm{He})\right]}{\alpha_B(\mathrm{H})}, \end{aligned} \tag{3.7}$$

where $\alpha_B(\mathrm{H})$ and $\alpha_B(\mathrm{He})$ are case B recombination rate coefficients and $\alpha_{1S}(\mathrm{H})$ and $\alpha_{1S}(\mathrm{He})$ are ground state recombination coefficients for hydrogen and helium respectively. Helium electron recombinations to the ground state creates photons with energies $E > 24.6\,\mathrm{eV}$, which can ionize another hydrogen or helium atom. The term y represents the ratio of hydrogen atoms ionized by these photons with respect to the total number of hydrogen and helium reionizations. In our calculation, we follow the prescription of Draine (2011) and set $y = 0.2$. The term z represents the fraction of case B helium recombination photons that can ionize a hydrogen atom. The values of z vary between 0.67-0.96, inversely proportional to the gas density. We use the prescription from Draine (2011) and set $z = 0.8$. The volume EM for hydrogen and helium emission for a given stellar population, assuming no overlap of HII regions, is obtained by integrating $\mathrm{EM}(m)$ over the whole stellar mass range, taking the IMF into account:

$$\begin{aligned} \mathrm{EM}^{\mathrm{H}^+}{}_V &= \int_{M_l}^{M_u} \mathrm{EM}_V^{\mathrm{H}^+}(m) \cdot \xi(m) dm, \\ \mathrm{EM}^{\mathrm{He}^+}{}_V &= \int_{M_l}^{M_u} \mathrm{EM}_V^{\mathrm{He}^+}(m) \cdot \xi(m) dm, \end{aligned} \tag{3.8}$$

where $\xi(m)$ is the Kroupa (2001) IMF. Where $Q_1(m)/Q_0(m) \gtrsim 0.15$ or $N(\mathrm{He}^+) \approx 0.1N(\mathrm{H}^+)$, helium is ionized throughout the HII region, so we set $\mathrm{EM}_V^{\mathrm{He}^+}(m) = \mathrm{EM}_V^{\mathrm{H}^+} \times 10^{-2}$ for these cases. Q_1 fluxes for stellar masses $m \lesssim 15\,M_\odot$ were not readily available, we set take two extreme case into consideration while calculating $\mathrm{EM}^{\mathrm{He}^+}{}_V$. In the first case the helium ionizing photon flux, Q_1, for all stars below $15\,M_\odot$ is fixed at its $15\,M_\odot$ value, and in the second case Q_1 is set to zero for all stars below

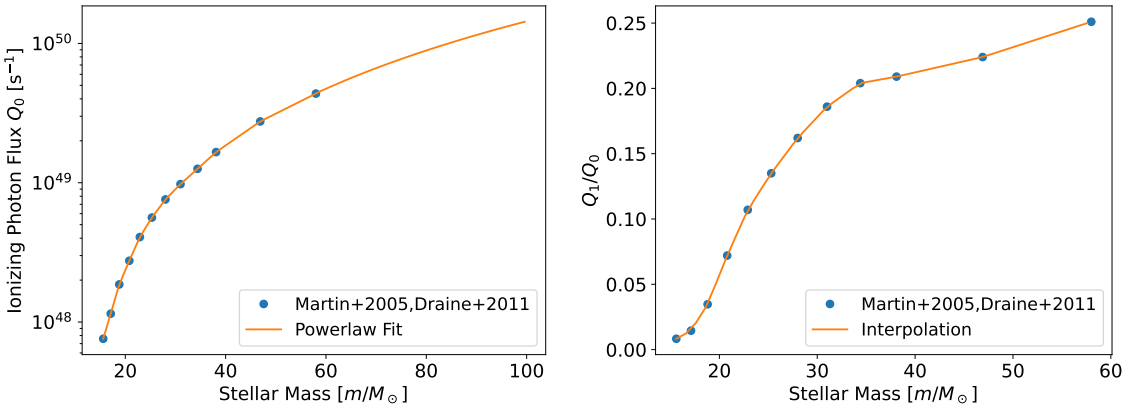

Figure 3.1: Left: Hydrogen ionizing photon flux, Q_0, as a function of stellar mass. The data is adapted from Martins et al. (2005) by (Draine, 2011), and is fit with a powerlaw. Right: Helium to Hydrogen ionizing photon flux ratio, Q_1/Q_0, as a function of stellar mass. The data is adapted from Martins et al. (2005) by (Draine, 2011), where we have interpolated between the datapoints. In the case where $Q_1/Q_0 > 0.15$, i.e., stellar masses above $30\,M_\odot$, helium is ionized throughout the HII region. For stellar masses lower than $15\,M_\odot$, we take two extreme cases into consideration: $Q_1(m < 15\,M_\odot) = Q_1(15\,M_\odot$ and $Q_1(m < 15\,M_\odot) = 0\,\mathrm{s}^{-1}$

$15\,M_\odot$. The two cases are thus either $Q_1(m < 15\,M_\odot) = Q_1(15\,M_\odot)$ or $Q_1(m < 15\,M_\odot) = 0\,\mathrm{s}^{-1}$. The resulting values corresponding to the two cases should bracket the real value of $\mathrm{EM}^{\mathrm{He}^+}{}_V$. The ratio of the two EM values corresponding to hydrogen and helium emission give the overall contribution of helium to the free-free continuum emission. By integrating over the stellar mass range of 1-100 $M_\odot$, we find the helium contribution to the free-free emission to be below 5%.

3.3 From mm-RL flux to star formation rates

Equations 3.3 and 3.5 link the observables $I_{\mathrm{n}\alpha}$ and $F_{\nu,\mathrm{ff}}$ to the volume emission measure, $\mathrm{EM_V}$, which in turn can be related to the ionizing photon flux, Q_0, of massive stars. In an ionization-bounded HII region,

$$Q_0 = \int_V n_e n_p\, \alpha_B(T_e)\, \mathrm{d}V = \overline{\alpha}_B\, \mathrm{EM_V}, \tag{3.9}$$

where $\alpha_B(T_e)$ is the case-B hydrogen recombination rate coefficient, and $\overline{\alpha}_B$ is the n_e^2 weighted mean thereof. Based on the computations of Storey & Hummer (1995), at temperatures between 3000 and 20000 K, its dependence on the electron temperature, $T_e \equiv 10^4\,T_4$ K, can be approximated to within 3% by

$$\alpha_B(T_e) = 2.61 \times 10^{-13}\, T_4^{-0.77} \mathrm{cm}^3\mathrm{s}^{-1}. \tag{3.10}$$

The ionizing photon emission, Q_0, depends on the number of stars with given initial mass and metallicity, and on the age of the HII region. It is convenient and reasonable to assume that the SFR is constant for at least 8 Myr, in which case Q_0 becomes directly proportional to the SFR and nearly independent of time (Ramachandran et al., 2019). Bendo et al. (2015) used STARBURST99 models (Leitherer et al., 1999, 2014), ignoring dust, with two times solar metallicity and a Kroupa (2001)

n	$\nu_{n\alpha}$ [GHz]	$\epsilon_{\mathrm{n}\alpha,4}$ [10^{-32}erg cm^{3}s^{-1}]
26	353.62	24.85
27	316.41	19.92
30	231.90	10.79
33	174.99	6.225
34	160.21	5.243
40	99.022	2.068
41	92.034	1.797
42	85.688	1.566

Table 3.1: H$n\alpha$ line frequency and normalization at $T = 10^4$ K of the $10^3 \leq n_e/\mathrm{cm}^{-3} \leq 10^5$ fit to the specific line volume emissivity, $\epsilon_{\mathrm{n}\alpha}$, for the lines relevant to this work. Volume emissivities are derived from the power law fit in T_e (eq. 3.14) to the data provided by Storey & Hummer (1995).

IMF for initial stellar masses of 0.1 – 100 $\mathrm{M}_\odot$ to compute the ratio

$$\frac{\mathrm{SFR}}{Q_0} = 5.41 \times 10^{-54}\ \mathrm{M}_\odot \mathrm{yr}^{-1}\ \mathrm{s} \equiv \left(\frac{\mathrm{SFR}}{Q_0}\right)_{B15}. \tag{3.11}$$

A narrower mass range 1 – 50 $\mathrm{M}_\odot$ would correspond to the Salpeter IMF with slope 1.35, reducing the total stellar mass and SFR by 1.81. Combining eqs. 3.3, 3.9, and 3.11 yields a relation between the SFR and the line flux,

$$\mathrm{SFR}_{\mathrm{n}\alpha} = 4\pi D^2 I_{\mathrm{n}\alpha}\, \frac{\overline{\alpha}_B}{\overline{\epsilon}_{\mathrm{n}\alpha}} \left(\frac{\mathrm{SFR}}{Q_0}\right)_{B15}, \tag{3.12}$$

and eqs. 3.5, 3.9 and 3.11 provide a relation between the SFR and the free-free flux density,

$$\mathrm{SFR}_{\mathrm{ff}} = 4\pi D^2\, F_{\nu,\mathrm{ff}}\, \frac{\overline{\alpha}_B}{\overline{\epsilon}_{\nu\mathrm{ff}}} \left(\frac{\mathrm{SFR}}{Q_0}\right)_{B15}. \tag{3.13}$$

These relations are formally accurate, but impractical since the weighted rate coefficients require prior knowledge about the density and temperature structure. In all these relations, the effects of dust on the ionizing photon flux have been ignored. Dust can absorb some of the ionizing photons, resulting in a smaller HII region than what is calculated when ignoring the dust. This leads to an underestimation of SFR proportional to the fraction of ionizing photons absorbed by dust. This fraction weakly depends on the density of the gas and its distribution, its temperature, and the ionizing photon flux emitted by the stars, while it is directly proportional to the UV attenuation cross-section of the dust. Considering a typical HII region, while still allowing for significant variation of the conditions, with $10^2 < n_{\mathrm{rms}} < 10^5\ \mathrm{cm}^{-3}$, $0.5 < T_4 < 1.5$, and $Q_0 \approx 10^{49}\ \mathrm{s}^{-1}$, Draine (2011) find that the fraction of hydrogen ionizing photons in the HII region is between 0.7 and 0.4.

3.4 Estimating the electron temperature

The simplifying approximation that the gas is at uniform density and temperature allows for an explicit expression of the temperature dependence of the SFR. The electron temperature of the ionized gas can thus be derived from the line-to-continuum emission ratio (e.g. Gordon & Sorochenko, 2002).

Because $\epsilon_{\mathrm{n}\alpha}$ has a strong dependence on temperature and a weak density dependence, we fit a power law in temperature, based on the values of Storey & Hummer (1995)

$$\epsilon_{n\alpha}(T_e, n_e) \approx \epsilon_{n\alpha,4}\, T_4^{-1.35}, \tag{3.14}$$

which is accurate to within 10% in the range 3,000 - 12,500 K and $n_e \approx 10^3 - 10^5\,\mathrm{cm}^{-3}$. The normalization $\epsilon_{n\alpha,4}$ is given in Table 1. The SFR implied by the H-RL flux (eq. 3.12) can now be approximated as

$$\frac{\mathrm{SFR}_{\mathrm{n}\alpha}}{\mathrm{M}_\odot\,\mathrm{yr}^{-1}} = 0.0269\, T_4^{0.58}\, \frac{\nu_{\mathrm{n}\alpha}}{\nu_{40\alpha}} \left[\frac{D}{\mathrm{Mpc}}\right]^2 \frac{\epsilon_{40\alpha,4}}{\epsilon_{n\alpha,4}}\, \frac{I_{\mathrm{n}\alpha}}{\mathrm{Jy\,km\,s}^{-1}}\,. \tag{3.15}$$

The free-free specific volume emissivity can be written as

$$\epsilon_{\nu\mathrm{ff}}(T_e) = \frac{8}{3}\left(\frac{2\pi}{3}\right)^{1/2} g_{\mathrm{ff}}(\nu, T_e)\, \frac{\mathrm{e}^6}{m_e^{3/2} c^3}\, \frac{e^{-h\nu/kT_e}}{(kT_e)^{1/2}}, \tag{3.16}$$

where e is the electron charge, m_e is the electron mass, and the Gaunt factor accounting for quantum effects – see e.g. Draine (2011),

$$g_{\mathrm{ff}}(\nu, T_e) = 0.5525\, \ln\left[\frac{\mathrm{GHz}}{\nu}\left(\frac{T_e}{\mathrm{K}}\right)^{1.5}\right] - 1.682. \tag{3.17}$$

The corresponding free-free absorption opacity is derived from Kirchhoff's law, $B_\nu = n_i n_e \epsilon_{\nu\mathrm{ff}}/\kappa_{\mathrm{ff}}$, where B_ν is the Planck function, so that in the Rayleigh-Jeans limit $h\nu \ll kT_e$ (eq. 2.94 Gordon & Sorochenko, 2002),

$$\frac{\kappa_{\mathrm{ff}}}{\mathrm{cm}^{-1}} = 9.77 \times 10^{-3} \left[\frac{n_e n_i}{\mathrm{cm}^{-6}}\right] \left[\frac{\nu}{\mathrm{Hz}}\right]^{-2} \left[\frac{T_e}{\mathrm{K}}\right]^{-1.5} g_{\mathrm{ff}}(\nu, T_e). \tag{3.18}$$

The SFR can be related to the free-free flux density (eq. 3.13) using Eq. 3.10, and considering $h\nu \ll kT_e$ and $g_{\mathrm{ff}}(\nu_{40\alpha}, 10^4\mathrm{K}) = 3.4$,

$$\frac{\mathrm{SFR}_{\mathrm{ff}}}{\mathrm{M}_\odot\,\mathrm{yr}^{-1}} = 0.73\, T_4^{-0.271} \left[\frac{3.4}{g_{\mathrm{ff}}(\nu, T_e)}\right] \left[\frac{D}{\mathrm{Mpc}}\right]^2 \left[\frac{F_{\nu,\mathrm{ff}}}{\mathrm{Jy}}\right]\,. \tag{3.19}$$

With prior knowledge of, or assumptions about the gas temperature, the observed H-RL line fluxes and free-free continuum flux density provide independent estimates of the star formation rate. Alternatively, the ratio between the line flux and continuum flux density yields the gas temperature through the

implicit relation

$$\frac{I_{\mathrm{n}\alpha}}{F_{\nu,\mathrm{ff}}}\frac{\mathrm{Jy}}{\mathrm{Jy\,km\,s^{-1}}} \approx 27.1\, T_4^{-0.85}\, \frac{g_{\mathrm{ff}}(\nu,T_e)}{3.4}\, \frac{\epsilon_{n\alpha,4}}{\epsilon_{40\alpha,4}}\, \frac{\nu_{40\alpha}}{\nu_{\mathrm{n}\alpha}}\,. \tag{3.20}$$

This temperature estimate can be used to derive $\mathrm{SFR}_{\mathrm{n}\alpha}$ and $\mathrm{SFR}_{\mathrm{ff}}$. Note that the free-free continuum can be measured at a frequency different from that of the line(s), and that different lines may produce different results for $\mathrm{SFR}_{\mathrm{n}\alpha}$, due to measurement uncertainties or optical depth effects.

3.5 Optically thick line emission, amplification and attenuation

The specific line volume emissivity calculated by Storey & Hummer (1995) takes into account non-LTE effects which can lead to line amplification and attenuation, as a function of optical depth. The effects of radiative transfer along the line of sight on the line intensities have to be taken into consideration when calculating SFR. This section explains how the optical depth affects the relative line intensities.

In LTE conditions and in the Rayleigh-Jeans limit, the frequency-dependent H-RL absorption opacity is (Gordon & Sorochenko (2002) eq. 2.116)

$$\begin{aligned}\frac{\kappa^*_{\mathrm{n}\alpha}}{\mathrm{cm^{-1}}} = 3.47{\times}10^{-12}\, f_{n,n+1}\, e^{h\nu/kT_e} \\ \times\left[\frac{\phi_\nu}{\mathrm{Hz^{-1}}}\right]\left[\frac{n_e n_p}{\mathrm{cm^{-6}}}\right]\left[\frac{T_e}{\mathrm{K}}\right]^{-5/2}\left(\frac{n-3/2}{n^2}\right),\end{aligned} \tag{3.21}$$

where ϕ_ν is the line profile ($\int \phi_\nu \mathrm{d}\nu = 1$), the absorption oscillator strength $f_{\mathrm{n,n+1}} \approx 0.19(n+3/2)$ (Menzel, 1968), and the asterisk denotes quantities that are derived under the assumption of LTE. Under non-LTE conditions,

$$\kappa_{\mathrm{n}\alpha} = b_n \gamma_n \kappa^*_{\mathrm{n}\alpha}, \tag{3.22}$$

where the departure coefficient, b_n (Fig. 3.2 top), is the ratio between the level population of state n relative to its value in LTE. The factor

$$\gamma_n \;=\; \frac{1-(b_{n+1}/b_n)e^{-h\nu/kT_e}}{1-e^{-h\nu/kT_e}} \tag{3.23}$$

(Fig. 3.2) accounts for stimulated emission (Gordon & Sorochenko, 2002; Draine, 2011). For mm-RL frequencies, with $T_e > 10^3$, $e^{-h\nu/kT_e} \to 1$. Thus γ_n can take large negative values when $b_{n+1} > b_n$ (Fig. 3.2). When $\gamma_n < 0$, it follows from Eq. 3.22 that $\kappa_{\mathrm{n}\alpha} < 0$, i.e. line amplification occurs.

The total optical depth (line or continuum) is the integral of the opacity along the line of sight,

$$\tau(\nu) = \int_{\mathrm{LOS}} \kappa(\nu)\, \mathrm{d}l\,. \tag{3.24}$$

Thus, in a medium of constant temperature and density, the optical depth scales linearly with the-line-of-sight emission measure, $\mathrm{EM_{LOS}} \equiv \int n_e^2\, \mathrm{d}l$.

The solution of the radiative transfer integral yields the frequency-integrated H-RL line flux (Gordon

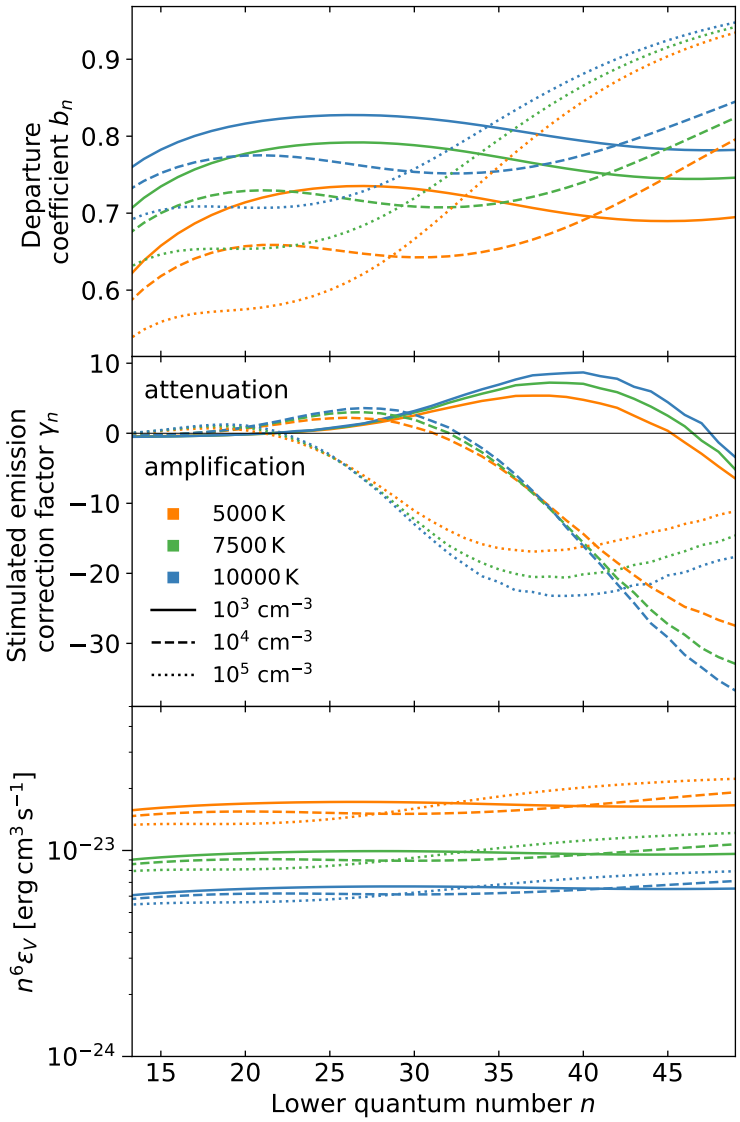

Figure 3.2: *Top:* Departure coefficients for Hnα lines as a function of transition quantum number, n, calculated by Storey & Hummer (1995). *Center:* Stimulated emission correction factor γ_n as a function of transition quantum number n. *Bottom:* H-RL volume emissivity $\epsilon_{\mathrm{n}\alpha}$ as a function of transition quantum number n. For better visibility, we display $n^6\epsilon_{n\alpha}$.

& Sorochenko, 2002)

$$\frac{\mathrm{d}I_{\mathrm{n}\alpha}}{\mathrm{d}\Omega} = \int_{\nu} \left[\eta B_\nu(T_e)\left(1 - e^{-\tau_{\mathrm{n}\alpha}-\tau_{\mathrm{ff}}}\right) - B_\nu(T_e)\left(1 - e^{-\tau_{\mathrm{ff}}}\right)\right] \mathrm{d}\nu \,, \tag{3.25}$$

where the first term in the integral is the total flux density, and the second term is the free-free continuum flux density. The factor

$$\eta = \frac{1 + b_{n+1}(\kappa^*_{\mathrm{n}\alpha}/\kappa_{\mathrm{ff}})}{1 + b_n(\kappa^*_{\mathrm{n}\alpha}/\kappa_{\mathrm{ff}})\gamma_n} \tag{3.26}$$

corrects the Planck function for any departure from LTE.

Considering Kirchhoff's law, $n_i n_e \epsilon_{n\alpha} = \kappa^*_{n\alpha} b_{n+1} B_\nu$ in the optically thin limit, i.e. $\tau_{\mathrm{n}\alpha} \ll 1$, eq. 3.25 yields:

$$\left.\frac{\mathrm{d}I_{\mathrm{n}\alpha}}{\mathrm{d}\Omega}\right|_{\tau \ll 1} = \epsilon_{\mathrm{n}\alpha} \mathrm{EM_{LOS}}/4\pi. \tag{3.27}$$

For uniform electron densities and temperatures along a line of sight, the ratio between eqs. 3.25 and 3.27 expresses the effect of optical depth on the line intensity, which can be either attenuating or amplifying. We introduce an optical depth correction factor, $C_{n\alpha}(T_e, n_e, \mathrm{EM_{LOS}})$, such that

$$\frac{\mathrm{d}I_{\mathrm{n}\alpha}}{\mathrm{d}\Omega} = C_{n\alpha} \cdot \epsilon_{\mathrm{n}\alpha} \mathrm{EM_{LOS}}/4\pi. \tag{3.28}$$

The optical depth correction factor can be applied to the SFR obtained from H-RL line fluxes that assumed optically thin emission. Figure 3.3 displays our calculations of the optical depth factor $C_{n\alpha}$ for two different emission measures and a range of temperatures and densities, for the mm-RL lines relevant in this work. For mm-RL, line absorption or amplification become significant at $\mathrm{EM_{LOS}} > 10^8 \mathrm{cm}^{-6}\mathrm{pc}$, which would lead to an over or underestimation of SFR, respectively, if optically thin emission is assumed. Because of this, it is important identify if amplification or attenuation of the line intensity occurs. Measurements of multiple lines intensities can in principle be used to identify the level of amplification or attenuation and help constrain T_e, n_e, or $\mathrm{EM_{LOS}}$ (e.g. Zhu et al., 2019). To investigate which mm-RL observations are best suited for constraining these parameters, we perform a more detailed analysis of the effects of optical depth on the line intensities in Section 3.5.2.

3.5.1 Comparison with line amplification calculations in the optically thin limit

Among the first attempts of quantifying the effects of stimulated emission on the intensity of low frequency H-RLs were done by Goldberg (1966). An approximation for the level of amplification or attenuation for mm or cm-RL was developed by (Goldberg, 1968), with the assumption that $|\tau_{\mathrm{n}\alpha}| \ll |\tau_{\mathrm{ff}}| \ll 1$:

$$I^{\mathrm{app}}_{\mathrm{n}\alpha} = I^{\mathrm{LTE}}_{\mathrm{n}\alpha} b_{\mathrm{n}+1} \left(1 - \frac{\tau_{\mathrm{ff}}}{2}\gamma_n\right), \tag{3.29}$$

where the line optical depth $\tau_{\mathrm{n}\alpha}$ is not explicitly used, $I^{\mathrm{LTE}}_{\mathrm{n}\alpha}$ is the line emission in LTE conditions, while $I^{\mathrm{LTE}}_{\mathrm{n}\alpha} b_{\mathrm{n}+1}$ is the line emission accounting for non-LTE effects, in the optically thin limit. This approximation is still used in recent works such as Gordon & Sorochenko (2002); Zhu et al. (2019). In this section we evaluate for which conditions is this approximation valid by calculating the relative difference between the integrated line flux obtained using equation 3.29 and the ones obtained using the radiative transfer formulation shown in equation 3.25. We call this difference the relative error and express it as a percentage deviation from the radiative transfer result:

$$\mathrm{Relative\,Error} = \frac{\left|I_{\mathrm{n}\alpha} - I^{\mathrm{app}}_{\mathrm{n}\alpha}\right|}{I_{\mathrm{n}\alpha}} \times 100. \tag{3.30}$$

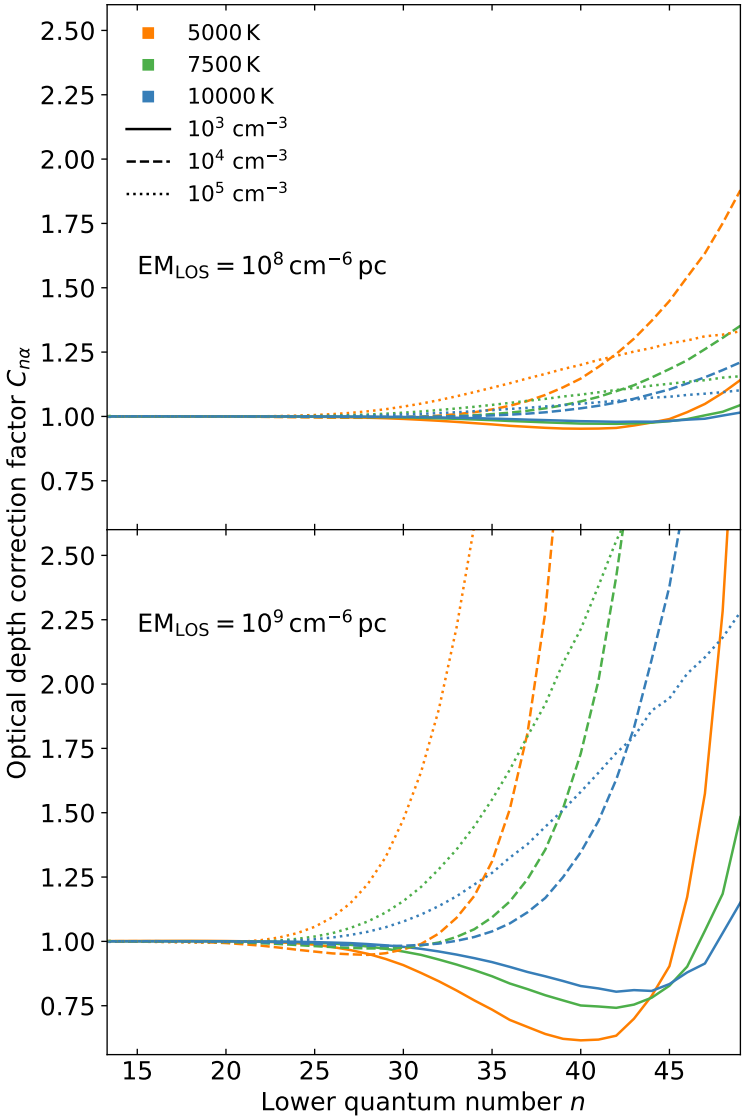

Figure 3.3: Optical depth correction factor $C_{n\alpha}$ for two values of the line of sight emission measure, EM$_{LOS}$. With increasing emission measure and optical depth, ever lower transition lines are affected by absorption or maser amplification.

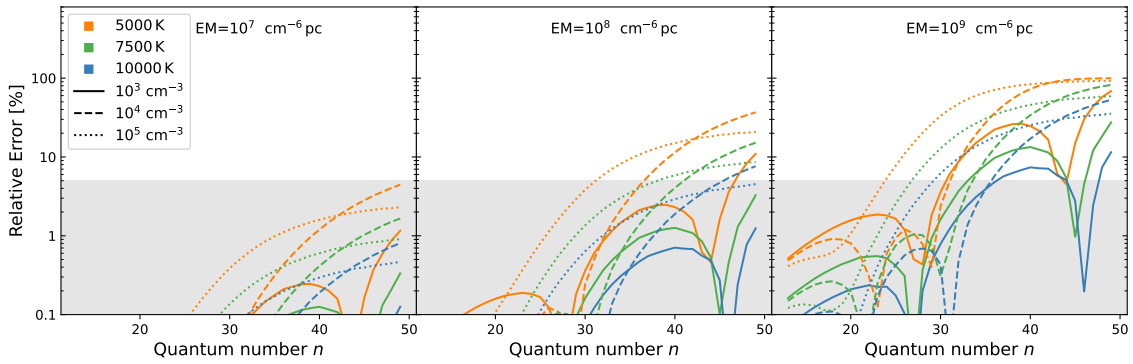

Figure 3.4: The relative difference in line intensity between the approximation given by Eq. 3.29 Gordon & Sorochenko (2002) and the radiative transfer equation in 3.25, as a function of RL quantum number. The shaded region is the area with a relative error below 5%. The relative error is given in percentages and is calculated using Eq. 3.30

In figure 3.4, we show this relative error, for a range of electron densities and temperatures relevant to the observations in this work. The gray shaded region indicates a relative error below 5%. This relative error between the approximation and full radiative equation is largest at lower gas temperatures and higher densities, i.e., $n_e \gtrsim 10^5\,\mathrm{cm}^{-3}$ and $T_e \lesssim 5000\,\mathrm{K}$. At EM values below $\sim 10^7\,\mathrm{cm}^{-6}\,\mathrm{pc}$, the relative error introduced by the approximation formula is below 5% for all quantum numbers of interest. The relative error drastically increases with EM, such that, starting with EM$\sim 10^8\,\mathrm{cm}^{-6}\,\mathrm{pc}$, the approximation of line intensities using Eq. 3.29 introduces a relative error well above 10% for $T_e \lesssim 7500\,\mathrm{K}$ and $n_e \gtrsim 10^4\,\mathrm{cm}^{-3}$. For EM$\geq 10^9\,\mathrm{cm}^{-6}\,\mathrm{pc}$, the integrated line fluxes calculated with equation 3.29 differ from the full radiative transfer result by almost an order of magnitude. The relative error is also larger for lines having longer, i.e., millimeter rather than submillimeter, wavelengths. Approximating the intensity of recombination lines with corresponding quantum numbers below 25, using Eq. 3.29, introduces negligible errors. Thus, for submillimeter recombination lines, Eq. 3.29 is a good approximation for all lines studied here, in most conditions found in the ISM.

In Figure 3.5, we show how the relative error defined in equation 3.30 varies with EM for some of the H-RL analyzed in this work. The nine panels show how the relative error varies with increasing EM for a range of densities and temperatures, revealing that Eq. 3.29 proves to be a poor approximation for mm and submm-RL at densities of $n_e = 10^5\,\mathrm{cm}^{-3}$, while towards lower densities the approximation becomes problematic only at higher EM values, of EM $10^9\,\mathrm{cm}^{-6}\,\mathrm{pc}$. For these reasons, and since Eq. 3.29 approximates the level of line amplification without taking the line optical depth $\tau_{\mathrm{n}\alpha}$ into account, throughout this work we use the solutions to the radiative transfer equation and the prescription from Gordon & Sorochenko (2002) to calculate the amount of amplification and attenuation of mm-RL.

3.5.2 Line Intensities as a Diagnostic Tool of HII Gas Properties

Observations of recombination lines and the underlying free free continuum can be used not only as a measurement of SFR, but also as a way to probe the state of HII gas in star-forming regions. In this section we explore how mm-RL, which can be observed with ALMA at high resolution in nearby galaxies, can be used to constrain electron temperature and density. Previous work focused on

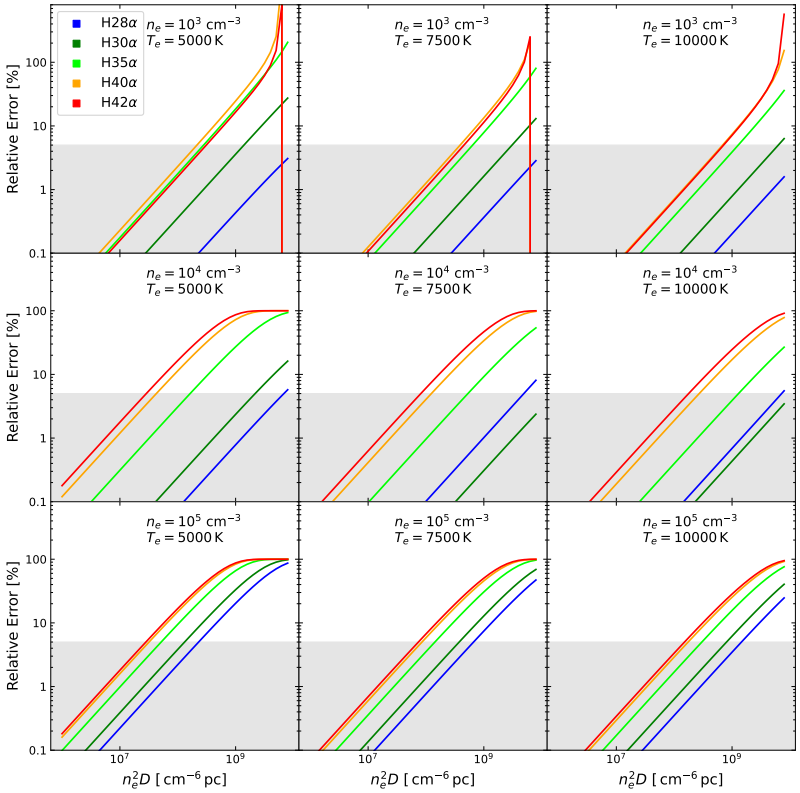

Figure 3.5: The relative error in line intensity between the approximation given by Eq. 3.29 and the radiative transfer equation in 3.25, as a function of EM. The shaded region is the area with a relative error below 5%. The relative error is given in percentages and is calculated using Eq. 3.30

the theoretical aspects of longer, usually centimeter, wavelength recombination lines (e.g Gordon & Sorochenko, 2002; Draine, 2011), or used the approximating formula in Sec. 3.5.1 (e.g. Zhu et al., 2019). Here we investigate the effects of n_e, T_e, and EM on optical depth and mm-RL intensity using the full theoretical prescriptions of Gordon & Sorochenko (2002), and the departure coefficients and recombination rates calculated by Storey & Hummer (1995).

In figure 3.6 the variation of the parameters used in the line intensity, Eq. 3.25, are shown as a function of principal quantum number n for electron temperatures $T_e = 3000 - 12500$ K and densities $n_e = 10^2 - 10^7$ cm^{-3}. The departure coefficients, b_n, are shown in the top panel. The departure coefficients have, in general, lower values at submm wavelengths, i.e. low quantum numbers, and increase to the LTE value of 1 at mm or cm wavelengths, i.e. for high quantum numbers (Gordon & Sorochenko, 2002; Draine, 2011). Since b_n represents the ratio between the number density of atoms in a quantum state n and the same number density expected from LTE conditions, if b_n is increasing as a function of quantum number n, the conditions for population inversion, and thus stimulated emission, are fulfilled, i.e. there are more atoms in a state $n + 1$ than in state n. Thus, the actual value of the departure coefficients is just as the rate at which they change with increasing quantum number n. At densities of $10^2 - 10^4$, the departure coefficients have values of 0.6-0.8, showing little variation with quantum numbers at mm and submm wavelengths. At densities of 10^5 cm^{-3} and above, the departure

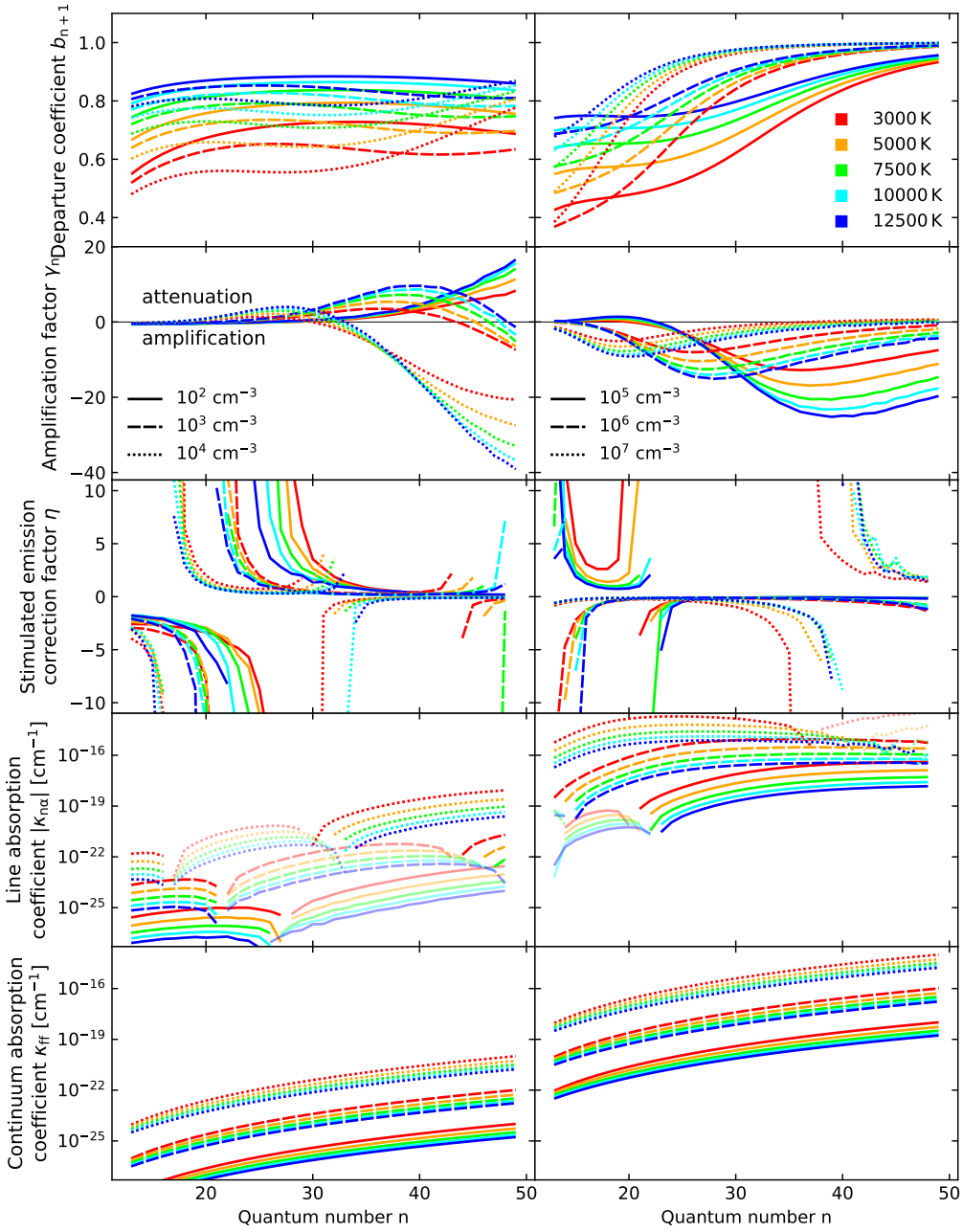

Figure 3.6: Parameters affecting mm-RL and continuum intensity in HII regions for different electron temperatures and densities. From top to bottom, the left and right panels show the departure coefficients, amplification factors, stimulated emission correction factors, line absorption coefficients, and continuum absorption coefficients. The panels on the right show the parameters for $n_e = 10^2 - 10^4$ cm^{-3} and the right panels for $n_e = 10^5 - 10^7$ cm^{-3}. The line absorption coefficient shown with shaded lines has positive values and results in line attenuation. In contrast, the non-shaded lines in the same panel represent negative values of $\kappa_{n\alpha}$, where the line is amplified.

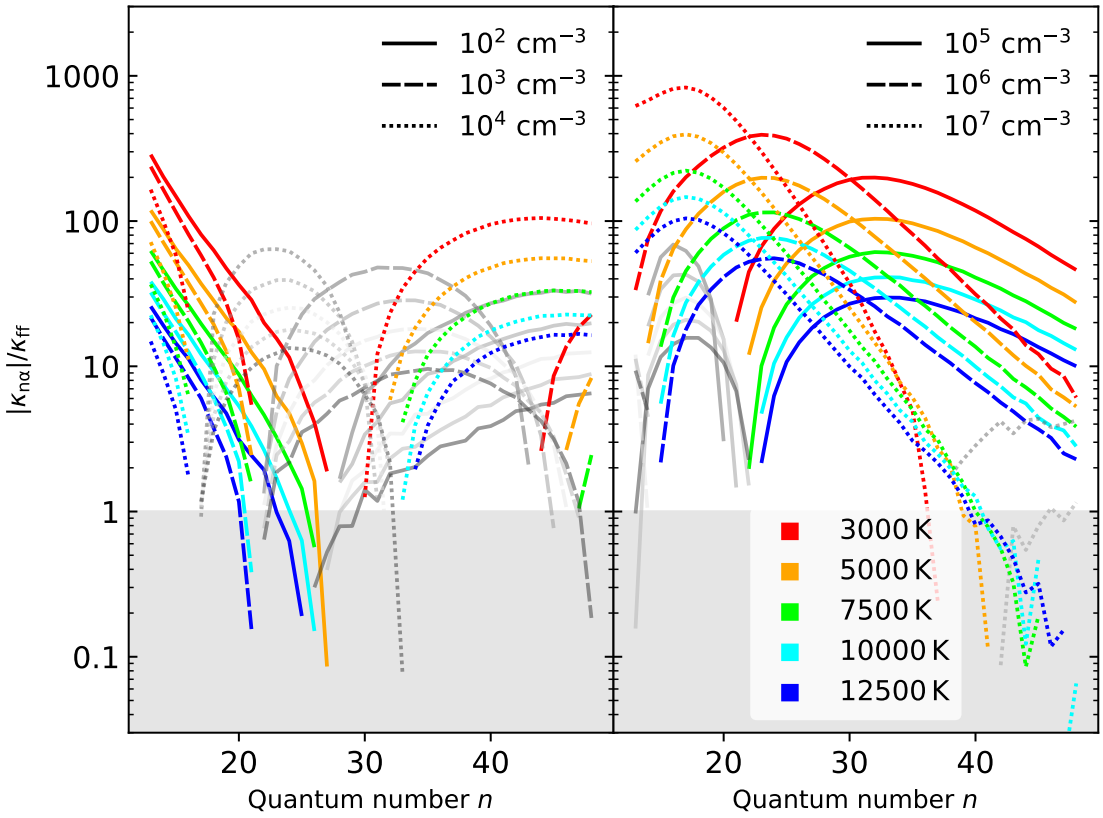

Figure 3.7: The ratio of the absolute value of the line absorption coefficient to the continuum absorption coefficient. The gray-shaded lines represent positive values of $\kappa_{n\alpha}$ which to line absorption, while the colored lines are for its negative values, which lead to line amplification. The shaded region indicates places where $|\kappa_{n\alpha}| \leq \kappa_{ff}$.

coefficients approach the value of 1 at mm-wavelengths, and increase with the quantum number n. The departure coefficients show the largest variation with quatnum number at lower temperatures, i.e. at $T_e = 3000 - 5000$ K. Thus, to a first order approximation, the greatest amplification of mm or submm-RL should happen in higher density and lower temperature gas in HII regions.

The amplification factor γ_n as a function of quantum number n is shown in the second panel of figure 3.6. The amplification factor, together with the departure coefficients, determines if the absorption coefficient is positive or negative, and influences it's absolute value. When γ_n is negative, line amplification occurs, and a large absolute value implies a large amplification. Amplification occurs for all mm-RL in gas having densities of $n_e = 10^3$ cm^{-3} and above. For lower gas densities, mm-RL are attenuated and amplification occurs at cm-wavelengths.

The amount of mm-RL attenuation or amplification is determined not only by γ_n, but also by the stimulated emission correction factor η_n. In the middle panel of Fig. 3.6 η_n as a function of quantum number n is shown. This factor, just like γ_n, has negative values when amplification occurs. In this case, the negative value inside the first bracket in equation X, given by $\gamma_n < 0$, is turned positive by its multiplication with a negative η_n. Thus, η_n follows the evolution of γ_n with the values of the quantum

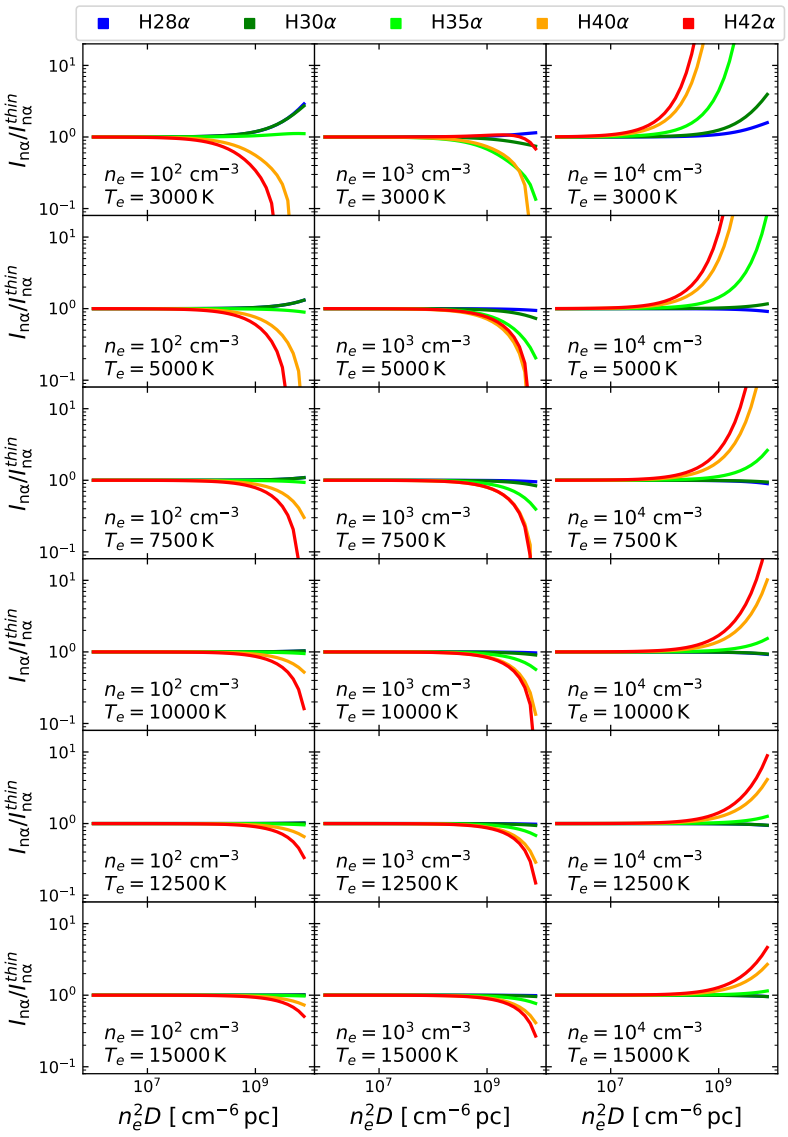

Figure 3.8: The ratio between the optically thick and optically thin integrated H-RL flux densities as a function of EM, for the H28α, H30α, H35α, H40α, H42α lines, as a function of increasing EM, for various electron densities and temperatures. The electron densities considered are in the range $n_e = 10^2 - 10^4$ cm$^-3$, and the electron temperatures considered are in the range $T_e = 3000 - 15000$ K. The temperature is increasing from the top to the bottom panels, while the electron density is increasing from the left to right panels.

number n.

The last two panels in figure 3.6 show the values of the line and continuum absorption coefficients, $\tau_{n\alpha}$ and τ_{ff}, respectively. The negative values of $\tau_{n\alpha}$ indicate line amplification. The line absorption coefficient is negative at sub-mm and towards the longer end of millimeter wavelengths for gas having lower densities of $n_e = 10^2 - 10^3\,\mathrm{cm}^{-3}$. In higher density gas, where $n_e \geq 10^4\,\mathrm{cm}^{-3}$, line $\tau_{n\alpha}$ is negative for almost all mm and sub-mm wavelengths. As the gas temperature decreases from 12500 K to 3000 K, the absolute value of $\tau_{n\alpha}$ increases, which results in amplification when the sign of $\tau_{n\alpha}$ is negative. This effect is also seen for the continuum, however, since τ_{ff} is always positive, a decrease in temperature always results in the decrease in the intensity of the emitted free-free radiation.

The ratio $|\kappa_{n\alpha}|/\kappa_{ff}$, between the line and continuum absorption coefficients, is useful in visualizing whether amplification of a mm-RL is due to maser emission. For maser emission to take place, the sum of continuum and line absorption coefficients must be negative, i.e. $\tau_{n\alpha} + \tau_{ff} < 0$, by definition. In figure 3.7, which shows the $|\tau_{n\alpha}|/\tau_{ff}$ values as a function of quantum number n, amplification due to masing which occurs only for $|\tau_{n\alpha}| > \tau_{ff}$, depicted by the colored lines above above the shaded grey region. The partial maser effect, occurring when $\tau_{n\alpha} < 0$ and $|\tau_{n\alpha}| < \tau_{ff}$, is thus depicted by the colored lines in the shaded grey region. In gas having electron densities $n_e = 10^2 - 10^3\,\mathrm{cm}^{-3}$, masing occurs only for submm-RL at all temperatures between 3000 – 12500 K, while for $n_e = 10^4\,\mathrm{cm}^{-3}$, only mm-RL exhibit masing. In gas at higher densities, $n_e = 10^5 - 10^7\,\mathrm{cm}^{-3}$, masing occurs for most submm- and mm-RL, given the same 3000 – 12500 K temperature range. Thus, figure 3.7 suggests that masing of submm- and mm-RL would rather be the norm than the exception, given plausible densities and temperatures of HII regions.

In figures 3.8 and 3.9 the ratio between the integrated line fluxes for the optically thick and optically thin emission, $I^{thick}_{n\alpha}/I^{thin}_{n\alpha}$, for the H28$\alpha$, H30$\alpha$, H35$\alpha$, H40$\alpha$ and H42α lines, is shown as a function of EM. The considered range of electron temperatures is $T_e = 3000 - 15000$ K, and for electron densities densities it is $n_e = 10^2 - 10^7\,\mathrm{cm}^{-3}$. The specific mm-RL lines shown here have been selected because they have been previously detected, are also used in this work, cover a wide range of wavelengths, from submillimeter to millimeter, and are representative for the types of lines that can be observed with the ALMA telescope.

The EM is shown as a product of the squared electron density and the line of sight distance, such that $\mathrm{EM} = n_e^2 \times D$. As a helpful example, the EM for corresponding to electron densities $n_e = 10^3$, 10^4, and $10^5\,\mathrm{cm}^-3$, and sizes $D = 100$, 1, and 0.1 pc, respectively, is the same, and has a value of $\mathrm{EM} = 10^8\,\mathrm{cm}^{-6}\,\mathrm{pc}$. For $\mathrm{EM} \lesssim 10^7\,\mathrm{cm}^{-6}\,\mathrm{pc}$, we can consider the emission to be optically thin for all millimeter and submillimeter H-RL, and the $I^{thick}_{n\alpha}/I^{thin}_{n\alpha}$ ratio is independent of optical depth and EM, $I_{n\alpha}$ showing little variation with electron density and temperature. As the EM increases, at $\mathrm{EM} \gtrsim 10^8\,\mathrm{cm}^{-6}\,\mathrm{pc}$, the effects of optical depth become visible, and the integrated line flux of H-RL starts to be amplified or attenuated. For electron densities $n_e = 10^2 - 10^3\,\mathrm{cm}^{-3}$ and all considered temperatures, most lines are attenuated. The exception are the H28α and H30α, i.e. lines with wavelengths below $\sim$ 1 mm, which are slightly amplified at electron temperatures of 3000 to 5000 K, otherwise remaining unaffected by optical depth or EM. For electron densities $n_e = 10^4 - 10^6\,\mathrm{cm}^{-3}$, most lines are amplified, with the $I^{thick}_{n\alpha}/I^{thin}_{n\alpha}$ increasing with EM. The effect is present at all temperatures, but is particularly more pronounced at lower temperatures, where $T_e = 3000 - 5000$ K, and for lower frequency mm-RL, with the H40α or H42α lines showing significant amplification as EM exceeds $10^8\,\mathrm{cm}^{-6}\,\mathrm{pc}$. The H28$\alpha$ and H30α are again, less affected, being amplified only when $\mathrm{EM} \gtrsim 10^9\,\mathrm{cm}^{-6}\,\mathrm{pc}$, for electron densities $n_e = 10^4 - 10^6\,\mathrm{cm}^{-3}$ and temperatures $T_e = 3000 - 5000$ K. At the highest density examined here, $n_e = 10^7\,\mathrm{cm}^{-3}$, line

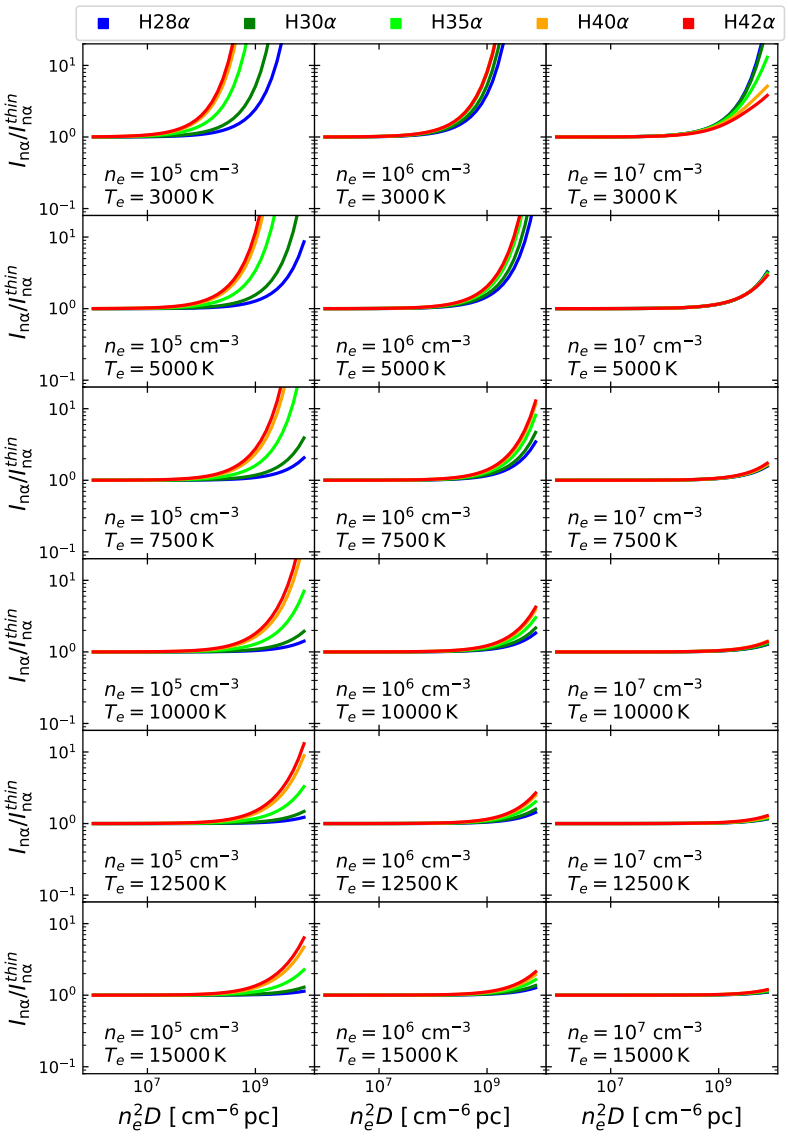

Figure 3.9: The ratio between optically thick and optically thin emission, for integrated mm-RL flux densities as a function of EM, for the H28α, H30α, H35α, H40α, H42α lines, and various electron densities and temperatures. The electron densities considered are in the range $n_e = 10^5 - 10^7$ cm$^-3$, and the electron temperatures considered are in the range $T_e = 3000 - 15000$ K. The temperature is increasing from the top to the bottom panels, while the electron density is increasing from the left to right panels.

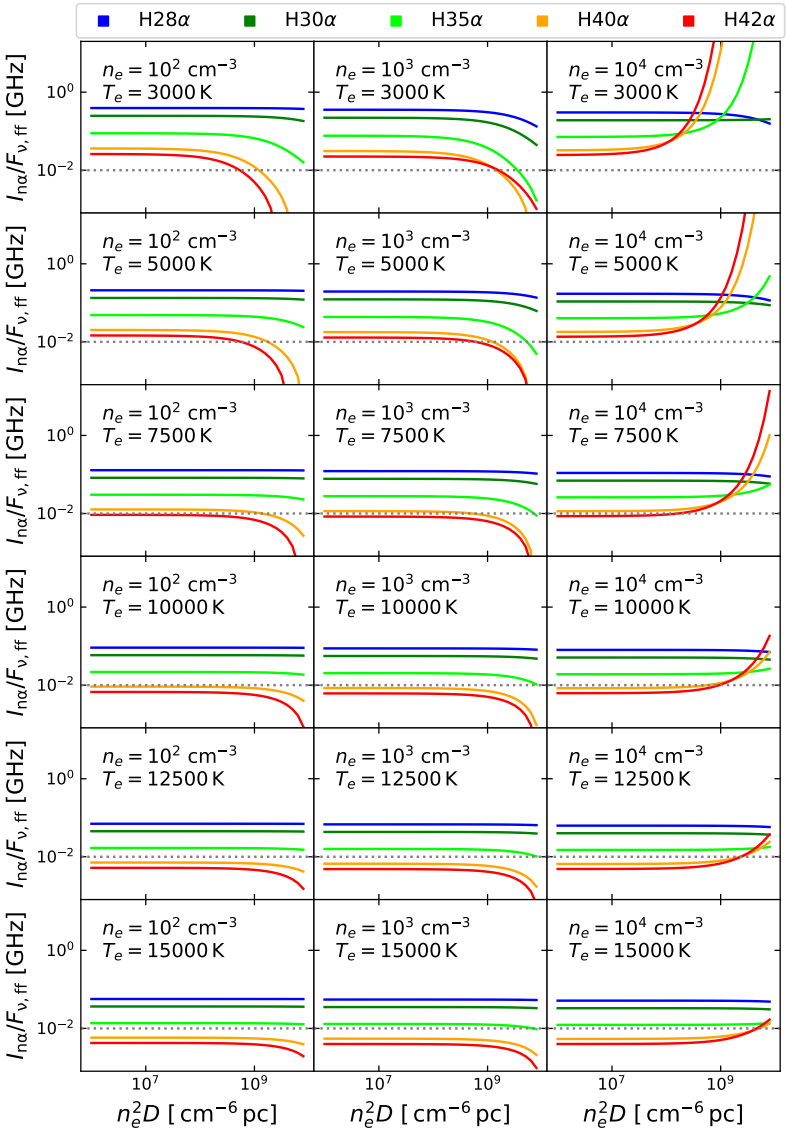

Figure 3.10: Integrated line flux to the underlying free-free continuum flux density ratio as a function of increasing EM, for the H28α, H30α, H35α, H40α, H42α lines, and various electron densities and temperatures. The electron densities considered are in the range $n_e = 10^2 - 10^4$ cm$^-$3, and the electron temperatures considered are in the range $T_e = 3000 - 15000$ K. The temperature is increasing from the top to the bottom panels, while the electron density is increasing from the left to right panels. The grey dashed line at the $10^{-2}\,GHz$ is only for visual guidance.

amplification is weak, and becomes at temperatures above $T_e \gtrsim 7500\,\mathrm{K}$, as collisions increase and the departure coefficients start to approach the value of unity.

In general, line attenuation and amplification can be considerable especially when observing longer wavelength mm-RL such as H40α or H42α, if we expect electron temperatures below $T_e = 5000\,\mathrm{K}$, and densities in the range of $n_e = 10^4 - 10^6\,\mathrm{cm}^{-3}$. A possible solution to this problem is to observe multiple H-RL, or to observe H-RL at shorter wavelengths, i.e. H-RL with quantum numbers below that of H30α.

The electron temperature, T_e, of the ionized gas can be inferred from the integrated line flux to free-free continuum flux density ratio, shown in equation 4.2. In optically thin conditions this ratio only weakly depends on electron density, n_e, and can thus can reliably be used to determine T_e for a wide range of n_e values. When the optically thin assumption is no longer valid, and line amplification affects the integrated line flux to the underlying free free continuum flux density ratio, $I_{\mathrm{n}\alpha}/F_{\nu,\mathrm{ff}}$, the T_e values calculated using eq. 4.2 become unreliable.

In figures 3.10 and 3.11 we show the $I_{\mathrm{n}\alpha}/F_{\nu,\mathrm{ff}}$ ratios for the H28α, H30α, H35α, H40α and H42α lines as a function of EM. Here we consider the same lines as in figures 3.8 and 3.9, as well as the same electron temperatures, and densities, i.e. $T_e = 3000 - 15000\,\mathrm{K}$, and $n_e = 10^2 - 10^7\,\mathrm{cm}^{-3}$. The $I_{\mathrm{n}\alpha}/F_{\nu,\mathrm{ff}}$ ratio varies with T_e, as expected, and shows a weak dependence on n_e. For the lines considered here, the effects of line amplification or attenuation affect this ratio only when $\mathrm{EM} \gtrsim 10^9\,\mathrm{cm}^{-6}\,\mathrm{pc}$, with very few exceptions. When $\mathrm{EM} \gtrsim 10^8\,\mathrm{cm}^{-6}\,\mathrm{pc}$, at temperatures below $T_e \simeq 5000\,\mathrm{K}$ and densities of $n_e = 10^2 - 10^3$, using $I_{\mathrm{n}\alpha}/F_{\nu,\mathrm{ff}}$ in equation 4.2 equation starts to overestimate T_e when considering lower frequency lines, like H40α or H42α. For these lines, the reverse is true, when the electron densities are in the range $n_e = 10^4 - 10^6\,\mathrm{cm}^3$ equation 4.2, using the $I_{\mathrm{n}\alpha}/F_{\nu,\mathrm{ff}}$ ratio, underestimates T_e. The $I_{\mathrm{n}\alpha}/F_{\nu,\mathrm{ff}}$ ratio corresponding to lines with higher frequencies, i.e. lines low quantum numbers such as those with quantum numbers lower than that of H30α, are almost unaffected. The same effect is observed at higher temperatures and high densities, when $n_e \gtrsim 10^5\,\mathrm{cm}^{-3}$ and $T_e \gtrsim 7500\,\mathrm{K}$, the $I_{\mathrm{n}\alpha}/F_{\nu,\mathrm{ff}}$ ratio can reliably be used to determine T_e at even as $\mathrm{EM} \simeq 10^9\,\mathrm{cm}^{-6}\,\mathrm{pc}$. However, even though the assumption of optically thin emission can potentially lead to unreliable estimation of T_e, especially when $T_e \lesssim 5000\,\mathrm{K}$ and $n_e \lesssim 10^6$, the SFR has a weak dependence on T_e, somewhat mitigating this effect. Thus, the use of the optically thin assumption is in general justified when investigating SFR, especially in cases where only one mm-RL is detected.

To emphasize how the two ratios, $I_{\mathrm{n}\alpha}/F_{\nu,\mathrm{ff}}$ and $I^{\mathrm{thick}}_{\mathrm{n}\alpha}/I^{\mathrm{thin}}_{\mathrm{n}\alpha}$ depend on the quantum numbers of all sub-mm and mm-RL, we show them Figure 3.12 and 3.13, respectively, for a range of temperatures, densities, and EM values. Significant line amplification or attenuation, leading to under or over-estimation of T_e, clearly affects H-RL with high quantum numbers and lower frequencies, especially for lower temperatures of $T_e = 3000 - 5000\,\mathrm{K}$. Nevertheless, as stated previously, the SFR only depends weakly on T_e, meaning the $I_{\mathrm{n}\alpha}/F_{\nu,\mathrm{ff}}$ remains useful in determining T_e and SFR, especially when only one H-RL has been detected. A more difficult quantity to constrain here is the free-free continuum flux density itself, which has to be disentangled from the synchrotron and dust continuum emission. Line attenuation or amplification affects $I^{\mathrm{thick}}_{\mathrm{n}\alpha}/I^{\mathrm{thin}}_{\mathrm{n}\alpha}$ ratio with a strong dependency on quantum numbers as well. At a given density and temperature, it is possible for specific lines to be amplified while others are attenuated or largely unaffected. This leads to the possibility of using line ratios to pinpoint the electron densities and temperatures in a H-RL emitting region and removes the difficulties of measuring the free-free continuum. This is also advantageous when using telescopes that do not simultaneously measure the continuum emission while observing spectral line emission, like ALMA does.

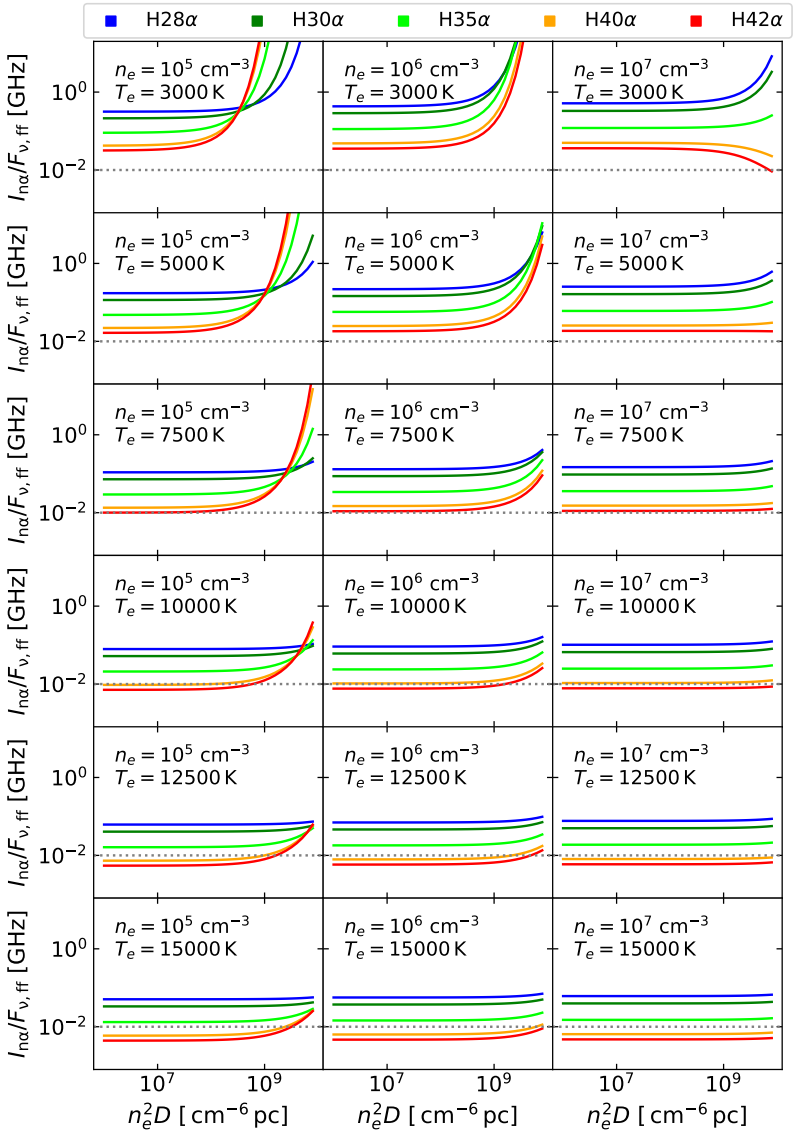

Figure 3.11: Integrated line flux to the underlying free-free continuum flux density ratio as a function of increasing EM,, for the H28α, H30α, H35α, H40α, H42α lines, and various electron densities and temperatures. The electron densities considered are in the range $n_e = 10^5 - 10^7$ cm$^-$3, and the electron temperatures considered are in the range $T_e = 3000 - 15000$ K. The temperature is increasing from the top to the bottom panels, while the electron density is increasing from the left to right panels. The grey dashed line at the $10^{-2}\,GHz$ is only for visual guidance.

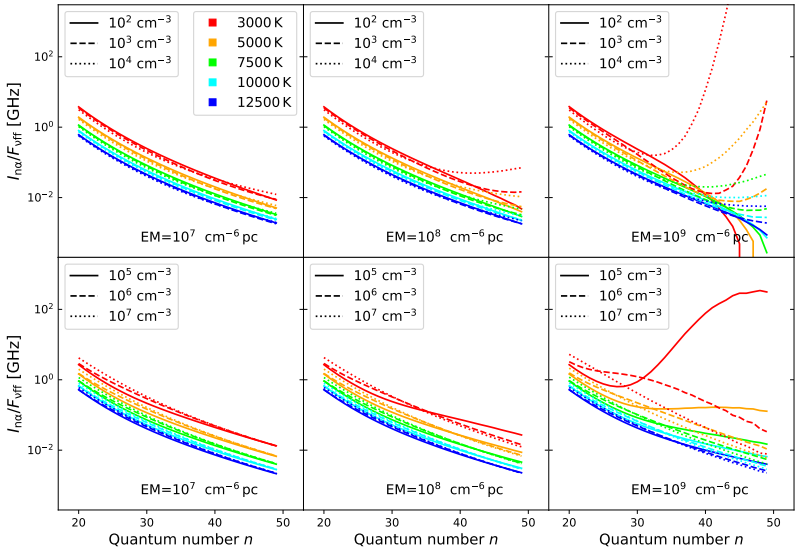

Figure 3.12: Integrated line flux to underlying free-free continuum flux density ratios as a function of H-RL principal quantum number n, for a range of electron temperatures and densities. The temperatures considered are in the range $T_e = 3000 - 12500$ K. Top panels correspond to densities of $n_e = 10^2 - 10^4$ cm^{-3} and the bottom panels to $n_e = 10^5 - 10^7$ cm^{-3}. The EM is increasing from the left to the right panels.

While the line to free-free continuum ratio can be used to estimate the electron temperature T_e, it does not constrain electron the density. In figure 3.14 we plot the ratios of the integrated line fluxes of the H35α and H40α lines against those of the H28α and H35α lines, for wide range of electron temperatures, densities, at three EM values, respectively. The frequencies of the H28α, H35α, and H40α lines are observable with ALMA in bands 3, 4, and 7, respectively. The two ratios define positions in figure 3.14 which are radially separated for each density, centered on the optically thin limit values. As the EM increases, and the electron temperature decreases, the line ratios corresponding to specific densities diverge from the center of the figure. Therefore, using figure 3.14, n_e and T_e become easier to constrain as the optical depth effects increase. This complements the line-to-continuum ratio method of determining T_e, which which is less reliable as line amplification or attenuation increase. This type of analysis can be done with other H-RL triplets, as long as they their three quantum numbers are well separated, so as to capture the variations in intensity induced by line amplification or absorption well. It is also possible to perform a less accurate analysis using only one line ratio of certain H-RL. A ratio of the Hmα and Hnα line fluxes, where Hmα and Hnα are sub-mm and mm-RL, respectively, above the optically thin values would indicate that $n_e = 10^2 \sim 10^3$ cm^{-3}. If the line ratio is below the optically thin one it would indicate that $n_e = 10^4 \sim 10^6$ cm^{-3}. As seen in figure 3.14, the usefulness of using one line-ratio is somewhat limited when its value is close to the optically thin one, as at that location there is a degeneracy between the effects of n_e and T_e. In conclusion, using at least two line ratios, thus three or more submm- and mm-RL observations, the presence of significant line amplification can be identified, the values of n_e and T_e can be constrained without the need for free-free continuum measurements. This greatly reduces the uncertainties in the SFR values estimated from mm-RL emission.

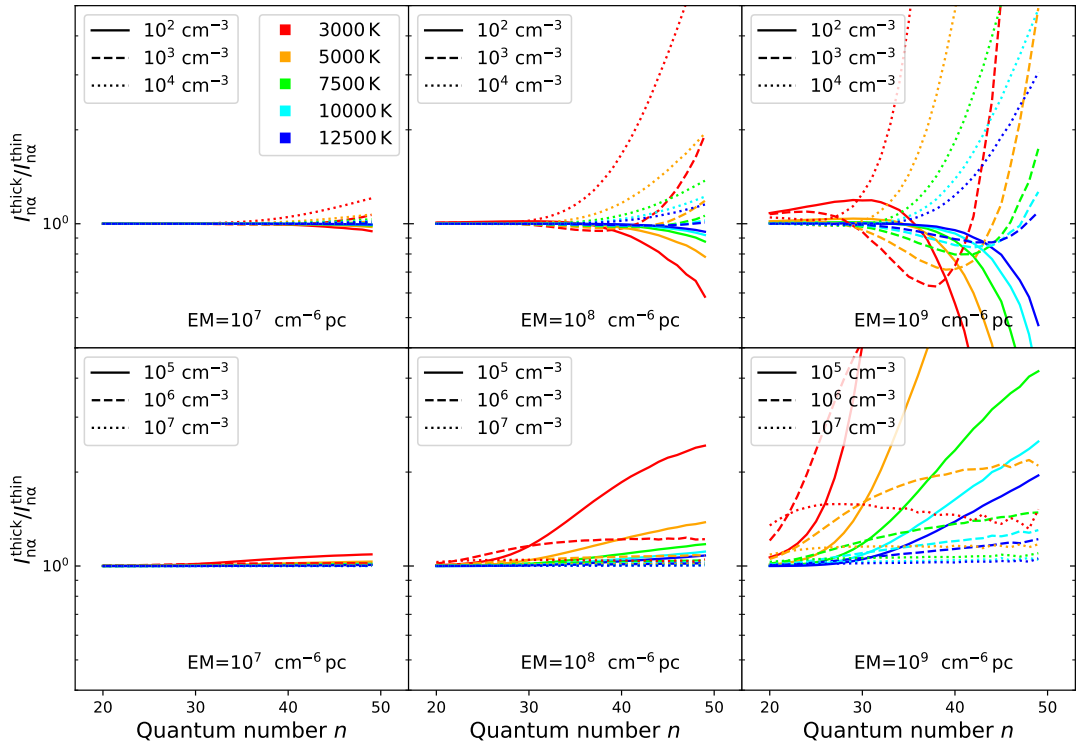

Figure 3.13: The ratio between the optically thick and optically thin integrated mm-RL flux densities as a function of mm-RL principal quantum number n, for a range of electron temperatures and densities. The temperatures considered are in the range $T_e = 3000 - 12500$ K. Top panels correspond to densities of $n_e = 10^2 - 10^4$ cm^{-3} and the bottom panels to $n_e = 10^5 - 10^7$ cm^{-3}. The EM is increasing from the left to the right panels.

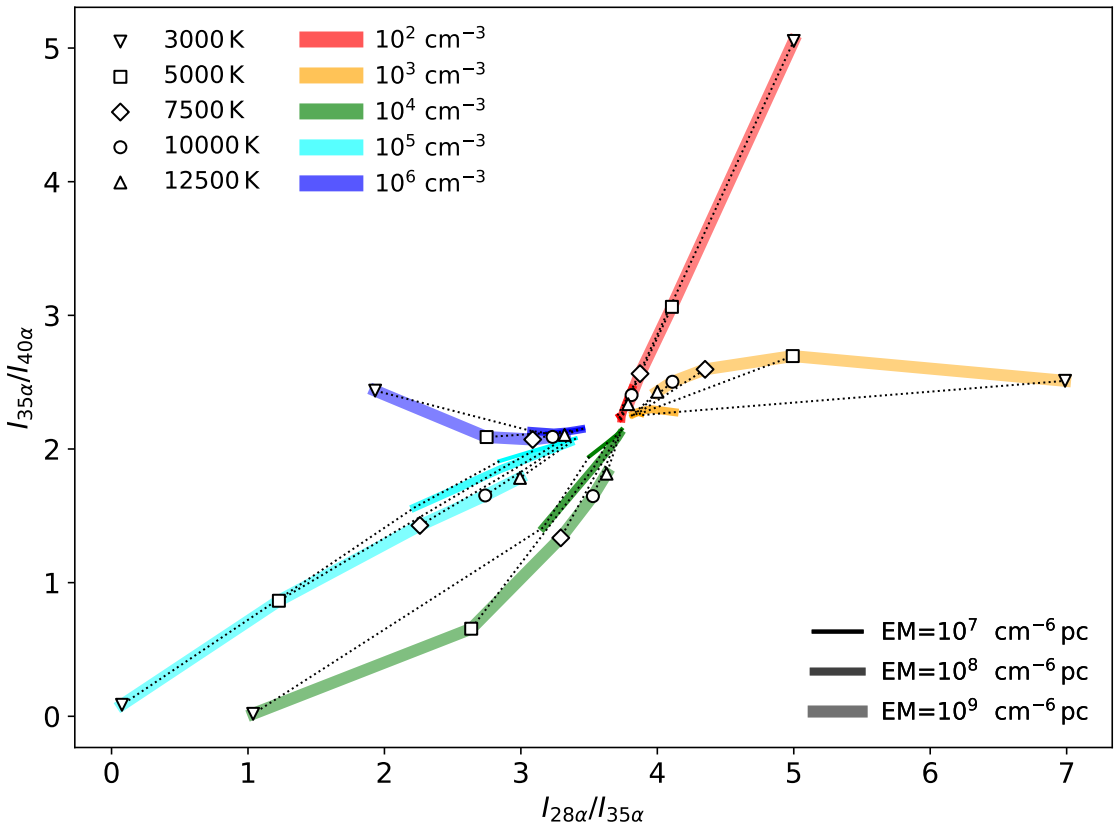

Figure 3.14: The ratio of the H35α to H40α integrated line fluxes as a function of the H28α to H35α integrated line flux ratios. The evolution of this ratios is shown for electron densities in the range of $n_e = 10^2 - 10^6$ cm^{-3}, identified as colors, and for electron temperatures in the range of $T_e = 3000 - 12500$ K, identified with symbols. The solid lines connect points of equal density, while their thickness represents the EM value. The thin dotted black lines connect points of equal temperature.

CHAPTER 4

Probing Extragalactic SFR and SFH Using mm-RL

In this section we present the results obtained by analyzing our two galaxy samples. One sample was obtained by mining the ALMA archive, and one was obtained by performing our own observations with the IRAM30m telescope (see chapter 2). The two samples differ in several respects. The ALMA archival sample is the result of interferometric observations and has an arcsecond or sub-arcsecond spatial resolution. Shortcomings of the archival data include the narrow field of view, which often covers only the nuclei of the observed galaxies, and possible undetected flux due to limitations imposed by the maximum recoverable scale inherent to all radio interferometric observations. In contrast, our IRAM30m observations have a resolution of the order of 25", cover an area more than an order of magnitude larger than the ALMA observations, and are not limited by a maximum recoverable scale. The ALMA sample consists of 20 infrared bright nearby galaxies, and we recover mm-RL emission from nine of them. Multiple recombination line detections are recovered in NGC253, NGC4945, NGC3256, NGC1808, and M83, while single mm-RL line detections are recovered in NGC5253, NGC3627, NGC3628, and Arp220. The IRAM 30m sample consists of six galaxies, NGC0660, NGC1614, NGC2903, IC694, NGC4102, and NGC4418, and no mm-RL emission was detected in any of them. The heterodyne receivers used for our IRAM30m observations do not provide continuum data. Because of all these differences, the type of analysis possible for the two samples differs, with the main difference being the analysis and extraction of the total infrared flux. The resolution of the IRAM30m data is comparable to that of several infrared observatories, allowing us to use archival data to determine the total infrared flux of the observed regions. In contrast, the resolution of the ALMA data is too high for the use of infrared archival data, and the infrared flux is extrapolated from submm ALMA archival data.

The FWHM of the mm-RL is determined by fitting a single or double peaked Gaussian to the recovered spectra. The integrated line flux is extracted from apertures placed over the mm-RL moment 0 maps (the images and apertures can be seen in Chapter 2). The continuum flux is extracted from the continuum images using the same apertures as for the line flux. The integrated line flux, the continuum flux density and the FWHM of the mm-RL for the ALMA sample are given in Table 4.2. In the case of the IRAM 30m sample, where no mm-RL are detected, upper bounds are placed on the mm-RL integrated line fluxes. These are shown in the table 4.3.

4.1 The relevant ISM conditions and obsevables

Due to the presence of continuum data as well as mm-RL detections, it is possible to analyze the conditions in the ISM for galaxies in the ALMA sample, namely the free-free continuum and the electron temperature. These are later used to determine the SFR from the mm-RL luminosity. This type of analysis is not possible for the IRAM 30m sample, which lacks mm-RL detections and the associated continuum data. Thus, for the IRAM30m sample, the upper limits of the SFR are established using an electron temperature of 5000 K, as validated by the ALMA results and other mm-RL observations (e.g. Bendo et al., 2015, 2016, 2017; Michiyama et al., 2020).

4.1.1 Free-free emission

The SFR in an observed aperture can be estimated from both the free-free or the mm-RL flux, as explained in Chapter 3. Both quantities depend on the density and temperature distribution of the photoionized gas, which may be modeled with spatially resolved observations of individual HII regions, but hardly so when the spatial resolution is of order 100 pc, as is the case for the observations presented here. Thus we must make the simplifying assumption of a uniform density and temperature, and try to constrain these parameters. One must keep in mind that these parameters represent a weighted average of the actual density and temperature in these HII regions. The integrated flux of a mm-RL and its underlying free-free continuum flux density can be used to yield an estimate of the (weighted average) gas temperature (see 3).

At millimeter wavelengths, the continuum flux density has contributions from free-free, synchrotron, and thermal dust emission. To separate the three components, a seven-parameter SED model,

$$F_\nu = F_\nu^{\rm sync} + F_{\nu,\rm ff} + F_\nu^{\rm dust} = a\nu^\alpha + bg_{\rm ff}(\nu, T_e) + cB_\nu(T_{\rm dust})\nu^\beta \tag{4.1}$$

where a, b, c scale the relative intensities, is fit to archival data covering the frequencies of the three types of emission. The synchrotron flux density is modeled as a single power law. The free-free spectral slope is not very sensitive to temperature and we set $T_e = 5000$ K to evaluate the Gaunt-factor, following Bendo et al. (2016) and Michiyama et al. (2020). With a strong degeneracy between β and $T_{\rm dust}$ in the Rayleigh-Jeans part of the modified black body spectrum, the dust emission at this wavelength range can be modeled using only one of the parameters, and thus we fix $T_{\rm dust} = 30$ K, leaving β free to govern the slope of the dust emission spectrum.

The above SED fit was performed only for galaxies with mm-RL detections and available continuum radio, millimeter, and sub-millimeter archival data at comparable spatial resolution. In the sample presented here, NGC253, Arp220, NGC3256, M83, NGC1808 have sufficient spectral coverage to permit a fit, and thus to separate the free-free emission from the synchrotron and dust emission. For NGC4945 we find no archival radio data matching the ALMA archival resolution and use the data compiled by Bendo et al. (2016). Continuum data in the 1.5 to 20 GHz range were taken from the VLA public archive, at higher frequencies from the ALMA archive. The flux densities are extracted over the matched apertures presented in Section 2.1.2, and are shown in Table 4.2. We include a conservative 10% calibration error for all fluxes, based on the ALMA/VLA flux calibration error (Remijan et al., 2019; Bonato et al., 2018).

When fitting the photometry to our model SED, the fractional free-free flux level at, e.g., 100 GHz, $f_{\rm ff} \equiv F_{100}^{\rm ff}/F_{100}$, is sensitive to the slopes of the synchrotron and thermal dust emission spectra, which

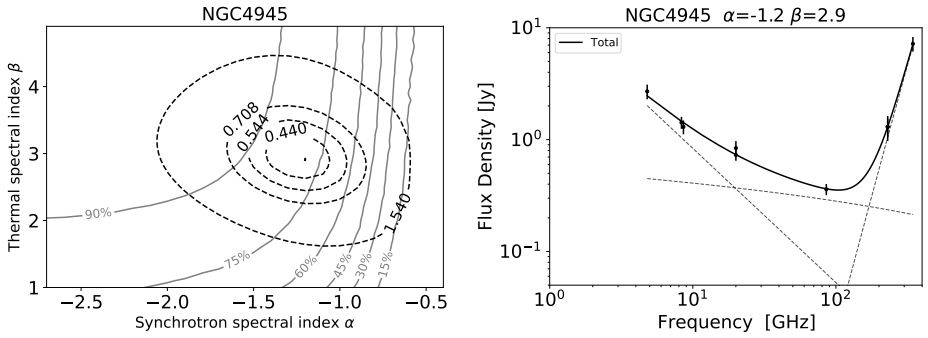

Figure 4.1: *Left*: The free-free contribution to the overall continuum at 100GHz (solid lines) and the minimized χ^2 values of the SED fits (dotted lines) for different values of α and β, corresponding the the nucleus of NGC4945. The outermost contour corresponds to the 68% confidence level. The uncertainties of α and β are defined as the values these two parameteres take along the 68% confidence interval contour that give the minimum and maximum values of the free-free fraction at 100 GHz. *Right*: SED fit using the values of α and β which correspond to the minimum χ^2 value.

is illustrated in Fig. 4.1 for the case of NGC 4945. Figures for the other galaxies in this sample, as well as details about the fitting procedure are presented in Appendix B. This strongly affects the derived electron temperature uncertainty, and consequently the derived SFR. Previous works therefore fixed the synchrotron, free-free, and dust spectral slopes (Bendo et al., 2015, 2016; Michiyama et al., 2020; Mills et al., 2021).

Table 4.1 lists the best fit values of α and β for each galaxy, the free-free flux fraction, and their uncertainties. The large uncertainties in the free-free fraction of the continuum translate into large uncertainties in the line to free-free continuum ratios and electron temperatures.

We calculate the uncertainties in the free-free continuum fraction associated with SED fits where α and β are fixed to their best fit values for each galaxy. Without this procedure, the free-free continuum fraction, and thus the electron temperature and SFR are not constrained. Similar approaches have been used in the literature, where the values of these parameters are fixed according to studies of the synchrotron or dust emission in various galaxies (e.x. Bendo et al., 2015, 2016; Michiyama et al., 2020). The results in Table 4.2 are derived using the free-free continuum with uncertainties corresponding to the fixed best fit values of α and β. However, all figures show both uncertainties.

4.1.2 Electron temperatures

SFR can be inferred from the mm-RL intensities, provided the electron temperature T_e in the star-forming region is known. This temperature is derived from the line to free-free continuum ratio expressed in equation 3.20,

$$\frac{T_e}{10^4\,\mathrm{K}} \approx \left\{ \frac{g_{\mathrm{ff}}(\nu, T_e)}{3.4} \left[\frac{I_{\mathrm{n}\alpha}/F_{\nu,\mathrm{ff}}}{27\,\mathrm{Jy\,km\,s^{-1}\,Jy^{-1}}} \right] \left[\frac{\epsilon_{n\alpha,4}}{\epsilon_{40\alpha,4}} \right]^{-1} \left[\frac{\nu_{n\alpha}}{\nu_{40\alpha}} \right] \right\}^{-1.17}, \tag{4.2}$$

where $27\,\mathrm{Jy\,km\,s^{-1}\,Jy^{-1}}$ is the equivalent width (EW) of the H40α line at an electron temperature of 10^4 K and a density of $10^3 - 10^5\,\mathrm{cm^{-3}}$. Since the normalization g_{ff} also depends on the electron

Galaxy	Region	α	β	$f_{\mathrm{free-free}}$
NGC4945	Total	$1.2^{+0.7}_{-0.6}$	$2.9^{+1.1}_{-0.3}$	$0.79^{+0.17}_{-0.69}$
NGC253	Total	$1.2^{+1.0}_{-0.6}$	$1.5^{+0.7}_{-0.3}$	$0.84^{+0.11}_{-0.52}$
M83	A	$0.5^{+1.7}_{-0.1}$	$0.6^{+0.8}_{-0.2}$	$0.46^{+0.46}_{-0.20}$
	B	$0.8^{+0.8}_{-0.4}$	$0.9^{+0.9}_{-0.1}$	$0.62^{+0.31}_{-0.53}$
	C	$0.5^{+0.5}_{-0.2}$	$1.2^{+0.6}_{-0.2}$	$0.18^{+0.64}_{-0.11}$
	Total	$0.6^{+0.4}_{-0.2}$	$1.0^{+1.0}_{-0.4}$	$0.56^{+0.35}_{-0.49}$
NGC1808	H40	$0.7^{+0.9}_{-0.4}$	$1.7^{+0.3}_{-0.3}$	$0.84^{+0.11}_{-0.63}$
	H42	$0.7^{+0.4}_{-0.2}$	$1.6^{+0.2}_{-0.4}$	$0.64^{+0.27}_{+0.51}$
Arp220	A	$0.7^{+0.7}_{-0.1}$	$2.0^{+0.2}_{-0.4}$	$0.39^{+0.48}_{-0.31}$
	B	$1.0^{+0.8}_{-0.6}$	$1.6^{+0.4}_{-0.2}$	$0.67^{+0.21}_{-0.63}$
NGC3256	A	$1.9^{+0.9}_{-1.5}$	$2.5^{+1.1}_{-0.3}$	$0.96^{+0.03}_{-0.89}$
	B	$1.6^{+1.4}_{-1.2}$	$1.9^{+1.3}_{-0.9}$	$0.95^{+0.04}_{-0.89}$
	Total	$1.6^{+0.8}_{-1.2}$	$2.6^{+1.2}_{-0.6}$	$0.95^{+0.03}_{-0.90}$

Table 4.1: The values of α and β resulting from the SED fits. The first and second columns list the galaxy and the name of the mm-RL emitting regions, respectively. The third and fourth columns show the values for α and β, respectively, which minimize the SED goodness-of-fit reduced χ^2 values. The last column shows the free-free fraction of the continuum at 100 GHz. All listed uncertainties result from the 68% confidence level of the SED fit where α and β are left free to vary.

temperature, eq. 4.2 is solved numerically for the electron temperature.

The electron temperature is calculated only for regions where the free-free contribution to the continuum emission could be calculated using the SED fit, i.e., NGC4945, NGC253, M83, Arp220, NGC1808, and NGC3256, which are galaxies from the ALMA sample. We list the line-to-free-free continuum ratios and calculated electron temperatures of these galaxies in Table 4.2. In Figure 4.2, we show the derived electron temperature values alongside literature measurements. The large open errorbars correspond to the uncertainties in the estimated free-free continuum flux densities when the α and β indices are left free to vary when fitting the SED of the respective galaxies (see Section 4.1.1). The smaller capped errorbars represent the uncertainties resulting from fixing α and β to their best fit values. Because in eq. 4.2, $I_{n,\alpha}$ and $F_{\nu,\mathrm{ff}}$ correspond to the same frequency and ALMA dataset, their flux calibration uncertainties cancel out. Even though the uncertainties in electron temperature are large, the dependence of the SFR on electron temperature remains moderate, i.e., SFR $\propto T_e^{0.58}$, mitigating some of the detrimental effects of uncertain temperature values.

Almost all electron temperatures derived here are in the range of $4000-8000$ K. Although measured in the nuclei of starbursting galaxies, they are consistent with the electron temperatures of HII regions in the inner ~ 8 kpc of the Milky Way's galactic disk (Quireza et al., 2006b). This suggests that HII regions with vastly different SFR (see Section 4.2.1) have very similar electron temperatures. Furthermore, this implies that even though, in principle, one needs to constrain electron temperature

Object	Line	Region	$I_{n\alpha}$ [Jy km s^{-1}]	FWHM [km s^{-1}]	F_ν [mJy]	$F_\nu/F_{\nu,\mathrm{ff}}$ [%]	$I_{n\alpha}/F_{\nu,\mathrm{ff}}$ [Jy km s^{-1} Jy^{-1}]	T_e [K]	SFR [$M_\odot$ yr^{-1}]
NGC4945	H30α		9.27 ± 0.37	158 ± 28	748.1 ± 0.8	17.1 ± 3.0	72.6 ± 12.9	9700^{+1800}_{-1300}	$1.56^{+0.24}_{-0.21}$
NGC4945	H40α		3.54 ± 0.22	114 ± 11	332.4 ± 0.7	79.5 ± 14.5	13.4 ± 2.6	19300^{+4400}_{-2900}	$1.98^{+0.35}_{-0.31}$
NGC4945	H42α		13.2 ± 0.3	237 ± 20	333.8 ± 0.6	79.9 ± 14.6	49.5 ± 9.1	5100^{+1000}_{-700}	$3.85^{+0.61}_{-0.51}$
NGC4945	H42α		13.3 ± 0.3	179 ± 16	343.7 ± 0.26	79.9 ± 14.6	48.3 ± 8.9	4900^{+900}_{-700}	$4.06^{+0.62}_{-0.53}$
NGC253	H26α		9.54 ± 0.37	144 ± 5	1737 ± 5	7.1 ± 0.6	77.4 ± 6.8	13700^{+1200}_{-1000}	$0.95^{+0.11}_{-0.11}$
NGC253	H27α		6.83 ± 0.23	158 ± 6	639 ± 2	10.1 ± 0.8	105 ± 9	9300^{+700}_{-600}	$0.61^{+0.07}_{-0.07}$
NGC253	H30α		10.4 ± 0.1	178 ± 2	471 ± 2	25.0 ± 1.9	88.4 ± 6.8	7700^{+500}_{-500}	$1.16^{+0.13}_{-0.12}$
NGC253	H33α		10.5 ± 0.1	188 ± 2	338.2 ± 0.3	47.1 ± 3.6	65.9 ± 5.1	7700^{+600}_{-500}	$1.49^{+0.16}_{-0.16}$
NGC253	H34α		8.03 ± 0.05	173 ± 1	256.9 ± 1.3	54.8 ± 4.2	57.1 ± 4.4	7800^{+600}_{-500}	$1.28^{+0.14}_{-0.14}$
NGC253	H40α		6.39 ± 0.03	171 ± 1	275.8 ± 0.3	84.6 ± 7.2	27.4 ± 2.4	9500^{+800}_{-700}	$1.76^{+0.21}_{-0.19}$
M83	H40α	A	0.207 ± 0.017	46 ± 3	5.84 ± 0.01	46.6 ± 15.9	76.3 ± 26.8	3800^{+1700}_{-900}	$0.14^{+0.04}_{-0.03}$
M83	H40α	B	0.111 ± 0.024	57 ± 6	4.56 ± 0.01	62.9 ± 11.3	39.0 ± 11.1	6700^{+2300}_{-1300}	$0.11^{+0.03}_{-0.03}$
M83	H40α	C	0.109 ± 0.023	73 ± 7	2.68 ± 0.01	18.2 ± 14.6	224 ± 186	1600^{+5700}_{-600}	$0.05^{+0.09}_{-0.01}$
M83	H40α	T	0.452 ± 0.049	63 ± 3	15.39 ± 0.02	56.3 ± 10.5	52.1 ± 11.3	5300^{+1300}_{-800}	$0.38^{+0.08}_{-0.06}$
M83	H41α	A	0.137 ± 0.011	59 ± 5	5.68 ± 0.01	47.9 ± 16.5	50.4 ± 17.8	5000^{+2400}_{-1200}	$0.12^{+0.04}_{-0.02}$
M83	H41α	B	0.148 ± 0.011	57 ± 4	4.36 ± 0.01	64.2 ± 11.6	53.2 ± 10.4	4900^{+1000}_{-700}	$0.13^{+0.02}_{-0.02}$
M83	H41α	T	0.488 ± 0.024	90 ± 5	14.59 ± 0.02	57.0 ± 10.7	58.7 ± 11.4	4200^{+900}_{-600}	$0.40^{+0.06}_{-0.05}$
NGC5128	H40α		< 0.35	–	7866 ± 5	–	–	–	< 0.1
NGC1068	H40α		< 1.4	–	111.1 ± 0.1	–	–	–	< 2.3
NGC1068	H42α		< 1.6	–	128.1 ± 0.1	–	–	–	< 3.9
NGC0055	H40α		< 1.1	–	0.79 ± 0.05	–	–	–	< 0.01
NGC1365	H30α		< 2.5	–	18.9 ± 0.1	–	–	–	< 5.3
NGC1808	H40α	A	0.327 ± 0.033	99 ± 7	6.41 ± 0.02	84.5 ± 10.1	60.4 ± 9.6	4500^{+700}_{-500}	$0.52^{+0.09}_{-0.08}$
NGC1808	H42α	B	0.731 ± 0.051	224 ± 14	11.79 ± 0.01	67.0 ± 10.4	92.5 ± 15.7	3000^{+500}_{-400}	$0.93^{+0.15}_{-0.13}$
NGC3627	H30α	A	2.93 ± 0.23	89 ± 5	4.20 ± 0.07	–	–	5000^{+1000}_{-1000}	$2.16^{+0.34}_{-0.34}$
NGC3627	H30α	B	1.91 ± 0.16	153 ± 7	0.42 ± 0.04	–	–	5000^{+1000}_{-1000}	$1.21^{+0.21}_{-0.21}$
NGC2903	H40α		< 1.3153	–	8218 ± 108	–	–	–	< 1.6
ARP220	H40α	B	1.00 ± 0.05	230 ± 11	22.79 ± 0.02	67.2 ± 9.6	65.4 ± 9.9	4700^{+700}_{-500}	101^{+15}_{-14}
ARP220	H40α	A	0.73 ± 0.07	204 ± 22	12.22 ± 0.02	39.3 ± 10.8	152.5 ± 44.4	2300^{+800}_{-400}	$49.1^{+11.9}_{-8.9}$
NGC3256	H30α	B	0.269 ± 0.024	318 ± 26	2.61 ± 0.02	54.8 ± 4.1	188 ± 22	4300^{+500}_{-400}	$3.15^{+0.49}_{-0.47}$
NGC3256	H40α	A	0.298 ± 0.022	182 ± 20	7.44 ± 0.01	96.6 ± 7.8	41.5 ± 4.6	6700^{+800}_{-600}	$10.3^{+1.5}_{-1.4}$
NGC3256	H40α	B	0.189 ± 0.020	202 ± 21	6.49 ± 0.01	95.2 ± 7.4	30.7 ± 4.0	8900^{+1300}_{-1000}	$7.60^{+1.31}_{-1.24}$
NGC3256	H40α	T	0.515 ± 0.061	186 ± 16	16.04 ± 0.02	95.9 ± 7.9	33.5 ± 4.8	7800^{+1200}_{-900}	$20.3^{+3.6}_{-3.4}$
NGC3256	H41α	A	0.412 ± 0.039	254 ± 20	7.29 ± 0.02	97.2 ± 7.9	58.2 ± 7.3	4400^{+500}_{-400}	$12.7^{+1.9}_{-1.9}$
NGC3256	H41α	B	0.323 ± 0.039	406 ± 42	6.47 ± 0.02	95.6 ± 7.5	52.3 ± 7.6	4800^{+700}_{-500}	$10.5^{+1.9}_{-1.8}$
NGC3256	H41α	T	0.886 ± 0.078	338 ± 31	15.72 ± 0.04	96.1 ± 7.9	58.7 ± 7.1	4400^{+500}_{-400}	$26.8^{+4.1}_{-3.9}$
NGC3256	H42α	A	0.225 ± 0.021	194 ± 11	6.75 ± 0.01	97.5 ± 7.9	34.2 ± 4.3	6300^{+800}_{-600}	$9.48^{+1.45}_{-1.39}$
NGC3256	H42α	B	0.189 ± 0.020	247 ± 25	5.67 ± 0.01	95.8 ± 7.5	35.0 ± 4.6	6200^{+800}_{-600}	$7.92^{+1.26}_{-1.21}$
NGC3256	H42α	T	0.516 ± 0.044	234 ± 16	15.23 ± 0.01	96.1 ± 7.9	35.3 ± 4.2	6200^{+700}_{-600}	$21.3^{+3.1}_{-2.9}$
NGC3628	H30α		1.15 ± 0.05	142 ± 23	24.72 ± 0.03	–	–	5000 ± 1000	$0.86^{+0.13}_{-0.13}$
NGC1097	H40α		< 1.02	–	10.5 ± 0.1	–	–	–	< 11.4
NGC6822	H40α		< 0.095	–	2.42 ± 0.02	–	–	–	< 0.0001
NGC4038	H30α		< 1.4	–	8.9 ± 0.1	–	–	–	< 4.8
NGC7582	H30α		< 0.4	–	9.34 ± 0.06	–	–	–	< 1.3
NGC5253	H30α		0.756 ± 0.023	68 ± 2	20.07 ± 0.03	–	–	5000 ± 1000	$0.07^{+0.01}_{-0.01}$
NGC4418	H40α		< 0.09	–	10.04 ± 0.02	–	–	–	< 1.8
NGC1614	H30α		< 0.4	–	5.33 ± 0.05	–	–	–	< 13.3

Table 4.2: Temperatures and Star Formation Rates in Galaxies with detected mm-RL emission. The third column shows individual regions with mm-RL emission in galaxies, with T representing total. The fourth and fifth columns show the extracted integrated line flux (ILF) and continuum flux density (CFD). The sixth and seventh columns show the free-free fraction of the continuum and line to free-free continuum fraction (L/C) at the line frequency. The last two columns show the electron temperature, derived in section 4.1.2, and the SFR, derived in section 4.2.1.

to use mm-RL as a SFR proxy, in practice, assuming an electron temperature $T_e \approx 5000$ K would also be appropriate. Doubling this electron temperature would increase the SFR by ∼49%.

Several galaxies have multiple electron temperature measurements. In these cases, the electron temperatures are consistent with one another. This consistency strengthens the accuracy of the electron temperatures measured here, and of the radio SED fits which directly influence these temperature estimates. Two outliers in this analysis are the inferred temperatures of ∼ 20000 K, derived from the H40α line in NGC4945 and of ∼ 16000 K, derived from the H26α line in NGC253. Both values seem very high compared to typical temperatures of HII regions in the Milky Way (Draine, 2011; Shaver et al., 1983; Quireza et al., 2006b) or with the other temperatures derived in this work. These values, however, are still in agreement with a canonical 5000-8000 K range when considering the uncertainties resulting from our SED fit where the α and β indices are left free to vary (see section 4.1.1). These discrepancies show that accurately determining the free-free continuum level is the key to constraining electron temperature values.

Overall, the temperatures derived here are in good agreement with those from the literature. All the literature measurements shown in Figure 4.2 were inferred using cm-RL or mm-RL and their underlying continuum. One exception is M83, where the [OII], [NII], and [SIII] transitions were used instead of mm-RL, to measure the electron temperature (Bresolin et al., 2005). In slight disagreement with literature measurements are the temperature values for NGC253 (Bendo et al., 2015). However, this discrepancy can be explained by our use of different spectral indexes and aperture sizes when extracting the mm-RL and underlying continuum fluxes.

In conclusion, we find that in regions with vastly different SFR, electron temperatures have values of $T_e \approx 4000 - 8000$ K. This, together with the moderate dependence of SFR on electron temperature, indicates that there is no stringent need to constrain electron temperature to use mm-RL as a SFR proxy. We also find that not fixing the values of the synchrotron and dust emissivity spectral indices are during fitting, results in very high uncertainties for free-free continuum fraction, electron temperature, and SFR.

4.2 Star formation rates measured using mm-RL emission

4.2.1 The ALMA archival sample

The SFR for the ALMA sample are presented in Fig. 4.3, and are calculated with eq. 3.15, using the mm-RL intensities presented in Table 4.2 and the temperatures measured in Section 4.1.2. We adopt electron density of 10^3 cm^{-3}, as the optically thin mm-RL is marginally affected by it (e.g. Bendo et al., 2015, 2016). Similar to the electron temperature uncertainties in section 4.1.2, the large relative uncertainties in the free-free continuum flux densities, resulting from SED fits where the synchrotron and dust emissivity spectral indices are free variables, propagate into large relative uncertainties in the SFR. Thus, these are a factor of a few larger than those obtained by fixing the spectral indices to their best SED fit values. All SFR estimates include the ALMA 10% calibration uncertainty in the observed integrated line flux (Bonato et al., 2018; Remijan et al., 2019) added in quadrature. In galaxies with mm-RL detections where an SED fit could not be performed, i.e., NGC3627, NGC3628, and NGC5253, an electron temperature of 5000 K was assumed, with an uncertainty of 20%, i.e., similar to the temperature uncertainties we calculated in galaxies where an SED fit was performed. Since the SFR depends weakly on electron temperature, i.e. SFR$\propto T_e^{0.58}$, adopting an electron temperatures of 10^4 K would increase the SFR of these galaxies by 49%.

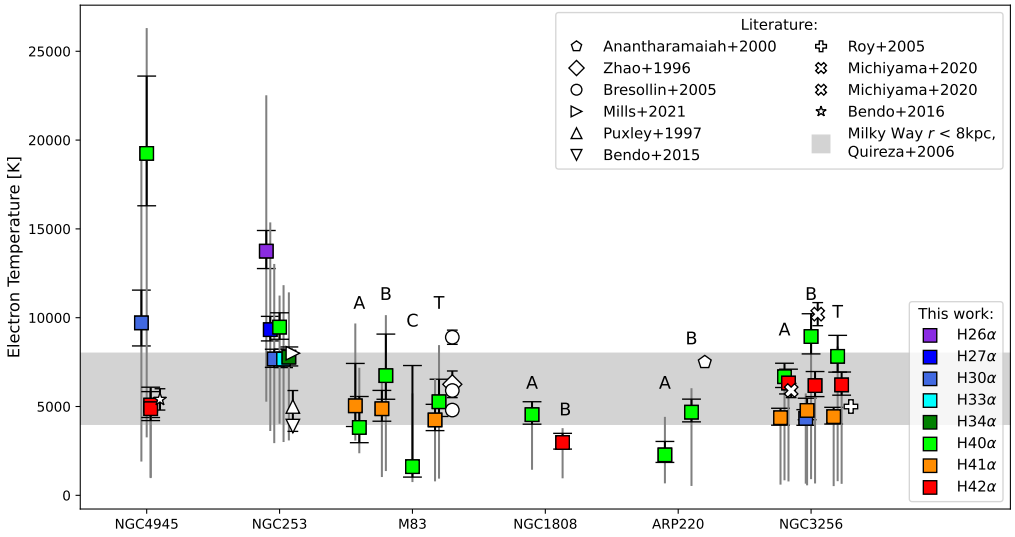

Figure 4.2: Electron temperatures of the line emitting regions. Vertical open error bars mark the uncertainty deriving from SED fits to the synchrotron and dust emissivity indices, while the capped error ranges assume priors on these indices. Literature values are shown with open symbols. The gray region shows the electron temperature range found for Milky Way HII regions within 8 kpc from the nucleus (Quireza et al., 2006b).

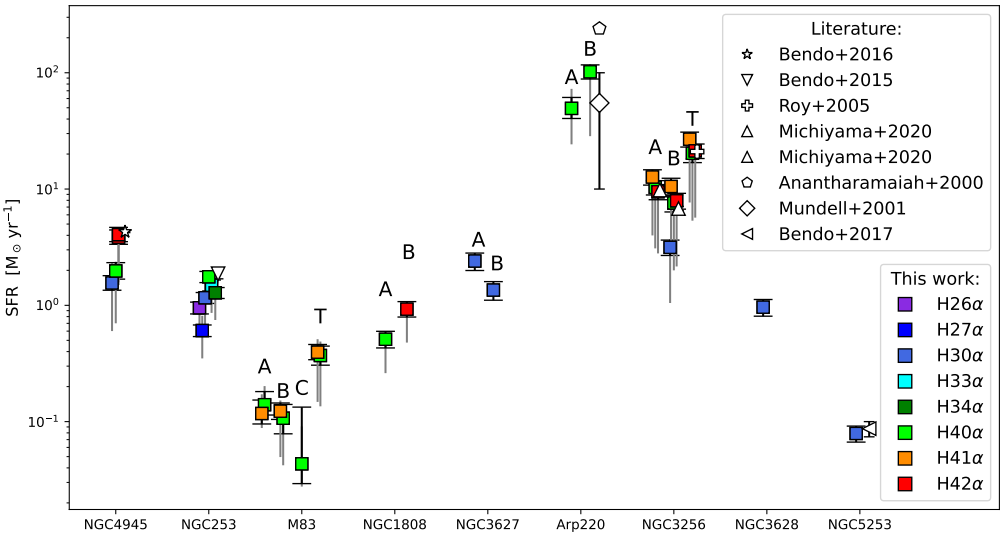

Figure 4.3: Star formation rates of the mm-RL emitting regions. The literature data is shown with open symbols. Vertical open error bars mark the uncertainty deriving from SED fits to the synchrotron and dust emissivity indices, while the capped error ranges assume priors on these indices. For NGC3627, NGC3628, and NGC5253, no SED -fit was possible to determine the electron temperature, and we adopt $T_e = 5000 \pm 1000$ K.

Our results agree with mm-RL-based literature values in NGC253 (Bendo et al., 2015), NGC3256 (Michiyama et al., 2020; Roy et al., 2005), and NGC5253 (Bendo et al., 2017). In the case of Arp220, the values of Anantharamaiah et al. (2000) are higher than our own and probably wrong, for reasons we discussed in section 2.1.2.

For galaxies NGC253, NGC4945, and region B in NGC3256, we obtain discrepant SFR from our different mm-RL. Since optically thin emission was assumed when calculating their SFR, this discrepancy motivates us to analyze the effects of optical depth on the emission line intensities in these regions.

Possible effects of optical depth

In section 4.2.1, for galaxies with more than one mm-RL detection, considering optically thin emission and accounting for non-LTE effects, we obtain for the same regions different values of the electron temperature and SFR from each mm-RL. This discrepancy could be explained by optically thick emission in these regions. For this reason, we investigate the impact of optical depth on the mm-RL fluxes and SFR of the observed regions.

Optically thin mm-RL emission is only marginally affected by the electron temperature and density. The amount of amplification or attenuation of a mm-RL, when the line emission is no longer optically thin, depends on the properties of the emitting hydrogen gas, i.e., T_e and n_e, and $\mathrm{EM_{LOS}}$. As the optical depth increases, the mm-RL intensities and ratios start to differ from their optically thin values. Line amplification or attenuation also leads to an over- or underestimation of the SFR, respectively. Here we model the HII gas as slab with constant thickness, having a uniform density, temperature, and emission measure. These aspects are described in more detail in Section 3.5. Line attenuation or amplification due to optical depth in an observed region can be studied by comparing mm-RL fluxes obtained from theory, and their associated SFR, with observations. In principle, given some values for the electron density n_e, temperature T_e, and emission measure, $\mathrm{EM_{LOS}}$, integrated mm-RL fluxes can be calculated from theory (eq. 3.25), provided the angular extent, Ω, of the emitting region is also known. With the current data, the resolution of the ALMA observations makes it impossible to determine the actual angular extent, Ω, of the line emitting regions. However, our analysis uses matched apertures that capture all the mm-RL emission from a given source, such that the unknown angular size of the emitting region would affect all integrated mm-RL fluxes identically. This allows us to scale the integrated mm-RL fluxes generated using eq. 3.25, for different values of n_e, T_e, and $\mathrm{EM_{LOS}}$, to the observed mm-RL fluxes, while preserving their line ratios. With eq. 3.28, the optical depth correction factors, $C_{n\alpha}$, correponding to the n_e, T_e, and $\mathrm{EM_{LOS}}$ that generate line fluxes that best fit the observations, can be calculated and applied to the observed SFR. If the conditions corresponding to the best-fitting theoretical line fluxes are close to the real ones, the optical depth corrected SFR from different mm-RL should all be in agreement.

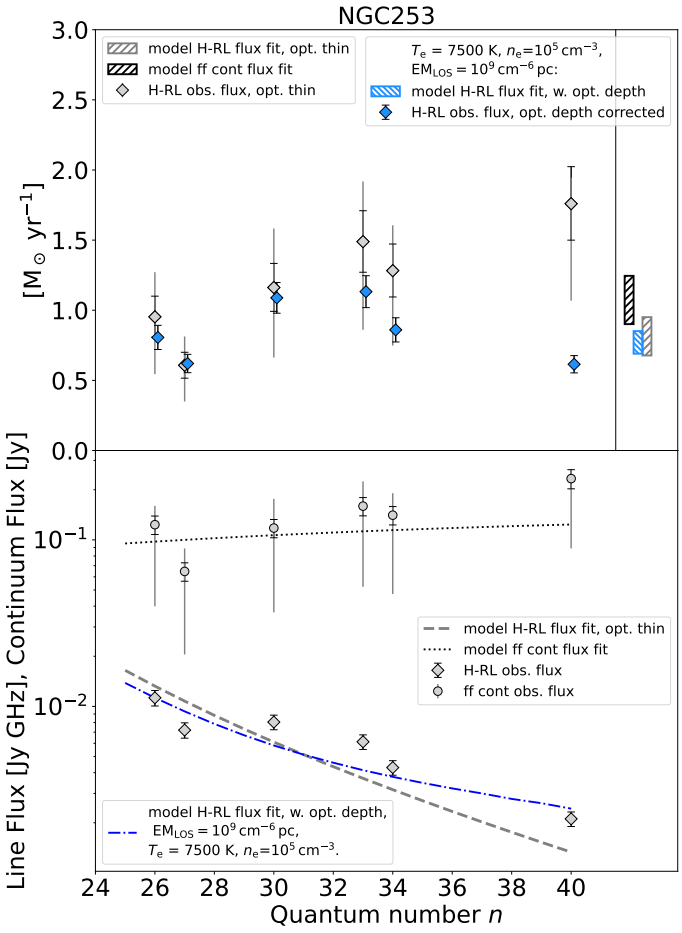

Figure 4.4: *Bottom*: Model and observed integrated mm-RL fluxes and continuum flux densities at the corresponding mm-RL frequency. The models of the optically thin and best fit mm-RL fluxes considering optical depth are shown with dashed and dot-dashed lines, respectively. The dotted line represents the model continuum flux density fit to the observed values. *Top*: SFR obtained from the observed line fluxes and fits shown in the bottom panel. The black, gray, and blue rectangles show the SFR obtained from the three fitted models in the bottom panel. The gray symbols show the SFR obtained from the observed mm-RL fluxes, assuming optically thin emission - see Sec. 4.2.1. The blue symbols show the SFR obtained from the observed line fluxes, after applying the optical depth correction factor, $C_{n\alpha}$. The correction factor was calculated using the n_e, T_e, and EM$_{\rm LOS}$ corresponding to the best-fit mm-RL emission model, which takes optical depth into account. Open error bars mark the uncertainty deriving from SED fits to the synchrotron and dust emissivity indices, while the capped error ranges assume priors on these indices.

This type of analysis is possible only for regions where multiple mm-RL are detected spanning a wide range of quantum numbers, e.g., H30α and H40α. Three objects in the sample satisfy this condition: NGC253, NGC4945, and region B in NGC3256. For these galaxies, theoretical integrated

mm-RL fluxes are calculated for densities $n_e = 10^3, 10^4, 10^5$ cm^{-3}, temperatures $T_e = 5000, 7500, 10000$ K, and emission measures $EM_{LOS} = 10^7, 10^8, 10^9, 10^{10}$ cm^{-6} pc, and then fitted to the observed line fluxes. In the bottom panels of Fig. 4.4 and 4.5 the observed line and continuum fluxes are shown, together with the theoretical line fluxes that best-fit the observations, for NGC253 and NGC3256 B respectively. In the case of NGC253, the theoretical mm-RL fluxes that best fit the observations indicate that the emission is optically thick, corresponding to $T_e = 7500$ K, $n_e = 10^5$ cm^{-3}, and $EM_{LOS} = 10^9$ cm^{-6} pc. Similarly, for NGC3256, the emission is also optically thick, corresponding to $T_e = 10^4$ K, $n_e = 10^5$ cm^{-3}, and $EM_{LOS} = 10^9$ cm^{-6} pc. These temperatures, densities and emission measures will then used to calculate optical depth correction factors, $C_{n\alpha}$, for the observed SFR of both galaxies. In the upper panel of Fig. 4.4 and 4.5 we show the observed SFR obtained in Section 4.2.1 where we assumed optically thin emission, as well as the SFR after the optical depth correction factor, $C_{n\alpha}$, has been applied. For both galaxies, maser amplification leads to an overestimation of SFR obtained from lower frequency mm-RL, such as H40α. This effect is clearly visible in the case of NGC 253, where the SFR derived from the observed H40α line flux without taking optical depth into account is overestimated by a factor of 2.5. The SFR derived from higher frequency lines, such as H26α or H30α are much less affected by optical depth effects, where taking optical depth into account changes the resulting SFR by only 30%.

The same type of analysis is also done for NGC4945, shown in figure 4.6. In this galaxy, however, the H30α and H40α relative line intensities are indistinguishable from those corresponding to optically thin emission. This means that the SFR derived in sec. 4.2.1 do not need any corrections. For illustrative purposes, in Figure 4.6, we show the line intensities and SFR fit, corresponding to a temperature $T_e = 10^4$ K and a density $n_e = 10^3$ cm^{-3}, as well as the contaminated H42α flux density that was not used in the fit.

In these three regions, with multiple mm-RL detections, where the analysis of optical depth is possible, we find that only one is consistent with optically thin emission. In the other two cases, assuming optically thin emission, the SFR inferred from lower quantum number transitions, such as H26α, would be slightly affected, while for higher quantum number transitions, such as H40α or H42α, the SFR could be severely overestimated. The electron temperatures derived here are of the order of 7500-10000 K, slightly higher but still in agreement with the average temperature of the sample. In these regions, using the intensities of multiple mm-RL, together with a model for the mm-RL emission, attenuation and amplification, allow us to obtain the T_e needed for the determination of the SFR, without having to use the highly uncertain free-free continuum emission.

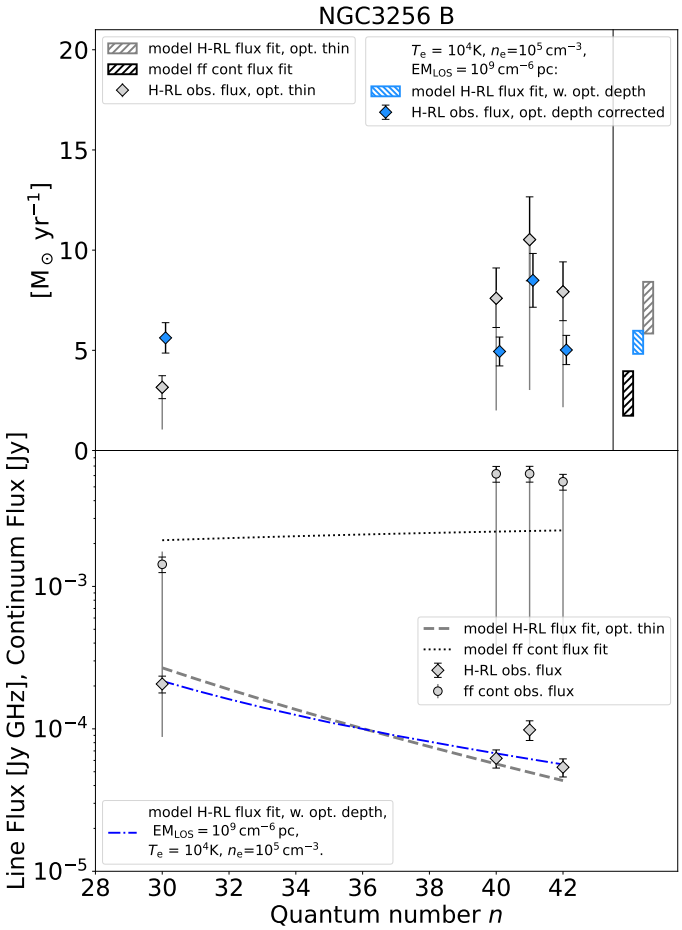

Figure 4.5: Same as figure 4.4, with the best fit to the line emission indicating optically thick emission, $T_e = 10^4$ K and $n_e = 10^5$ cm^{-3}

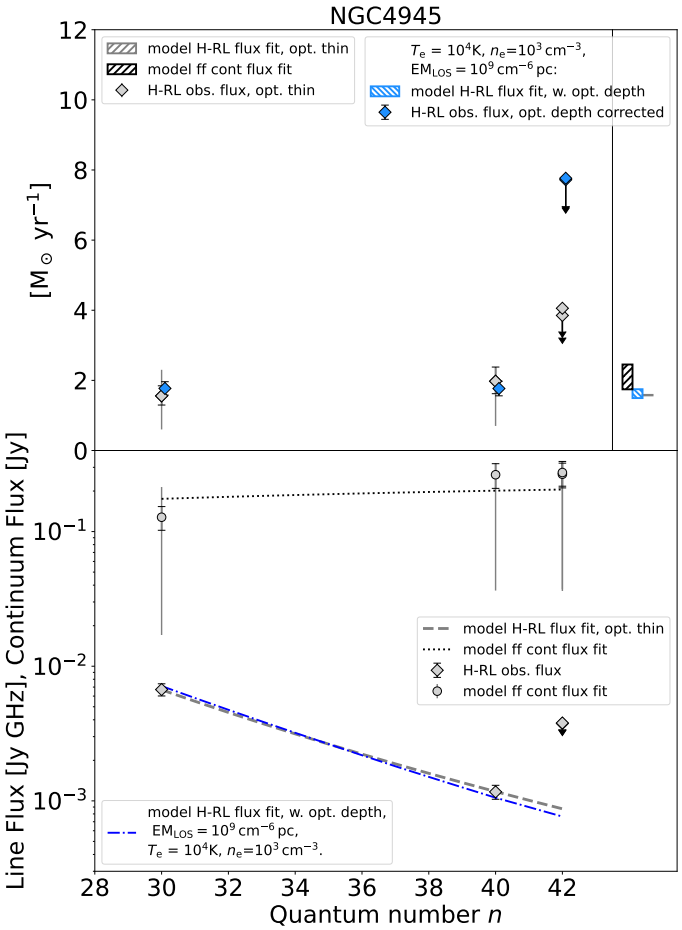

Figure 4.6: Same as Fig. 4.4. Here, the intensities H30α and H40α transitions suggest the emission in this region is optically thin (bottom panel). The fit to the line emission which takes optical depth into account is shown for illustrative purposes only. Only the H30α and H40α lines are considered for the fit, since the H42α is potentially contaminated by molecular emission, we mark it as an upper limit. The SFR (top panel) calculated in section 4.2.1 from the H30α and H40α line fluxes need no correction for optical depth. The SFR calculated from the possibly contaminated H42α line fluxes are marked as upper limits.

4.2.2 The IRAM 30m sample

Using the IRAM mm-RL observations, upper limits can be placed on the mm-RL-traced SFR. The upper limits for the mm-RL integrated line flux are calculated using thrice the sensitivity value of each observation (three sigma), assuming a mm-RL FWHM of 200 km s^{-1}. With the data in table 2.2, the integrated line flux limits are $I_{n\alpha} = 3 \times F_{\rm RMS}\sqrt{200\,km\,s^{-1}/\delta v}$. Our observations did not provide continuum data. For this reason, we assume optically thin emission, and the same electron temperature

Galaxy	H42α		H40α	
	$I_{n\alpha}$ [Jy km s^{-1}]	SFR [M$_\odot$ yr^{-1}]	$I_{n\alpha}$ [Jy km s^{-1}]	SFR [M$_\odot$ yr^{-1}]
NGC 0660	<0.41	<0.83	<0.41	<0.74
NGC 1614	<0.57	<80	<0.56	<70
NGC 2903	<1.11	<2.7	<0.4	<0.80
IC694	–	–	<0.55	<38
NGC 4102	–	–	<0.77	<6.0
NGC 4418	<0.64	<23	<0.69	<22

Table 4.3: The upper limits on the H42α and H40α integrated line fluxes, and the corresponding SFR, respectively, for the IRAM sample.

and density as for the cases in the ALMA sample where these values could not be determined. Thus, to calculate the SFR from the mm-RL integrated flux, we use equation 3.12, assuming optically thin emission, an electron density of $n_e = 10^3$ cm^{-3} and a temperature of $T_e = 5000$ K. The integrated line flux limits, and the SFR, are shown in Table 4.3.

4.3 Star formation rates measured using the dust emission

In order to investigate the reliability of using mm-RL to measure SFR, a comparison with an already calibrated and established SFR tracer is needed. For this reason, we determine the SFR in the galaxies in our sample using the total FIR emission from dust. Infrared emission from dust is a well established tracer of massive star formation, especially for star-forming, infrared-bright galaxies like those in our sample (see Sec. 1.3.2).

4.3.1 The ALMA archival sample

The high sensitivity of ALMA enables the measurement of the mm-RL, free-free, and submm emission from massive star-forming regions in nearby galaxies, facilitating high resolution measurements of the SFR. The drawback is that ALMA can only measure the Rayleigh-Jeans part of the dust FIR emission. The mm-RL emitting regions detected in the ALMA archival sample have angular areas approximately an order of magnitude or more below the resolution of FIR telescopes such as Herschel, e.g., the PACS instrument on *Herschel* has a resolution of 7.″04 at 100 μm. Thus, the high resolution, narrow field of view, and the maximum recoverable scale of the ALMA interferometric observations preclude a meaningful comparison with the FIR data available from space based telescopes. Undeterred, we use ALMA submm flux density measurements to estimate the total (8-1000 μm) IR luminosity, $L_{\rm TIR}$. To this end, we fit a modified black body (MBB) function, $F_\nu = {\rm MBB}(\beta, T_{\rm dust}) \propto \nu^\beta B_\nu(T)$ to ALMA archival observations in the 350 $\sim$ 700 GHz range, shown in Table 4.4. The integral of this function over the 42–122μm wavelength range gives the total FIR flux. The FIR luminosity is obtained from the integrated FIR flux, $L_{\rm FIR} = 4\pi D^2 \int_{\rm FIR} F_\nu \, d\nu$, where D is the distance to the observed region. The SFR is obtained assuming a Kroupa (2002) IMF following, (Murphy et al., 2011):

$$ {\rm SFR_{TIR}} \, [{\rm M_\odot \, yr^{-1}}] = 1.49 \times 10^{-10} \, (L_{\rm TIR}/L_\odot). \tag{4.3} $$

Galaxy	ALMA Project	Region	Frequency [GHz]	F_ν [Jy]	$L_{\rm FIR}$ $\log[L_{\rm FIR}/L_\odot]$	$\rm SFR_{TIR}$ $M_\odot\ \rm yr^{-1}$
NGC4945	2018.1.01236.S		357.0	3.1 ± 0.3	$10.52^{+0.16}_{-0.13}$	$5.0^{+2.3}_{-1.8}$
NGC253	2016.1.01285.S		409.6	3.21 ± 0.01	$9.80^{+0.16}_{-0.13}$	$2.1^{+0.95}_{-0.73}$
M83	2015.1.01593.S	A	345.8	0.0258 ± 0.0003	$8.52^{+0.16}_{-0.13}$	$0.11^{+0.05}_{-0.038}$
		B	345.8	0.0235 ± 0.0003	$8.56^{+0.16}_{-0.13}$	$0.12^{+0.055}_{-0.043}$
		C	345.8	0.0194 ± 0.0002	$8.85^{+0.16}_{-0.13}$	$0.23^{+0.11}_{-0.086}$
		T	345.8	0.0525 ± 0.0001	$8.42^{+0.16}_{-0.13}$	$0.087^{+0.04}_{-0.033}$
NGC1808	2017.1.00984.S	A	492.4	0.132 ± 0.002	$9.08^{+0.16}_{-0.13}$	$0.39^{+0.18}_{-0.14}$
		B	492.4	0.168 ± 0.003	$9.16^{+0.15}_{-0.13}$	$0.5^{+0.22}_{-0.18}$
Arp220	2011.0.00175.S	A	697.7	4.12 ± 0.01	$11.65^{+0.16}_{-0.13}$	$150.0^{+67.0}_{-51.0}$
Arp220		B	697.7	2.24 ± 0.01	$11.89^{+0.15}_{-0.11}$	$280.0^{+120.0}_{-88.0}$
Arp220		T	697.7	6.36 ± 0.02	$12.09^{+0.15}_{-0.13}$	$440.0^{+180.0}_{-160.0}$
NGC3256	2018.1.00493.S	A	343.8	0.0443 ± 0.0004	$10.62^{+0.16}_{-0.13}$	$14.0^{+6.2}_{-5.1}$
		B	343.8	0.0219 ± 0.0004	$10.09^{+0.15}_{-0.13}$	$4.2^{+1.8}_{-1.5}$
		T	343.8	0.073 ± 0.001	$10.39^{+0.15}_{-0.13}$	$8.6^{+3.7}_{-3.0}$
NGC5253	2012.1.00105.S		344.3	0.0183 ± 0.0001	$7.90^{+0.15}_{-0.13}$	$0.028^{+0.012}_{-0.01}$

Table 4.4: ALMA submm data and the resulting SFR. The first column lists the name of the galaxies with mm-RL detection and available high frequency ALMA archival data. The second columns shows the name of the high frequency ALMA project. The third column shows the individual regions where mm-RL were detected. The fourth column lists the frequency where the dust continuum was measured. The fifth column shows the continuum flux density at that frequency. The last two columns list the derived $L_{\rm TIR}$ and $\rm SFR_{TIR}$, respectively.

where we use $L_{\rm TIR} = 1.91 \times L_{\rm FIR}$ (Magnelli et al., 2015; Delhaize et al., 2017).

The two parameters of the MBB function, $T_{\rm dust}$ and β, have a strong influence on the resulting $L_{\rm FIR}$, and by extension, on the calculated SFR. Lacking the FIR data to fit MBB functions and constrain β and $T_{\rm dust}$, we adopt adopt appropriate values for these two parameters using existing studies of the FIR emission in nearby galaxies. Cortese et al. (2014); Galliano et al. (2018) perform Herschel/PACS 100 and 160 μm photometry and single temperature MBB fits to the infrared emission of 323 galaxies in the Herschel Reference Survey sample (HRS, Boselli et al., 2010). Clements et al. (2010, 2018) analyze a complete flux-limited sample of 43 ULIRGs selected at 60 um by IRAS and observed with *Herschel*-SPIRE as part of the *Herschel* ULIRG Survey (HERUS). They combine SPIRE photometry at 250, 350, and 500 μm with data from IRAS to fit the far-infrared SEDs with an MBB.

We examine the distribution of the β and $T_{\rm dust}$ values in the HRS and HERUS samples. The HRS sample yields values of $\beta \approx 1 - 2.5$ and $T_{\rm dust} \approx 15 - 30$ K, whereas the HERUS sample has higher temperatures of $T_{\rm dust} \approx 33 - 48$ K, with $\beta \approx 1.4 - 2.3$. We adopt the values from the HERUS sample to calculate $L_{\rm FIR}$, where $\beta = 1.73 \pm 0.22$ and $T_{\rm dust} = 37.9 \pm 4.7$ K, uncertainties representing the standard deviation (Clements et al., 2018). The values from HERUS sample were chosen because the ALMA observations cover the most active star-forming regions of the galaxies in the sample, which we expect to show dust properties more similar to ULIRGs.

Bayesian methods are use to estimate the probability distribution of β and $T_{\rm dust}$, and thus the posterior probability distribution of $L_{\rm FIR}$, for each star-forming region, given the priors and the uncertainty in the submm ALMA measurements. Because we model the flux as a MBB, the flux density for a given ALMA high frequency observation $F_{\rm hf}$ can be written as

$$F_{\rm hf} = N_{\rm hf} \times \nu^\beta B(\nu_{\rm hf}, T_{\rm dust}) \tag{4.4}$$

where the normalizing constant $N_{\rm hf}$ is determined by setting $T_{\rm dust} = 37.9\,{\rm K}$ and $\beta = 1.73$, corresponding to the HERUS sample. The calculation of the joint probability distribution of β and $T_{\rm dust}$ is done using the `emcee` package. The joint posterior probability of $(T_{\rm dust}, \beta)$ is:

$$P\left(\beta, T_{\rm dust}|F_{\rm hf}\right) \propto P\left(F_{\rm hf}|\beta, T_{\rm dust}\right) P\left(\beta\right) P\left(T_{\rm dust}\right), \tag{4.5}$$

where the first term on the right-hand-side is the likelihood of the flux density measurements given values of $T_{\rm dust}$ and β, and the last two terms are the prior probability distributions of and β. The likelihood function can be written as:

$$P\left(F_{\rm hf}|\beta, T_{\rm dust}\right) = \left(2\pi\sigma^2_{F_{\rm obs}}\right)^{-1/2} \exp \frac{\left(F_{\rm hf} - F_{\rm obs}\right)}{2\sigma^2_{F_{\rm obs}}} \tag{4.6}$$

where $F_{\rm obs}$ and $\sigma_{F_{\rm obs}}$ are the continuum flux density and its uncertainty from the ALMA archive. The priors $P\left(\beta\right)$ and $P\left(T_{\rm dust}\right)$ are modeled as normal distributions, $\beta \sim \mathcal{N}(1.73, 0.22)$ and $T_{\rm dust} \sim \mathcal{N}(37.9\,{\rm K}, 4.7\,{\rm K})$, respectively. The distribution of $L_{\rm FIR}$ and ${\rm SFR}_{\rm TIR}$ is calculated by integrating the MBB function using the values of β and $T_{\rm dust}$ sampled from their joint posterior distribution. The median and the 16th and 84th percentile values of the $L_{\rm FIR}$ and ${\rm SFR}_{\rm TIR}$ distributions are used as results and uncertainties. The joint probability distribution of β and $T_{\rm dust}$ is shown for each galaxy in Appendix C. The resulting $L_{\rm FIR}$ and ${\rm SFR}_{\rm TIR}$ are shown in the last two columns of table 4.4.

4.3.2 The IRAM 30m sample

Unlike the ALMA sample, the resolution of the IRAM 30m observations is comparable to that of some FIR space telescopes. Therefore, archival data from telescopes such as Spitzer or Herschel were used to perform a more detailed analysis and to calculate $L_{\rm FIR}$. This data covers MIR, FIR, and submm frequencies and is presented in the chapter 2.1.3. The SED fitting is performed using our own fitting method, described in section 2.2, which allows us to perform SED fits on data that contain flux measurements that only provide an upper bound at their respective frequency. This also allows us to determine the luminosities, $L_{\rm FIR}$, and constrain the values of the dust temperatures and dust emission spectral indices, i.e. $T_{\rm dust}$ and β, for regions in the IRAM sample for which archival data are lacking at the required resolution.

SED model fitting procedure

We fit a modified blackbody SED to the flux density measurements extracted from archival images. To compute the ${\rm SFR}_{\rm TIR}$ of the observed regions, we integrate over the resulting SEDs to obtain the $L_{\rm FIR}$. The total infrared luminosity is obtained from $L_{\rm FIR}$ using the same procedure as for the ALMA sample. A composite model is used to model the SED, which has two components, a modified blackbody component for sub-mm to FIR frequencies, and a frequency dependent powerlaw component for FIR to MIR frequencies, following (e.g. Blain et al., 2003; Casey, 2012). We consider both optically thick and optically thin dust emission models to test the stability of our fitting procedure together with the two-component model, and assess its impact on the results. For the optically thick case, the modified

black body component has the following form:

$$f_{\rm bb}\left(\nu, T_{\rm d}, \beta, \alpha, N_{\rm bb}, \nu_0\right) = N_{\rm bb} \times \frac{1 - \exp\left[-\left(\frac{\nu}{\nu_0}\right)^{\beta}\right]}{c^2} \cdot \frac{2h\nu^3}{\exp\left(\frac{h\nu}{k_{\rm B}T_{\rm d}}\right) - 1} \tag{4.7}$$

where ν_0 is the frequency at which the dust opacity, taken as $\tau(\nu) = (\nu/\nu_0)^{\beta}$, is unity (Draine, 2006), and $N_{\rm bb}$ is a normalization factor for the black body emission. For the optically thin case, we use the following approximation for the modified black body component:

$$f_{\rm bb}\left(\nu, T_{\rm d}, \beta, \alpha, N_{\rm bb}\right) = \frac{N_{\rm bb}}{c^2} \cdot \frac{2h\nu^{3+\beta}}{\exp\left(\frac{h\nu}{kT_{\rm d}}\right) - 1} \tag{4.8}$$

The powerlaw component, for both the optically thin and the optically thick cases, has the same form:

$$f_{\rm pl}(\nu, \alpha, N_{\rm pl}) = N_{\rm pl} \times \nu^{-\alpha} \tag{4.9}$$

where $N_{\rm pl}$ is a normalization factor for the powerlaw component, and α is its spectral index. The full model, $f_{\rm full}$, is taken as following a modified black body function at frequencies lower than a critical frequency ν_c, or the powerlaw function at frequencies above ν_c:

$$f_{\rm full}\left(\nu, T_{\rm d}, \beta, \alpha, N_{\rm bb}, \nu_0\right) = \begin{cases} f_{\rm bb}\left(\nu, T_{\rm d}, \beta, \alpha, N_{\rm bb}, \nu_0\right) & \text{if } \nu < \nu_c \\ f_{\rm pl}\left(\nu, \alpha, N_{\rm pl}\right) & \text{if } \nu > \nu_c \end{cases}$$

For the spectrum to be a continuous function at the critical frequency, the two functions, $f_{\rm bb}$ and $f_{\rm pl}$, should have the same value and the same slope at ν_c. This means that the following equations have to be satisfied simultaneously:

$$f_{\rm bb}(\nu_c) = f_{\rm pl}(\nu_c) \tag{4.10}$$

and

$$\left(\frac{d\log\left(f_{\rm bb}(\nu)\right)}{d\log(\nu)}\right)_{\nu=\nu_c} = \left(\frac{d\log\left(f_{\rm pl}(\nu)\right)}{d\log(\nu)}\right)_{\nu=\nu_c}, \tag{4.11}$$

. Equation 4.10 fixes the value of $N_{\rm pl}$ with respect to the other parameters:

$$N_{\rm pl} = f_{\rm bb} \times \nu^{\alpha} = N_{\rm bb} \times \frac{1 - \exp\left[-\left(\nu/\nu_0\right)^{\beta}\right]}{c^2} \cdot \frac{2h\nu^3}{e^{\frac{h\nu}{k_{\rm B}T_{\rm d}}} - 1}, \tag{4.12}$$

, while Eq. 4.11 fixes the value of ν_c with respect to α:

$$\left(\frac{d\log\left(f_{\rm bb}(\nu)\right)}{d\log(\nu)}\right)_{\nu=\nu_c} = -\alpha \tag{4.13}$$

. The value of ν_c is calculated by solving the expanded form of Eq. 4.13 for ν, which for the optically thick case is:

$$\beta \frac{(\nu/\nu_0)^\beta}{\exp\left[(\nu/\nu 0)^\beta\right]-1} - \frac{h\nu}{k_B T_d} \frac{\exp\left(\frac{h\nu}{k_B T_d}\right)}{\exp\left(\frac{h\nu}{k_B T_d}\right)-1} + 3 + \alpha = 0, \tag{4.14}$$

while for thin case it is:

$$\beta - \frac{h\nu}{k_B T_d} \frac{\exp\left(\frac{h\nu}{k_B T_d}\right)}{\exp\left(\frac{h\nu}{k_B T_d}\right)-1} + 3 + \alpha = 0. \tag{4.15}$$

.

Because N_{pl} and ν_c are fixed by the other parameters, an adopting fixed values for ν_0 in the optically thick case, these models have four free parameters: T_d, β, α, and N_{bb}.

The above models are fit to the continuum fluxes presented in Sec. 2.1.3 using our own method described in Section 2.2. During fitting, four parameters are free: the dust temperature T_d, the dust thermal emission index β, the MIR emission indexα, and the normalizing factor N_{bb}. For the optically thick models, the ν_0 parameter is fixed during fitting. We perform multiple fits using the optically thick model, fixing the value of ν_0 at the following frequencies: ν_0 = 1500, 2000, 3000, 4000, 5000 GHz. These frequencies, at which the dust optical depth is unity, cover the values found in various dust models considered in the literature (Blain et al., 2003; Draine & Li, 2007a; Casey, 2012). Thus, in total, we fit six models for each galaxy, one for the optically thin case, and five for the various values of ν_0 in the optically thick case. For each model fit with the emcee package, we use 70 walkers per parameter, for a total of 280 walkers per model. We adopt flat priors on all the parameters, having the ranges $T_d = 5 - 85$ K, $\beta = 0.2 - 4.5$, $\alpha = 0.2 - 4.5$, $\log_{10}(N_{bb}) = (-5) - (-22)$. The priors cover a wide range of values, the limits were chosen to avoid numerical overflow errors during fitting and to prevent the walkers from exploring regions non-physical parameter configurations.

SED fitting results

The posterior distribution of the four parameters T_d, β, α, and N_{bb}, resulting from the optically thick SED model fitting, with ν_0 = 1500 GHz and 5000 GHz, for NGC4102, are shown in Fig. 4.7. Because the results show negligible differences between the 25" and 27" apertures, only the results for the 25" apertures are shown. The rest of the distributions, for all galaxies and all values of ν_0, are shown in Appendix D.1. In these figures, an anti-correlation is observed between T_d and β, between T_d and N_{bb}, and to a lesser extent between α and β, and between α and N_{bb}. The degree of anti-correlation between all of these parameters increases with ν_0.

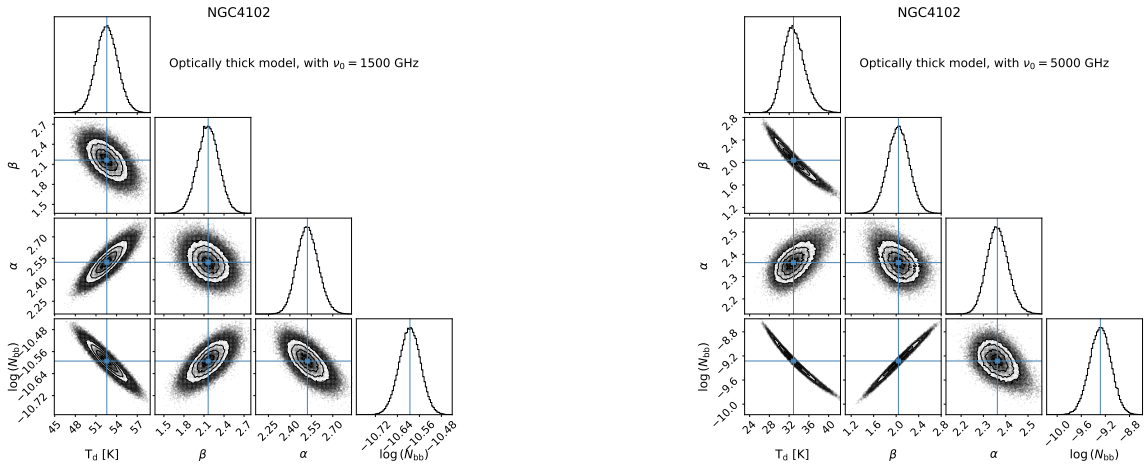

Figure 4.7: The posterior distributions of our optically thick model, resulting from the MCMC fit of the model to the observed data, for the 25" diameter aperture. The highlights show the median values of the parameters. The left and right figures correspond to $\nu_0 = 1500$ GHz and $\nu_0 = 5000$ GHz, respectively.

The anti-correlation between the dust temperature, T_d, and the dust emissivity index, β, is well known, having been observed and studied extensively (e.g. Dupac et al., 2001; Blain et al., 2003; Sajina et al., 2006; Désert et al., 2008; Smith et al., 2012; Davies et al., 2014; Hughes et al., 2014), and is intrinsic to a single temperature modified black body model, where the peak or total has to have a fixed value (e.g. Blain et al., 2003). The anti-correlation can also be influenced by the distribution dust grain shapes and sizes (e.g. Meny et al., 2007; Coupeaud et al., 2011; Ysard et al., 2012). Temperature mixing along the line of sight and inside the beam also affects the degree of correlation, e.g., observing through multiple layers cold dust components having low temperatures, i.e., $T_d < 15$ K, can reduce the observed anti-correlation and even lead to an observed correlation between T_d and β (Juvela & Ysard, 2012). The uncertainty in the flux density measurements, as well as their number, will also lead to an observed anti-correlation between the two parameters, especially when performing a least squares fit to the data Shetty et al. (2009). The degree to which each of these effects influences the correlation between T_d and β, especially at the spatial resolution of our data, is difficult to assess from observations (Galametz et al., 2012) and is beyond the scope of this thesis. The anti-correlation between N_{bb} and both T_d and β, and its correlation with α are also intrinsic to our model. Increasing the temperature or the dust emissivity index, would lead to an increase in the flux density, especially in the sub-mm and FIR wavelength ranges, requiring a decrease in the normalizing factor N_{bb}. The same mechanism would also give rise to the slight anti-correlation between α and both β and N_{bb}, especially in model fits to galaxies where the peak of the dust emission is poorly constrained observations. For our optically thick model here, we also observe an anti-correlation between ν_0 and T_d, which is explained by the use of a single temperature modified black body component. For any given galaxy, a decrease in the frequency ν_0, below which the modified black body component of our model starts to become optically thin, results in an increase in the dust temperature needed to maintain the same overall level of continuum emission flux density.

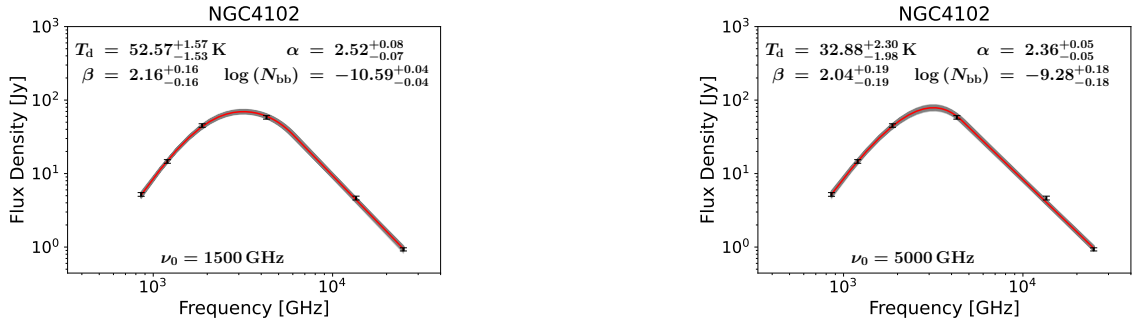

Figure 4.8: The SED function resulting from the MCMC fit of the optically thick SED model to the continuum data. The best fit SED function is shown in red, while the 68% confidence level is shown in gray. The archival continuum data is shown with black symbols. The left and right figures show the fitting results for $\nu_0 = 1500$ GHz and $\nu_0 = 5000$ GHz, respectively. These apertures cover the regions we observed with the IRAM 30m telescope, at the H40α and H42α line frequencies, respectively. The red line shows the emission of the best fit SED model, corresponding to the median values of T_d, β, α, and $\log(N_{bb})$. The 68% confidence interval is depicted by the gray shaded area. The model parameters resulting from the fit are displayed on the plot.

In Fig. 4.8 we show the emission corresponding to the optically thick SED model fits, with $\nu_0 = 1500$ GHz and 5000 GHz, respectively, alongside the measured continuum emission, for NGC4102. The figures for the remaining galaxies in our sample can be found in Appendix D.1.

We adopt the median values of the T_d, β, α, and N_{bb} posterior distributions, as our results. For the uncertainties we use the 16th and 84th percentile values of these four parameters, respectively. All the resulting parameter values, from model fits to flux densities in 25" and 27" diameter circular apertures, representing the regions covered by our IRAM 30m H40α and H42α observations, are listed in Appendix D in Tables D.1 and D.2, respectively. The resulting dust temperatures of galaxies NGC0660, NGC2903, and NGC4102 are all in the range of 30-50 K, similar to global temperatures of ULIRGS in the HERUS sample (Clements et al., 2018). The dust temperature values of NGC1614, IC694, and NGC4418 are higher, in the range of 50-75 K. All temperatures increase with a decrease in ν_0. Galaxies NGC0660 and NGC2903, where the data is incomplete, exhibit the largest uncertainties in the four parameters. In the case of NGC0660, the posterior distribution of T_{dust} is double peaked, with N_{bb} having a flat-topped posterior distribution and uncertainties spanning two orders of magnitude. A mixture of different dust masses with different temperatures, as well as the presence of an AGN, are other factors that can make our single temperature models inadequate at describing the physical properties of the dust from the observed regions in these galaxies.

In Fig. 4.9 we show the posterior distribution of the four parameters resulting from the MCMC fit of the optically thin SED model to the data, as well as the best fit optically thin SED model for NGC4102. The figures for the rest of the galaxies in this sample are shown in Appendix D.2.

These figures show that the parameters of the optically thin model show similar correlation and anti-correlation relations as to those of the optically thick model. Since both models are similar, i.e., using a modified black body and a power law component, the possible causes for the correlations between the different parameters are the same as those discussed previously, for the optically thick case. The values of the four parameters, as well as their uncertainties, resulting from the optically thin SED model fits, are shown in Ap. D in Table D.3. We find that the dust temperatures, T_d, for

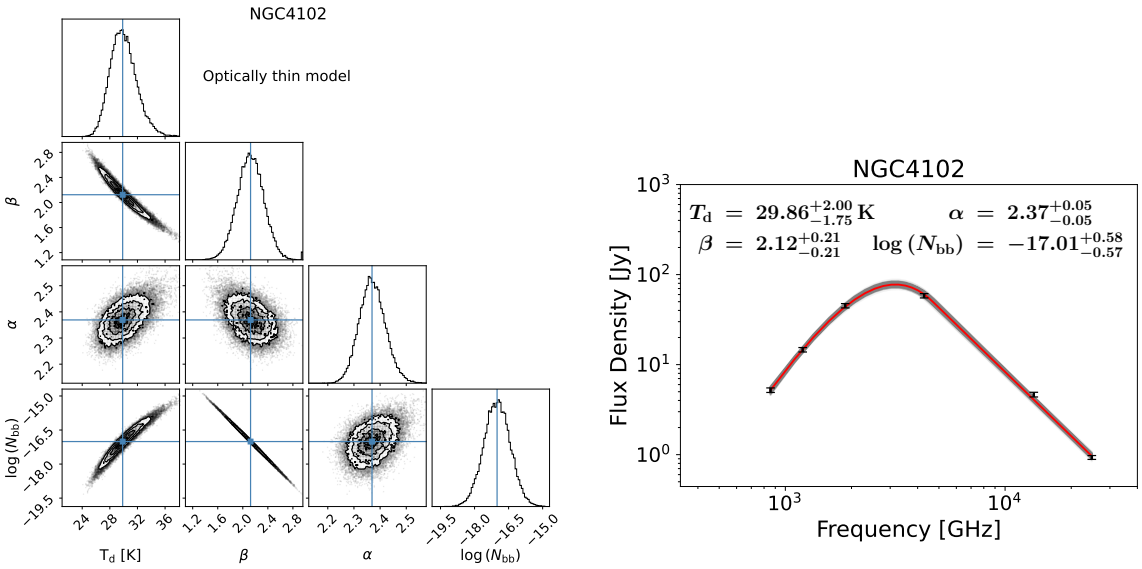

Figure 4.9: Left: The posterior distributions of the four parameters of our optically thin model, resulting from the MCMC fit of the model to the observed data. The highlights show the median values of the parameters. Right: The SED function resulting from the MCMC fit of the optically thin SED model to the continuum data. The best fit SED function is shown in red, and corresponds to the median values of the posterior distributions of T_d, β, α, and $\log(N_{bb})$, while the 68% confidence level is shown in gray.The archival continuum data is shown with black symbols.

the optically thin case, are systematically lower than those obtained for the optically thick case, for all observed regions. In the optically thin case, the dust temperatures of the observed regions are on average 5 K below the lowest temperatures resulting from the optically thick SED models.

L_{TIR} and SFR_{TIR}

The FIR luminosity, L_{FIR}, is determined using the same methods applied to the ALMA sample in Sec. 4.3, i.e. by first integrating the resulting SED between 44 and 122 μm to obtain the FIR flux. For this calculation we use the distributions of T_d, β, α, and $\log(N_{bb})$ resulting from the SED model fits. This gives a posterior distribution of L_{FIR} values for each model. We adopt the median values of these distributions, as our results, and their 16th and 84th percentile values, as our uncertainties. We calculate the SFR corresponding to each observed region, using SFR_{TIR} [$M_\odot$ yr^{-1}] = 1.49×10^{-10} ($L_{TIR}/L_\odot$) (Murphy et al., 2011), where $L_{TIR} = 1.91 \times L_{FIR}$ (Magnelli et al., 2015; Delhaize et al., 2017).

The total infrared luminosities, L_{TIR}, and star formations rates, SFR_{TIR}, of each observed region, are shown in Table D.4. Five different values of L_{TIR} are obtained for each galaxy when considering the optically thick scenario. These correspond to the five values at which ν_0 was fixed while fitting the optically thick SED models. Including the optically thin scenario, six different luminosities are obtained for each photometry aperture in each galaxy. For each galaxy and aperture, the six values of L_{TIR} and SFR_{TIR}, respectively, differ by at most 5%. This inter-model variation is comparable to the uncertainty level L_{TIR} and SFR_{TIR} resulting from any one given model fit. This consistency in the values of L_{TIR} implies that the values of the dust model parameters we obtain from our SED fitting method would reflect the actual L_{TIR}. This also indicates that the fitting procedure used here is

stable for both optically thick and optically thin models, and that for any given galaxy, the choice of a specific model has little effect on our results. Nevertheless, we rank the goodness-of-fit of each SED model using the reduced-χ^2 statistic. The best models are those with the lowest reduced-χ^2 value. We show the best-fit values of the parameters of these models, and the resulting $L_{\rm TIR}$ and $\rm SFR_{TIR}$, in Table 4.5. For each galaxy, we present the average between the results obtained from the 25" and the 27" diameter photometric apertures, respectively, as there is no significant difference between the results corresponding to the two aperture diameters. SED models that best fit the measured emission are all optically thick, having $\nu = 1500$ [GHz], with the exception of NGC2903, where the best fit model corresponds to $\nu_0 = 3000$ [GHz].

Comparison with previous Results

We have used SED models, having a powerlaw and a single temperature MBB component, to characterize the dust emission form the observed galaxies. We find high values for the dust temperatures in three of the observed regions, namely in NGC1614, IC694, and NGC4418 we find $T_{\rm d}$ values between 70 and 80 K. In the case of NGC1614, the dust temperature value of 35 K found in the literature (Xu et al., 2015), an average for the whole galaxy, is lower than our own value of 68 K. A two temperature dust model of the global dust emission from Arp299, which includes both IC694 and NGC3690, finds a warm dust component with a temperature of 58 K (Lanz et al., 2013), which is lower than our result of 73 K for the central region of IC694. In the case of NGC4418, the dust temperature of the nucleus, estimated from MIR subarcsecond resolution images, is of the order of 85 K (Evans et al., 2003). With Herschel FIR spectroscopy, González-Alfonso et al. (2012) find the temperature of the inner 9" nuclear region to be 85 – 110 K (González-Alfonso et al., 2012). Observations covering a subarcsecond diameter region in the nucleus of the NGC4418, at a wavelength of 1 mm, place a lower limit on the dust temperature at 70 K (Costagliola et al., 2013). Submillimeter continuum observations of this galaxy at wavelengths longer than 350 μm reveal an average dust temperature of 62 ± 12 K (Yang et al., 2007). These values are comparable our own estimate of 77 K. Previous estimates of the average dust temperature in NGC0660 have values of 31-37 K, and were calculated using the total continuum emission of this galaxy at submillimeter and FIR wavelengths (Stevens et al., 2005; Gao & Solomon, 2004). These values are lower than our result of 52 K for the inner 25"-27" diameter region of this galaxy. For NGC2903 a previous estimate using global submillimeter and FIR observaions put the average warm dust temperature of this galaxy 28 K (Stevens et al., 2005), which is lower but in agreement with our own value of 34 K, given the uncertainties. In the case of NGC4102, submillimeter continuum observations were used to estimate a global average dust temperature value of 32 K (Yang et al., 2007), lower than our own value of 52 K.

A comparison with literature values is difficult to make, as most estimates of the dust temperatures in these galaxies cover vastly different scales from our own. Our results, together with results from the literature presented here, show that for our sample the values of the dust temperature estimates depends on the extent of the region covered by observations. Overall, for a given galaxy, the average dust temperature measured using observations that cover regions more extended than our own has values which are lower than our estimates, the opposite being true for more compact regions. The reason for this effect is that the dust in the central or star-forming regions of galaxies is in a region with higher stellar density, and heated more than dust farther from the center, at higher galactic radii. This observed decrease in dust temperature with an increase in distance from the nucleus of galaxies is confirmed by observations (e.g. Bothun & Rogers, 1992; Galametz et al., 2012; Hunt et al., 2015;

Galaxy	Best Fitting SED Model		Results	
	Parameters		$\log(L_{\rm TIR}/L_\odot)$	$\mathrm{SFR}_{\rm TIR}[M_\odot\,\mathrm{yr}^{-1}]$
NGC0660	$T_{\rm d}$ [K]	$51.93^{+13.16}_{-8.10}$	$9.85^{+0.14}_{-0.13}$	$1.05^{+0.34}_{-0.32}$
	β	$1.32^{+0.50}_{-0.67}$		
	α	$2.25^{+0.16}_{-0.17}$		
	$N_{\rm bb}$	$-10.65^{+0.36}_{-0.49}$		
	ν_0[GHz]	1500		
NGC1614	$T_{\rm d}$ [K]	$69.26^{+2.06}_{-2.19}$	$11.66^{+0.02}_{-0.02}$	$68.50^{+2.56}_{-2.61}$
	β	$2.13^{+0.15}_{-0.15}$		
	α	$2.62^{+0.11}_{-0.11}$		
	$N_{\rm bb}$	$-11.18^{+0.04}_{-0.03}$		
	ν_0[GHz]	1500		
NGC2903	$T_{\rm d}$ [K]	$34.35^{+5.61}_{-5.69}$	$9.65^{+0.05}_{-0.05}$	$0.66^{+0.08}_{-0.07}$
	β	$1.91^{+0.38}_{-0.30}$		
	α	$1.95^{+0.08}_{-0.08}$		
	$N_{\rm bb}$	$-10.06^{+0.44}_{-0.35}$		
	ν_0[GHz]	3000		
IC694	$T_{\rm d}$ [K]	$73.00^{+1.63}_{-1.78}$	$11.79^{+0.01}_{-0.01}$	$92.47^{+3.02}_{-3.15}$
	β	$2.20^{+0.15}_{-0.15}$		
	α	$3.40^{+0.12}_{-0.13}$		
	$N_{\rm bb}$	$-10.88^{+0.03}_{-0.03}$		
	ν_0[GHz]	1500		
NGC4102	$T_{\rm d}$ [K]	$52.38^{+1.56}_{-1.52}$	$10.61^{+0.02}_{-0.02}$	$6.00^{+0.29}_{-0.28}$
	β	$2.15^{+0.16}_{-0.16}$		
	α	$2.51^{+0.08}_{-0.07}$		
	$N_{\rm bb}$	$-10.59^{+0.04}_{-0.04}$		
	ν_0[GHz]	1500		
NGC4418	$T_{\rm d}$ [K]	$77.57^{+1.61}_{-1.78}$	$11.12^{+0.01}_{-0.01}$	$19.56^{+0.58}_{-0.63}$
	β	$1.67^{+0.13}_{-0.13}$		
	α	$3.31^{+0.13}_{-0.13}$		
	$N_{\rm bb}$	$-11.29^{+0.03}_{-0.02}$		
	ν_0[GHz]	1500		

Table 4.5: The final results of the SED model fitting. The values, for each parameter, are taken as average between the results given by fits to data measured with the 25" and 27" diameter photometric apertures.

Abdurro'uf et al., 2022).

We also compare our SFR_{TIR} values with previous results in the literature. Because different luminosity distances have been used by various authors for the same galaxy, the SFR quoted here have been corrected to correspond to the luminosity distances used in this work. The total SFR in NGC0660 was estimated by De Looze et al. (2011) at 0.61 ± 0.22 and $0.85 \pm 0.17\, M_\odot\, yr^{-1}$, based on MIPS 24$\mu$m and GALEX UV data, and the conversion factors from Rieke et al. (2009) and Kennicutt et al. (2009), respectively. This is somewhat lower but still in agreement with our value of $1.05^{+0.34}_{-0.32}\, M_\odot\, yr^{-1}$. For NGC1614, a SFR of $58\, M_\odot\, yr^{-1}$ has been estimated using the L_{FIR} determined from IRAS fluxes (Alonso-Herrero et al., 2001b; Olsson et al., 2010), lower than our value of $68.50^{+2.56}_{-2.61}\, M_\odot\, yr^{-1}$. Using NIR and Pa$\alpha$ observations, Alonso-Herrero et al. (2001c) report a SFR of $0.85\, M_\odot\, yr^{-1}$ in the inner 42" of NGC2903, higher than our value of $0.66^{+0.08}_{-0.07}$. Using the L_{TIR} measurements of Armus et al. (2009) based on IRAS data Sanders et al. (2004), the SFR for Arp299, which contains IC694 and NGC3690, can be estimated to be $126\, M_\odot\, yr^{-1}$, using the L_{TIR} to SFR_{TIR} conversion factor of Murphy et al. (2011). Previous observations show that IC694 makes up 63% of the L_{FIR} of Arp299 (Alonso-Herrero et al., 2000), giving a rough estimate of SFR$\simeq 80\, M_\odot\, yr^{-1}$ in IC694, lower, but comparable to our result of $92.47^{+3.02}_{-3.15}\, M_\odot\, yr^{-1}$. For NGC4102, De Looze et al. (2014) calculate a SFR value of $\sim 7.5\, M_\odot\, yr^{-1}$, using FIR ISO data Brauher et al. (2008). Using radio continuum data, Jogee et al. (2005) estimate the SFR in the inner 24" of NGC4102 to be $7\, M_\odot\, yr^{-1}$, comparable to our result of $6.00^{+0.29}_{-0.28}\, M_\odot\, yr^{-1}$. Calculating the FIR luminosity from 80 μm IRAS observations (Soifer et al., 1989), Jogee et al. (2005) find the total SFR in NGC 4102 to have a value of $13.8\, M_\odot\, yr^{-1}$. In the case of NGC4418 Sakamoto et al. (2013) estimate the SFR at $30\, M_\odot\, yr^{-1}$ using radio continuum SMA observations, and at $15\, M_\odot\, yr^{-1}$ using the IRAS derived IR luminosity, the two values bracketing our result of $19.56^{+0.58}_{-0.63}\, M_\odot\, yr^{-1}$.

As in the case of the dust parameters, a direct comparison between these results and our own is difficult to make because the SFR found in the literature use the L_{TIR} of the whole galaxy, different initial mass functions, different luminosity-SFR conversion factors, or different SFR tracers altogether. Nevertheless, despite these shortcomings, our SFR_{TIR} values shown in Table 4.6 are within ~15% of the literature estimates.

4.4 Comparing SFR_{mm-RL} and SFR_{TIR}

In this section we compare the SFR resulting from the mm-RL to the SFR resulting from the dust emission for the galaxies in our sample. The latter is a well established and widely used SFR tracer (e.g. Galametz et al., 2012; Kennicutt & Evans, 2012). Agreement between the SFR using the two tracers, i.e., a one-to-one correlation, would be a strong indication that mm-RL are a reliable tracer of SFR.

4.4.1 Small Spatial Scales

Extragalactic Observations

The extragalactic ALMA observations resolve the mm-RL emission on subkpc spatial scales, the apertures used for measuring the mm-RL emission and $SFR_{n\alpha}$ having areas between 0.02 and 0.6 kpc^2. An exception is the aperture used to measure the total mm-RL in NGC3256, which has an area of $\sim 1.7\, kpc^2$.

From the ALMA sample, only seven galaxies had available data for determining both $SFR_{n\alpha}$ and SFR_{TIR}. In figure 4.10 we show the relation between $SFR_{n\alpha}$ with SFR_{TIR} for the regions observed in these seven galaxies. We find that, within the uncertainties, the mm-RL-based SFR are in agreement with the submm-flux-density-based ones. This may not come as a surprise, as both measures should trace the same source of energy, i.e., massive stars. The more interesting aspect of this plot is the nature of scatter.

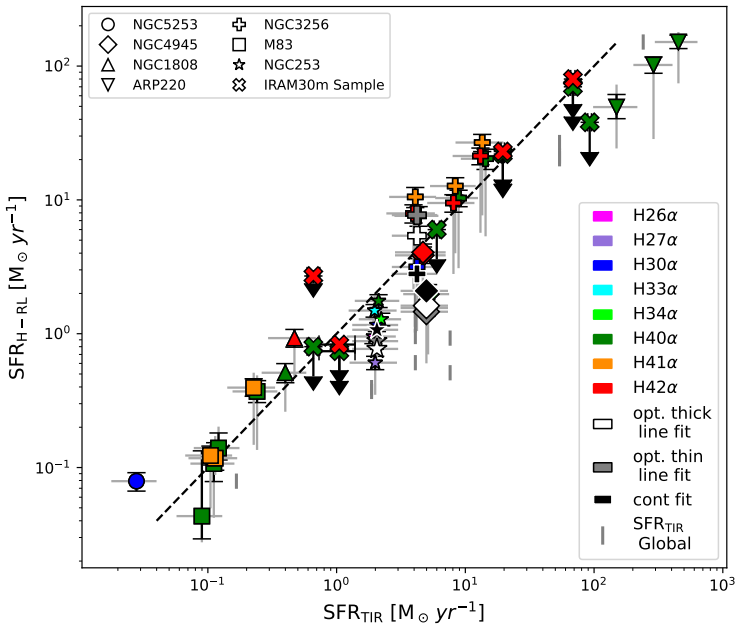

Figure 4.10: SFR_{mm-RL} compared to SFR_{TIR} for the ALMA sample. Colored symbols correspond to measurements from single transition lines, assuming optically thin emission and $n_e = 10^3\,cm^{-3}$. For three galaxies, white and grey symbols correspond to SFR resulting from line intensity fits for the optically thick and optically thin cases, respectively. For these galaxies, black symbols correspond to SFR resulting from fits to the free-free continuum. The dashed line is the unity relation. Vertical open error bars mark the uncertainty deriving from SED fits to the synchrotron and dust emissivity indices, while the capped error ranges assume priors on these indices. Horizontal error bars correspond to the uncertainties resulting from the MBB fit to ALMA submm observations, where we adopt the normally distributed priors: $\beta = 1.73 \pm 0.22$ and $T_{dust} = 37.9 \pm 4.7\,K$ (Clements et al., 2018). The vertical grey bars show the total SFR_{mm-RRL} of each galaxy, as a function of their global SFR_{TIR}, given by the galaxy-wide-integrated FIR luminosities reported by Sanders et al. (2004). Thus, they are simply offset horizontally from the datapoints showing the sum of SFR_{mm-RRL} and SFR_{TIR} for the each galaxy in the ALMA sample.

Systematic uncertainties deriving from the effects of optical depth on the line intensities may account for a factor two in the SFR, as indicated by the scatter between different line measurements in the same region and the difference between optically thin and optically thick cases in regions with multiple line measurements. When gas temperatures are computed from line and free-free measurements, those introduce larger uncertainties, which is due to the difficulty in decomposing the radio, free-free, and dust emission components.

This is particularly severe for sources with a flat radio synchrotron SED. It may not be unreasonable

to set the gas temperature to a reasonable range of 4000 − 8000 K, as found by Quireza et al. (2006b) for the inner Milky Way, instead of trying a derivation. This range may be narrowed by using priors on metallicity (Deharveng et al., 2000; Esteban et al., 2005). The relative uncertainties in the SFR_{TIR}, here derived only from submm continuum ALMA observations, can reach values of up to $\sim 50\%$. This is due to a lack of constraints on the dust SED at FIR wavelengths. At the spatial resolution of interferometers, prospects are meek to improve on this significantly, as it would require observations at frequencies that cover the SED peak, which are currently challenging with ground-based instruments. The star formation history can also introduce a dispersion between the two SFR indicators, because the mm-RL emission traces SFR on shorter-time scales than the FIR emission (see Sec. 1.3.2).

As an additional check, the global SFR_{TIR} for each galaxy, determined from the global L_{FIR} obtained using lower resolution FIR observations from Sanders et al. (2004) is also calculated. The SFR corresponding to individual regions of these galaxies, cannot exceed these SFR_{TIR} global values. We find that none of the SFR_{mm-RRL} of the regions studied here exceed the global SFR_{TIR} values. With the exception of Arp220, none of the SFR_{TIR} for the regions in this sample exceed the global SFR_{TIR} values.

Including Galactic Observations

We extend the analysis of the extragalactic SFR_{TIR} and SFR_{mm-RRL} correlation at small scales by including mm-RL data for galactic star-forming regions. One of the largest coherent samples of mm and submm-RL observations is provided by Kim et al. (2017) and Kim et al. (2018), respectively, who observed high-mass star-forming clouds found in the ATLASGAL survey (Schuller et al., 2009), using APEX, the IRAM 30m and Mopra (Urquhart et al., 2010) telescopes, covering multiple transitions from H25α to H42α. At these frequencies, these telescopes have a resolution of 15" $\sim$ 30" (Kim et al., 2017). At the distances reported for these star-forming regions, this corresponds to physical areas of $\lesssim 1\,pc^2$ (Kim et al., 2017, 2018). The number of sources with detected mm-RL or submm-RL emission in the ATLASGAL sample is 178 (Kim et al., 2017, 2018).

Examining the H41α and H42α fluxes reported by Kim et al. (2017) we noticed that the IRAM line fluxes are generally $\approx$1.5 times lower than those measured with Mopra. A likely cause of this discrepancy lies in the different beam sizes. If the mm-RL emission is more extended than the Mopra beam, the IRAM 30m telescope with a beam FWHM of 29" would observe a lower flux than the Mopra telescope, which has a beam FWHM of 36". Because the observed flux is proportional to the beam area, the flux observed by Mopra would be a factor $(36/29)^2 \sim 1.54$ higher than that observed by IRAM. In order to obtain a more accurate estimate of this factor, the beams of the IRAM 30m and Mopra telescopes are modeled as circularly symmetric 2D Gaussian functions, using the `astropy` `Gaussian2D` function, with FWHM values of 29" and 36", respectively. Using these two models, we calculate the ratios between the fluxes collected by the two telescopes, and recover the $\sim$ 1.54 value. We multiply the IRAM fluxes with this correction factor, eliminating the discrepancy.

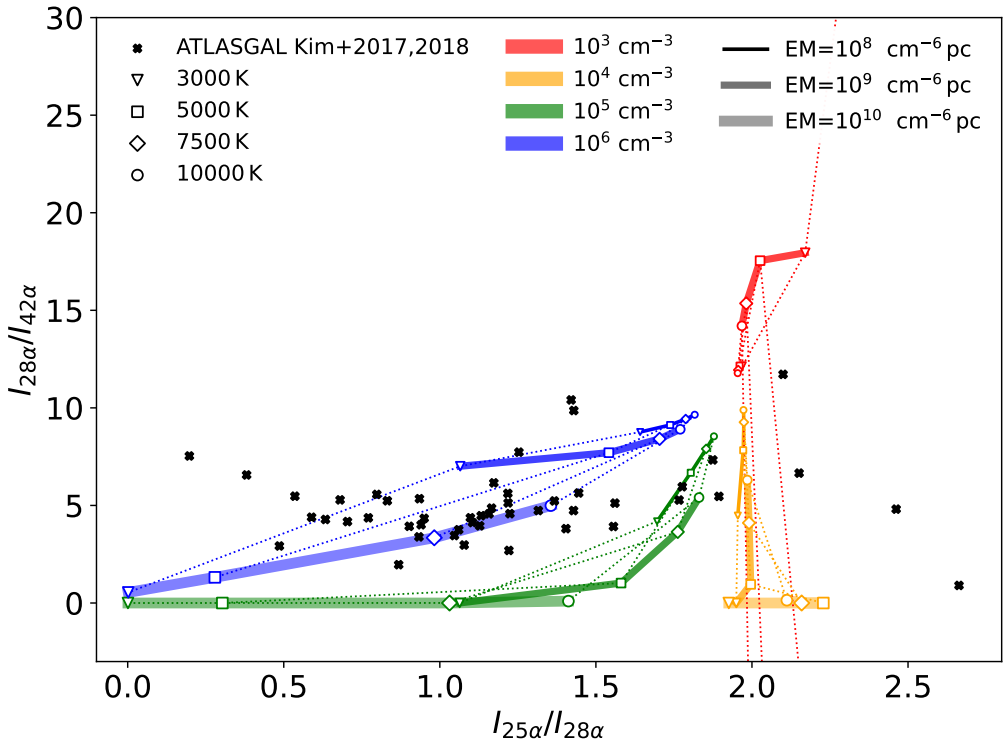

Figure 4.11: The H25α/H28α and H28α/H42α line ratios for 49 sources from the ATLASGAL sample (Kim et al., 2017, 2018) together with the theoretical values inferred using the relations presented in Chapter 3. The colors represent the densities, line thickness represents the emission measure, symbols represent the temperature, while the dotted lines connect the ratios resulting from emission at the same temperatures.

As explained in Chapter 3, submm-RL line ratios can be used to probe the conditions of the ionized gas and identify optically thick emission or masing. The relation between mm-RL line intensity ratios for the H25α, H28α, and H42α lines, for the ATLASGAL sample, is shown in Fig. 4.11 that is similar to that developed in Chapter 3 for the study of optical depth effects. Only 49 sources have measurements for all these three lines. The theoretical values are also shown, and are calculated using the relations in Chapter 3, for both optically thin and optically thick emission, and a range of densities and temperatures. Figure 4.11 reveals that the submm- and mm-RL emission from a significant part of the shown ATLASGAL sources deviates from the theoretical values expected for optically thin emission, which would lie in the area of the graph corresponding to the lowest EM. The line ratio values have a higher variance along the x-axis, corresponding to the H25α/H28α ratio, than along the y-axis. This covers a wide range of possible temperatures and EM values. Most of the line ratios are consistent with $n_e \sim 10^5 - 10^6$ cm^{-3} and $EM \gtrsim 10^9$ cm^6 pc^{-1}, with some clustering observed around the $n_e \sim 10^6$ cm^{-3} branches.

This is consistent with our results for the electron density in NGC253 and NGC3256B, where the line intensities were also best explained by an optically thick emission, with the ionized gas having $T_e \sim 10000$ K, $n_e \sim 10^5$ cm^{-3}. Because of this, we conclude that optically thick emission, together with line amplification and attenuation, should be taken into account when calculating SFR$_{\rm mm-RRL}$. However, unless multiple mm-RL are observed, quantifying these effects remains very challenging. For

this reason, we consider optically thin emission when calculating the SFR_{mm-RRL} of the ATLASGAL sample.

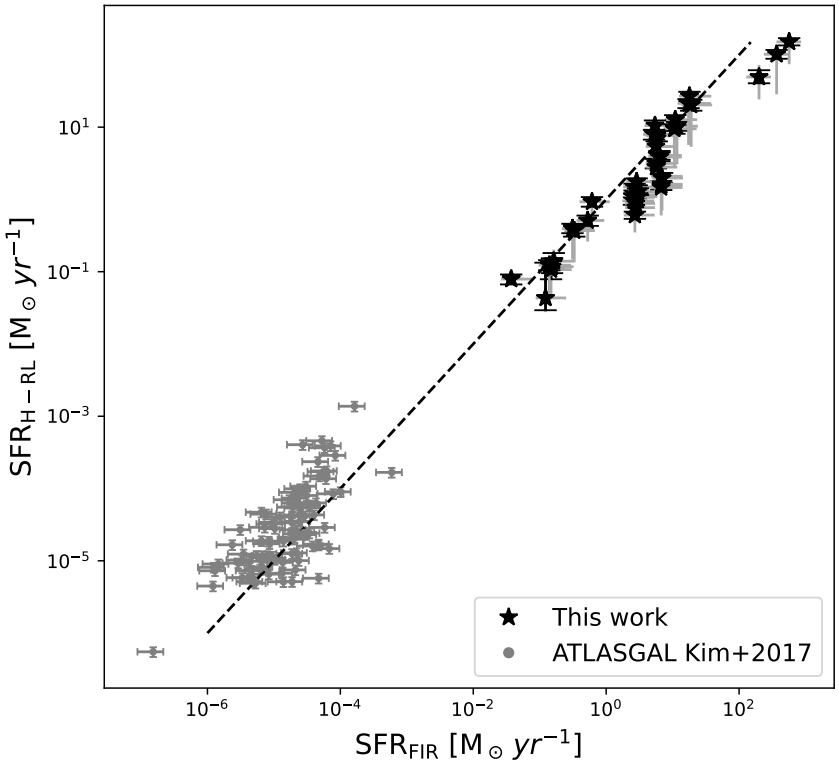

Figure 4.12: SFR_{mm-RL} compared to SFR_{TIR} for the extragalactic sample analyzed in this work and the ATLASGAL sample of massive star-forming regions (Kim et al., 2017, 2018). The black symbols indicate the extragalactic sample, while the grey symbols indicate the ATLASGAL sample H42α line detections (Kim et al., 2017). The uncertainties in the extragalactic sample are the same as in Fig. 4.10. The uncertainties in $SFR_{42\alpha}$ for the ATLASGAL sample arise from the adopted 20% relative uncertainty in electron temperature. For the same sample, the reported relative uncertainties in SFR_{TIR} are 42% (Schuller et al., 2009). The dotted black line indicates a 1:1 correlation.

For consistency, the H42α line is used to determine the SFR_{mm-RRL} of the ATLASGAL sources, as it has the most detections (Kim et al., 2017, 2018), and it is also detected in several galaxies in the ALMA sample. The H41α line intensities are overall consistent with the H42α intensities. Out of the ATLASGAL sample, 95 galactic sources have both H42α detections and a distance estimate, which are needed for determining the SFR. The SFR_{mm-RL} of the ATLASGAL sources is calculated using equation 3.15, using the same assumptions as for the extragalactic sources where no temperature estimate was possible, i.e., we assume optically thin emission from HII regions with homogeneous density and temperature, having $T_e = 5000 \pm 1000$ K. We derive the SFR_{FIR} for these sources from bolometric luminosities provided by Kim et al. (2017); Schuller et al. (2009) and 42% uncertainties (Schuller et al., 2009), using the Murphy et al. (2011) luminosity to SFR conversion relation. The SFR_{mm-RL} as a function of SFR_{FIR}, for the ATLASGAL sample and the galaxies in this work, are shown in Fig. 4.12, where the two SFR values seem to follow a one-to-one correlation over multiple

orders of magnitude.

We evaluate the correlation between SFR_{mm-RRL} and SFR_{TIR} by performing a linear fit of between these two quantities. The data is fit with a powerlaw relation, having the form $y = b \times x^a$, which has a linear form in logarithmic space, i.e. $\log(y) = \log(b) + a \times \log(x)$. Because both the x and the y quantities, i.e., SFR_{mm-RRL} and SFR_{TIR}, have associated uncertainties, orthogonal distance regression was used for fitting. This was performed using the `odr` submodule (Boggs & Rogers, 1990) from the `scipy` python package (Virtanen et al., 2020).

The fit is first performed using only the extragalactic data, where only the total SFR is considered for each galaxy. We find $a = 0.93 \pm 0.06$ and $b = 1.04 \pm 0.16$. If a pure powerlaw is used, where we fix $b = 1$, the resulting fit yields $a = 0.94 \pm 0.06$. These values of a agree, within the uncertainties, with the unity value expected from a one to one correlation between SFR_{mm-RRL} and SFR_{TIR}. Including the galactic sample does not change our results, resulting in a slope of $a = 0.94 \pm 0.02$. The fact that the galactic sample is much larger than the extragalactic one could introduce a bias. We thus perform the fit using a single value for the galactic regions, by averaging all the galactic SFR values. This also has no significant impact on the value of the slope, resulting in a value of $a = 0.93 \pm 0.06$.

We also attempt to determine the effect of overestimating the SFR_{TIR} for NGC4945 and Arp220, where our estimates exceed the global values estimated using FIR measurements from *Sanderset al.* (2004). We repeat the fitting procedure where the SFR_{TIR} for these two galaxies is replaced by their global values. Using this correction, and only the extragalactic sample, the slope has a value of $a = 1.01 \pm 0.09$, with $b = 1.3 \pm 0.2$. This correction represents only $\sim 6\%$ change in the slope value from our original calculation. Repeating the fit using the full galactic sample, and its average, respectively, has no significant impact on the fit, with resulting slope values of $a = 0.95 \pm 0.02$ and $a = 1.00 \pm 0.09$, respectively.

Thus, the SFR_{FIR} to SFR_{mm-RL} relation agrees with the one-to-one relation of the extragalactic objects, showing this relation holds over eight orders of magnitude. Amplification or attenuation of mm-RL lines and the absence of FIR data can lead to disagreements between the SFR_{FIR} and SFR_{mm-RL}, respectively, of individual regions. Furthermore, because mm-RL trace recent SFR, averaged over the past ~ 10 Myr, while FIR emission traces SFR averaged over the previous ~ 100 Myr the SFH can also influence the SFR_{FIR} to SFR_{mm-RL} relation.

4.4.2 Large Spatial Scales

The IRAM sample covers larger spatial scales than the ALMA sample, of the order of $0.77 \sim 53\,\mathrm{kpc}^2$. In Fig. 4.13 we show the SFR_{mm-RRL} and SFR_{TIR} data for the smaller, subkpc, spatial scales, together with the IRAM data. Because no mm-RL are detected for the galaxies in the IRAM30m sample, only upper limits were placed on the SFR_{mm-RRL}, and we do not perform a direct analysis of the SFR_{mm-RRL} and SFR_{TIR} correlation with this data. Instead, a more limited analysis is performed, aiming to establish if the upper limits we placed on the SFR_{mm-RRL} are in agreement with the measured values for SFR_{TIR}.

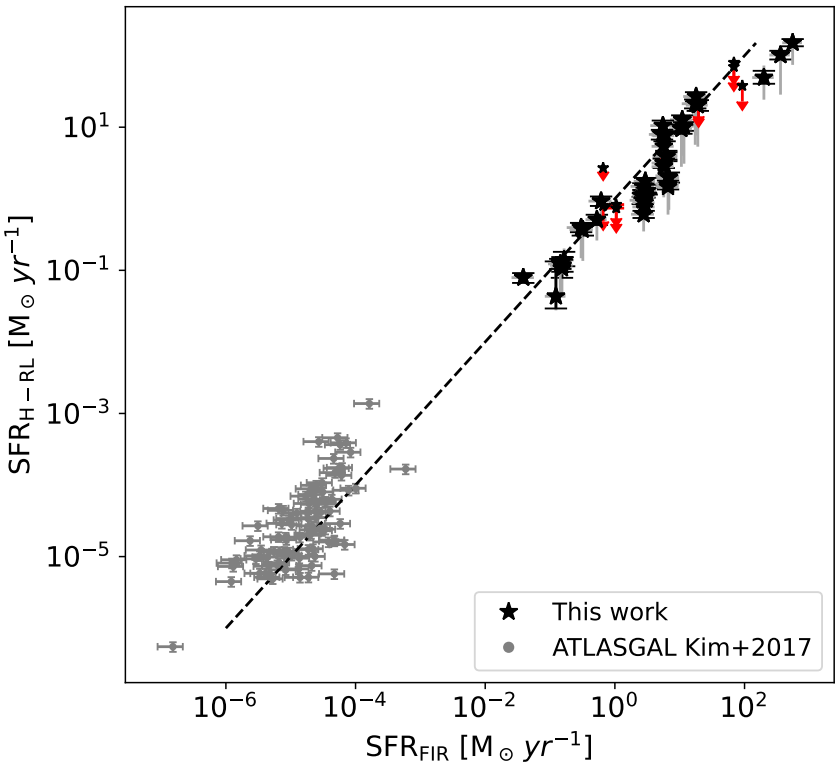

Figure 4.13: SFR_{mm-RL} compared to SFR_{TIR}. The black symbols indicate the data from this work, including the ALMA archival sample and the IRAM30m sample. The upper limits of the IRAM30m sample are indicated by the red arrows. The grey symbols indicate the ATLASGAL sample H42α line detections (Kim et al., 2017, 2018). The uncertainties in the extragalactic sample are the same as in Fig. 4.10. The uncertainties in $SFR_{42\alpha}$ for the ATLSAGAL sample arise from the adopted 20% relative uncertainty in electron temperature. For the same sample, the reported relative uncertainties in SFR_{TIR} are 42% (Schuller et al., 2009). The dotted black line indicates a 1:1 correlation.

We list the values of SFR_{mm-RRL} and SFR_{TIR} in table 4.6. The upper limits on SFR_{mm-RL} correspond to a 3σ confidence level. These upper limits agree with SFR_{TIR} for most of the galaxies in our sample, with the exception of IC694. For this galaxy, the values of $SFR_{H40\alpha}$ and $SFR_{H42\alpha}$, respectively, are significantly lower than SFR_{TIR}. These observed discrepancies can arise due to several reasons, such as the contamination of a SFR tracer with emission caused by non-star-forming activity, or a variation in the SFR over timescales that affect only one of the two tracers used here. By performing integral field spectroscopy (IFS) observations with the INTEGRAL instrument on the William Herschel Telescope (WHT), García-Marín et al. (2006) studied the young stellar population in Arp299. By observing the Hα/Hβ and Paα/Haα line ratios of star-forming regions and bright star clusters, they calculate the extinction corrected $H\alpha$ luminosity. The sum of the extinction-corrected Hα luminosities given by García-Marín et al. (2006) for the star-forming regions and star-clusters in the inner 15" of IC694 is $L_{H\alpha}$ 3.4×10^{44} erg s^{-1}. Using the $L_{H\alpha}$ to SFR conversion factor from Murphy et al. (2011) with a Kroupa IMF (Kroupa, 2001), we find $SFR_{H\alpha}$ 21 $M_\odot$ yr^{-1}. This value corresponds to the recent SFR, as they use extinction-corrected optical RL, and agrees with the upper

Galaxy	$SFR_{H42\alpha}$	$SFR_{H40\alpha}$	SFR_{TIR}
	$[M_\odot\ yr^{-1}]$	$[M_\odot\ yr^{-1}]$	$[M_\odot\ yr^{-1}]$
NGC0660	<0.83	<0.74	$1.05^{+0.34}_{-0.32}$
NGC1614	<80	<70	$68.50^{+2.56}_{-2.61}$
NGC2903	<2.7	<0.80	$0.66^{+0.08}_{-0.07}$
IC694	–	<38	$92.47^{+3.02}_{-3.15}$
NGC4102	–	<6.0	$6.00^{+0.29}_{-0.28}$
NGC4418	<23	<22	$19.56^{+0.58}_{-0.63}$

Table 4.6: SFR in the galaxies we observed with the IRAM 30m telescope. Both SFR_{mm-RL}, in columns two and three, as well as SFR_{TIR}, in column four, correspond to the same region in each galaxy. The upper limit values correspond to the 3σ confidence level.

limits on the SFR derived from our H40α observations.

4.5 Millimeter Recombination Lines Probing Star Formation History

The difference between the timescales probed by the IR and mm-RL emission implies that these two tracers agree only in the case of steady star formation over the past 100 Myr. Using SFH from the second generation cosmological zoom-in simulation Feedback in Realistic Environments (FIRE-2), Flores Velázquez et al. (2021) analyzed the SF timescales probed by the FUV and H-α luminosities of galaxies with halo masses of $10^9 - 10^{12}\,M_\odot$. In their work they compare the true SFR at time t with the ones traced by the Hα and FUV luminosities, $L_{FUV}(t)$ and $L_{H\alpha}(t)$. For constant SFH beginning at a time $t = 0$, both luminosities increase with t and eventually reach a steady state, defined by Flores Velázquez et al. (2021) as the luminosities at $t \longrightarrow \infty$. These luminosities reach 90% of $L(t \longrightarrow \infty)$ at 100 Myr for FUV and 10 Myr for Hα, respectively (Flores Velázquez et al., 2021). Flores Velázquez et al. (2021) also investigate over what are the minimum timescales, t^{min}_{avg} the real SFR should be averaged for it to best match the SFR given by the FUV and Hα tracers. They find that for steady and bursty SFH, the timescales for the Hα tracer is the same, at $t^{min}_{avg} \approx 5$ Myr. However, for the FUV tracer, there is a significant difference between bursty and steady state SFH. Namely, the timescale for the FUV tracer is $t^{min}_{avg} \approx 10$ Myr for the steady-state case and $t^{min}_{avg} \approx 100$ Myr for the bursty case. Thus, using the H_α to FUV luminosity ratio, one can determine the age of the massive stellar population, and whether the SFR changed in the past 100 Myr.

In the presence of dust, which is easily heated by absorbing UV photons from massive young stars, both FIR and UV/FUV luminosities are needed to determine the full SFR averaged over the last 100 Myr:

$$SFR^{100\,Myr}_{tot} = SFR_{UV} + SFR_{TIR}, \tag{4.16}$$

where we assume that any stellar UV photons that do not escape the SF region are absorbed by dust, thus FIR emission determining SFR over a similar timescale as UV emission. For the short scale time formation, SFR_{mm-RL} is used:

$$SFR^{10\,Myr}_{tot} = SFR_{mm-RL}, \tag{4.17}$$

where we assume that all hydrogen mm-RL emission originates from gas ionized by O-type stars. The relative values of $SFR^{10\,Myr}_{tot}$ and $SFR^{100\,Myr}_{tot}$ then indicate the recent star formation history. The SF

regions where this analysis is possible require mm-RL, FIR, and UV observations. From our sample, only NGC3256, NGC5253, NGC1808, NGC253, Arp220, and M83 satisfy all these conditions. The mm-RL and FIR observations of these galaxies have been described in section 4, while here we present a possible analysis of their UV emission and subsequently, their SFH.

Data from the Galactic Evolution Explorer (GALEX) telescope is used to obtain the (F)UV luminosities and SFR, and is presented in Chapter 2. Converting $L_{\rm FUV}$, shown in table 2.6, to $\rm SFR_{UV}$ is done following Hao et al. (2011):

$$\left[\frac{\rm SFR_{UV}}{\rm M_\odot\,yr^{-1}}\right] = 10^{-43.35} \times \left[\frac{\lambda}{\mathring{\rm A}}\right]\left[\frac{L_{\rm FUV}}{\rm erg\,s^{-1}\,\mathring{A}^{-1}}\right] \tag{4.18}$$

assuming a Kroupa IMF (Kroupa, 2001) with a steady SFR over the past 100 Myr. For NUV luminosities, the conversion factor in the equation above is $10^{-43.17}$ (Hao et al., 2011). Table 4.7 shows the UV, FIR, and mm-RL derived SFR for galaxies where data at these wavelengths was available. All the regions in the table have a negligible $\rm SFR_{UV}$ compared to $\rm SFR_{FIR}$, with $\rm SFR_{UV}/SFR_{TIR} \lesssim 0.001$. The only exception is NGC5253 which has $\rm SFR_{UV}/SFR_{TIR} \approx 0.02$. Since for NGC5253 the smallest possible aperture, having the size of the GALEX PSF – approximately 30 times larger than the aperture used to measure the mm-RL line emission – is used to extract the UV flux, that ratio is an upper limit. This suggests that the UV escape fraction from all these regions is close to zero, and that $\rm SFR_{tot}^{100\,Myr} \approx SFR_{FIR}$ is a reasonable assumption.

Target	$\rm SFR_{mm-RL}$	$\rm SFR_{TIR}$	$\rm SFR_{UV}$	$\rm SFR_{tot}^{100\,Myr}$	$\rm SFH_{100}^{10}$
	$[M_\odot\,\rm yr^{-1}]$	$[M_\odot\,\rm yr^{-1}]$	$[M_\odot\,\rm yr^{-1}]$		
NGC3256 T	20.3 ± 3.6	18^{+8}_{-7}	0.068 ± 0.003	18	1.1 ± 0.5
NGC5253 T	0.07 ± 0.01	$0.04^{+0.02}_{-0.01}$	$(15.2 \pm 0.7) \times 10^{-4}$	0.042	1.7 ± 0.7
NGC1808 A	0.52 ± 0.09	$0.5^{+0.2}_{-0.1}$	$(9.8 \pm 0.9) \times 10^{-5}$	0.5	1.1 ± 0.3
NGC1808 B	0.93 ± 0.15	$0.7^{+0.3}_{-0.2}$	$(21.9 \pm 1.5) \times 10^{-5}$	0.7	1.2 ± 0.6
NGC253 7m	0.77 ± 0.08	$2.9^{+1.2}_{-1.0}$	$(24.5 \pm 2.1) \times 10^{-5}$	2.9	0.3 ± 0.1
Arp220 T	150 ± 14	240	0.061 ± 0.008	~ 240	< 0.6
M83 T	0.37 ± 0.07	$0.3^{+0.1}_{-0.1}$	0.0089 ± 0.0004	0.3	1.2 ± 0.5

Table 4.7: Sample of regions where the SFR could be measured using mm-RL, TIR, and UV data. To remove any effects of our possible overestimation of the $\rm SFR_{TIR}$ in Arp220, here we use the $\rm SFR_{tot}^{100\,Myr}$ derived by Anantharamaiah et al. (2000) as a conservative upper limit.

We investigate the SFH of our sample by comparing recent star formation, averaged of the last $\sim$ 10 Myr, traced by mm-RL, and star formation averaged over the last 100 Myr, traced by FIR emission. In the last column of table 4.7 we show the ratio $\rm SFH_{10}^{100} = SFR^{10\,Myr}/SFR_{tot}^{100\,Myr} = SFR_{mm-RL}/SFR_{TIR}$. This ratio is illustrated in Figure 4.14. For the majority of regions, $\rm SFH_{10}^{100} \approx 1$. This means that SFR averaged over the last 10 and 100 Myr have the same value, i.e. star formation has been steady and ongoing for the past 100 Myr. A $\rm SFH_{10}^{100}$ value greater than unity means that the SFR averaged over the past 10 Myr is higher than the one averaged of the last 100 Myr. The only region in our analysis where this is clearly the case is NGC5253, with $\rm SFH_{10}^{100} = 1.7 \pm 0.7$. Our result is confirmed by other observations which show the young star formation activity in the central region

of NGC5253 (e.g. Calzetti et al., 2015; de Grijs et al., 2013; Pellerin & Robert, 2007; Calzetti et al., 1997).

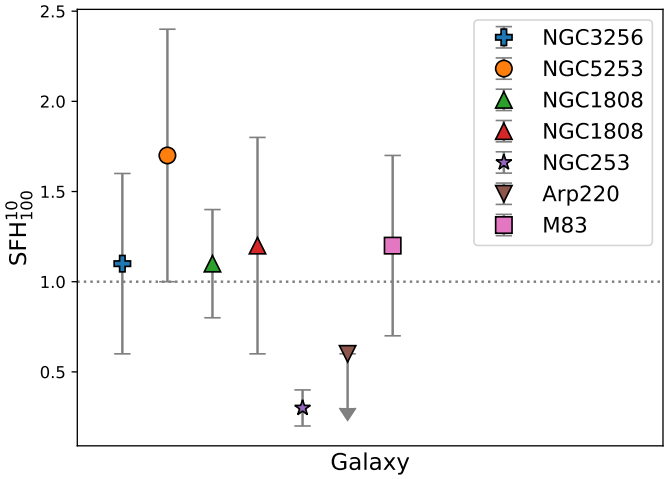

Figure 4.14: The values SFH_{10}^{100} for each galaxy where data was available to perform this analysis. It illustrates the ratio between recent star formation, averaged of the last ~ 10 Myr, traced by mm-RL, and star formation averaged over the last 100 Myr, traced by FIR emission. The unity value, indicated by the dotted line, indicates that the SFR has not change between the two timescales. A value above unity indicates that recent SFR has increased, and the average SFR over the past 10 Myr is higher than that averaged over the past 100 Myr. The reverse is true for values below unity.

When SFH_{10}^{100} is smaller than unity, it indicates that the average SFR over the previous 10 Myr is lower than that averaged over the previous 100 Myr. Two regions in our sample, the central regions of NGC253 and Arp220, show evidence of this. Recent optical, Hα, and Paβ line observations show that Arp220 is a post starburst galaxy, with galaxy wide star formation stopping 100 Myr ago (Chandar et al., 2023), and that starburst regions younger than 10 Myr, located in its nuclei, only contribute a few percent to the Hα line emission (Chandar et al., 2023). Earlier Hα line observations had also revealed that the central region of Arp220 is home to a starburst more recent than ~10 Myr, but that an even more intense star burst occurred a few tens of Myr ago (Taniguchi et al., 2012), the galaxy being in a post starburst state after undergoing multiple mergers over the past 0.2-1 Gyr (Taniguchi et al., 2012). Similarly, observations Hβ line absorption also seem to indicate that the SFR in Arp220 has rapidly decreased rapidly 300 400 Myr ago (Soto & Martin, 2010).

In the case of NGC253, the $SFR_{mm-RRL} = 0.77 \pm 0.08\, M_\odot\, yr^{-1}$ value shown in Table 4.7 is the result of considering optically thick emission of several mm-RL. The SFR derived from several lines, ranging from H26α to H40α, takes values between $\sim 0.6\, M_\odot\, yr^{-1}$ and $1.9\, M_\odot\, yr^{-1}$, assuming optically thin mm-RL emission (see chapter 3) resulting in an average SFR of $\sim 1.5\, M_\odot\, yr^{-1}$. The latter values agree with $\sim 1.6\, M_\odot\, yr^{-1}$ value reported by from previous H40α mm-RL, IR, and radio observations (Bendo et al., 2015; Leroy et al., 2015), after adjusting to the 3.2 Mpc luminosity distance of NGC253 used in this work. This SFR is still slightly below our measurements of $SFR_{TIR} = 2.9^{+1.9}_{-1.0}\, M_\odot\, yr^{-1}$ for the central region of NGC253. Taken at face value, this would imply that the average SFR in the

nucleus of NGC253 over the past ~ 10 Myr is lower than the one over the past ~ 100 Myr. Studies of the star formation activity, molecular outflows, and metallicity indicate that the age of the starburst in the center of NGC253 is of the order of a few Myr, and host to young star-forming super clusters (Mills et al., 2021; Leroy et al., 2015, 2018). Although there is evidence of intense star formation in the past, due to a possible merger (Davidge, 2010), this does not provide sufficient information to conclude that the average SFR has decreased over the previous ~ 100 Myr. All the comparisons shown here are affected by the lack of FIR data that matches the ALMA spatial resolution. In the absence of high resolution FIR observations that would match the ALMA mm-RL observations, ALMA dust continuum observations at ~ 350 GHz were used to determine the $L_{\rm TIR}$ and $\rm SFR_{TIR}$ of the mm-RL emitting regions, which can introduce large uncertainties in the value of $\rm SFR_{TIR}$ (see Section 4.3). These results indicate that in order to investigate the SFH using mm-RL observations, the SFR over short and long timescales need to be estimated using observations having similar spatial resolutions, or cover the whole galaxy.

CHAPTER 5

Discussion and Outlook

5.1 Using ALMA to observe mm-RL

Observing the faint mm-RL in extragalactic sources remains a challenging task. Our single-dish observations have yielded no detections, while mining the ALMA archive has yielded a limited number of detections. However, ALMA is the most sensitive millimeter-wavelength observatory currently available, so it may be the best telescope for detecting mm-RL observations in extragalactic sources. Here we discuss the effect of ALMA's spatial resolution and sensitivity on the detectability of mm-RL.

5.1.1 Spatial resolution

An advantage of observing mm-RL is the possibility to measure instantaneous, dust-unbiased SFR at high resolution using ground-based telescopes such as ALMA. In contrast, FIR observations are limited to space-based observatories because the atmosphere is opaque to FIR emission. These observatories have limited resolutions due to mirror size constraints imposed by the size of launch vehicles or the overall cost of a space-based mission. At the time of writing, the highest spatial resolution available for the 80-150μm wavelength range, the peak of the dust emission spectrum, is provided by Herschel data with an FWHM of 7-18 arcseconds (Pilbratt et al., 2010). At the same time, ALMA data typically have sub-arcsecond spatial resolution at the hydrogen mm-RL frequencies (Privon et al., 2023). This means that in the case of nearby galaxies, at distances below $\sim$ 100 Mpc, using FIR data results in a relatively low resolution ($\sim$ 10 kpc) map of the SFR. For the same galaxies, mm-RL observations can easily reach sub-kpc resolutions. For example, a band 7 observation of the H30α line at the best possible resolution of $0\farcs01$ currently offered by ALMA in cycle 10 (Privon et al., 2023) corresponds to a physical resolution of $\sim$ 5 pc at a distance of $\sim$ 100 Mpc. This resolution can resolve most star-forming regions of interest, i.e. HII regions, which typically have sizes larger than a few parsecs, typically tens of parsecs (e.g. Ye, 1992; Tremblin et al., 2014), and can reach hundreds of parsecs, especially around areas of intense high-mass star formation (e.g. Shields, 1990; Tachihara et al., 2018). No other direct tracer of star formation, other than the free-free continuum emission from ionized gas, can achieve this resolution while remaining unaffected by dust extinction. However, unlike mm-RL emission, free-free continuum emission is difficult to separate from synchrotron and thermal dust emission, as shown in chapter 4.

5.1.2 Observability

Here we evaluate the capabilities of ALMA in detecting mm-RL and in measuring $\mathrm{SFR}_{\mathrm{mm-RRL}}$. We focus our attention on the H30α and the H40α lines because they are convenient to observe with ALMA. Indeed, the H40α line at ~ 99 GHz falls in ALMA's band 3 and can be observed together with the H42α line (Privon et al., 2023). ALMA can simultaneously observe the continuum flux, and the $\sim 80-100$ GHz frequency window is dominated by the free-free emission continuum, which is used to determine T_e and to constrain the SFR obtained from the mm-RL emission. On the other hand, the H30α line at 231.9 GHz has the advantage of being less affected by amplification, is a factor ~ 5.6 brighter than the H40α line, and is close enough in frequency to the CO(2-1), ^{13}CO(2-1), and ^{18}CO(2-1) transitions that all these lines can be observed simultaneously with ALMA (Privon et al., 2023). We use eq. 3.15 as the calibration between the integrated line flux of a hydrogen mm-RL and the SFR:

$$\frac{\mathrm{SFR}_{\mathrm{n}\alpha}}{\mathrm{M}_\odot\,\mathrm{yr}^{-1}} = 0.0269\,T_4^{0.58}\,\frac{\nu_{\mathrm{n}\alpha}}{\nu_{40\alpha}}\left[\frac{D}{\mathrm{Mpc}}\right]^2\frac{\epsilon_{40\alpha,4}}{\epsilon_{n\alpha,4}}\,\frac{F_{\mathrm{n}\alpha}}{\mathrm{Jy\,km\,s}^{-1}} \tag{5.1}$$

where $T_4 = T_e/10^4$ K is the electron temperature, $\nu_{\mathrm{n}\alpha}$ is the frequency of the Hnα recombination line, D is the distance to the SF region, $\epsilon_{\mathrm{n}\alpha,4}$ is a normalization factor for the specific volume emissivity of the Hnα recombination line in the optically thin limit, and $F_{\mathrm{n}\alpha}$ is the integrated line flux of the Hnα line. This conversion between $F_{n\alpha}$ and SFR for a given line and temperature can be simplified and written as:

$$\frac{\mathrm{SFR}_{\mathrm{n}\alpha}}{\mathrm{M}_\odot\,\mathrm{yr}^{-1}} = C^{T_e}_{\mathrm{n}\alpha}\times D^2_{\mathrm{Mpc}}\frac{F_{\mathrm{n}\alpha}}{\mathrm{Jy\,km\,s}^{-1}} \tag{5.2}$$

where D_{Mpc} is the distance in megaparsecs, $C^{T_e}_{\mathrm{n}\alpha}$ represents a conversion factor which depends on the line frequency, $\epsilon_{n\alpha,4}$, and T_e. Using tabulated values for these three parameters from 3, we show the values of $C^{T_e}_{\mathrm{n}\alpha}$ for the H30α and H40α lines in table 5.1. The T_e values were chosen to reflect the

T_e	$C^{T_e}_{30\alpha}$	$C^{T_e}_{40\alpha}$
[K]		
5000	0.0081	0.0179
7500	0.0101	0.0228
10000	0.0120	0.0269

Table 5.1: Factors used in Eq. 5.2 to convert H30α and H40α mm-RL integrated line flux to SFR, for three electron temperatures.

temperatures determined in this work, and they are consistent with the temperatures of HII regions found in the literature (e.g. Bendo et al., 2016, 2015; Quireza et al., 2006b). We consider FWHM values of 100 and 200km s^{-1}, which are representative of the widths of the mm-RL in this work and in the literature for extragalactic sources (Bendo et al., 2016, 2015, 2017). In Table 5.2 we list the flux density that can be detected with ALMA in one spectral channel after 1, 10, and 50 hours of integration time, respectively, at the H30α and H40α line frequencies, considering a 3σ peak confidence level, and spectral resolutions of 33 km s^{-1} and 66 km s^{-1}. The spectral resolution values are chosen such that they cover the considered FWHM of the lines with three spectral resolution elements. The flux density values were calculated using the ALMA sensitivity calculator (Heywood et al., 2011). The

Line	H30α		H40α	
Frequency [GHz]	99.02 GHz		231.9 GHz	
FWHM [km s^{-1}]	100	200	100	200
Δv [km s^{-1}]	33	66	33	66
$3\sigma_{\rm F}^{1\,\rm hr}$ [mJy]	0.855	0.603	0.789	0.558
$3\sigma_{\rm F}^{10\,\rm hr}$ [mJy]	0.252	0.178	0.271	0.189
$3\sigma_{\rm F}^{50\,\rm hr}$ [mJy]	0.112	0.078	0.121	0.084

Table 5.2: The sensitivity at the 3σ level achievable with ALMA for the H40α and H30α lines. The spectral velocity resolutions Δv =33 and 66 km s^{-1} were chosen to cover the two possible linewidths considered, FWHM=100 and 200 km s^{-1}, respectively, with three spectral channels. The $\sigma_{\rm F}^{1\,\rm hr}$, $\sigma_{\rm F}^{1\,\rm hr}$, $\sigma_{\rm F}^{1\,\rm hr}$ terms represent the flux density sensitivity reached, per resolution element Δv, after 1, 10, and 50 hours of integration time, respectively

integrated line fluxes of H30α and H40α lines with a peak flux density and FWHM listed in 5.2 are taken as the faintest reliably detectable line intensities within an ALMA synthesized beam. The SFR that would correspond to these H30α and H40α integrated line fluxes are calculated using Eq. 5.2 with $F_{n\alpha}$, the conversion factors in Table 5.1 for a distance range from 1 to 500 Mpc. We consider these to be the lowest SFRs that can be reliably measured within an ALMA-synthesized beam at a given distance, and they are shown as lines in Fig. 5.1. Star-forming regions above the detectability limits shown in Fig. 5.1 can be detected by ALMA through their H30α and H40α line emission, and the corresponding SFR can be determined. To show a region with known SFR and angular size in the figure 5.1, its corresponding SFR per synthesized ALMA beam has to be calculated. Regions with angular sizes smaller than the angular size of the synthesized ALMA beam can be placed directly in Fig. 5.1, since the entire star formation activity, and thus its integrated line flux emission, is covered by one synthesized ALMA beam. Instead, if the star-forming region is extended and covers an area with an angular size larger than one ALMA synthesized beam, the SFR per ALMA synthesized beam is obtained by dividing the total SFR in the extended region by the number of ALMA synthesized beams needed to cover it. Thus, a nearby star-forming region with a high SFR but a very large angular diameter might not be detectable, while a star-forming region with the same SFR concentrated in a small angular area that fits within the ALMA beam could be detected.

In Fig. 5.1, we also show the SFR per ALMA-synthesized beam for a sample of 95 star-forming regions in 17 nearby LIRGs and ULIRGs (Piqueras López et al., 2016), with no mm-RL observations. The physical size and SFR of each star-forming region were determined using extinction-corrected Hα observations (Piqueras López et al., 2016). The angular sizes of these regions are smaller than the ALMA synthesized beam for the frequencies and source distances considered, so their SFR can be placed in Fig. 5.1 as reported by Piqueras López et al. (2016). About 50% of these regions are individually detectable up to distances of $\sim$ 150 Mpc. The closed symbols represent the total SFR of the individual galaxies, while the open symbols represent the SFR of the individual regions. These regions have been considered in isolation, whereas in galaxies they are often clustered. Several regions with SFRs below the ALMA detectability threshold can fit into an ALMA synthesized beam, resulting in a detectable SFR. Thus, the positions along the SFR axis of Fig. 5.1 of the star-forming regions in the 17 LIRGs and ULIRGs from Piqueras López et al. (2016) represent the most conservative estimate. The peak SFRs per beam of the sources analyzed in the 4 section are also shown in Fig. 5.1. Of

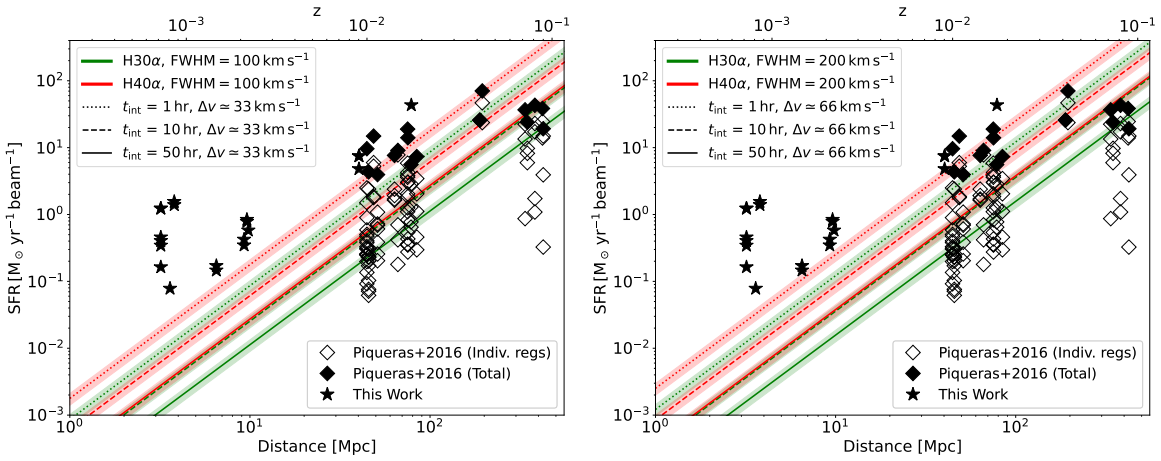

Figure 5.1: Minimum SFR detectable with ALMA as a function of distance. The green and red lines show the minimum SFR that can be measured within an ALMA synthesized beam using the H30α and H40α lines, respectively. For the sensitivity calculations, spectral resolutions of 33 km s^{-1} (left) and 66 km s^{-1} (right) were considered, with integration times of 1, 10, and 50 hours and a peak S/N of 3. These flux densities were converted to SFR assuming a mm-RL with an FWHM three times the spectral resolution, i.e. e. $\sim$ 100 km s^{-1} (left) and $\sim$ 200 km s^{-1} (right), and an electron temperature in the range T_e = 5000 − 10000 K, represented by the shaded regions, with the lines corresponding to T_e = 7500 K. An average electron density of $n_e = 10^3$ cm^{-3} was assumed. The symbols represent the SFR per ALMA beam corresponding to a sample of star-forming regions in 17 nearby LIRGs and ULIRGs (Piqueras López et al., 2016), and the detected peak SFR per ALMA beam from each galaxy in our sample 4. The filled symbols correspond to the total SFR of the galaxies in (Piqueras López et al., 2016), while the open symbols represent individual regions.

course, all these sources are well above the detection limit.

Overall, mm-RL emission from compact regions with high SFR is most likely to be detected with ALMA, and star-forming regions with SFRs of the order of $\gtrsim 10\,M_\odot$ yr^{-1} can be observed in $\sim$ 50 hr integration times out to a few hundred Mpc. Such high SFRs are mostly observable in local (U)LIRGs. Within the accessible sky, the number of (U)LIRGS is of the order of $\sim$ 100 Armus et al. (2009). Since dust often obscures starburst regions, mm-RL observations with ALMA could be used to probe the state of the ionized gas, measure the SFR, and reveal the recent SFH of these dust-obscured star-forming regions in galactic nuclei or in the case of galaxy mergers. At even greater distances, the minimum detectable SFR reaches the so-called hyper-LIRGs population with $L_{\rm TIR} > 10^{13} L_\odot$. While such hyper-LIRGs do exist in the Universe (Gao et al., 2021), they are all located at much higher redshifts (z¿2; so-called submillimeter-selected galaxies (Blain et al., 2002)), where RL are no longer observable with ALMA at mm wavelengths.

We also investigate the relationship between the SFR surface density, $\Sigma_{\rm SFR}$, the size of the star-forming region, and the peak mm-RL flux density that can be detected by ALMA. In Fig. 5.2 we show the peak flux density per ALMA beam of the H30α and H40α lines as emitted by star-forming regions with radii $R_{\rm SFR}$ = 50, 200, 1000 pc and $\Sigma_{\rm SFR}$ = 10 and 100 M$_\odot$ yr^{-1} kpc^{-2}. These values are representative of regions where intense star formation is taking place, such as (U)LIRGs, nuclei of starburst galaxies, mergers (e.g. Piqueras López et al., 2016; Alonso-Herrero et al., 2000; Kennicutt, 1998; Wuyts et al., 2011; García-Burillo et al., 2012). For these extended sources, the line flux per beam is independent of the distance to the source, as long as the angular size of the source is

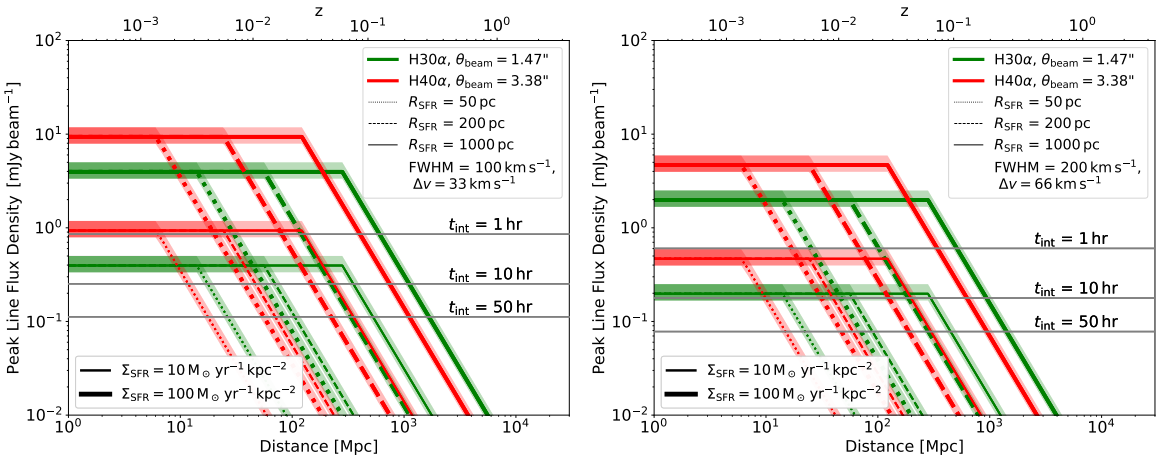

Figure 5.2: Peak mm-RL flux density inside an ALMA beam. The green and red lines show the peak H30α and H40α line flux emission, respectively, that can be measured inside an ALMA synthesized beam from star-forming regions with a physical range of sizes and star formation rate surface densities. The dashed, dotted, and solid lines represent regions with radii of 50, 200, and 1000 pc, respectively. The thicknesses of the lines correspond to star formation rate densities $\Sigma_{\rm SFR}$ of 10 $M_\odot$ yr^{-1}kpc^{-2} and 100 $M_\odot$ yr^{-1}kpc^{-2}, respectively. The FWHM of the lines is taken as three times the spectral resolution, i.e. $\sim 100\,{\rm km\,s^{-1}}$ (left) and $\sim 200\,{\rm km\,s^{-1}}$ (right). The electron temperatures are in the range $T_e = 5000 - 10000$ K, represented by the shaded regions, with the lines corresponding to $T_e = 7500$ K. An average electron density of $n_e = 10^3\,{\rm cm^{-3}}$ was assumed. The horizontal lines represent the ALMA peak line flux density per beam that can be detected at the 3σ confidence level at a spectral resolution of $33\,{\rm km\,s^{-1}}$ (left) and $66\,{\rm km\,s^{-1}}$ (right).

larger than that of the beam. This is because the physical area of the source covered by the beam is $A_{\rm beam} \propto \Omega_{\rm beam} D^2$, while the mm-RL flux emission from SFR is $F_{{\rm n}\alpha} \propto A_{\rm beam}\Sigma_{\rm SFR}/D^2$. The size of the ALMA synthesized beam depends on the observation frequency and the actual configuration of the interferometric array. Here we consider the largest possible FWHM of the ALMA synthesized beam, which are 1.″47 and 3.″38 at the line frequencies H30α and H40α, respectively. If the source is distant or compact enough to be completely covered by the ALMA synthesized beam, the physical area term remains constant and is equal to the total area of the source. In this case, $F_{{\rm n}\alpha}$ decreases with D^{-2}, the so-called beam dilution.

Fig. 5.2 shows that for the SFR surface densities found in starbursting regions, in LIRGs or ULIRGs, ALMA integration times of a few hours would be enough to detect starbursts up to a distance of ~ 500 Mpc corresponding to a redshift $z \sim 0.1$. In the case of more compact regions, having radii of 50 or 200 pc, and a $\Sigma_{\rm SFR} \sim 10{\rm M_\odot\,yr^{-1}\,kpc^{-2}}$ integration times of 10 - 50 hours are needed to detecting them, up to a distance of ~ 100 Mpc. Thus, the prime candidates for mm-RL detections in these configurations are mostly (U)LIRGs. Thus, mm-RL can be observed by ALMA and used to measure SFR. However, mm-RL are faint, and thus difficult to detect, observations being likely limited to galaxies with high SFR, such as local starbursts and (U)LIRGs. Despite this, at the highest resolution of ALMA, of 10-100 pc, it is possible to detect nearby compact star-forming regions with high $\Sigma_{\rm SFR}$, but with moderate overall SFR.

5.2 Sources of bias and uncertainty when measuring SFR

The conversion factors between observables such as line emission, continuum or integrated flux, and SFR are influenced by parameters that depend on the evolution of the stellar population, its mass distribution, its formation history, as well as the metallicity and the properties and composition of the ISM. Failure to take these parameters into account when measuring SFR could lead to uncertainties of at least a factor of a few. To mitigate this problem, physics-based models are used to estimate the values of the above parameters. These models are developed and calibrated with simulations or observations of our own galaxy or a limited sample of galaxies. These models are also based on various assumptions about the properties of the observed galaxy, some well-known examples are the assumption of a Kroupa IMF (e.g. Kroupa, 2001) or of a certain dust emission model (e.g. Dale & Helou, 2002; Draine & Li, 2007a). These assumptions allow one to calculate the SFR, while possibly introducing their own biases. Using a sample of ~ 90000 galaxies with extensive multiwavelength observations of continuum and line emission, at wavelengths ranging from the FUV at ~ 1550 Å to the submm 500 μm, Figueira et al. (2022) calculates the SFR resulting from a SED fitting program (CIGALE) that incorporates various models for AGN and dust emission, radiation transfer, stellar population, and star formation history. These global SFR estimates are among the most accurate available because they use a multiple tracer consisting of observations at many different wavelengths. This would allow one to account for different properties of the observed galaxy, such as those of the ISM, the stellar population and evolution, or the AGN fraction, and the interactions between stellar radiation, gas, and dust. Figueira et al. (2022) compares these SFRs with the SFRs of these galaxies obtained from individual tracers, such as UV or TIR emission. Each individual tracer considered was calibrated taking into account parameters such as IMF, SFH, and metallicity Figueira et al. (2022). For the sample of ~ 90000 galaxies, the deviation of the SFR using the FUV, NUV, $ltir$, and $L(\mathrm{H}\beta)$ tracers from the multiwavelength SFR had a mean of -0.02, -0.01, 0.04, and 0.07 dex, respectively, with a scatter of 0.25, 0.24, 0.13, and 0.19 dex, respectively. The mm-RL observations would in principle show a scatter below that of the Hβ SFR tracer, since they are not affected by the presence of dust. The uncertainties introduced by the unknown properties of the HII regions can be reduced by multiple mm-RL observations, which are possible with ALMA.

All of the SFR tracers discussed so far also have advantages and disadvantages due to the environment or physical processes that give rise to their respective observables. Often, certain assumptions have to be made when calculating the SFR, reflecting our incomplete knowledge of the various properties of the observed galaxies. These assumptions, about the IMF, the dust composition, the densities or temperatures of HII regions, etc., introduce uncertainties in the estimation of the SFR. Here we briefly discuss these sources of bias and uncertainty, and how they affect the various SFR tracers, in the context of mm-RL observations.

5.2.1 The IMF

The most basic assumption, used by virtually all SFR tracers, especially in an extragalactic setting, is the stellar IMF. This function, that quantifies the relative numbers of stars that are born as a function of their mass, i.e. their mass distribution, has been determined from observations of our Galaxy and its satellites, yielding several models (e.g. Kroupa, 2001; Chabrier, 2003). All the different models agree that the relative number of stars decreases with their mass like a powerlaw. The luminous massive stars dominate the IMF with their luminosity, but the intermediate and low mass stars dominate the mass of

the IMF due to their much larger number. Any SFR estimate using massive star tracers is extremely sensitive to the chosen IMF. Since star formation is a complex process, involving among others, the collapse of molecular gas clouds, accretion, and formation and evolution of protostars, it is expected to be highly dependent on the conditions of the environment, i.e. in the ISM. Despite its importance, an extragalactic IMF has not yet been established, and a consensus on how exactly the IMF depends on the ISM conditions, such as metallicity, molecular and dust chemical composition, or the SFH has not been reached (e.g. Cenarro et al., 2003; Treu et al., 2010; Cappellari et al., 2012; Conroy & van Dokkum, 2012; Martín-Navarro et al., 2015). Several trends have been however uncovered. Because, on average, higher mass stars are produced in higher temperature regions (Low & Lynden-Bell, 1976; Jermyn et al., 2018) and the dust temperature has been observed to be higher in galaxies at higher redshift (e.g. Casey, 2012; Magnelli et al., 2014; Magdis et al., 2017), it would be expected that the IMF would have a higher proportion of high mass stars in higher temperature regions and in galaxies at higher redshifts. Observations indeed seem to confirm that in galaxies at higher redshifts, or in galaxies where the gas and dust is hotter than in our galaxy, e.g. in ULIRGs, the IMF corresponds to a higher production of massive stars in proportion to low mass ones, in comparison to the IMF of our own Galaxy (Sneppen et al., 2022). The choice of IMF is important, as for example, the Salpeter IMF is more top heavy (yields a larger number of massive stars) than a Kroupa IMF. Indeed, for a Salpeter IMF, the SFR corresponding to a given ionizing photon production rate is $\sim 60\%$ higher than it would for a Kroupa IMF (Kennicutt, 1998; Calzetti et al., 2007), for stellar masses above $\sim 1 M_{\odot}$. This in turn would impact estimators using hydrogen RL, as well as the other tracers relying on the effects high mass stars have on the ISM.

It would thus be tempting at first to use an IMF that takes temperature into account, given the range in dust temperatures measured in section 4, however, there are multiple other factors affecting star formation and thus the IMF. For example, in regions with higher metallicities, fewer high mass stars are being formed than in those with lower metallicities (e.g. Cerviño & Mas-Hesse, 1994). High metallicity areas indeed seem to have an IMF with an increased low to high stellar mass ratio, in comparison to the established galactic IMF (e.g. Jeřábková et al., 2018; Li et al., 2023). Multiple observations of the Milky Way (e.g. Shaver et al., 1983; Rudolph et al., 1997; Afflerbach et al., 1997; Daflon & Cunha, 2004; Yong et al., 2006; Balser et al., 2011; Lian et al., 2023) and of other galaxies (e.g. Zaritsky et al., 1994; Ferguson et al., 1998; Bresolin, 2007; Bresolin et al., 2009; Sánchez et al., 2014; Werk et al., 2011; Magrini et al., 2016; Goddard et al., 2011) reveal the decrease in metallicity with respect to distance from the galactic center. This negative metallicity gradient as a function of galactocentric distance implies that central regions of galaxies have higher metallicity than the one average Milky Way value where the currently and widely used IMF have been established. Thus, the influence of high temperature on the IMF could plausibly be balanced by the influence of high metallicity. Given this degeneracy and the difficulty of pinpointing an exact IMF for each galaxy, the use of a standard galactic IMFs (e.g. Kroupa, 2001; Chabrier, 2003) when measuring SFR remains appropriate. The uncertainty introduced by the IMF is applicable to other SFR tracers that rely on high mass stars as well, and given the reasons above, it is difficult to quantify the relative influence of the IMF on different SFR tracers. However, since most of the regions presented in studied work are located in the central regions of their host galaxies, biases introduced by the metallicity should affect the measured SFR a similar way, i.e. not affect the slope of the $\mathrm{SFR}_{\mathrm{TIR}}$ to $\mathrm{SFR}_{\mathrm{mm-RRL}}$ correlation.

5.2.2 Interstellar dust properties

Interstellar dust grains absorb or scatter electromagnetic radiation, the most affected wavelengths being those shorter than MIR. (e.g. Draine, 2011). The amount of attenuation by dust is inversely proportional to the wavelength of the radiation, e.g. in a dusty star-forming region all FUV radiation from a young massive star is assumed to be absorbed by dust (e.g. Kennicutt, 1998). A very common tracer of SFR is the Hα line emission at 6564.6Å in the visible spectrum, a hydrogen recombination line used to trace massive star formation because it is emitted from HII regions around massive stars (e.g. Kennicutt & Evans, 2012). Measurements of line luminosity, $L_{\mathrm{H}\alpha}$, can be significantly affected by dust extinction. In galaxies with little or no dust, such as NGC5253, the attenuation of the Hα line can be close to 0 (Calzetti, 2001), in dusty starburst regions, such as the nucleus of NGC1614, the attenuation can reach a factor of ~ 8 (Buat, 2002), or even be almost completely attenuated, as in the case of Arp220 or other ULIRGs, where the attenuation can reach ~ 50 mag (Genzel et al., 1998).

The SFR tracer based on total infrared emission from dust is widely used in the literature and in this paper (e.g. Kennicutt, 1998; Murphy et al., 2011; Calzetti et al., 2010; Kennicutt & Evans, 2012). This is considered a reliable tracer as long as the assumptions behind it are valid, i.e. that all stellar radiation is absorbed by dust, that dust is heated mainly by young massive stars, and that star formation has been constant and ongoing for at least ~ 100 Myr (e.g. Kennicutt, 1998; Rieke et al., 2009; Kennicutt & Evans, 2012). For example, if a significant fraction of the UV emission from young stars escapes the star-forming region without being absorbed by dust, then the L_{TIR} tracer will underestimate the SFR. For dust-rich star-forming galaxies this is not a problem, as the UV escape fraction is less than 10% for regions with $\log(L_{\mathrm{TIR}}L_{\odot}^{-1}) \geq 10.5$, rising to more than 20% for $\log(L_{\mathrm{TIR}}L_{\odot}^{-1}) \geq 9.75$ (Bell, 2003; Buat et al., 2007; Schmitt et al., 2006; Kennicutt et al., 2009). Galaxies and regions with lower dust content, i.e. regions with lower metallicity or dwarf galaxies, can have an escape fraction of 100% (Kennicutt & Evans, 2012). However, such uncertainties can be reduced by combining UV observations of the radiation from massive stars with the TIR emission from dust (e.g. Calzetti et al., 2010; Murphy et al., 2011; Kennicutt & Evans, 2012). The combination of short and long wavelength observations, such as L_{UV} and L_{TIR}, counteracts the uncertainty due to an unknown escape fraction. For a sample of local galaxies, a linear combination of L_{FUV} and L_{TIR} is used to derive a corrected L_{FUV}, resulting in SFRs that are closely correlated with those obtained from dust corrected $L_{\mathrm{H}\alpha}$ (Hao et al., 2011). It should be noted, however, that the dispersion in this relation is small for low dust content; for galaxies dominated by infrared emission, the uncertainty in the relation of Hao et al. (2011) can reach values of 20%. Since our sample consists mainly of dusty starbursts and (U)LIRGs, the UV escape fraction is negligible, and thus the L_{TIR} is sufficient to estimate an SFR.

Infrared emission from dust heated by evolved stars rather than young massive stars can also introduce uncertainties in SFRs based on dust emission. Observations show that up to 80% of the dust in early-type galaxies is heated by older stellar populations of stars(Nersesian et al., 2019). In evolved galaxies with low sSFR, this can generally reach 90%. On average, the conversion factor for obtaining the SFR from L_{TIR} can vary by a factor of several between starburst galaxies and quiescent galaxies with a constant SFR (Kennicutt et al., 2009; Hao et al., 2011).

Since recombination lines are the result of hydrogen ions capturing a free electron and then emitting radiation as they evolve toward their ground state, dust absorbing ionizing radiation before it ionizes hydrogen results in a decrease in the RL. This would require the presence of gas in the HII regions around massive stars, and although the onset of star formation usually results in the destruction of the molecular cloud and dust around the young star, there could be cases where the absorption of ionizing

photons by dust can significantly reduce the amount of ionized hydrogen that would otherwise be present around young massive stars (e.g. Draine, 2011). To account for this effect, the SFR that relies on ionized gas should be corrected by a factor $f_{\rm ion}$, which represents the fraction of photons that ionize hydrogen instead of being absorbed by dust. Simulations have shown that the $f_{\rm ion}$ in an HII region is proportional to the ionization factor $U = Q_1/(cn_e)$, where c is the speed of light and n_e is electron density, and the amount of dust, parameterized by the abundance of oxygen as O/H. According to these simulations, the ionization fraction in dusty starburst regions could be less than $\sim 30\%$ (Dopita et al., 2003). This would imply that significant corrections to the SFR based on emission from ionized gas in dusty regions would be required. However, electron densities of up to $n_e = 10^2$ cm^3 have been considered (Dopita et al., 2003), which is at least a factor of 10 lower than what is considered in mm-RL observations (e.g. Anantharamaiah et al., 2000; Bendo et al., 2015, 2016; Kim et al., 2017). Furthermore, the simulations claim a reduced $f_{\rm ion}$ where hydrostatic, while dynamical simulations of HII regions show that when the ionizing photon flux Q_1 is high, the gas in HII regions is driven against its outer layer, increasing the rate of hydrogen ionization there and thus decreasing U (Krumholz & Matzner, 2009). This largely negates the effects of dust absorption and thus keeps $f_{\rm ion}$ closer to 100% (Krumholz & Matzner, 2009). In any case, it would be challenging to account for this effect across multiple unresolved HII regions when performing extragalactic observations, and we find no systematic use of this correction factor $f_{\rm ion}$ for SFR estimates based on the Hα or other recombination lines (e.g. Kennicutt & Evans, 2012; Murphy et al., 2011). For this reason we have not included $f_{\rm ion}$ in this work.

5.2.3 The choice of stellar populations models

Stellar Evolutionary Population Synthesis (EPS) models, i.e. models that describe the evolution of stellar populations through time in order to characterize the radiation field present in a galaxy. When observed directly or indirectly, this radiation is used to infer the SFR. There are several EPS models that use different stellar evolution models, catalogs of stellar spectra, etc., the most common are STARBURST99 (Leitherer et al., 1999, 2010), GISSEL98 (Bruzual A. & Charlot, 1993), BC03 (Bruzual & Charlot, 2003), POPSTAR (Mollá et al., 2009), PEGASE (Fioc & Rocca-Volmerange, 1999). The output of these models is affected by stellar mass loss rates, stellar rotation (Topping & Shull, 2015), and binary fraction (Belkus et al., 2003; Eldridge et al., 2008; Zhang et al., 2013).

An important parameter is the binary fraction, i.e. what percentage of stars are born and evolve in binary systems, and its influence on star formation tracers and their calibration. Binary stars are common in the Universe, and the binary fraction for high-mass stars appears to be between 0.66 and 1 (Kobulnicky & Fryer, 2007; Sana et al., 2013, 2014). The binary fraction also affects the total production rate of ionizing photons, Q_0, with stellar populations with a higher binary fraction producing more ionizing photons than single star populations (Zhang et al., 2013; Stanway et al., 2016). One reason for this effect is that in a binary, the layers of material inside massive stars are more easily mixed, leading to an increased supply of hydrogen that undergoes fusion deeper towards the stellar cores (Stanway et al., 2016). Overall, this binary interaction leads to an increased fraction of hotter stars in a given stellar population, and thus to an increased fraction of ionizing photons (Zhang et al., 2013). The excess of Q_0 due to the binary fraction is more pronounced for subsolar metallicities, where it can reach values of 60%, while no significant effect is predicted for supersolar metallicities (Stanway et al., 2016). The conversion factor between ionizing photon flux and SFR has a strong influence on the calibration of the hydrogen RL SFR tracers. For the RL tracer, the binary

fraction can introduce uncertainties of up to ~ 40% in the SFR Zhang et al. (2013). The TIR and UV tracers, however, are almost unaffected by the binary fraction Zhang et al. (2012).

Stellar rotation also affects the production of ionizing photons. The factor transforming the ionizing photon flux to SFR varies by a factor ~ 2.5 for metallicities between $0.1Z_{\odot}$ and $2Z_{\odot}$ (Stanway et al., 2016). Similar results have been obtained using different IMFs and taking stellar rotation into account for metallicities between 0.1-$1Z_{\odot}$ (Topping & Shull, 2015). Bendo et al. (2017) calculate the Q_0 to SFR conversion factors for 40% solar metallicity and two different stellar rotation velocities, using `starburst99` with a Kroupa IMF and a 10 Myr continuous star formation history. Their results suggest that the Q_0 to SFR scaling factor in these cases is 30% lower than expected at solar metallicity with no stellar rotation and the same IMF. At these high metallicity values of $2Z_{\odot}$, (Bendo et al., 2015) find the Q_0 to SFR conversion factor to be ~40% higher than that found for solar values (Murphy et al., 2011), assuming a Kroupa IMF. Since our observations are mostly aimed at dusty regions, we have adopted the conversion factor from Bendo et al. (2015) in our work.

Another important parameter influencing the stellar population model is the star formation history, which can be a source of uncertainty in the SFR measurement, especially when using IR tracers. Most calibrations of the various dust emission-based tracers, including $L_{\rm TIR}$, assume a constant SFR for the past ~ 100 Myr (e.g. Murphy et al., 2011; Hao et al., 2011; Kennicutt & Evans, 2012). Star formation rates can vary greatly with time in a starburst or quenching event (Hayward et al., 2014). In these cases, even if the SFR drops to levels of ~ 10^{-3} $M_{\odot}$ yr^{-1} after a starburst (Hayward et al., 2014), stars that live for a few 100 Myr still emit UV radiation that heats the dust. For example, a galaxy that forms a mass $M = 10^7$ $M_{\odot}$ of stars at 1 $M_{\odot}$ yr^{-1} over 10 Myr emits the same amount of UV radiation in the 1300 − 1500 Å wavelength range as a galaxy that forms a 2.5×10^8 $M_{\odot}$ mass of stars in a 50 Myr old starburst event (Calzetti, 2013). At first glance, it would seem that comparing $\rm SFR_{TIR}$ and $\rm SFR_{mm-RRL}$ would be problematic in such cases, since in such galaxies determining the SFR from $L_{\rm TIR}$ or $L_{\rm UV}$ can overestimate the SFR by a factor of several (Calzetti, 2013; Hayward et al., 2014). In our work, however, the one-to-one correlation between $\rm SFR_{TIR}$ and $\rm SFR_{mm-RRL}$ seems to hold. Furthermore, the deviation of individual galaxies from this one to one also provides a way to constrain their SFH.

Ultimately, the choice of model, which is influenced by the parameters described above, affects the calibration of each SFR tracer differently. Among the most commonly used tracers, the FIR one seems to be the most affected, with the choice of EPS model introducing variations in the $L_{\rm TIR}$-to-SFR conversion factor of up to 120%, while this number is of the order of ~ 20% for the mm-RL or UV-based SFR tracers (Zhang et al., 2013).

5.2.4 The AGN fraction

Active Galactic Nuclei are compact regions at the center of some galaxies where matter accretes on to a supermassive black hole. These regions emit large amounts of radiation across the electromagnetic spectrum, and are associated with a dusty torus, which absorbs short wavelength radiation and reemits it in at infrared wavelengths (e.g. Genzel et al., 1998). The IR radiation from this torus can be similar to that of star-forming regions (Genzel et al., 1998) and can dominate the luminosity of the galaxy.

For this reason, not taking into account the AGN contribution to $L_{\rm TIR}$, i.e. the AGN fraction, can lead to a significant overestimation of the $\rm SFR_{TIR}$. For merging galaxies, the AGN contribution to $L_{\rm TIR}$ can have values of up to 90% (Dietrich et al., 2018), with simulations showing that on average the contribution is of the order of ~ 50%. Observations of a sample of ~ 200 nearby galaxies, consisting of 21 starburst galaxies, 149 interacting and merging galaxies, and 29 AGN dominated galaxies, reveal

that the AGN contribution to the total luminosity is greater than 20% for about half of these galaxies, and greater than 40% for about a quarter of these galaxies (Ramos Padilla et al., 2020). The same observations reveal that, on average, $L_{\rm TIR}$ correlates with the AGN fraction, at $L_{\rm TIR} = 10^9\,L_\odot$ the AGN fraction is $\sim 5\%$, while at $L_{\rm TIR} = 10^{12}\,L_\odot$ it reaches $\sim 36\%$. A solution to this problem is using multiwavelength observations and SED fitting to constrain the AGN fraction, or other diagnostics that reveal the presence of an AGN, e.g. measuring the synchrotron spectral index (e.g. Biermann & Strittmatter, 1987; Kellermann et al., 1989; Ishibashi & Courvoisier, 2011), observing PAH emission lines (e.g. Genzel et al., 1998; Spoon et al., 2007; Herrero-Illana et al., 2014) or emission line ratios originating in ionized gas (e.g. Allen et al., 1998; Baldwin et al., 1981; Best et al., 2000). Nevertheless, there is little evidence of significant AGN contamination in our sample of star-forming galaxies, while observations of star-forming regions, that are not located in galactic nuclei would not be contaminated by AGN emission at all. Furthermore, observations of mm-RL can also be used to distinguish between starburst and AGN activity (Scoville & Murchikova, 2013).

5.2.5 The state of ionized gas

For a given hydrogen emission model and ionized gas properties, $L_{\rm H\alpha}$ can be used as a measure of the ionizing photon flux Q_0. Using an IMF and EPS model, Q_0 can then converted to SFR. For the most commonly assumed properties of an HII region, i.e., $T_e = 10000\,\rm K$, $n_e = 10^3$, (e.g. Draine, 2011) and, $|\tau_{\rm L}| \ll \tau_{\rm C} \ll 1$ (e.g. Gordon & Sorochenko, 2002), the effects of line amplification or absorption can be neglected for all hydrogen RL lines with quantum numbers $n \lesssim 40$. However, we find that the assumption of low optical depth is no longer valid for a range of densities and electron temperatures, and that mm-RL can be significantly amplified or attenuated under certain conditions, introducing large uncertainties in the values of $\rm SFR_{mm-RRL}$. The lines most affected are those with quantum numbers above $35 \sim 40$. For electron densities of $n_e = 10^2 \sim 10^3\,\rm cm^{-3}$ we find that mm-RL are mostly attenuated, and only when $\rm EM \gtrsim 10^9\,cm^{-6}\,pc$. The most affected lines are mm-RL with quantum numbers above ~ 40. For the given conditions these can be attenuated by more than $\sim 40\%$. At densities of $n_e = 10^4 \sim 10^5\,\rm cm^{-3}$ the most prominent effect is the line enhancement. This effect is particularly strong in the $3000 - 5000\,\rm K$ temperature range, where even lines such as H28α or H30α are amplified by a factor of $2 \sim 3$ when the emission measure is $\rm EM = 10^8 - 10^9\,cm^{-6}\,pc$. Beyond $\rm EM \gtrsim 10^9\,cm^{-6}\,pc$ these lines exceed a gain factor of 10. As the electron temperature increases, the amplification effect decreases. At $T_e \gtrsim 10000\,\rm K$ these lines are only amplified by a factor of a few when $\rm EM \gtrsim 10^9\,cm^{-6}\,pc$. For all electron densities mentioned so far, the amplification or attenuation effects increase with the mm-RL wavelength. At an electron density of $n_e = 10^6\,\rm cm^{-3}$ we are amplified by a factor of several at $\rm EM \gtrsim 10^9\,cm^{-6}\,pc$, but the differences in amplification between lines of different quantum numbers are smaller than at the lower densities mentioned above. At $n_e = 10^7\,\rm cm^{-3}$, the differences in gain between the different lines become negligible for almost all EM values, and the total gain of mm-RL can also be ignored.

Thus, the state of the ionized gas can strongly influence the intensity of the mm-RL. While this may seem like an insurmountable problem, it also presents an opportunity. Since different mm-RL are not all affected in the same way by the state of the ionized gas, using multiple mm-RL observations can constrain both the electron density and temperature, as well as the amount of amplification or attenuation (see chapter 3). This ultimately provides not only an accurate view of the SFR unaffected by dust attenuation, but also a diagnostic of the HII regions.

CHAPTER 6

Summary and Conclusion

In this work we have evaluated the reliability of hydrogen mm-RL as an extragalactic SFR tracer. To this end, we performed observations of 6 nearby star-forming galaxies with the IRAM30m telescope and searched the ALMA archive for mm-RL detections of the 20 brightest infrared galaxies in the Revised Bright Galaxy Sample (Sanders et al., 2004). The IRAM30m observations did not yield any mm-RL detections, but provide stringent upper limits on the mm-RL line emission from the central regions of these galaxies. From the ALMA sample we recover mm-RL detections for 9 of the 20 galaxies. The SFR calculated from the mm-RL, $\mathrm{SFR}_{\mathrm{mm-RRL}}$, is compared with the SFR obtained from an established tracer based on the total infrared luminosity of the dust emission, $\mathrm{SFR}_{\mathrm{TIR}}$.

The electron temperature of the ionized hydrogen gas is required to calculate $\mathrm{SFR}_{\mathrm{mm-RRL}}$. This was calculated from the ratio of the mm-RL integrated line flux to the free-free continuum. The free-free emission was extracted from the total continuum emission by fitting a multi-component SED function to the radio-to-submm continuum spectra of the observed regions. We find that if no priors are placed on the values of the synchrotron or dust emissivity spectral indices when performing a radio-to-submm SED fitting, the level of the free-free emission has large uncertainties. Accurate determination of the free-free continuum requires excellent observations covering the frequency range between ~1.5 and ~350 GHz, and is not always feasible with current archival data. This leads to large uncertainties in T_e. However, since $\mathrm{SFR}_{\mathrm{mm-RL}} \propto T_e^{0.58}$, the effects of these uncertainties could be mitigated. Doubling the electron temperature would increase the SFR estimate by ~50%.

We have investigated the effects of the electron n_e, T_e, and EM on the relative intensities of the submm and mm RLs. We find that observations of three lines, i.e. two line ratios, that are well separated in frequency, such as the H28α, H35α, and H40α lines, can be used to identify the presence of optically thick emission, i.e. line attenuation and amplification, and to constrain the values of n_e and T_e. For three of the galaxies in the ALMA sample, multiple H-RLs were detected, allowing us to study the effect of optical depth on the SFR determination. The optically thin assumption proves insufficient to explain the H-RL ratios emitted by NGC253 and Region B in NGC3256. We also find that optically thick emission, resulting in line attenuation or amplification, is present in the galactic sources from the ATLASGAL survey (Kim et al., 2017, 2018). In regions where the H-RL emission is not optically thin, SFR estimates based on observations of a single, lower frequency H-RL, such as H40α, could be off by more than a factor of several compared to SFR estimates obtained by taking optical depth into account.

$\mathrm{SFR}_{\mathrm{H-RL}}$ and $\mathrm{SFR}_{\mathrm{TIR}}$ for galaxies in the ALMA sample are in agreement. This is also the case

when we consider the ATLASGAL data for galactic star-forming regions. This relationship between SFR_{TIR} and SFR_{mm-RRL} spans eight orders of magnitude in SFR, corresponding to very different environments, from star-forming regions in the Milky Way to the cores of starburst galaxies. The upper bounds we place on the SFR_{H-RL} of the galaxies in the IRAM30m sample are consistent with their SFR_{TIR}, with the exception of IC694. However, it is plausible that the discrepancy is caused by the SFH of these galaxies, where the SFR averaged over the last ~ 10 Myr is different from the SFR averaged over the last 10 to 100 Myr.

Since mm-RL and UV or TIR trace the average SFR over very different timescales, ~ 10 Myr and $\gtrsim 100$ Myr respectively, their analysis can provide insight into the SFH of galaxies. For this purpose we calculate the ratio between the SFR corresponding to the two timescales, $SFR^{10\,Myr}/SFR^{100\,Myr}_{tot}$. Due to the limited data available at suitable resolutions, we were able to perform this analysis only for a few of the galaxies in our sample. For NGC5253 we find that $SFR^{10\,Myr}/SFR^{100\,Myr}_{tot} > 1$, implying an increase in SFR from the previous ~ 10 Myr. For NGC253 and Arp220 we find that $SFR^{10\,Myr}/SFR^{100\,Myr}_{tot} < 1$, implying that the SFR over the past ~ 10 Myr is lower than that averaged over the past 10 to 100 Myr. Literature results using other indicators confirm our results regarding the SFH for NGC5253 and Arp220, (e.g. Calzetti et al., 2015; de Grijs et al., 2013; Pellerin & Robert, 2007; Calzetti et al., 1997; Taniguchi et al., 2012; Soto & Martin, 2010; Chandar et al., 2023).

Millimeter RLs are thus potentially a valuable tool for measuring SFRs, especially in dust-obscured star-forming regions. The H30α or H40α lines are particularly good candidates, as they are easily observable with ALMA, do not seem to be easily contaminated by other emission lines, and also have a high probability of being present in the ALMA archive due to serendipitous observations, owing to their proximity to other well-studied molecular lines. However, mm-RLs are also difficult to detect due to their intrinsic faintness and may require long observing times. The distance at which a mm-RL can be expected to be detected from a starbursting galaxy is currently limited to a few hundred Mpc. Mm-RLs are also affected by attenuation and amplification, however, this problem also presents an opportunity: using the wide-band capabilities of the ALMA observatory, multiple mm-RLs can be observed simultaneously, and their ratios can be used not only to obtain a correct estimate of the SFR, but also to constrain the properties of the HII regions that emit them.

APPENDIX A

Continuum Images and Spectra of ALMA Archival mm-RL Data

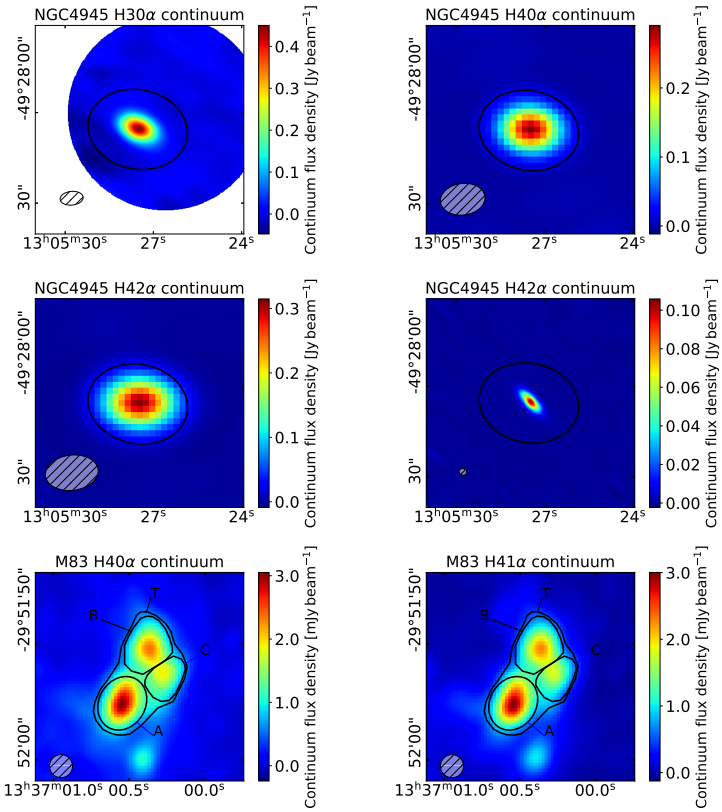

Figure A.1: Continuum ALMA images of NGC4945 and M83 at the detected mm-RL frequencies.

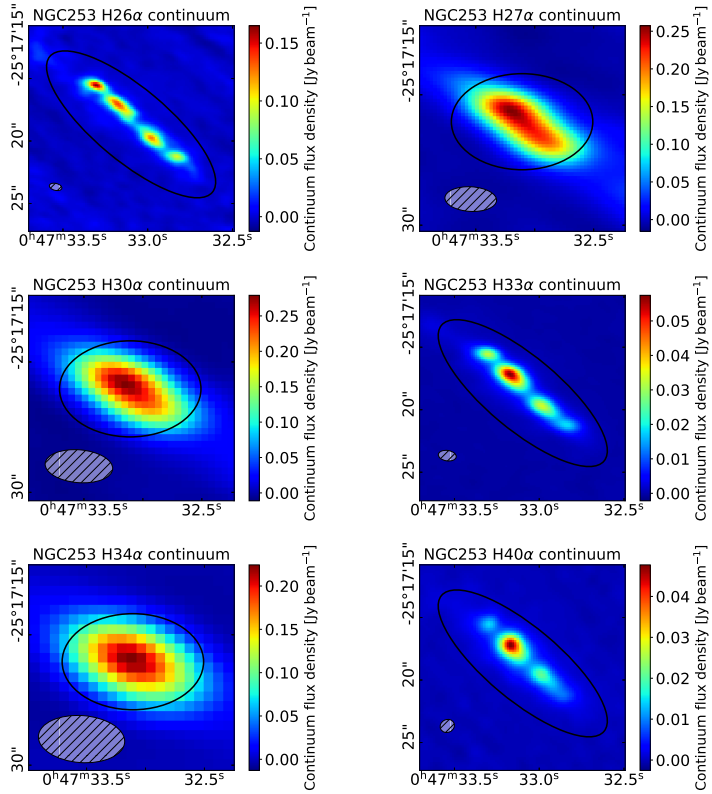

Figure A.2: Continuum ALMA images of NGC253 at the detected mm-RL frequencies.

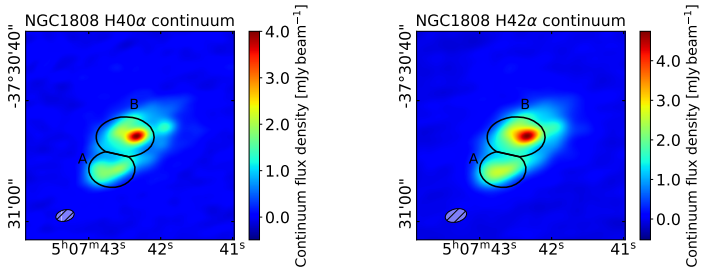

Figure A.3: Continuum ALMA images of NGC1808 at the detected mm-RL frequencies.

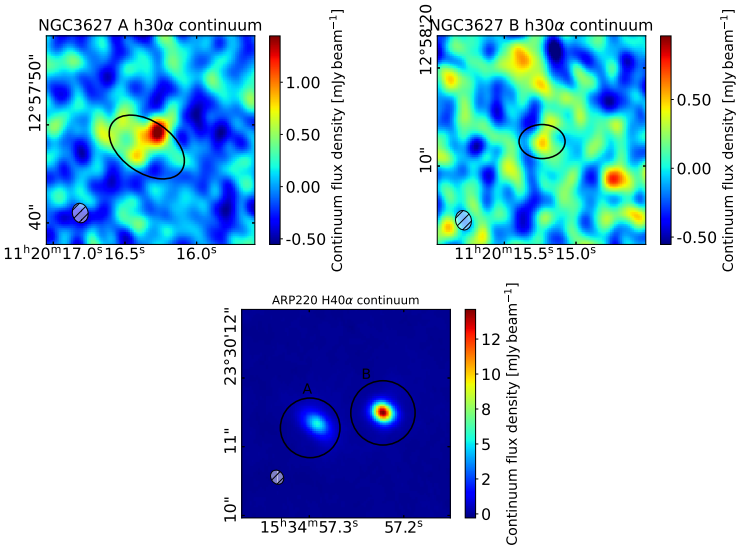

Figure A.4: Continuum ALMA images of NGC3627 and Arp220 at the detected mm-RL frequencies.

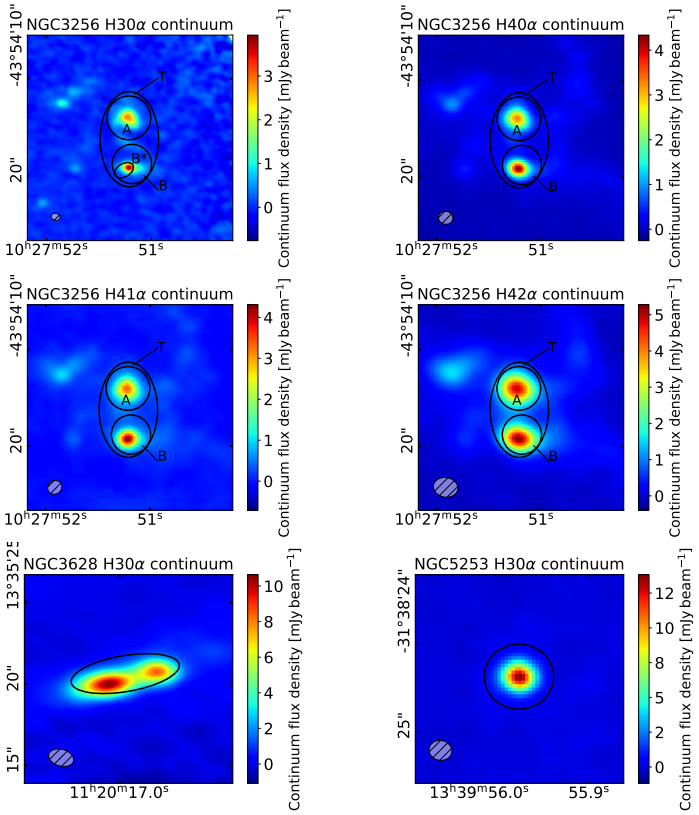

Figure A.5: Continuum ALMA images of NGC3256, NGC3628 and NGC5253 at the detected mm-RL frequencies.

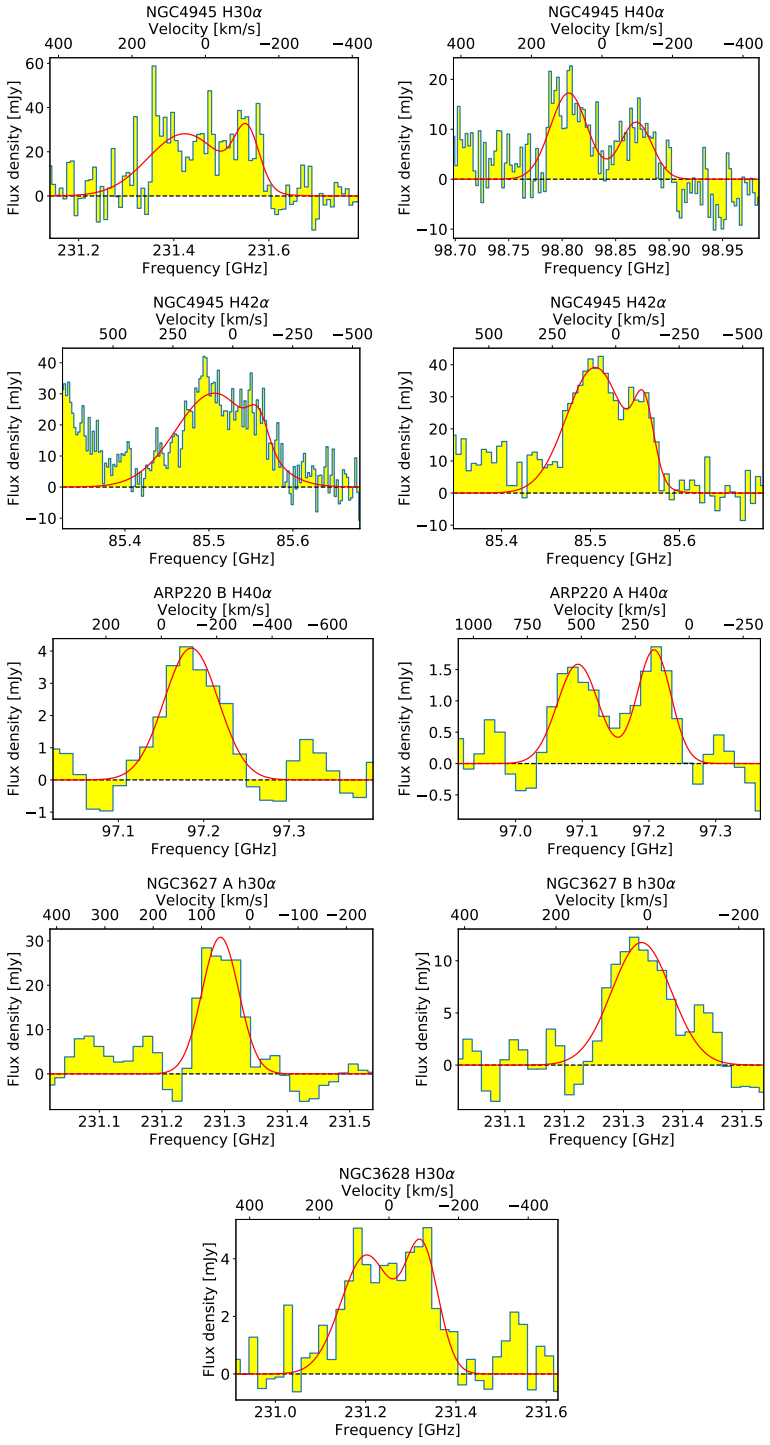

Figure A.6: Spectra of detected mm-RL in NGC4945, Arp220, NGC3627, and NGC3628

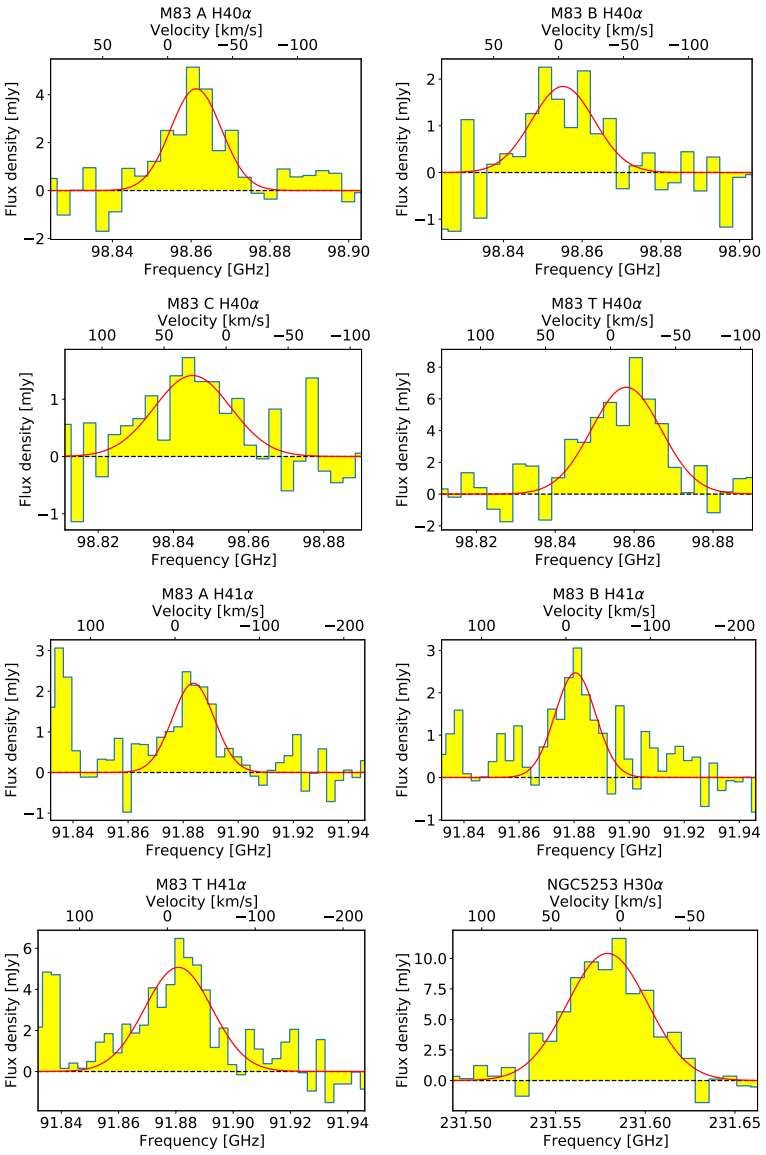

Figure A.7: Spectra of detected mm-RL in M83 and NGC5253.

Galaxy	Frequency [GHz]	Data Origin	Flux density in region [Jy]			
			A	B	C	T
NGC253	1.69	VLA 1991 OCT 22				1.340 ± 0.008
	4.86	VLA 1983 OCT 27				0.627 ± 0.006
	4.86	VLA 1995 JUL 08				0.68 ± 0.01
	8.43	VLA 1995 JUL 08				0.42 ± 0.03
	8.43	VLA 1990 JUL 03				0.44 ± 0.01
	14.9	VLA 1991 DEC 10				0.297 ± 0.003
	23.5	VLA 1991 NOV 17				0.27 ± 0.02
	98.1	ALMA 2017.1.00161.L				0.275 ± 0.002
	135	ALMA 2017.1.00161.L				0.289 ± 0.001
	174	ALMA 2017.1.00028.S				0.338 ± 0.001
	224	ALMA 2017.1.00161.L				0.593 ± 0.002
	353	ALMA 2013.1.00735.S				1.73 ± 0.06
	395	ALMA 2016.1.01285.S				2.88 ± 0.09
	397	ALMA 2016.1.01285.S				3.01 ± 0.09
	407	ALMA 2016.1.01285.S				3.1 ± 0.1
	409	ALMA 2016.1.01285.S				3.2 ± 0.1
NGC3256	4.89	VLA 2002 APR 29	0.0330 ± 0.0002	0.0266 ± 0.0001		0.0731 ± 0.0006
	8.49	VLA 2001 FEB 08	0.0185 ± 0.0001	0.0164 ± 0.0001		0.0442 ± 0.0005
	14.9	VLA 2002 APR 21	0.0100 ± 0.0040	0.0099 ± 0.0033		0.02 ± 0.01
	85.2	ALMA 2015.1.00993.S	0.0071 ± 0.0001	0.0061 ± 0.0001		0.0159 ± 0.0001
	91.5	ALMA 2015.1.00412.S	0.0084 ± 0.0001	0.0072 ± 0.0001		0.0182 ± 0.0001
	97.4	ALMA 2015.1.00412.S	0.0072 ± 0.0001	0.0062 ± 0.0001		0.0155 ± 0.0001
	217	ALMA 2015.1.00412.S	0.0124 ± 0.0003	0.0086 ± 0.0002		0.0224 ± 0.0009
	218	ALMA 2015.1.00902.S	0.0118 ± 0.0001	0.0080 ± 0.0001		0.0214 ± 0.0004
	220	ALMA 2015.1.00412.S	0.0128 ± 0.0003	0.0096 ± 0.0003		0.024 ± 0.001
	227	ALMA 2015.1.00412.S	0.0139 ± 0.0004	0.0100 ± 0.0003		0.026 ± 0.001
	229	ALMA 2015.1.00714.S	0.0136 ± 0.0002	0.0093 ± 0.0001		0.0243 ± 0.0005
	255	ALMA 2015.1.00412.S	0.0186 ± 0.0002	0.0119 ± 0.0001		0.0339 ± 0.0006
	267	ALMA 2017.1.00379.S	0.0168 ± 0.0002	0.0104 ± 0.0001		0.0299 ± 0.0006
	343	ALMA 2018.1.00493.S	0.0443 ± 0.0004	0.0219 ± 0.0004		0.072 ± 0.001
NGC1808	1.51	VLA 1985 FEB 21	0.019 ± 0.002	0.072 ± 0.001		
	4.89	VLA 2002 JAN 28	0.0131 ± 0.0007	0.0374 ± 0.0009		
	85.4	ALMA 2016.1.00562.S	0.0066 ± 0.0001	0.0117 ± 0.0001		
	98.6	ALMA 2016.1.00562.S	0.0064 ± 0.0001	0.0112 ± 0.0001		
	228	ALMA 2017.1.00984.S	0.0168 ± 0.0009	0.022 ± 0.002		
	235	ALMA 2017.1.00984.S	0.0133 ± 0.0009	0.021 ± 0.002		
	492	ALMA 2017.1.00984.S	0.132 ± 0.002	0.168 ± 0.003		
M83	1.45	VLA 1998 JUN 07				0.0723 ± 0.0002
	4.86	VLA 1995 SEP 30	0.0134 ± 0.0002	0.0150 ± 0.0002	0.0085 ± 0.0001	0.0365 ± 0.0001
	14.9	VLA 1998 MAY 31	0.0090 ± 0.0001	0.0095 ± 0.0001	0.0051 ± 0.0001	0.0233 ± 0.0001
	92.3	ALMA 2016.1.00164.S	0.0056 ± 0.0001	0.0043 ± 0.0001	0.0024 ± 0.0001	0.0119 ± 0.0001
	98.5	ALMA 2015.1.01177.S	0.0058 ± 0.0001	0.0045 ± 0.0001	0.0026 ± 0.0001	0.0127 ± 0.0001
	226	ALMA 2016.1.00164.S	0.0118 ± 0.0001	0.0091 ± 0.0001	0.0066 ± 0.0001	0.0213 ± 0.0001
	286	ALMA 2016.1.00164.S	0.0181 ± 0.0003	0.0141 ± 0.0003	0.0112 ± 0.0002	0.0337 ± 0.0001
	345	ALMA 2015.1.01593.S	0.0258 ± 0.0003	0.0235 ± 0.0003	0.0194 ± 0.0002	0.0525 ± 0.0001
Arp220	4.89	VLA 1984 DEC 03	0.0807 ± 0.0001	0.0536 ± 0.0001		
	8.43	VLA 1990 FEB 24	0.0669 ± 0.0003	0.0559 ± 0.0002		
	8.43	VLA 1990 MAR 04	0.0599 ± 0.0003	0.0503 ± 0.0002		
	8.43	VLA 1990 MAR 08	0.0633 ± 0.0001	0.0477 ± 0.0001		
	8.43	VLA 2002 APR 12	0.0604 ± 0.0005	0.0503 ± 0.0005		
	14.9	VLA 1984 DEC 03	0.042 ± 0.002	0.0292 ± 0.0006		
	14.9	VLA 1988 DEC 10	0.0400 ± 0.0008	0.027 ± 0.002		
	22.4	VLA 1984 DEC 03	0.0257 ± 0.0098	0.015 ± 0.008		
	99.1	ALMA 2017.1.00042.S	0.0274 ± 0.0001	0.0140 ± 0.0002		
	113	ALMA 2017.1.00042.S	0.0260 ± 0.0001	0.0131 ± 0.0001		
	220	ALMA 2017.1.00042.S	0.111 ± 0.002	0.036 ± 0.002		
	229	ALMA 2015.1.00113.S	0.138 ± 0.001	0.057 ± 0.001		
	346	ALMA 2015.1.00113.S	0.378 ± 0.003	0.179 ± 0.002		
	358	ALMA 2015.1.00736.S	0.432 ± 0.002	0.201 ± 0.002		
	440	ALMA 2015.1.00736.S	0.833 ± 0.006	0.418 ± 0.005		
	697	ALMA 2011.0.00175.S	4.12 ± 0.01	2.24 ± 0.01		
NGC4945	4.8	ATCA Lenc & Tingay (2009)				2.7 ± 0.3
	8.6	ATCA Roy et al. (2010)				1.3 ± 0.1
	8.3	ATCA Lenc & Tingay (2009)				1.4 ± 0.1
	20	ATCA Lenc & Tingay (2009)				0.8 ± 0.1
	20	ATCA Massardi et al. (2008)				0.73 ± 0.04
	85	ALMA Bendo et al. (2016)				0.36 ± 0.02
	230	SEST Wang et al. (2004)				1.3 ± 0.3
	230	SMA Chou et al. (2007)				1.3 ± 0.2
	345	APEX Weiß et al. (2008)				7.2 ± 0.8

Table A.1: The archival data used for the SED fits in Section 4.1.1. The first column shows the frequency of the observations. The second column provides the telescope name and the date of observation or project code, for the archival VLA and ALMA data respectively. In the case of NGC4945 archival data was not readily available, so we provide references to the flux densities used for the SED fit. The third, fourth, fifth, and sixth columns show the continuum flux density in regions A, B, C, and T, respectively, for the galaxies listed.

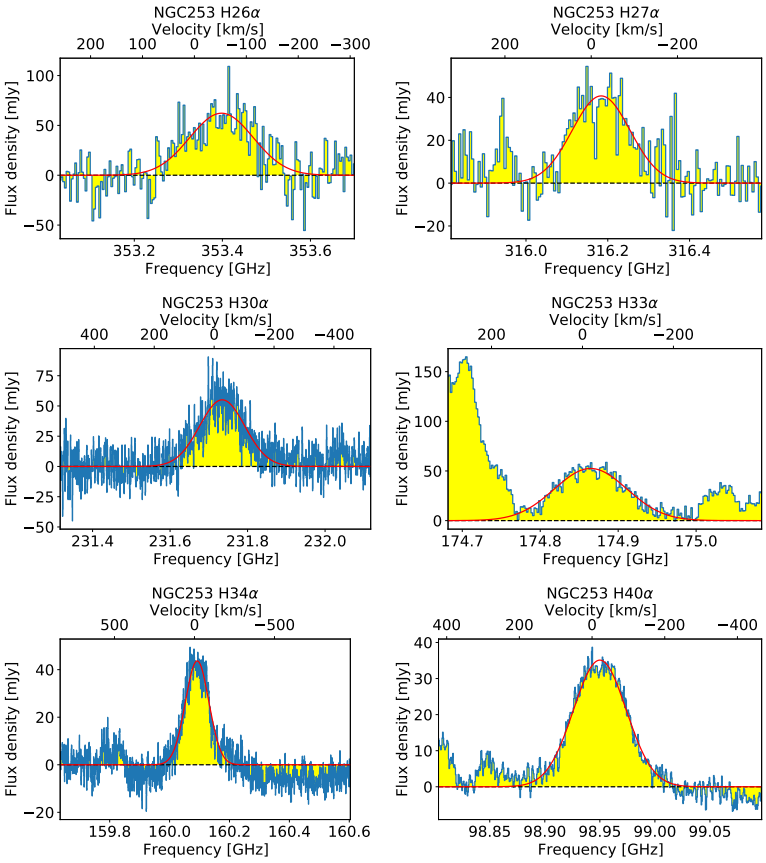

Figure A.8: Spectra of detected mm-RL in NGC253

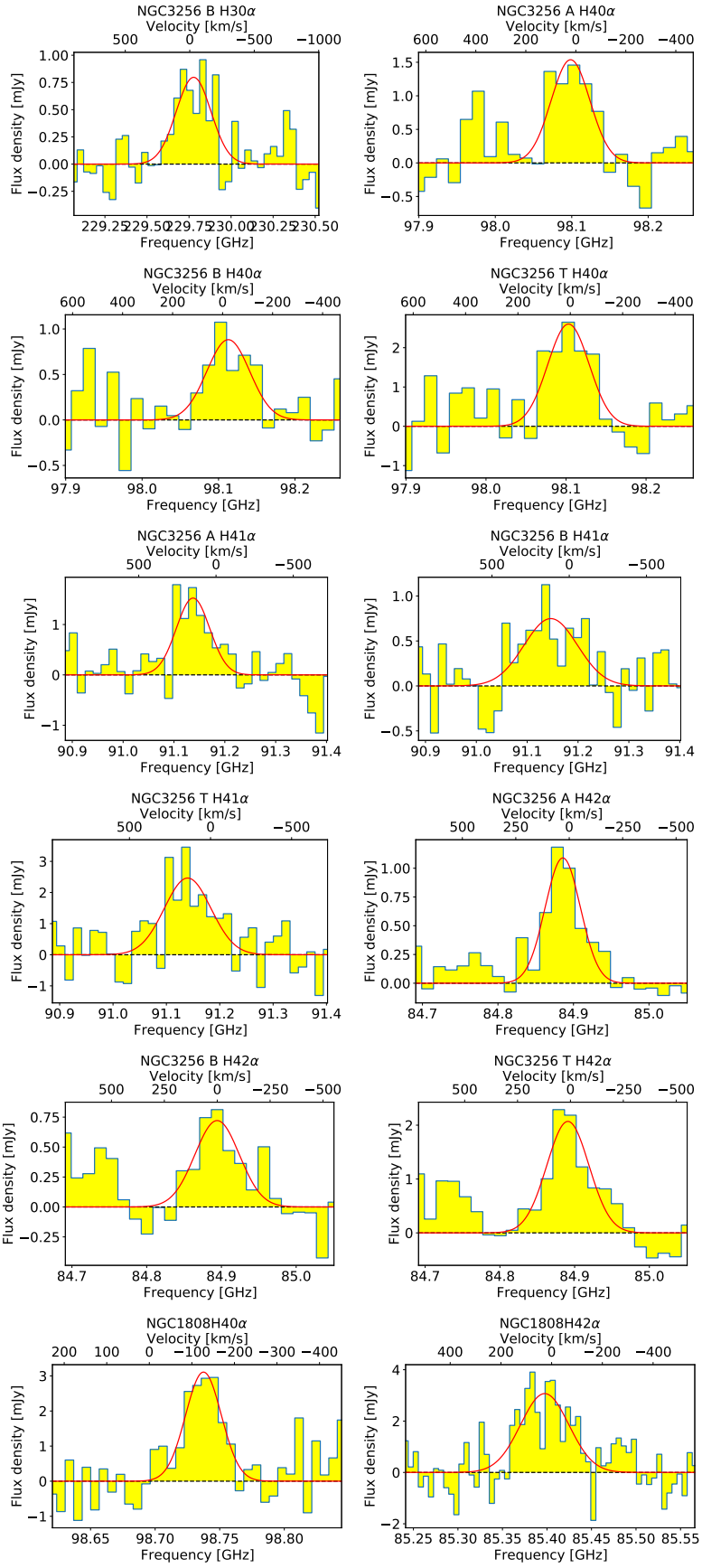

Figure A.9: Spectra of detected mm-RL in NGC3256 and NGC1808

APPENDIX B

Radio to Submillimeter SED Fits

To determine the level of the free-free continuum, we fit a three component SED covering radio to submm wavelengths. In this appendix we provide details about the SED fitting procedures for each galaxy in the ALMA archival sample.

M83 SED Fit

The data used to fit the SED of M83 is comprised of radio to sub-mm continuum maps. For the radio part of the SED, VLA archival data were used, with frequencies of 1.5 GHz, 4.8 GHz, 14.9 GHz and 22 GHz. For frequencies between 80 and 350 GHz, ALMA archival data were used. All maps have a similar resolution of 1-2 arcseconds, with the exception of the VLA continuum data at 1.5 GHz which has a resolution of $4\farcs2$. Thus, for the region surrounding the total mm-RL emission in M83, the continuum flux density in beam-matched (FWHM = 4.2 arcsec) images between 1.5 to 350 GHz is extracted. However, the apertures surrounding the individual sources which make up the nucleus, A, B, and C, have diameters of 3 arcsec. In their case, the continuum fluxes are extracted from the original data, without beam matching, and omitting the low resolution 1.5 GHz continuum VLA map.

The free-free fraction of the continuum and χ^2 plots corresponding to values of α and β varying from -0.3 to 1.0 and 0.5 to 1.3, respectively, are shown in the left panels of figure B.1 for regions A, B, C, and Total. The SED corresponding to the lowest χ^2 values are shown in the right panels of figure B.1.

NGC3256 SED Fit

For NGC3256, radio data for 4.8 GHz, 8.5 GHz and 14.9 GHz were acquired from the VLA archive. For frequencies between 80 and 350 GHz, ALMA archival data were used. The VLA archival data provides multiple radio maps of NGC3256 for each of the three frequencies. The flux density measured in regions A and B, corresponding to the Northern and Southern nuclei, varies by a factor of a few between different VLA maps taken at the same frequency. Therefore, the newest VLA data at 4.8 GHz, 8.5 GHz and 14.9 GHz were used for the SED fitting. Due to the high resolution of the 14.9 GHz data (FWHM = $0\farcs61 \times 0\farcs1$), beam matching was not performed on the rest of the radio maps, which have a resolution of 1-2 arcseconds. The free-free fraction of the continuum and χ^2 plots corresponding to

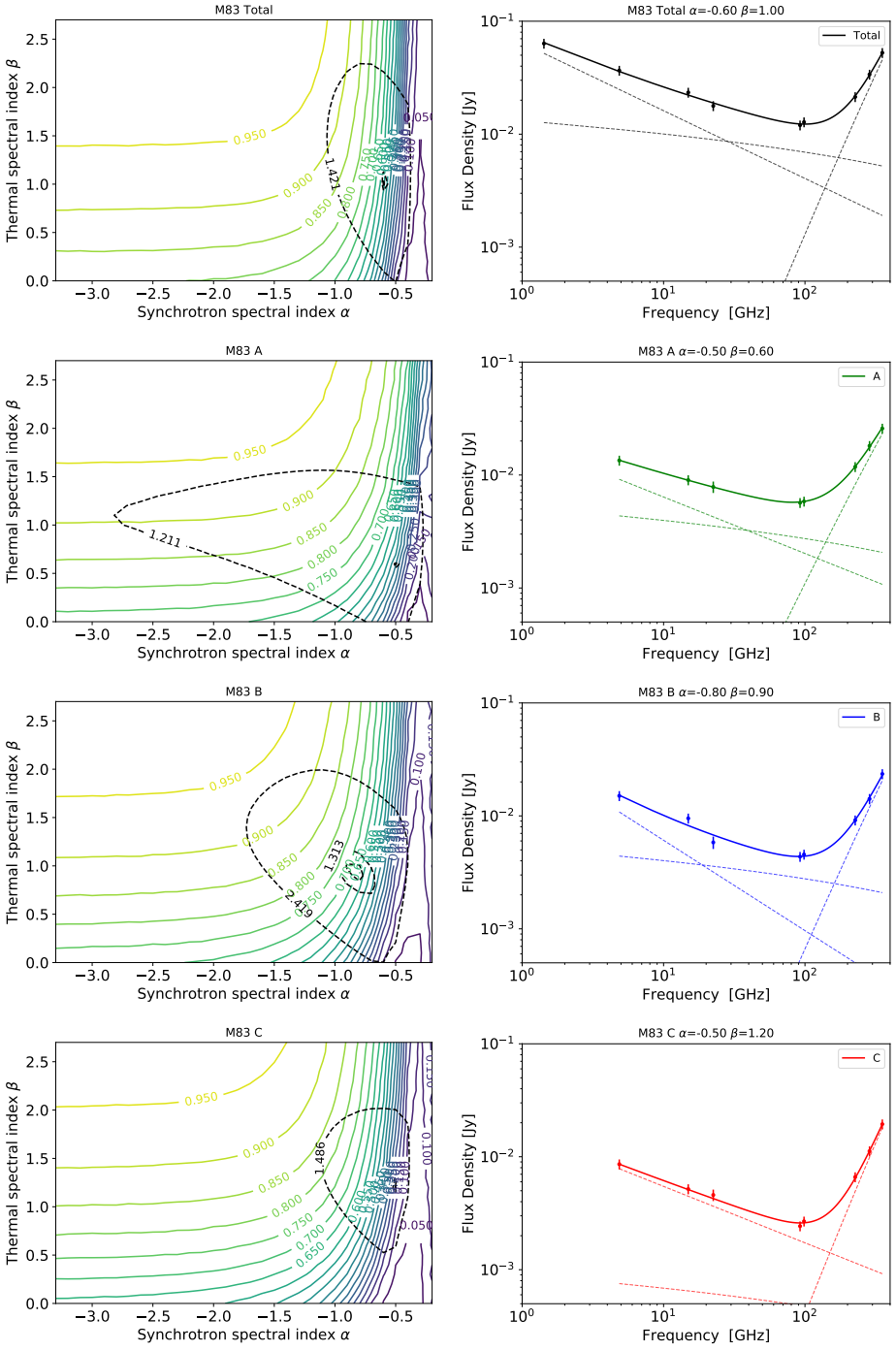

Figure B.1: Grids showing the free-free contribution to the overall continuum at 100GHz (solid lines) and the minimized χ^2 values of the SED fits (dotted lines) for different values of α and β, corresponding to sources Total, A, B, and C in M83 (left panels). SED fits using the values of α and β which correspond to the minimum χ^2 values (right panels).

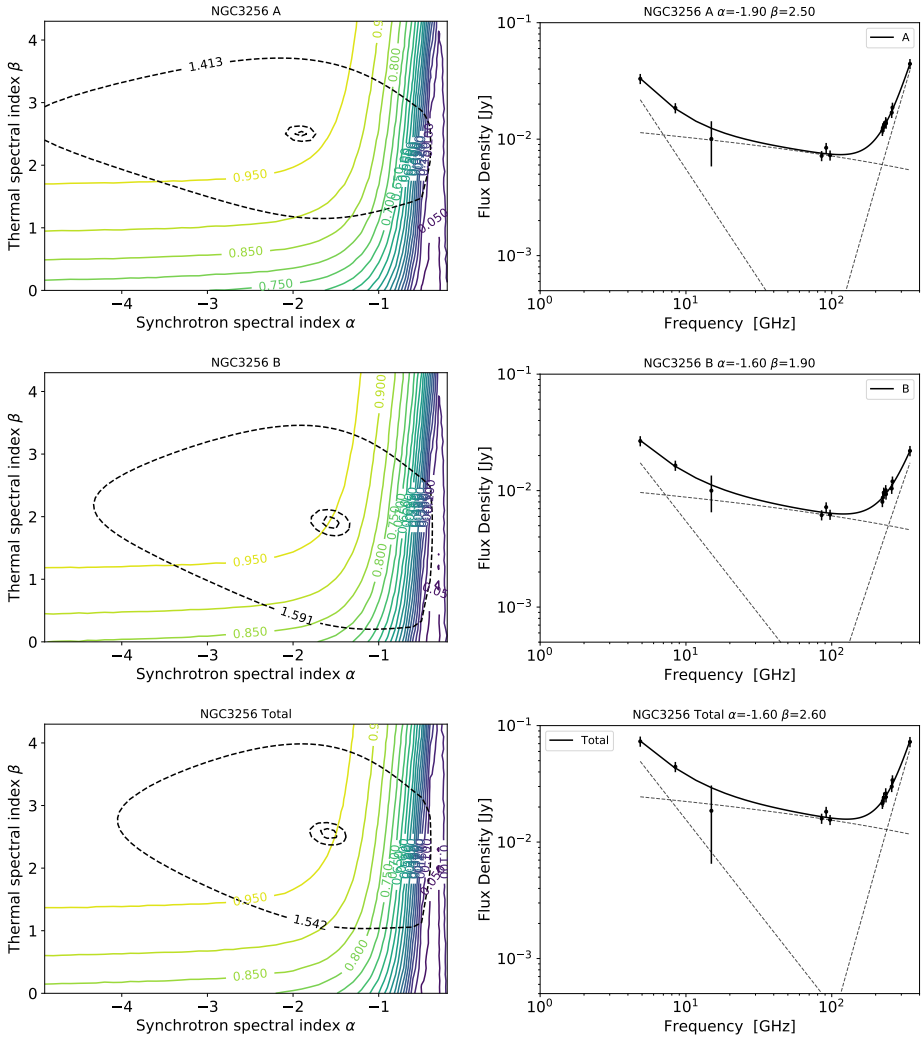

Figure B.2: Grids showing the free-free contribution to the overall continuum at 100GHz (solid lines) and the minimized χ^2 values of the SED fits (dotted lines) for different values of α and β, corresponding to sources A, B, and Total in M83 (left panels). SED fits using the values of α and β which correspond to the minimum χ^2 values (right panels).

values of α and β varying from -1.3 to -2.2 and 1.6 to 2.9, respectively, are shown in the left panels of figure B.2 for regions A, B, and Total.

NGC253 SED Fit

In the case of NGC253, radio continuum data from VLA archive, with frequencies of 1.6 GHz, 4.8 GHz, 8.5 GHz and 14.9 GHz were used, while for frequencies between 80 GHz to 350 GHz, continuum ALMA archival data were acquired. The free-free fraction of the continuum and χ^2 plot corresponding to values of α and β varying from -1.0 to -1.6 and 1.3 to 1.9, respectively, are shown in the left panel

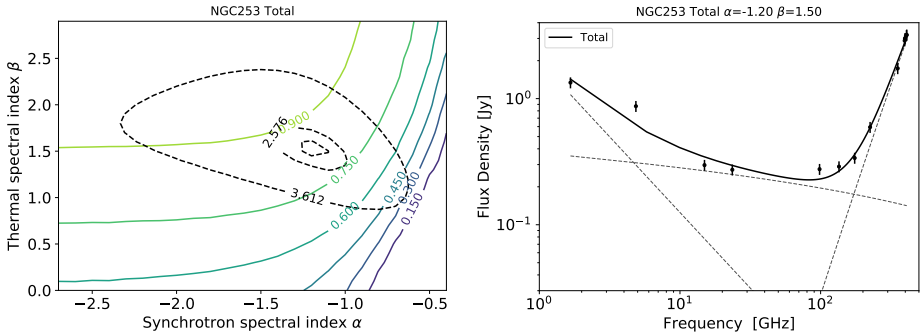

Figure B.3: Grid showing the free-free contribution to the overall continuum at 100GHz (solid lines) and the minimized χ^2 values of the SED fits (dotted lines) for different values of α and β, corresponding the the nucleus of NGC253 (left). SED fit using the values of α and β which correspond to the minimum χ^2 value (right).

of figure B.3 for regions A, B, and Total. The SED corresponding to the lowest χ^2 values are shown in the right panel of figure B.3.

Arp220 SED Fit

The radio data used in the SED fit of Arp220 consists of VLA archival data, at frequencies between 4.8 GHz and 22 GHz. For the millimeter part of the SED, ALMA archival data with frequencies between 99 GHz and 697 GHz are used. For the flux extraction and SED fitting, maps with resolutions below 0.″3 are used, in order to match as closely as possible the 0.″1 resolution of the mm-RL map. One exception is the 0.″6 resolution 4.8 GHz continuum VLA map, the only available map in the archive at this frequency. The free-free fraction of the continuum and χ^2 plot corresponding to values of α and β varying from -0.5 to -1.4 and 1.4 to 2.7, respectively, are shown in the left panel of figure B.4 for regions A and B. The SED corresponding to the lowest χ^2 values are shown in the right panel of figure B.4.

NGC5253 SED Fit

NGC5253 is a young starburst galaxy, with the age of a starburst having an age less than 15 Myr. The emission in the nucleus of this galaxy is completely dominated by free-free emission (Rodríguez-Rico et al., 2007). In this case, no SED fit converged, and we consider the continuum emission underlying the detected mm-RL to be purely free-free in origin.

NGC1808 SED Fit

For the case of NGC1808, the radio data for the SED fit consists of VLA archival maps, at frequencies between 1.5 GHz and 4.8 GHz. For the millimeter part of the SED, ALMA archival data with frequencies between 85 GHz and 490 GHz are used. Two apertures, named H40 and H42, which surround the H40α and H42α mm-RL emition are defined. The free-free fraction of the continuum and χ^2 plot corresponding to values of α and β varying from -0.5 to -1.0 and 1.4 to 2.0, respectively,

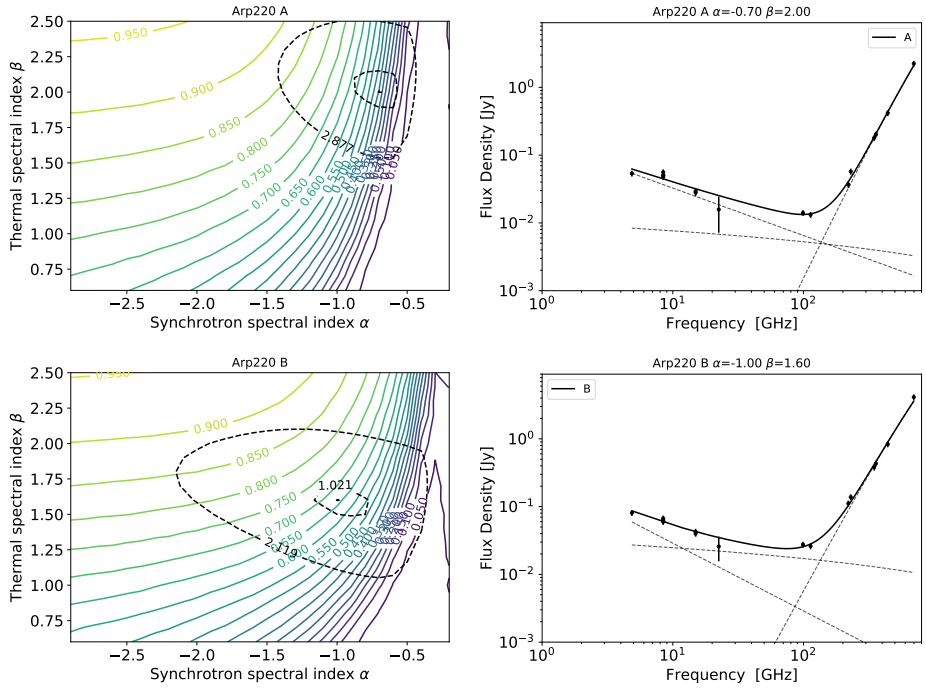

Figure B.4: Grids showing the free-free contribution to the overall continuum at 100GHz (solid lines) and the minimized χ^2 values of the SED fits (dotted lines) for different values of α and β, corresponding to sources A and B in Arp220 (left panels). SED fits using the values of α and β which correspond to the minimum χ^2 values (right panels).

are shown in the left panel of figure B.5 for regions H40 and H42. The SED corresponding to the lowest χ^2 values are shown in the right panel of figure B.5.

NGC4945 SED Fit

For this galaxy, no VLA archival data is available. Bendo et al. (2016) use radio and mm-data available in the literature. In our analysis, the same literature data is used to fit the SED as in Bendo et al. (2016), omitting the literature values for which no uncertainties are reported. For the radio spectrum, data at 4.8 GHz (Lenc & Tingay, 2009), 8.5 GHz (Lenc & Tingay, 2009; Roy et al., 2010), and 20 GHz (Massardi et al., 2008; Lenc & Tingay, 2009) are used. For millimeter and sub-mm wavelenghts, data at 85 GHz (Bendo et al., 2016), 230 GHz (Wang et al., 2004; Chou et al., 2007), and 345 GHz (Weiß et al., 2008) are used. Using these data, we apply the same procedures in fitting the SED as for the other galaxies in our sample. The free-free fraction of the continuum and χ^2 plot corresponding to values of α and β varying from -0.8 to -1.4 and 2.5 to 3.4, respectively, are shown in the left panel of figure B.6. The SED corresponding to the lowest χ^2 values are shown in the right panel of figure B.6.

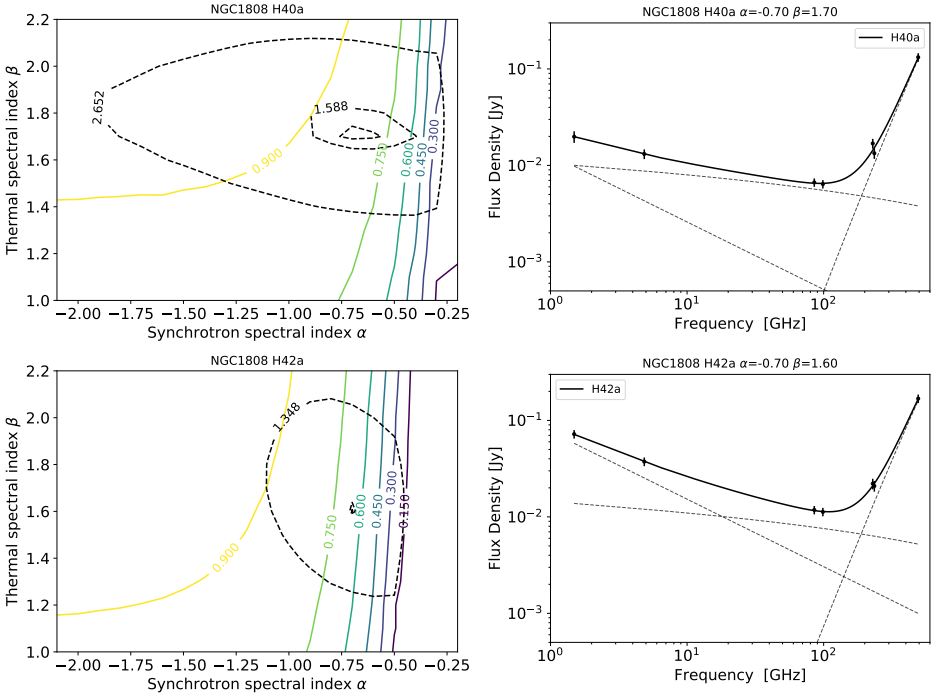

Figure B.5: Grids showing the free-free contribution to the overall continuum at 100GHz (solid lines) and the minimized χ^2 values of the SED fits (dotted lines) for different values of α and β, corresponding to regions H40 and H42 in NGC1808 (left panels). SED fits using the values of α and β which correspond to the minimum χ^2 values (right panels).

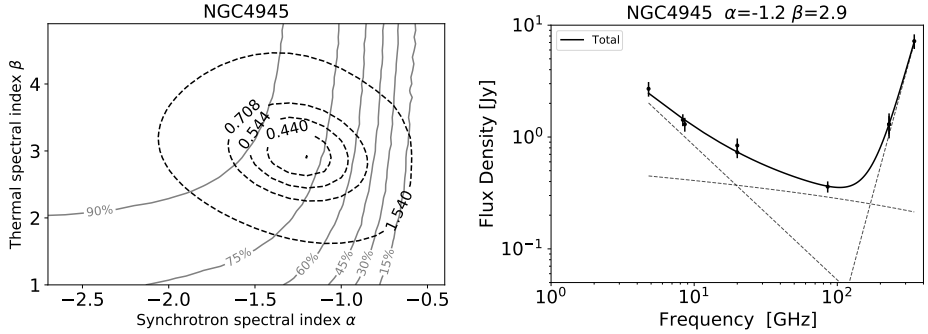

Figure B.6: Grid showing the free-free contribution to the overall continuum at 100GHz (solid lines) and the minimized χ^2 values of the SED fits (dotted lines) for different values of α and β, corresponding the the nucleus of NGC4945 (left). SED fit using the values of α and β which correspond to the minimum χ^2 value (right).

APPENDIX C

The joint probability distribution of $T_{\rm dust}$ and β

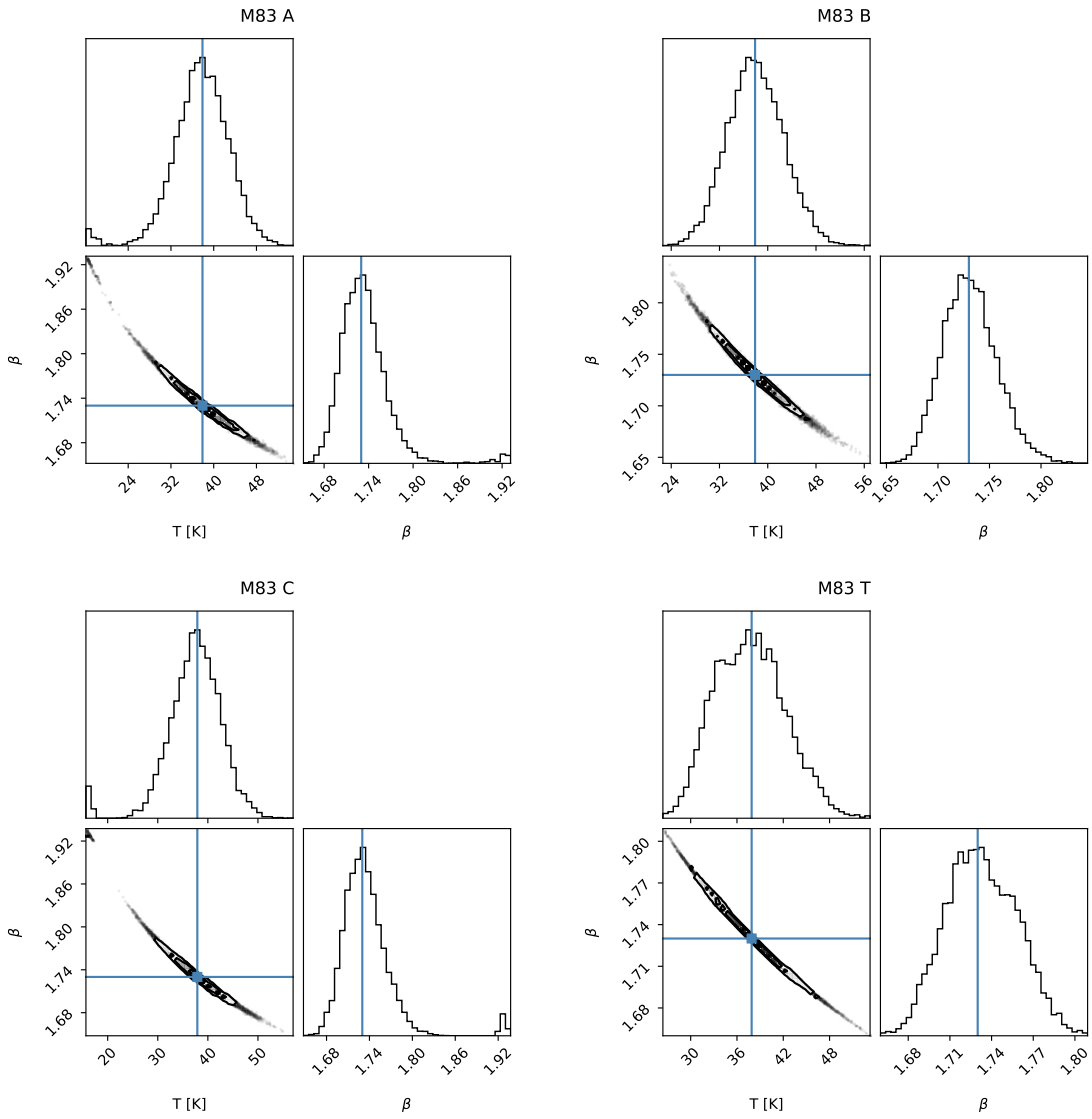

Figure C.1: The joint probability of $T_{\rm dust}$ and β, in the case of M83, resulting from fitting a single temperature modified black body model to the ALMA measured continuum emission of at GHz. The four panels show the posterior distribution for the A, B, C, and T (total) regions of M83. The fitting procedure is described in 4.3.1.

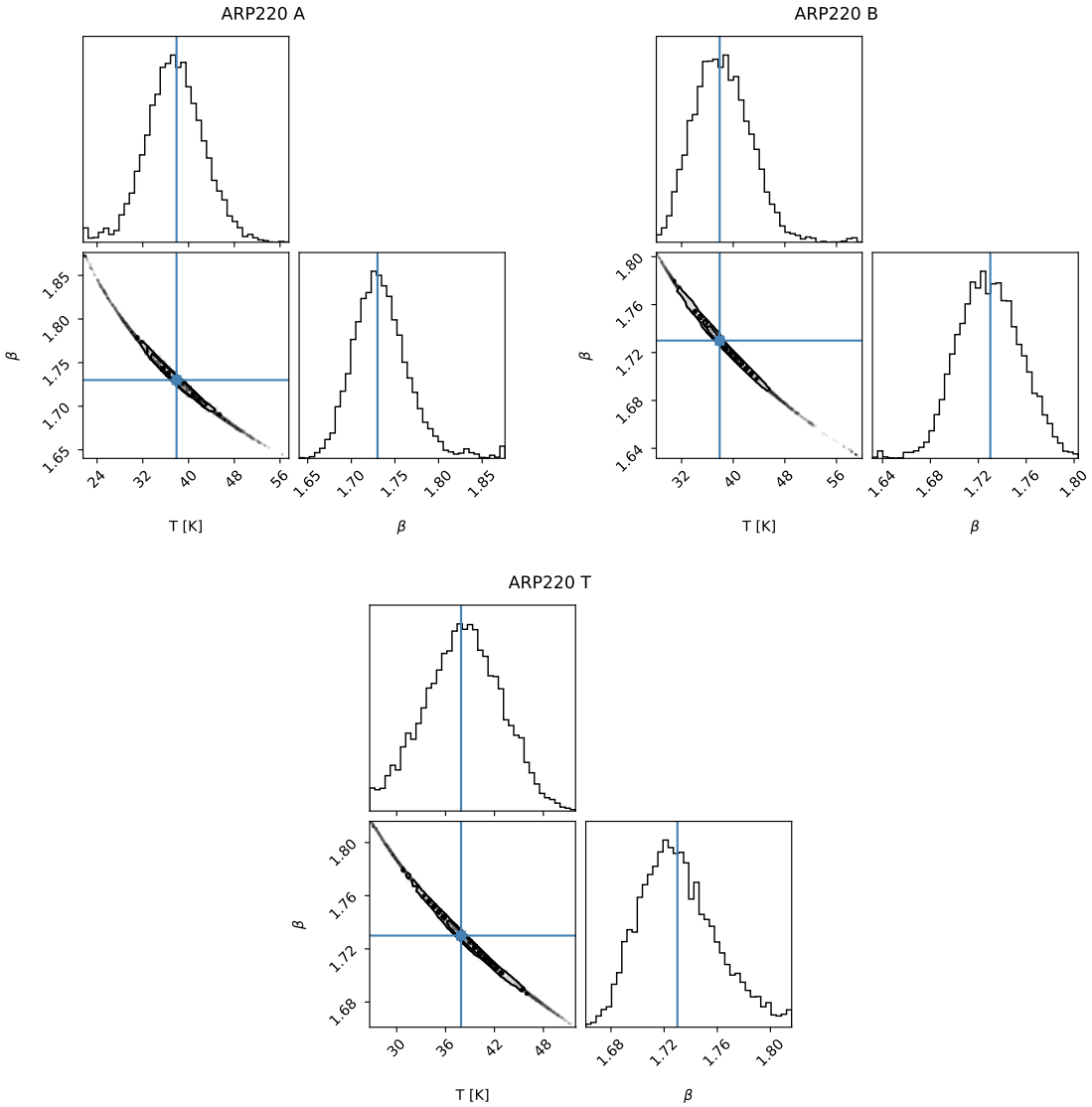

Figure C.2: Same as C.1. The panels show the results the A, B, and T (total) regions of Arp220. The fitting procedure is described in 4.3.1.

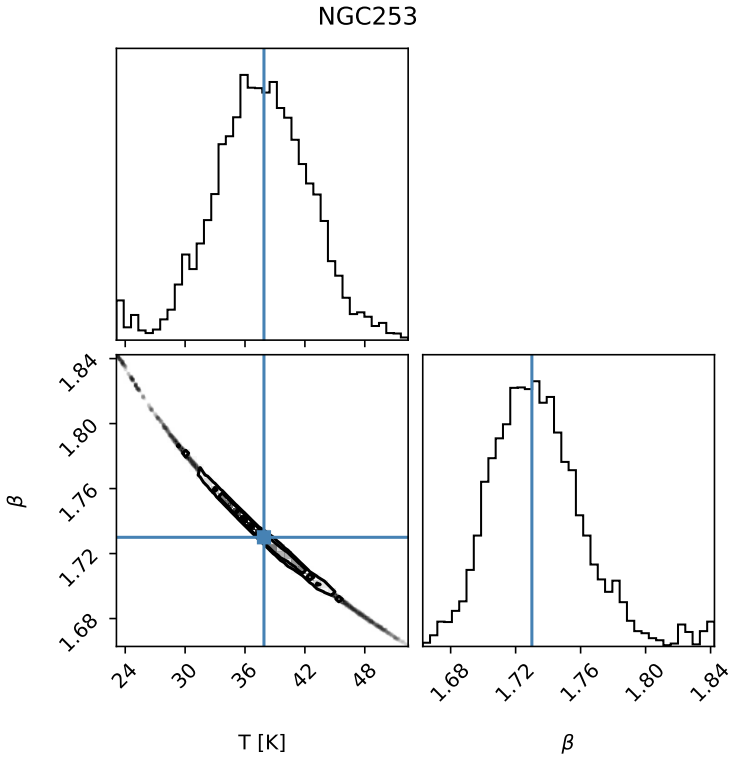

Figure C.3: Same as C.1, for NGC253. The fitting procedure is described in 4.3.1.

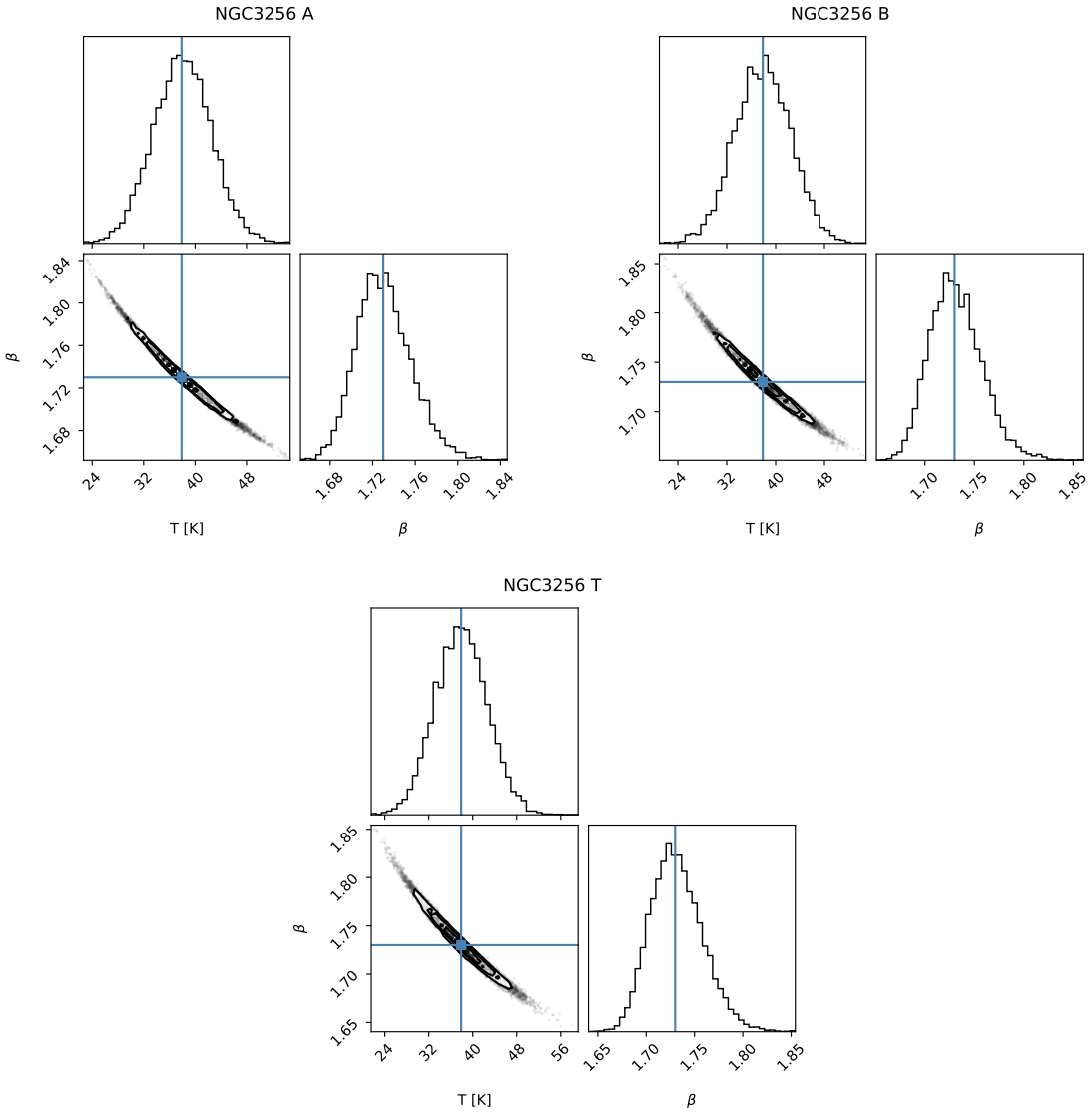

Figure C.4: Same as C.1. The panels show the results the A, B, and T (total) regions of NGC3256. The fitting procedure is described in 4.3.1.

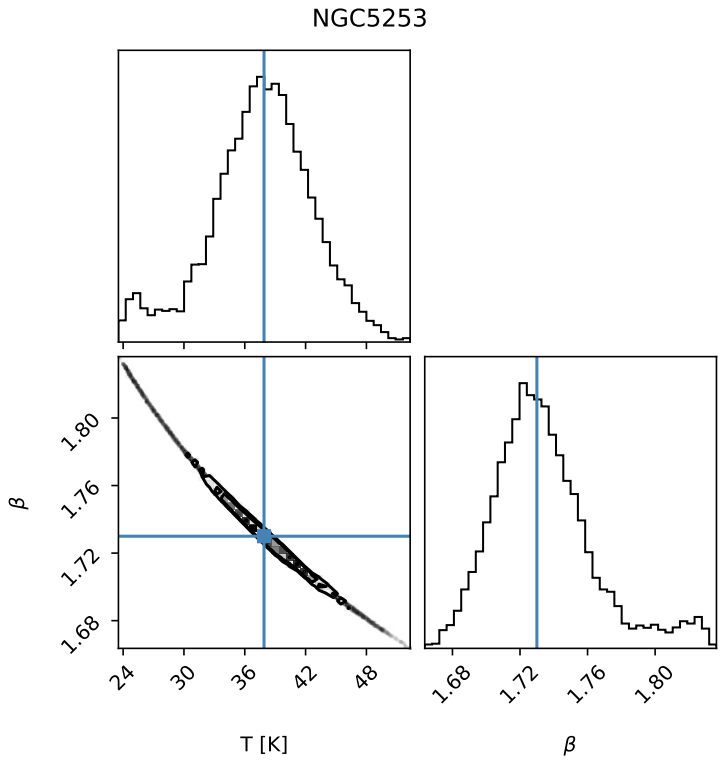

Figure C.5: Same as C.1, for NGC5253. The fitting procedure is described in 4.3.1.

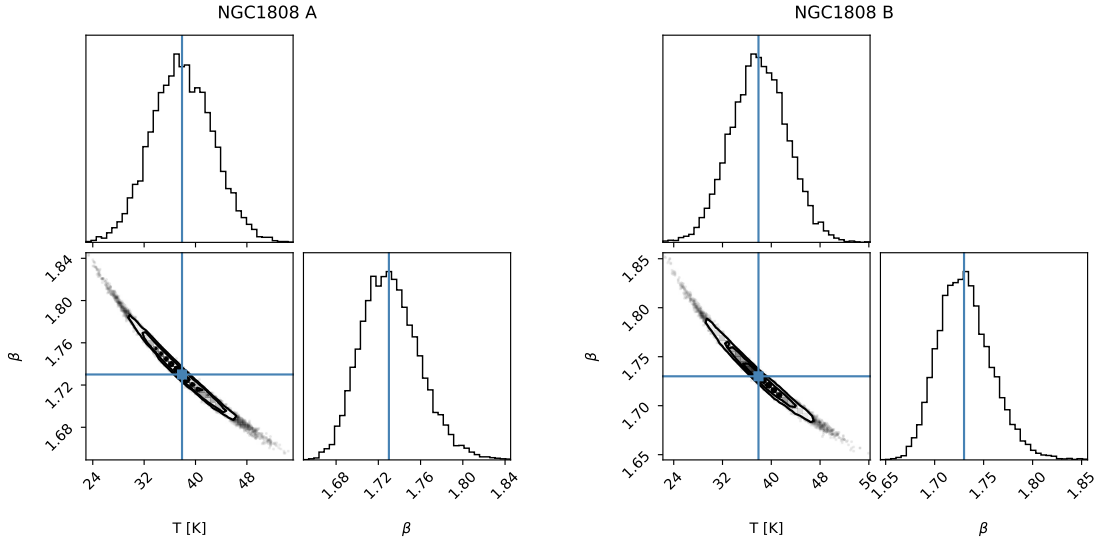

Figure C.6: Same as C.1. The panels show the results the A and B regions of NGC1808. The fitting procedure is described in 4.3.1.

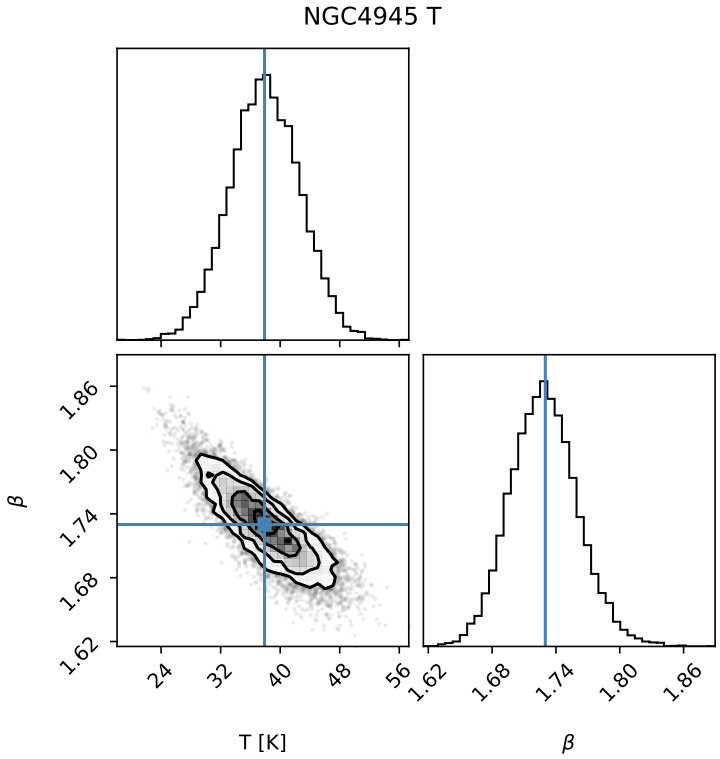

Figure C.7: Same as C.1, for NGC4945. The fitting procedure is described in 4.3.1.

APPENDIX D

Infrared SED Fitting of the IRAM Sample

D.1 The Optically Thick Model

D.2 The Optically Thin Model

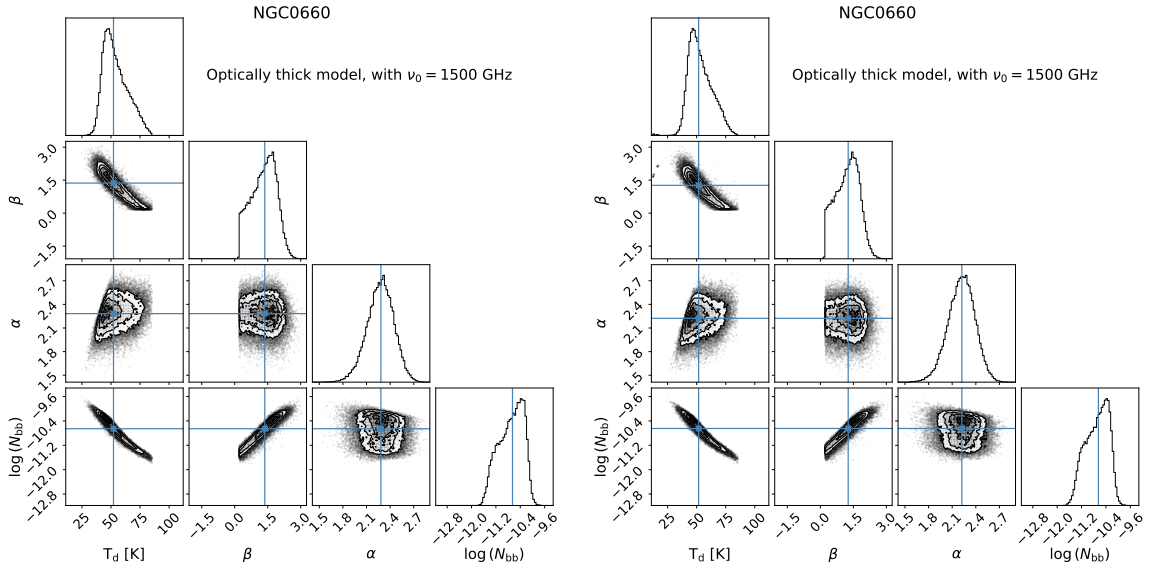

Figure D.1: The posterior probability distributions of the four parameters of our optically thick model, resulting from the MCMC fit of the model to the observed data. The highlights show the median values of the parameters. The left and right figures correspond to fits of models to fluxes originating from 25" and 27" diameter circular apertures, respectively. These apertures cover the regions we observed with the IRAM 30m telescope, at the H40α and H42α line frequencies, respectively. In this case, the ν_0 parameter was fixed at 1500 GHz.

Galaxy	ν_0 [GHz]:	1500	2000	3000	4000	5000
NGC0660	T_d [K]	$52.16^{+13.63}_{-8.22}$	$48.80^{+15.28}_{-9.41}$	$45.36^{+18.18}_{-10.80}$	$44.32^{+19.27}_{-11.69}$	$43.27^{+19.94}_{-11.68}$
	β	$1.37^{+0.52}_{-0.69}$	$1.33^{+0.52}_{-0.67}$	$1.27^{+0.55}_{-0.67}$	$1.23^{+0.59}_{-0.66}$	$1.22^{+0.60}_{-0.66}$
	α	$2.28^{+0.16}_{-0.17}$	$2.28^{+0.16}_{-0.17}$	$2.27^{+0.16}_{-0.17}$	$2.28^{+0.16}_{-0.17}$	$2.28^{+0.16}_{-0.17}$
	N_{bb}	$-10.66^{+0.37}_{-0.50}$	$-10.49^{+0.46}_{-0.60}$	$-10.27^{+0.62}_{-0.75}$	$-10.15^{+0.75}_{-0.85}$	$-10.04^{+0.83}_{-0.92}$
NGC1614	T_d [K]	$69.72^{+2.04}_{-2.17}$	$63.49^{+2.97}_{-3.12}$	$57.10^{+4.11}_{-4.48}$	$53.41^{+4.67}_{-5.04}$	$50.90^{+5.00}_{-5.26}$
	β	$2.11^{+0.15}_{-0.15}$	$1.63^{+0.13}_{-0.12}$	$1.44^{+0.15}_{-0.13}$	$1.41^{+0.17}_{-0.14}$	$1.42^{+0.19}_{-0.16}$
	α	$2.64^{+0.11}_{-0.11}$	$2.49^{+0.13}_{-0.13}$	$2.43^{+0.15}_{-0.15}$	$2.41^{+0.16}_{-0.15}$	$2.39^{+0.16}_{-0.15}$
	N_{bb}	$-11.19^{+0.04}_{-0.03}$	$-11.03^{+0.06}_{-0.06}$	$-10.79^{+0.12}_{-0.10}$	$-10.59^{+0.16}_{-0.13}$	$-10.43^{+0.20}_{-0.16}$
NGC2903	T_d [K]	$43.53^{+4.26}_{-4.26}$	$39.41^{+4.89}_{-5.33}$	$34.39^{+5.62}_{-5.68}$	$32.30^{+5.52}_{-5.51}$	$31.23^{+5.49}_{-5.25}$
	β	$2.07^{+0.28}_{-0.26}$	$1.96^{+0.33}_{-0.27}$	$1.93^{+0.37}_{-0.30}$	$1.92^{+0.39}_{-0.31}$	$1.93^{+0.40}_{-0.32}$
	α	$1.95^{+0.08}_{-0.08}$	$1.95^{+0.08}_{-0.08}$	$1.96^{+0.08}_{-0.08}$	$1.95^{+0.08}_{-0.08}$	$1.96^{+0.07}_{-0.08}$
	N_{bb}	$-10.67^{+0.21}_{-0.20}$	$-10.45^{+0.31}_{-0.25}$	$-10.06^{+0.44}_{-0.35}$	$-9.79^{+0.50}_{-0.40}$	$-9.58^{+0.55}_{-0.44}$
IC694	T_d [K]	$73.29^{+1.61}_{-1.76}$	$68.66^{+2.13}_{-2.45}$	$63.85^{+2.59}_{-3.04}$	$60.81^{+2.84}_{-3.41}$	$58.76^{+3.05}_{-3.68}$
	β	$2.20^{+0.15}_{-0.15}$	$1.64^{+0.11}_{-0.10}$	$1.37^{+0.09}_{-0.08}$	$1.31^{+0.10}_{-0.08}$	$1.29^{+0.11}_{-0.09}$
	α	$3.44^{+0.13}_{-0.13}$	$3.30^{+0.14}_{-0.15}$	$3.27^{+0.15}_{-0.16}$	$3.25^{+0.15}_{-0.17}$	$3.24^{+0.16}_{-0.17}$
	N_{bb}	$-10.89^{+0.03}_{-0.03}$	$-10.76^{+0.04}_{-0.04}$	$-10.56^{+0.07}_{-0.05}$	$-10.41^{+0.09}_{-0.07}$	$-10.28^{+0.11}_{-0.08}$
NGC4102	T_d [K]	$52.57^{+1.57}_{-1.53}$	$45.44^{+1.69}_{-1.55}$	$37.93^{+2.08}_{-1.81}$	$34.59^{+2.25}_{-1.94}$	$32.88^{+2.30}_{-1.98}$
	β	$2.16^{+0.16}_{-0.16}$	$1.98^{+0.14}_{-0.14}$	$1.97^{+0.16}_{-0.16}$	$2.01^{+0.18}_{-0.18}$	$2.04^{+0.19}_{-0.19}$
	α	$2.52^{+0.08}_{-0.07}$	$2.41^{+0.06}_{-0.06}$	$2.37^{+0.05}_{-0.05}$	$2.36^{+0.05}_{-0.05}$	$2.36^{+0.05}_{-0.05}$
	N_{bb}	$-10.59^{+0.04}_{-0.04}$	$-10.32^{+0.06}_{-0.06}$	$-9.87^{+0.10}_{-0.11}$	$-9.54^{+0.14}_{-0.15}$	$-9.28^{+0.18}_{-0.18}$
NGC4418	T_d [K]	$77.65^{+1.60}_{-1.75}$	$74.11^{+1.85}_{-2.10}$	$70.06^{+2.14}_{-2.49}$	$67.78^{+2.35}_{-2.68}$	$66.38^{+2.41}_{-2.72}$
	β	$1.66^{+0.14}_{-0.13}$	$1.31^{+0.09}_{-0.09}$	$1.13^{+0.07}_{-0.07}$	$1.08^{+0.07}_{-0.07}$	$1.05^{+0.07}_{-0.07}$
	α	$3.33^{+0.12}_{-0.13}$	$3.27^{+0.13}_{-0.14}$	$3.26^{+0.14}_{-0.14}$	$3.25^{+0.14}_{-0.14}$	$3.25^{+0.14}_{-0.14}$
	N_{bb}	$-11.29^{+0.03}_{-0.02}$	$-11.18^{+0.03}_{-0.03}$	$-11.02^{+0.05}_{-0.04}$	$-10.90^{+0.06}_{-0.05}$	$-10.81^{+0.07}_{-0.06}$

Table D.1: The parameter values resulting from the optically thick SED model fits to the observed emission from our galaxies. The first two columns list the name of the galaxy and the parameters of the model, while the rest of the columns show the values of the parameters resulting from the optically thick SED model fits, where ν_0 was fixed to the values shown in the table header. The models here were fit to flux densities measured in 25" diameter circular regions, covering the IRAM 30m observations at the H40α line frequency.

Galaxy	ν_0 [GHz]:	1500	2000	3000	4000	5000
NGC0660	T_d [K]	$51.70^{+12.70}_{-7.99}$	$48.82^{+14.69}_{-9.22}$	$45.62^{+17.14}_{-10.36}$	$44.47^{+17.93}_{-11.14}$	$43.64^{+18.44}_{-11.24}$
	β	$1.26^{+0.49}_{-0.64}$	$1.21^{+0.51}_{-0.62}$	$1.18^{+0.53}_{-0.62}$	$1.14^{+0.56}_{-0.61}$	$1.13^{+0.56}_{-0.61}$
	α	$2.22^{+0.16}_{-0.18}$	$2.22^{+0.16}_{-0.17}$	$2.22^{+0.16}_{-0.17}$	$2.22^{+0.16}_{-0.17}$	$2.22^{+0.16}_{-0.17}$
	N_{bb}	$-10.65^{+0.34}_{-0.47}$	$-10.51^{+0.44}_{-0.56}$	$-10.30^{+0.58}_{-0.70}$	$-10.18^{+0.70}_{-0.77}$	$-10.08^{+0.77}_{-0.84}$
NGC1614	T_d [K]	$68.79^{+2.09}_{-2.20}$	$62.13^{+3.03}_{-3.14}$	$55.09^{+4.36}_{-4.48}$	$50.90^{+5.04}_{-4.85}$	$48.30^{+5.29}_{-4.98}$
	β	$2.14^{+0.15}_{-0.15}$	$1.66^{+0.13}_{-0.13}$	$1.48^{+0.16}_{-0.14}$	$1.48^{+0.18}_{-0.16}$	$1.50^{+0.20}_{-0.18}$
	α	$2.60^{+0.11}_{-0.11}$	$2.44^{+0.13}_{-0.12}$	$2.36^{+0.15}_{-0.14}$	$2.33^{+0.16}_{-0.13}$	$2.31^{+0.16}_{-0.13}$
	N_{bb}	$-11.17^{+0.04}_{-0.03}$	$-11.00^{+0.06}_{-0.06}$	$-10.73^{+0.12}_{-0.11}$	$-10.51^{+0.17}_{-0.15}$	$-10.33^{+0.21}_{-0.18}$
NGC2903	T_d [K]	$43.18^{+4.17}_{-4.22}$	$39.04^{+4.93}_{-5.34}$	$34.32^{+5.59}_{-5.71}$	$32.27^{+5.57}_{-5.55}$	$31.16^{+5.47}_{-5.31}$
	β	$2.02^{+0.28}_{-0.26}$	$1.92^{+0.33}_{-0.27}$	$1.89^{+0.38}_{-0.29}$	$1.89^{+0.39}_{-0.31}$	$1.89^{+0.40}_{-0.32}$
	α	$1.93^{+0.08}_{-0.08}$	$1.93^{+0.08}_{-0.08}$	$1.93^{+0.08}_{-0.08}$	$1.93^{+0.08}_{-0.08}$	$1.93^{+0.08}_{-0.08}$
	N_{bb}	$-10.65^{+0.21}_{-0.19}$	$-10.42^{+0.31}_{-0.25}$	$-10.05^{+0.44}_{-0.34}$	$-9.79^{+0.51}_{-0.40}$	$-9.57^{+0.56}_{-0.44}$
IC694	T_d [K]	$72.70^{+1.66}_{-1.79}$	$67.84^{+2.25}_{-2.56}$	$62.83^{+2.83}_{-3.33}$	$59.75^{+3.06}_{-3.75}$	$57.68^{+3.31}_{-4.02}$
	β	$2.19^{+0.15}_{-0.15}$	$1.64^{+0.11}_{-0.10}$	$1.37^{+0.10}_{-0.09}$	$1.32^{+0.11}_{-0.09}$	$1.31^{+0.12}_{-0.10}$
	α	$3.36^{+0.12}_{-0.12}$	$3.21^{+0.14}_{-0.15}$	$3.17^{+0.16}_{-0.17}$	$3.16^{+0.16}_{-0.17}$	$3.15^{+0.16}_{-0.17}$
	N_{bb}	$-10.87^{+0.03}_{-0.03}$	$-10.73^{+0.05}_{-0.04}$	$-10.53^{+0.07}_{-0.06}$	$-10.37^{+0.10}_{-0.08}$	$-10.24^{+0.12}_{-0.09}$
NGC4102	T_d [K]	$52.18^{+1.54}_{-1.52}$	$45.19^{+1.69}_{-1.55}$	$37.90^{+2.07}_{-1.83}$	$34.62^{+2.24}_{-1.95}$	$32.96^{+2.25}_{-2.00}$
	β	$2.14^{+0.16}_{-0.16}$	$1.96^{+0.14}_{-0.14}$	$1.95^{+0.16}_{-0.16}$	$1.99^{+0.18}_{-0.18}$	$2.02^{+0.19}_{-0.19}$
	α	$2.50^{+0.07}_{-0.07}$	$2.39^{+0.06}_{-0.06}$	$2.35^{+0.05}_{-0.05}$	$2.35^{+0.05}_{-0.05}$	$2.35^{+0.05}_{-0.05}$
	N_{bb}	$-10.58^{+0.04}_{-0.04}$	$-10.30^{+0.06}_{-0.06}$	$-9.86^{+0.10}_{-0.11}$	$-9.54^{+0.14}_{-0.15}$	$-9.29^{+0.18}_{-0.17}$
NGC4418	T_d [K]	$77.49^{+1.62}_{-1.81}$	$73.89^{+1.93}_{-2.14}$	$69.86^{+2.19}_{-2.56}$	$67.54^{+2.40}_{-2.71}$	$66.08^{+2.51}_{-2.86}$
	β	$1.67^{+0.13}_{-0.13}$	$1.31^{+0.09}_{-0.09}$	$1.13^{+0.08}_{-0.07}$	$1.08^{+0.07}_{-0.07}$	$1.06^{+0.07}_{-0.07}$
	α	$3.30^{+0.13}_{-0.13}$	$3.24^{+0.13}_{-0.14}$	$3.23^{+0.14}_{-0.15}$	$3.22^{+0.14}_{-0.14}$	$3.22^{+0.14}_{-0.14}$
	N_{bb}	$-11.28^{+0.03}_{-0.02}$	$-11.17^{+0.03}_{-0.03}$	$-11.01^{+0.05}_{-0.04}$	$-10.90^{+0.06}_{-0.05}$	$-10.80^{+0.07}_{-0.06}$

Table D.2: The parameter values resulting from the optically thick SED model fits to the observed emission from our galaxies. The first two columns list the name of the galaxy and the parameters of the model, while the rest of the columns show the values of the parameters resulting from the optically thick SED model fits, where ν_0 was fixed to the values shown in the table header. The models here were fit to flux densities measured in 27" diameter circular regions, covering the IRAM 30m observations at the H42α line frequency.

Galaxy	Parameters	25” aperture	27” aperture
NGC0660	$T_{\rm d}$ [K]	$38.62^{+17.45}_{-9.75}$	$39.42^{+16.64}_{-9.67}$
	β	$1.25^{+0.63}_{-0.65}$	$1.14^{+0.59}_{-0.61}$
	α	$2.27^{+0.16}_{-0.18}$	$2.22^{+0.16}_{-0.17}$
	$N_{\rm bb}$	$-14.57^{+1.47}_{-1.48}$	$-14.24^{+1.36}_{-1.41}$
NGC1614	$T_{\rm d}$ [K]	$42.98^{+4.80}_{-4.23}$	$41.01^{+4.47}_{-3.94}$
	β	$1.52^{+0.22}_{-0.21}$	$1.61^{+0.22}_{-0.21}$
	α	$2.33^{+0.15}_{-0.13}$	$2.27^{+0.14}_{-0.11}$
	$N_{\rm bb}$	$-15.89^{+0.55}_{-0.60}$	$-16.11^{+0.57}_{-0.60}$
NGC2903	$T_{\rm d}$ [K]	$28.94^{+4.77}_{-4.49}$	$28.94^{+4.71}_{-4.50}$
	β	$1.96^{+0.41}_{-0.34}$	$1.92^{+0.41}_{-0.33}$
	α	$1.95^{+0.08}_{-0.08}$	$1.93^{+0.08}_{-0.08}$
	$N_{\rm bb}$	$-16.75^{+0.79}_{-0.95}$	$-16.61^{+0.77}_{-0.95}$
IC694	$T_{\rm d}$ [K]	$50.86^{+3.32}_{-3.76}$	$49.73^{+3.57}_{-4.14}$
	β	$1.31^{+0.14}_{-0.12}$	$1.33^{+0.17}_{-0.13}$
	α	$3.20^{+0.16}_{-0.17}$	$3.09^{+0.17}_{-0.18}$
	$N_{\rm bb}$	$-15.05^{+0.33}_{-0.39}$	$-15.09^{+0.35}_{-0.45}$
NGC4102	$T_{\rm d}$ [K]	$29.86^{+2.00}_{-1.75}$	$29.93^{+2.03}_{-1.73}$
	β	$2.12^{+0.21}_{-0.21}$	$2.10^{+0.21}_{-0.21}$
	α	$2.37^{+0.05}_{-0.05}$	$2.36^{+0.05}_{-0.05}$
	$N_{\rm bb}$	$-17.01^{+0.58}_{-0.57}$	$-16.93^{+0.59}_{-0.57}$
NGC4418	$T_{\rm d}$ [K]	$59.67^{+2.70}_{-2.98}$	$59.42^{+2.71}_{-2.99}$
	β	$0.99^{+0.09}_{-0.08}$	$1.00^{+0.09}_{-0.08}$
	α	$3.23^{+0.14}_{-0.15}$	$3.20^{+0.14}_{-0.14}$
	$N_{\rm bb}$	$-14.50^{+0.23}_{-0.25}$	$-14.50^{+0.23}_{-0.25}$

Table D.3: The parameter values resulting from fitting the optically thin SED models to the observed emission from our galaxies. The first two columns show the target galaxies and the parameter names. The last two columns show the values of the parameters, resulting from fitting the optically thin SED models to flux densities measured in 25” and 27” diameter apertures, centered on our IRAM 30m observations. The two aperture diameters are the FWHM of the IRAM 30m beam when observing at the H40α and H42α line frequencies.

Galaxy	Model	Optically thick, with ν_0 values in GHz:					Optically thin
		1500	2000	3000	4000	5000	
NGC 0660	$\log(L_{\rm TIR})^a$	$9.86^{+0.14}_{-0.14}$	$9.87^{+0.15}_{-0.14}$	$9.87^{+0.16}_{-0.14}$	$9.87^{+0.15}_{-0.15}$	$9.87^{+0.16}_{-0.14}$	$9.88^{+0.15}_{-0.12}$
	$\rm SFR_{TIR}{}^a$	$1.07^{+0.35}_{-0.34}$	$1.11^{+0.38}_{-0.36}$	$1.10^{+0.40}_{-0.37}$	$1.10^{+0.39}_{-0.38}$	$1.09^{+0.40}_{-0.36}$	$1.12^{+0.39}_{-0.32}$
	$\log(L_{\rm TIR})^b$	$9.84^{+0.14}_{-0.13}$	$9.85^{+0.15}_{-0.13}$	$9.86^{+0.15}_{-0.13}$	$9.85^{+0.15}_{-0.13}$	$9.85^{+0.15}_{-0.13}$	$9.86^{+0.14}_{-0.12}$
	$\rm SFR_{TIR}{}^b$	$1.03^{+0.33}_{-0.30}$	$1.05^{+0.36}_{-0.32}$	$1.06^{+0.36}_{-0.33}$	$1.06^{+0.38}_{-0.32}$	$1.06^{+0.37}_{-0.32}$	$1.07^{+0.36}_{-0.30}$
NGC 1614	$\log(L_{\rm TIR})^a$	$11.66^{+0.02}_{-0.02}$	$11.66^{+0.02}_{-0.02}$	$11.66^{+0.02}_{-0.03}$	$11.65^{+0.02}_{-0.03}$	$11.65^{+0.03}_{-0.03}$	$11.64^{+0.03}_{-0.02}$
	$\rm SFR_{TIR}{}^a$	$68.38^{+2.46}_{-2.60}$	$67.87^{+3.10}_{-3.29}$	$67.12^{+3.67}_{-3.98}$	$66.66^{+3.77}_{-4.24}$	$66.22^{+3.99}_{-4.19}$	$64.75^{+4.17}_{-3.61}$
	$\log(L_{\rm TIR})^b$	$11.66^{+0.02}_{-0.02}$	$11.66^{+0.02}_{-0.02}$	$11.65^{+0.03}_{-0.02}$	$11.64^{+0.03}_{-0.03}$	$11.64^{+0.03}_{-0.03}$	$11.64^{+0.03}_{-0.02}$
	$\rm SFR_{TIR}{}^b$	$68.62^{+2.66}_{-2.61}$	$67.62^{+3.17}_{-3.47}$	$66.31^{+3.91}_{-3.85}$	$65.50^{+3.92}_{-4.05}$	$65.13^{+4.16}_{-4.10}$	$64.24^{+3.90}_{-3.59}$
NGC 2903	$\log(L_{\rm TIR})^a$	$9.63^{+0.05}_{-0.05}$	$9.64^{+0.05}_{-0.05}$	$9.65^{+0.05}_{-0.05}$	$9.64^{+0.05}_{-0.05}$	$9.64^{+0.05}_{-0.05}$	$9.63^{+0.05}_{-0.04}$
	$\rm SFR_{TIR}{}^a$	$0.64^{+0.07}_{-0.07}$	$0.65^{+0.08}_{-0.07}$	$0.66^{+0.08}_{-0.07}$	$0.65^{+0.08}_{-0.07}$	$0.65^{+0.07}_{-0.07}$	$0.64^{+0.07}_{-0.07}$
	$\log(L_{\rm TIR})^b$	$9.63^{+0.05}_{-0.05}$	$9.65^{+0.05}_{-0.05}$	$9.65^{+0.05}_{-0.05}$	$9.65^{+0.05}_{-0.05}$	$9.64^{+0.05}_{-0.05}$	$9.64^{+0.05}_{-0.05}$
	$\rm SFR_{TIR}{}^b$	$0.64^{+0.07}_{-0.07}$	$0.66^{+0.08}_{-0.07}$	$0.66^{+0.08}_{-0.08}$	$0.66^{+0.08}_{-0.07}$	$0.65^{+0.08}_{-0.08}$	$0.65^{+0.08}_{-0.07}$
NGC 3690	$\log(L_{\rm TIR})^a$	$11.79^{+0.01}_{-0.01}$	$11.80^{+0.02}_{-0.02}$	$11.81^{+0.02}_{-0.02}$	$11.81^{+0.02}_{-0.02}$	$11.81^{+0.02}_{-0.02}$	$11.81^{+0.02}_{-0.02}$
	$\rm SFR_{TIR}{}^a$	$91.36^{+2.93}_{-3.10}$	$94.33^{+3.48}_{-3.61}$	$95.80^{+3.98}_{-3.97}$	$96.17^{+3.93}_{-4.18}$	$96.24^{+3.98}_{-4.29}$	$95.81^{+4.35}_{-4.88}$
	$\log(L_{\rm TIR})^b$	$11.80^{+0.01}_{-0.01}$	$11.81^{+0.02}_{-0.02}$	$11.82^{+0.02}_{-0.02}$	$11.82^{+0.02}_{-0.02}$	$11.82^{+0.02}_{-0.02}$	$11.81^{+0.02}_{-0.02}$
	$\rm SFR_{TIR}{}^b$	$93.58^{+3.12}_{-3.19}$	$96.25^{+3.68}_{-3.93}$	$97.35^{+4.13}_{-4.49}$	$97.55^{+4.17}_{-4.66}$	$97.32^{+4.17}_{-4.64}$	$96.56^{+4.35}_{-5.31}$
NGC 4102	$\log(L_{\rm TIR})^a$	$10.61^{+0.02}_{-0.02}$	$10.60^{+0.02}_{-0.02}$	$10.60^{+0.02}_{-0.02}$	$10.60^{+0.02}_{-0.02}$	$10.60^{+0.02}_{-0.02}$	$10.60^{+0.02}_{-0.02}$
	$\rm SFR_{TIR}{}^a$	$5.99^{+0.28}_{-0.28}$	$5.94^{+0.26}_{-0.25}$	$5.92^{+0.25}_{-0.24}$	$5.92^{+0.25}_{-0.24}$	$5.92^{+0.24}_{-0.25}$	$5.90^{+0.25}_{-0.24}$
	$\log(L_{\rm TIR})^b$	$10.61^{+0.02}_{-0.02}$	$10.60^{+0.02}_{-0.02}$	$10.60^{+0.02}_{-0.02}$	$10.60^{+0.02}_{-0.02}$	$10.60^{+0.02}_{-0.02}$	$10.60^{+0.02}_{-0.02}$
	$\rm SFR_{TIR}{}^b$	$6.02^{+0.29}_{-0.28}$	$5.97^{+0.26}_{-0.26}$	$5.97^{+0.25}_{-0.25}$	$5.98^{+0.24}_{-0.25}$	$5.96^{+0.25}_{-0.24}$	$5.95^{+0.24}_{-0.26}$
NGC 4418	$\log(L_{\rm TIR})^a$	$11.12^{+0.01}_{-0.01}$	$11.14^{+0.01}_{-0.02}$	$11.14^{+0.02}_{-0.02}$	$11.14^{+0.02}_{-0.02}$	$11.15^{+0.02}_{-0.02}$	$11.15^{+0.02}_{-0.02}$
	$\rm SFR_{TIR}{}^a$	$19.53^{+0.58}_{-0.63}$	$20.29^{+0.67}_{-0.72}$	$20.59^{+0.76}_{-0.77}$	$20.72^{+0.74}_{-0.76}$	$20.75^{+0.79}_{-0.77}$	$20.84^{+0.81}_{-0.80}$
	$\log(L_{\rm TIR})^b$	$11.12^{+0.01}_{-0.01}$	$11.14^{+0.01}_{-0.02}$	$11.14^{+0.02}_{-0.02}$	$11.14^{+0.02}_{-0.02}$	$11.15^{+0.02}_{-0.02}$	$11.15^{+0.02}_{-0.02}$
	$\rm SFR_{TIR}{}^b$	$19.59^{+0.58}_{-0.63}$	$20.28^{+0.68}_{-0.71}$	$20.60^{+0.75}_{-0.75}$	$20.68^{+0.79}_{-0.80}$	$20.75^{+0.76}_{-0.81}$	$20.80^{+0.77}_{-0.81}$

Table D.4: The values of $L_{\rm TIR}$ and $\rm SFR_{TIR}$ resulting from all the SED model fits, corresponding to the 25" and 27" diameter photometric apertures. The first two columns show the name of the galaxy and of the quantities that are calculated. Columns three to seven correspond show the values derived using the optically thick SED model fit results, for each value of ν_0, respectively. The last column shows the $L_{\rm TIR}$ and$\rm SFR_{TIR}$ values derived using the optically thin SED model fit results. For each galaxy, the superscripts *a* and *b* denote the values that were derived from fits to the 25" and 27" diameter photometric aperture measurements, respectively.

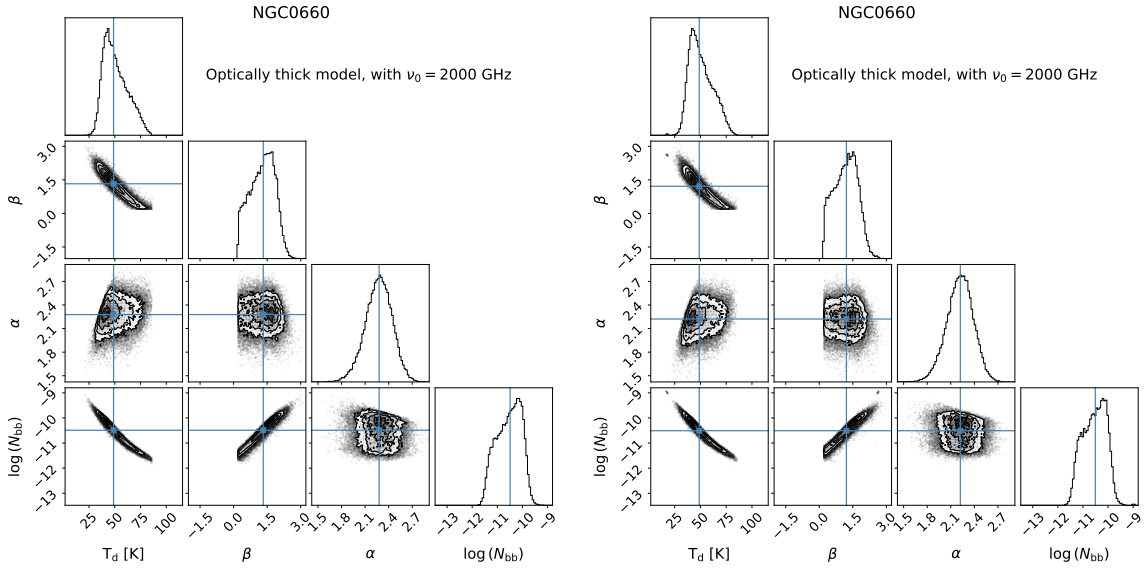

Figure D.2: The posterior probability distributions of the four parameters of our optically thick model, resulting from the MCMC fit of the model to the observed data. The highlights show the median values of the parameters. The left and right figures correspond to fits of models to fluxes originating from 25" and 27" diameter circular apertures, respectively. These apertures cover the regions we observed with the IRAM 30m telescope, at the H40α and H42α line frequencies, respectively. In this case, the ν_0 parameter was fixed at 2000 GHz.

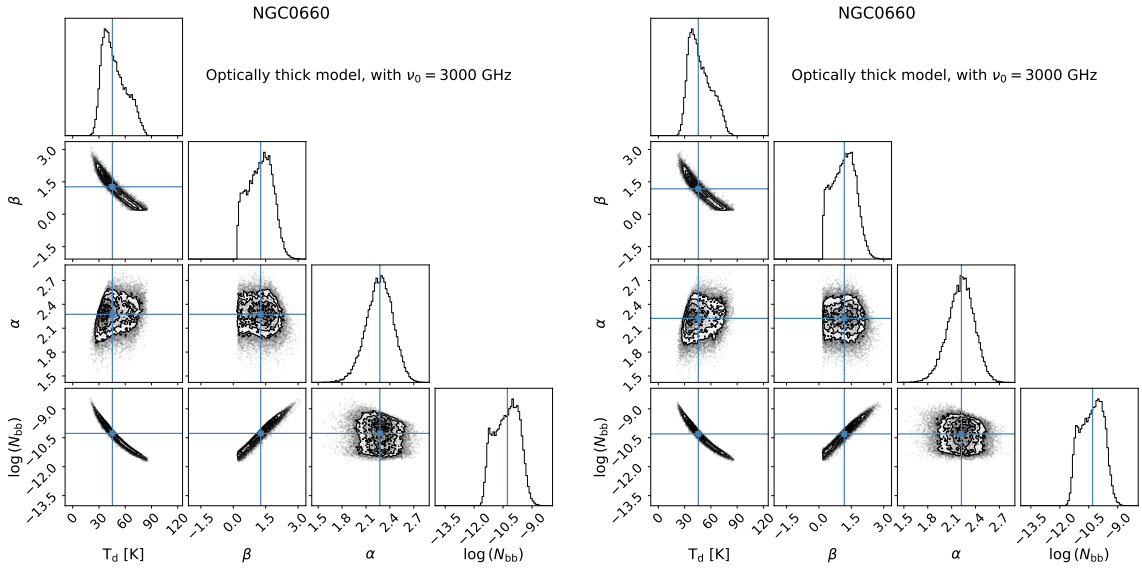

Figure D.3: The posterior probability distributions of the four parameters of our optically thick model, resulting from the MCMC fit of the model to the observed data. The highlights show the median values of the parameters. The left and right figures correspond to fits of models to fluxes originating from 25" and 27" diameter circular apertures, respectively. These apertures cover the regions we observed with the IRAM 30m telescope, at the H40α and H42α line frequencies, respectively. In this case, the ν_0 parameter was fixed at 3000 GHz.

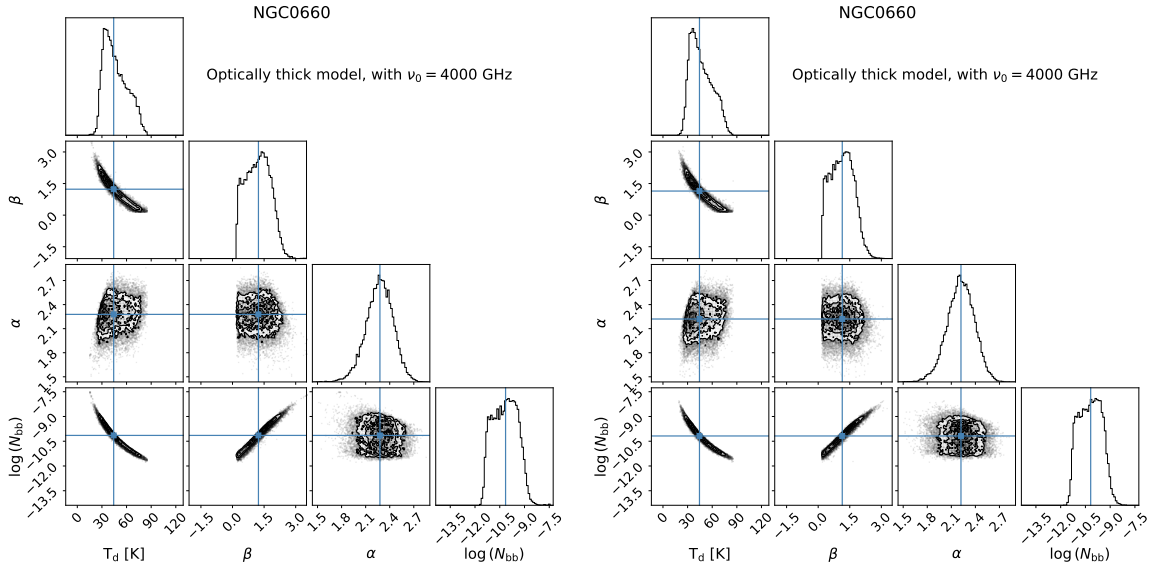

Figure D.4: The posterior probability distributions of the four parameters of our optically thick model, resulting from the MCMC fit of the model to the observed data. The highlights show the median values of the parameters. The left and right figures correspond to fits of models to fluxes originating from 25" and 27" diameter circular apertures, respectively. These apertures cover the regions we observed with the IRAM 30m telescope, at the H40α and H42α line frequencies, respectively. In this case, the ν_0 parameter was fixed at 4000 GHz.

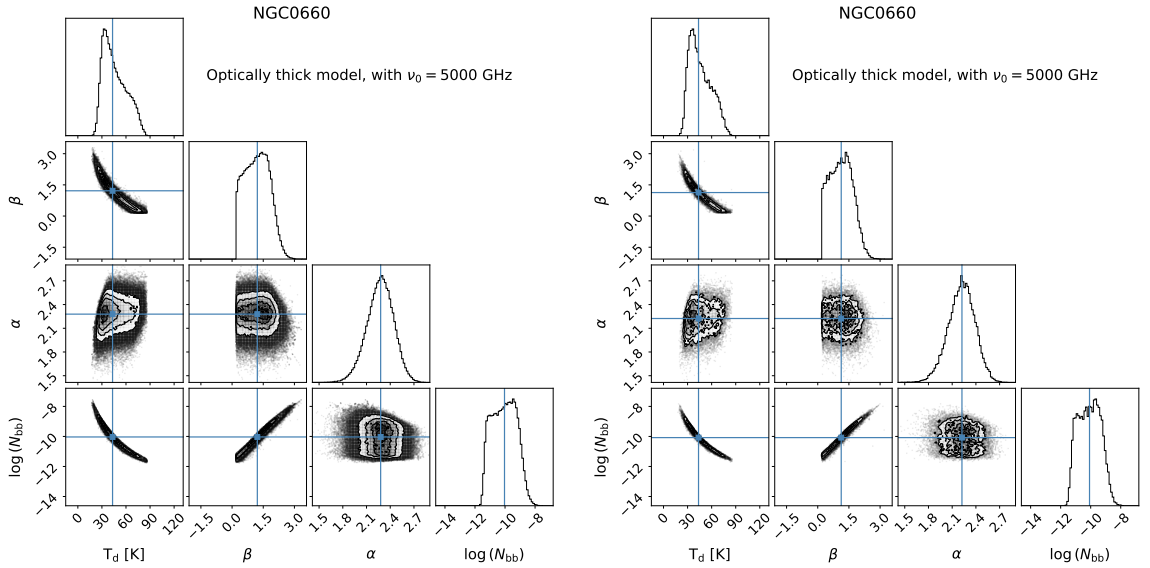

Figure D.5: The posterior probability distributions of the four parameters of our optically thick model, resulting from the MCMC fit of the model to the observed data. The highlights show the median values of the parameters. The left and right figures correspond to fits of models to fluxes originating from 25" and 27" diameter circular apertures, respectively. These apertures cover the regions we observed with the IRAM 30m telescope, at the H40α and H42α line frequencies, respectively. In this case, the ν_0 parameter was fixed at 5000 GHz.

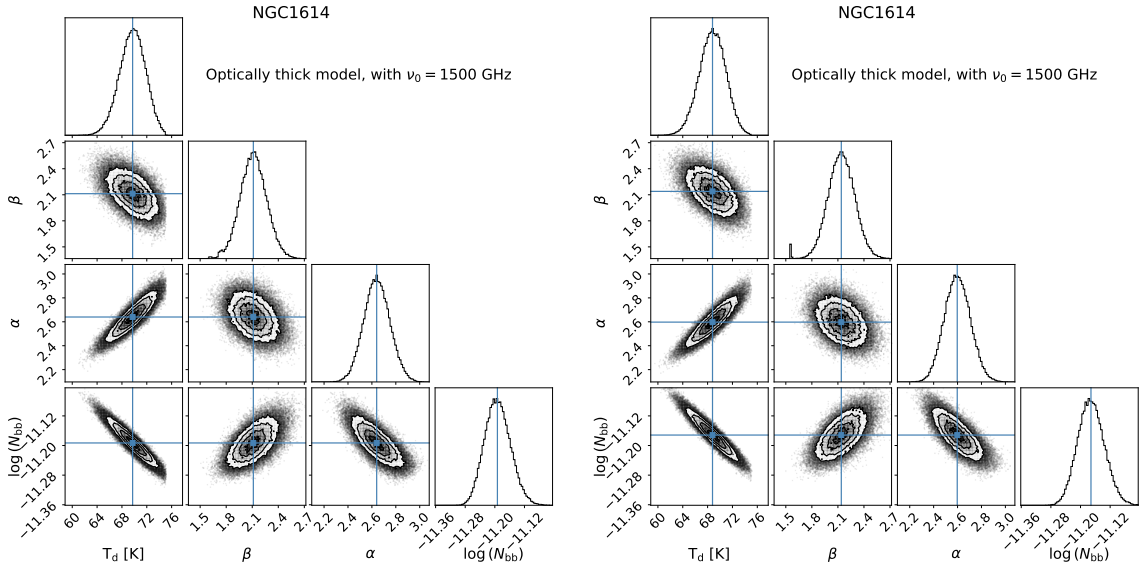

Figure D.6: The posterior probability distributions of the four parameters of our optically thick model, resulting from the MCMC fit of the model to the observed data. The highlights show the median values of the parameters. The left and right figures correspond to fits of models to fluxes originating from 25" and 27" diameter circular apertures, respectively. These apertures cover the regions we observed with the IRAM 30m telescope, at the H40α and H42α line frequencies, respectively. In this case, the ν_0 parameter was fixed at 1500 GHz.

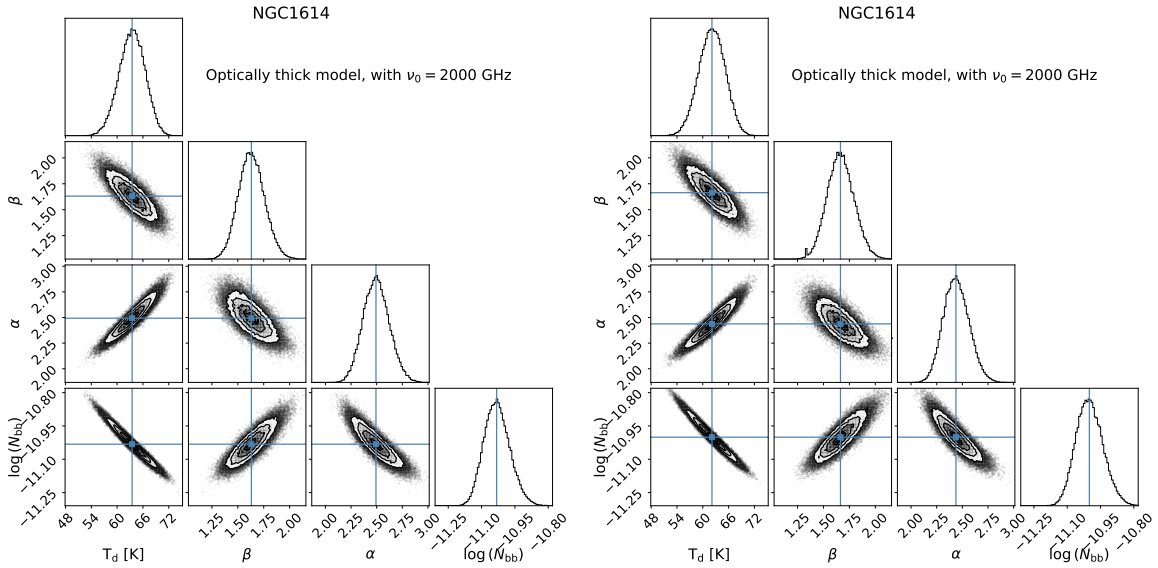

Figure D.7: The posterior probability distributions of the four parameters of our optically thick model, resulting from the MCMC fit of the model to the observed data. The highlights show the median values of the parameters. The left and right figures correspond to fits of models to fluxes originating from 25" and 27" diameter circular apertures, respectively. These apertures cover the regions we observed with the IRAM 30m telescope, at the H40α and H42α line frequencies, respectively. In this case, the ν_0 parameter was fixed at 2000 GHz.

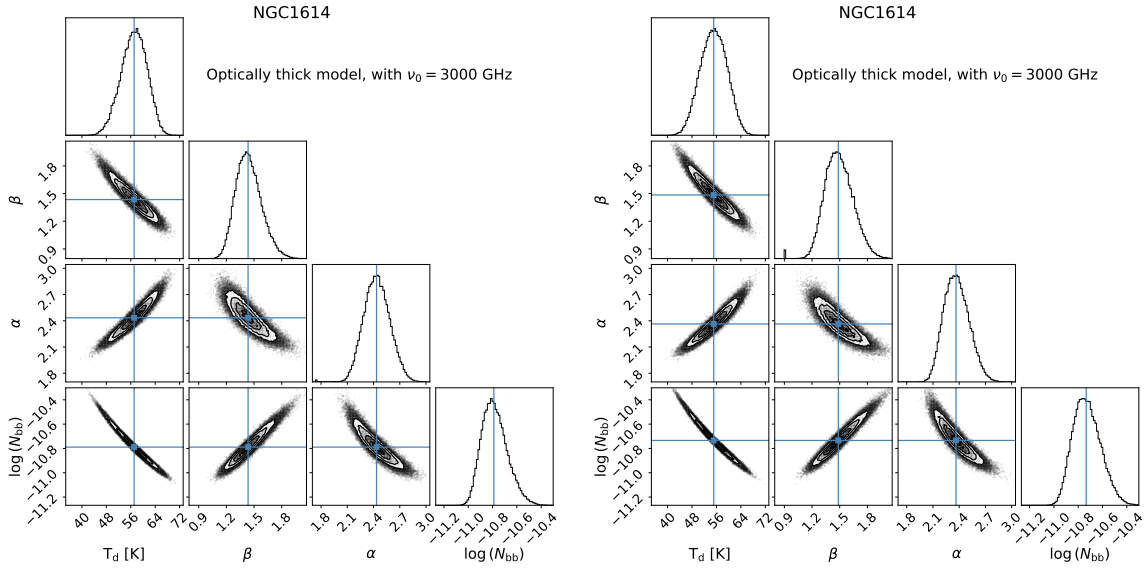

Figure D.8: The posterior probability distributions of the four parameters of our optically thick model, resulting from the MCMC fit of the model to the observed data. The highlights show the median values of the parameters. The left and right figures correspond to fits of models to fluxes originating from 25" and 27" diameter circular apertures, respectively. These apertures cover the regions we observed with the IRAM 30m telescope, at the H40α and H42α line frequencies, respectively. In this case, the ν_0 parameter was fixed at 3000 GHz.

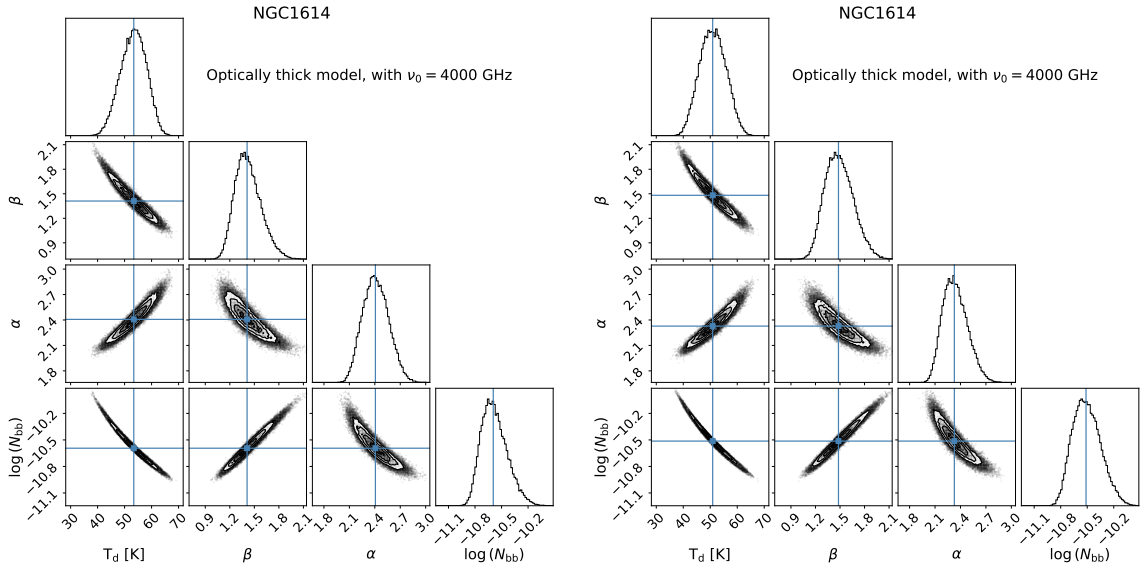

Figure D.9: The posterior probability distributions of the four parameters of our optically thick model, resulting from the MCMC fit of the model to the observed data. The highlights show the median values of the parameters. The left and right figures correspond to fits of models to fluxes originating from 25" and 27" diameter circular apertures, respectively. These apertures cover the regions we observed with the IRAM 30m telescope, at the H40α and H42α line frequencies, respectively. In this case, the ν_0 parameter was fixed at 4000 GHz.

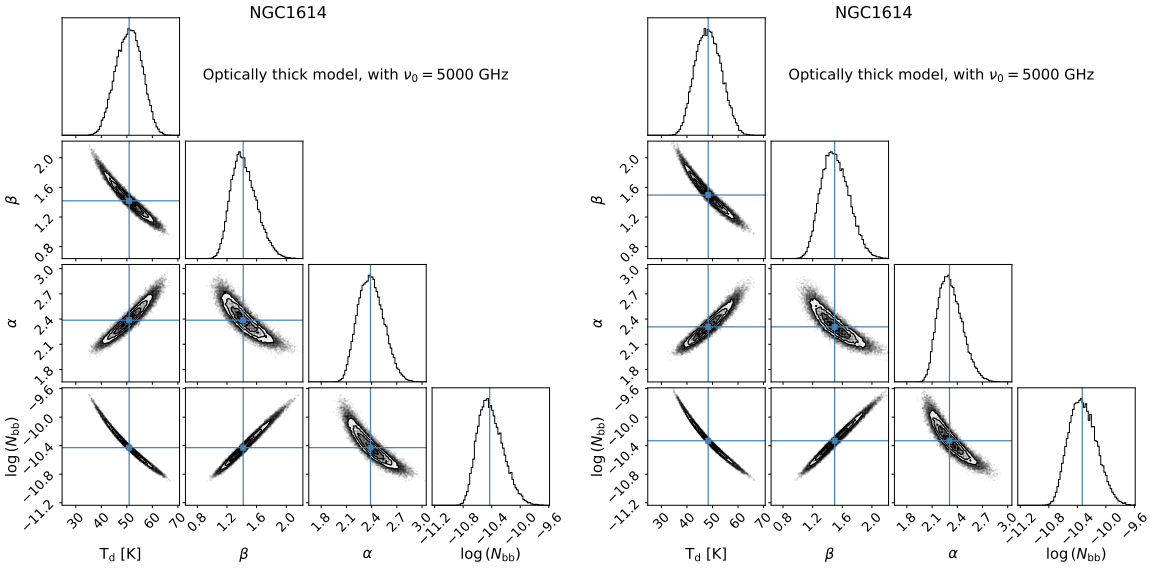

Figure D.10: The posterior probability distributions of the four parameters of our optically thick model, resulting from the MCMC fit of the model to the observed data. The highlights show the median values of the parameters. The left and right figures correspond to fits of models to fluxes originating from 25" and 27" diameter circular apertures, respectively. These apertures cover the regions we observed with the IRAM 30m telescope, at the H40α and H42α line frequencies, respectively. In this case, the ν_0 parameter was fixed at 5000 GHz.

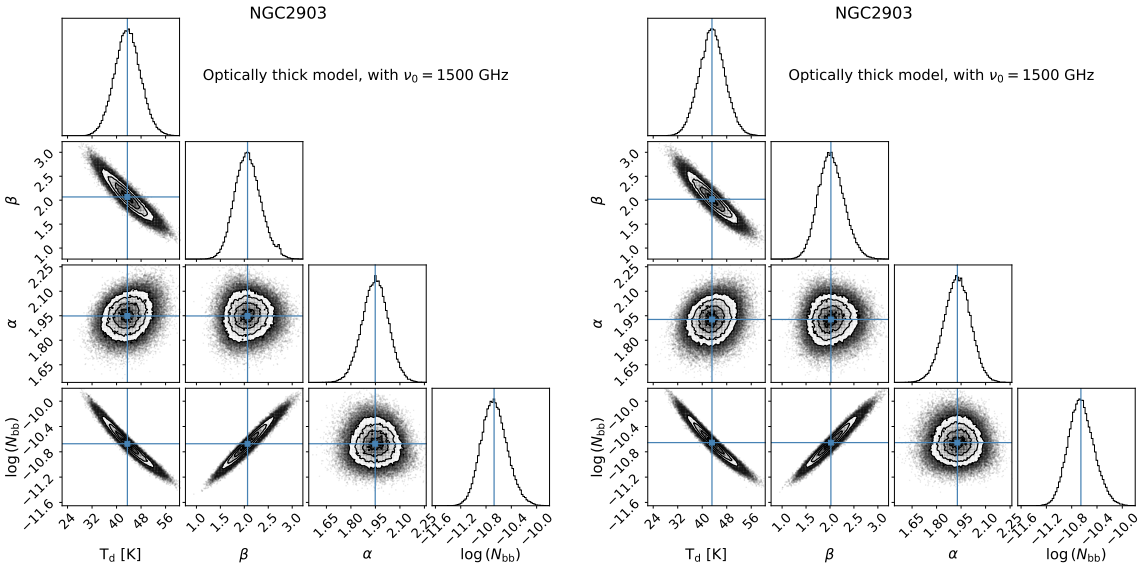

Figure D.11: The posterior probability distributions of the four parameters of our optically thick model, resulting from the MCMC fit of the model to the observed data. The highlights show the median values of the parameters. The left and right figures correspond to fits of models to fluxes originating from 25" and 27" diameter circular apertures, respectively. These apertures cover the regions we observed with the IRAM 30m telescope, at the H40α and H42α line frequencies, respectively. In this case, the ν_0 parameter was fixed at 1500 GHz.

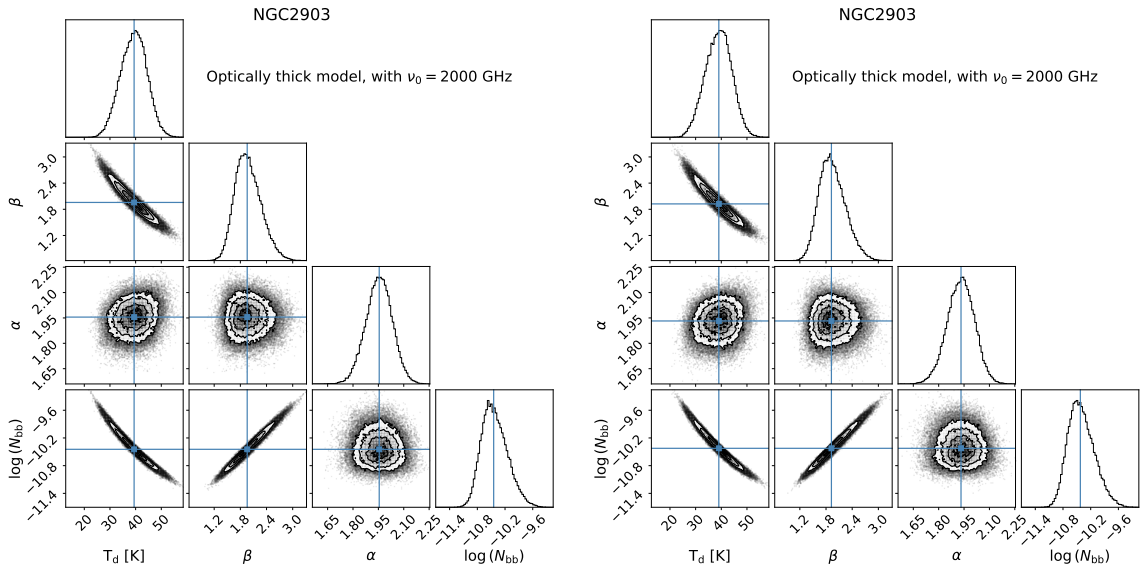

Figure D.12: The posterior probability distributions of the four parameters of our optically thick model, resulting from the MCMC fit of the model to the observed data. The highlights show the median values of the parameters. The left and right figures correspond to fits of models to fluxes originating from 25” and 27” diameter circular apertures, respectively. These apertures cover the regions we observed with the IRAM 30m telescope, at the H40α and H42α line frequencies, respectively. In this case, the ν_0 parameter was fixed at 2000 GHz.

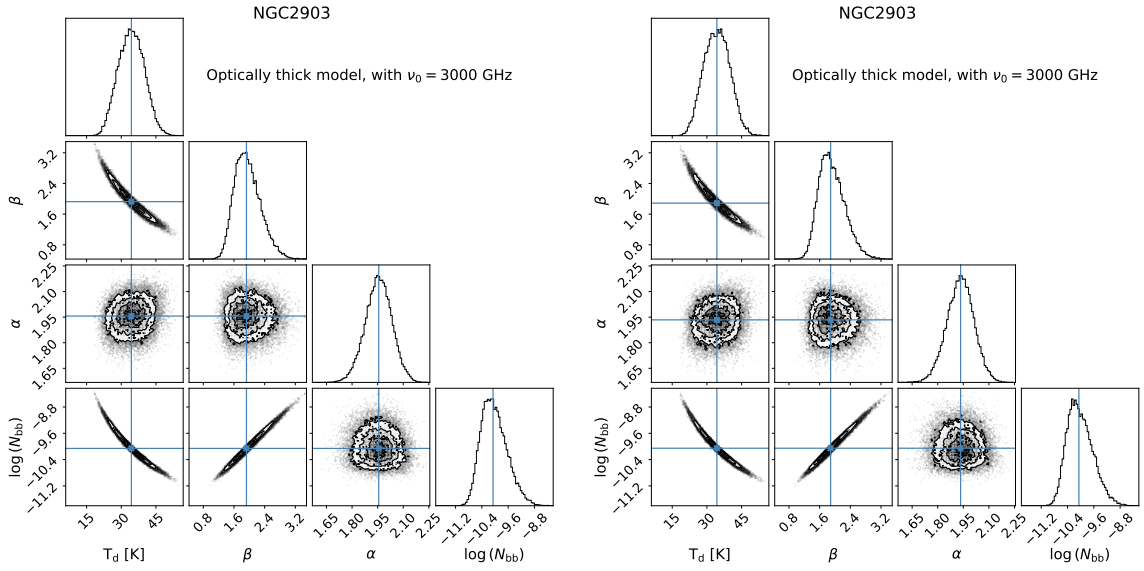

Figure D.13: The posterior probability distributions of the four parameters of our optically thick model, resulting from the MCMC fit of the model to the observed data. The highlights show the median values of the parameters. The left and right figures correspond to fits of models to fluxes originating from 25” and 27” diameter circular apertures, respectively. These apertures cover the regions we observed with the IRAM 30m telescope, at the H40α and H42α line frequencies, respectively. In this case, the ν_0 parameter was fixed at 3000 GHz.

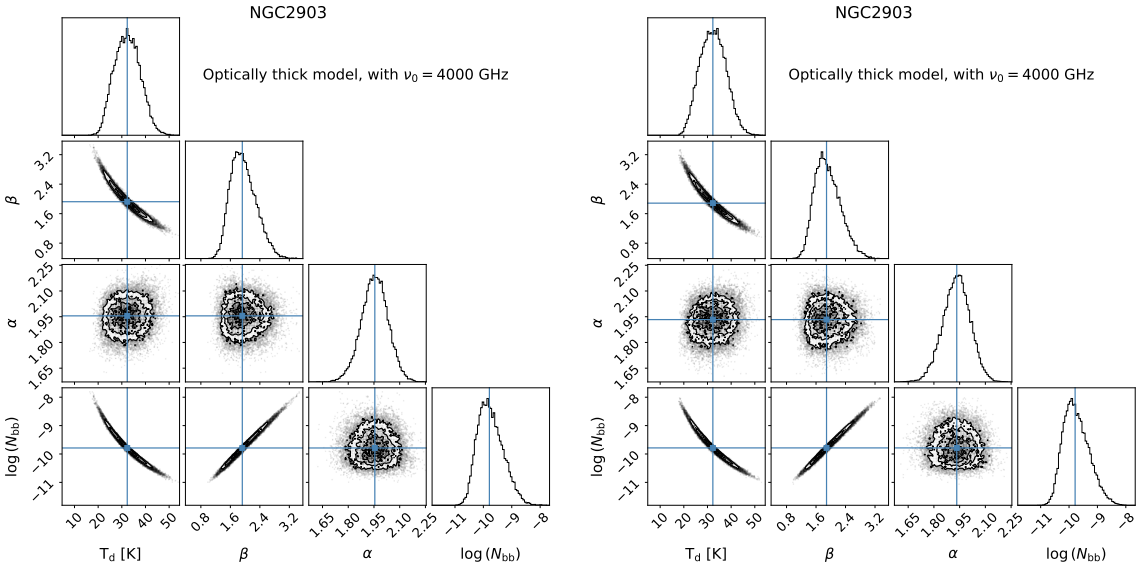

Figure D.14: The posterior probability distributions of the four parameters of our optically thick model, resulting from the MCMC fit of the model to the observed data. The highlights show the median values of the parameters. The left and right figures correspond to fits of models to fluxes originating from 25" and 27" diameter circular apertures, respectively. These apertures cover the regions we observed with the IRAM 30m telescope, at the H40α and H42α line frequencies, respectively. In this case, the ν_0 parameter was fixed at 4000 GHz.

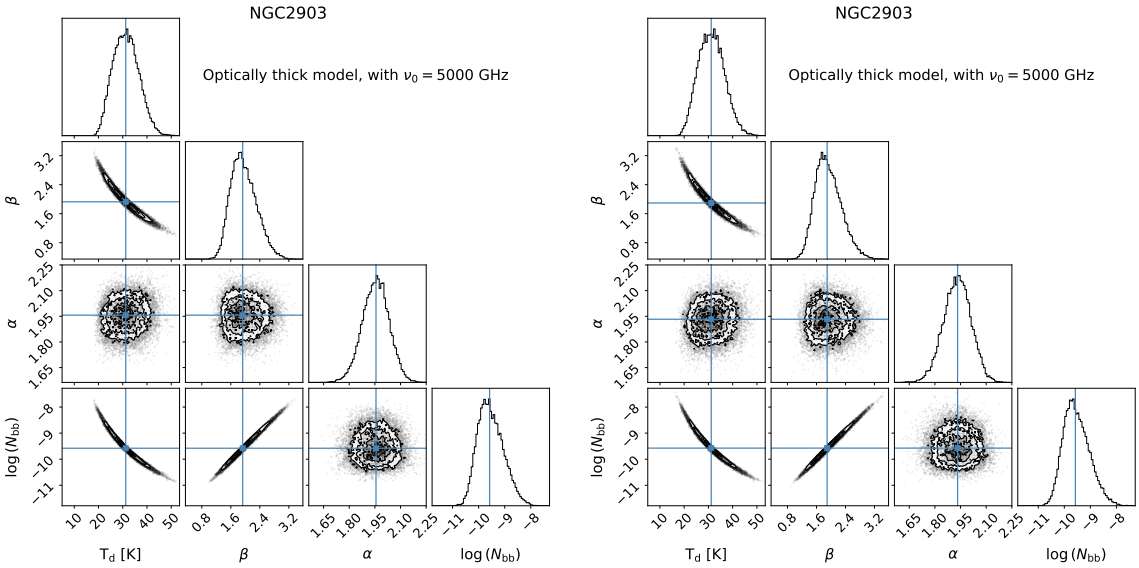

Figure D.15: The posterior probability distributions of the four parameters of our optically thick model, resulting from the MCMC fit of the model to the observed data. The highlights show the median values of the parameters. The left and right figures correspond to fits of models to fluxes originating from 25" and 27" diameter circular apertures, respectively. These apertures cover the regions we observed with the IRAM 30m telescope, at the H40α and H42α line frequencies, respectively. In this case, the ν_0 parameter was fixed at 5000 GHz.

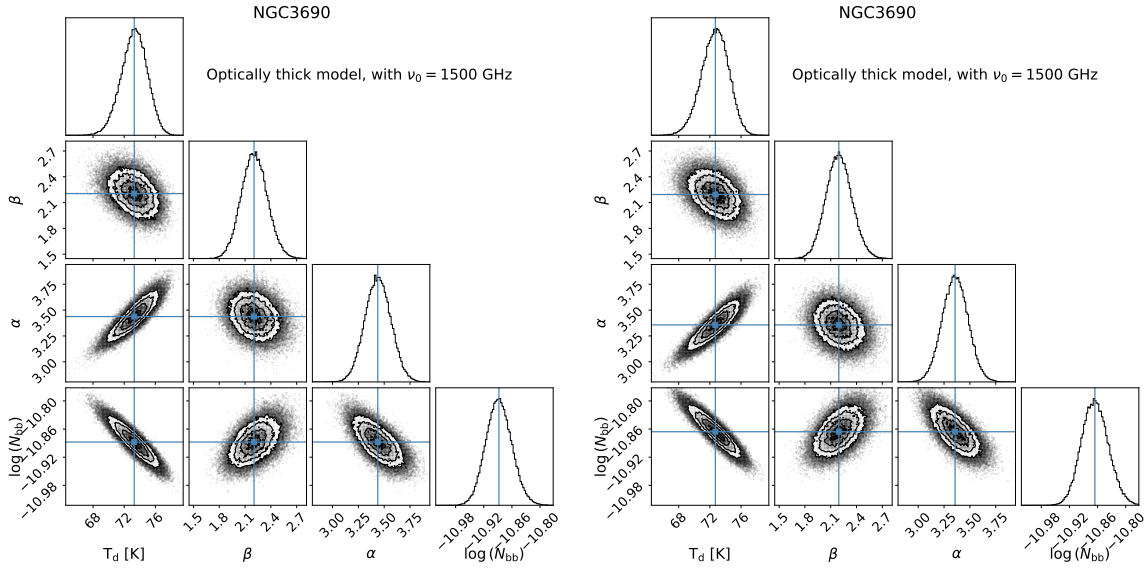

Figure D.16: The posterior probability distributions of the four parameters of our optically thick model, resulting from the MCMC fit of the model to the observed data. The highlights show the median values of the parameters. The left and right figures correspond to fits of models to fluxes originating from 25" and 27" diameter circular apertures, respectively. These apertures cover the regions we observed with the IRAM 30m telescope, at the H40α and H42α line frequencies, respectively. In this case, the ν_0 parameter was fixed at 1500 GHz.

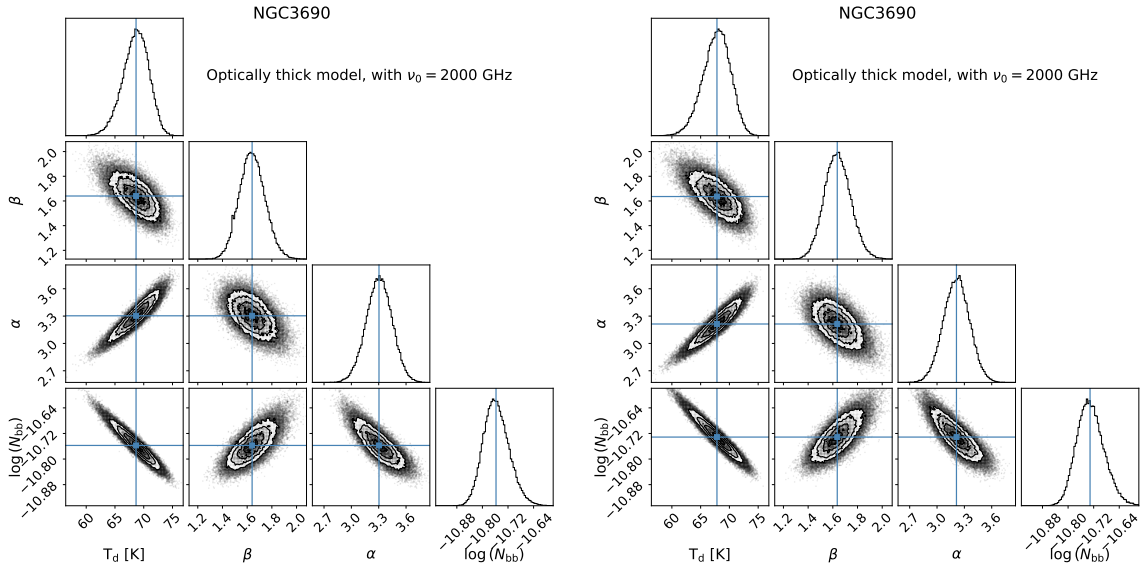

Figure D.17: The posterior probability distributions of the four parameters of our optically thick model, resulting from the MCMC fit of the model to the observed data. The highlights show the median values of the parameters. The left and right figures correspond to fits of models to fluxes originating from 25" and 27" diameter circular apertures, respectively. These apertures cover the regions we observed with the IRAM 30m telescope, at the H40α and H42α line frequencies, respectively. In this case, the ν_0 parameter was fixed at 2000 GHz.

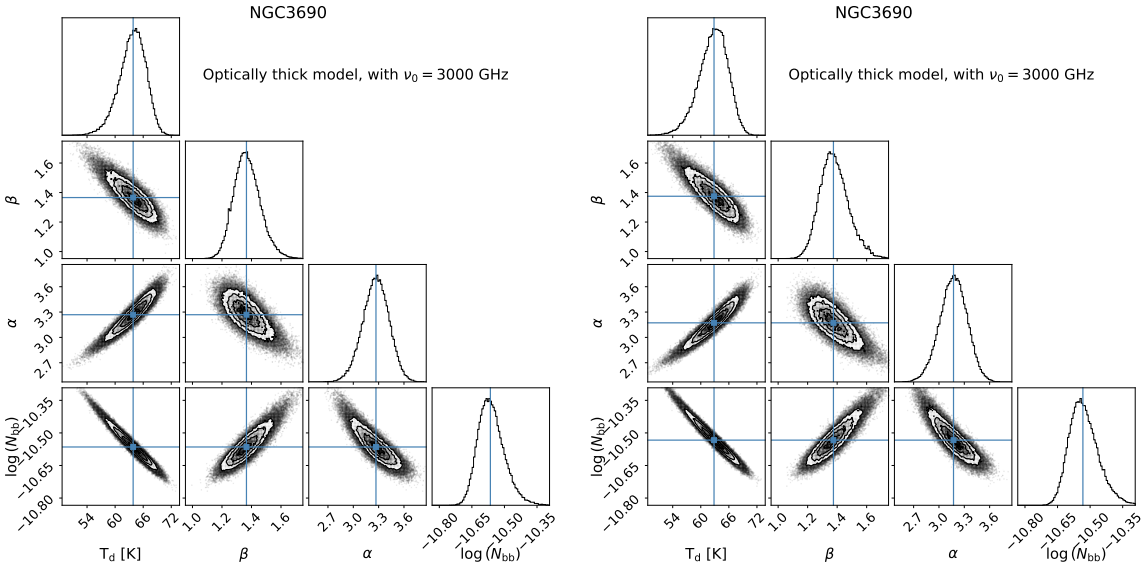

Figure D.18: The posterior probability distributions of the four parameters of our optically thick model, resulting from the MCMC fit of the model to the observed data. The highlights show the median values of the parameters. The left and right figures correspond to fits of models to fluxes originating from 25" and 27" diameter circular apertures, respectively. These apertures cover the regions we observed with the IRAM 30m telescope, at the H40α and H42α line frequencies, respectively. In this case, the ν_0 parameter was fixed at 3000 GHz.

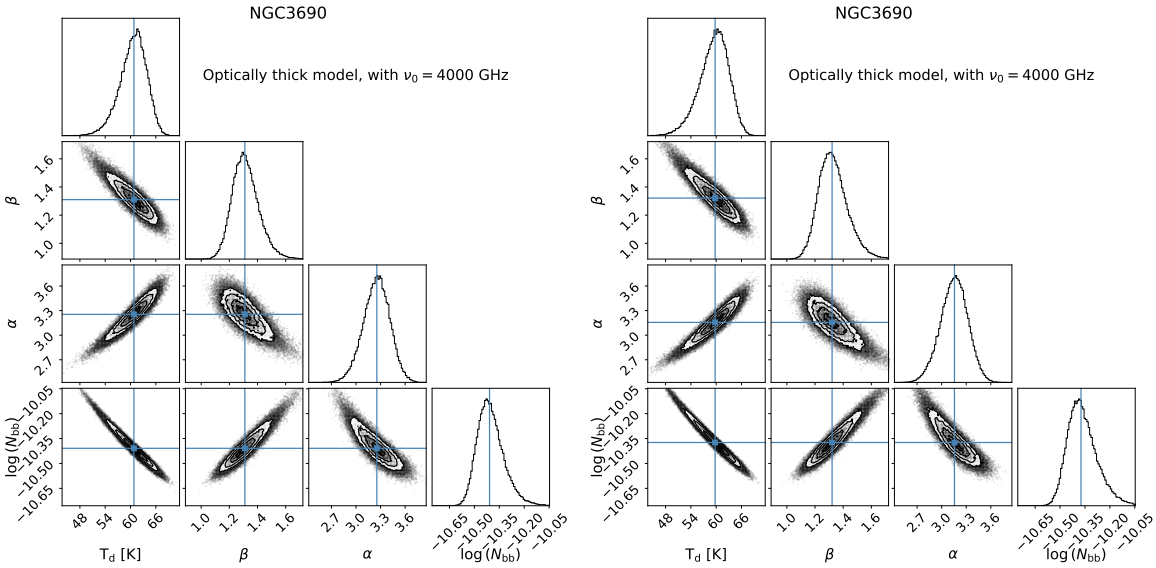

Figure D.19: The posterior probability distributions of the four parameters of our optically thick model, resulting from the MCMC fit of the model to the observed data. The highlights show the median values of the parameters. The left and right figures correspond to fits of models to fluxes originating from 25" and 27" diameter circular apertures, respectively. These apertures cover the regions we observed with the IRAM 30m telescope, at the H40α and H42α line frequencies, respectively. In this case, the ν_0 parameter was fixed at 4000 GHz.

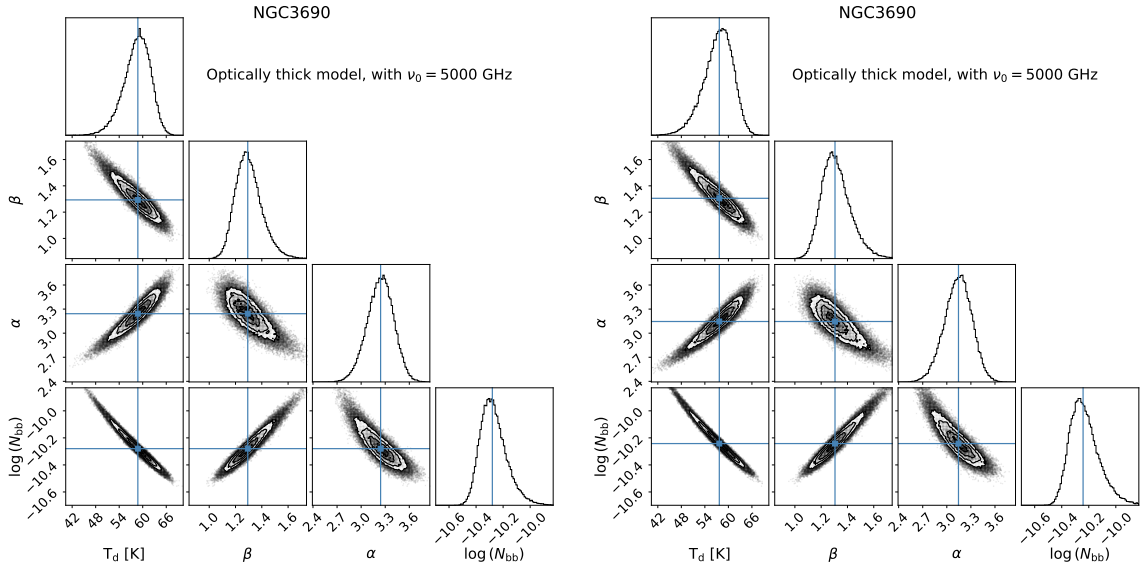

Figure D.20: The posterior probability distributions of the four parameters of our optically thick model, resulting from the MCMC fit of the model to the observed data. The highlights show the median values of the parameters. The left and right figures correspond to fits of models to fluxes originating from 25" and 27" diameter circular apertures, respectively. These apertures cover the regions we observed with the IRAM 30m telescope, at the H40α and H42α line frequencies, respectively. In this case, the ν_0 parameter was fixed at 5000 GHz.

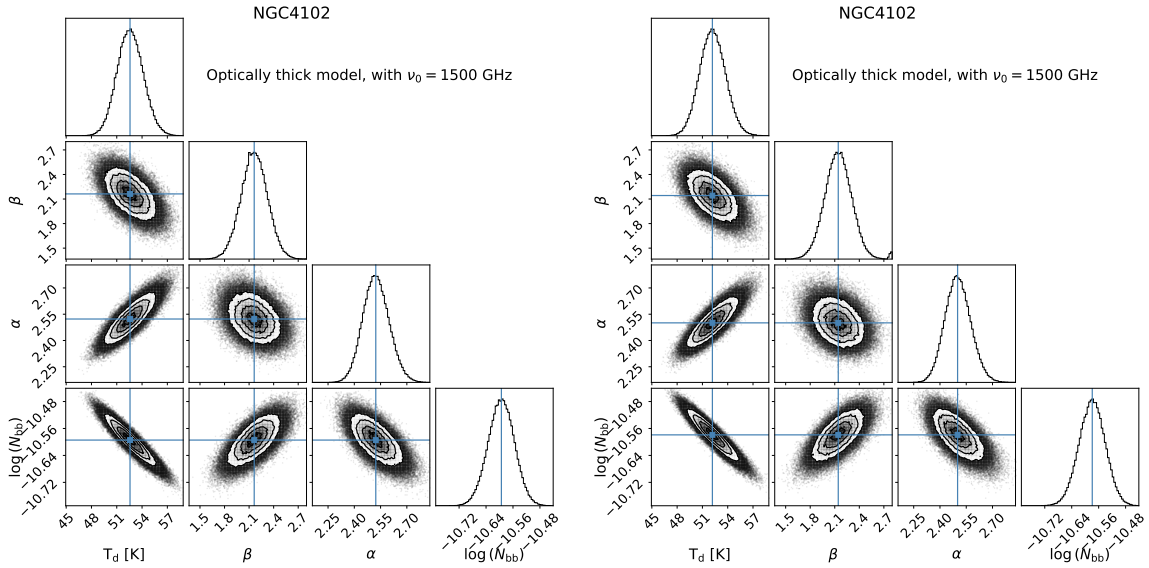

Figure D.21: The posterior probability distributions of the four parameters of our optically thick model, resulting from the MCMC fit of the model to the observed data. The highlights show the median values of the parameters. The left and right figures correspond to fits of models to fluxes originating from 25" and 27" diameter circular apertures, respectively. These apertures cover the regions we observed with the IRAM 30m telescope, at the H40α and H42α line frequencies, respectively. In this case, the ν_0 parameter was fixed at 1500 GHz.

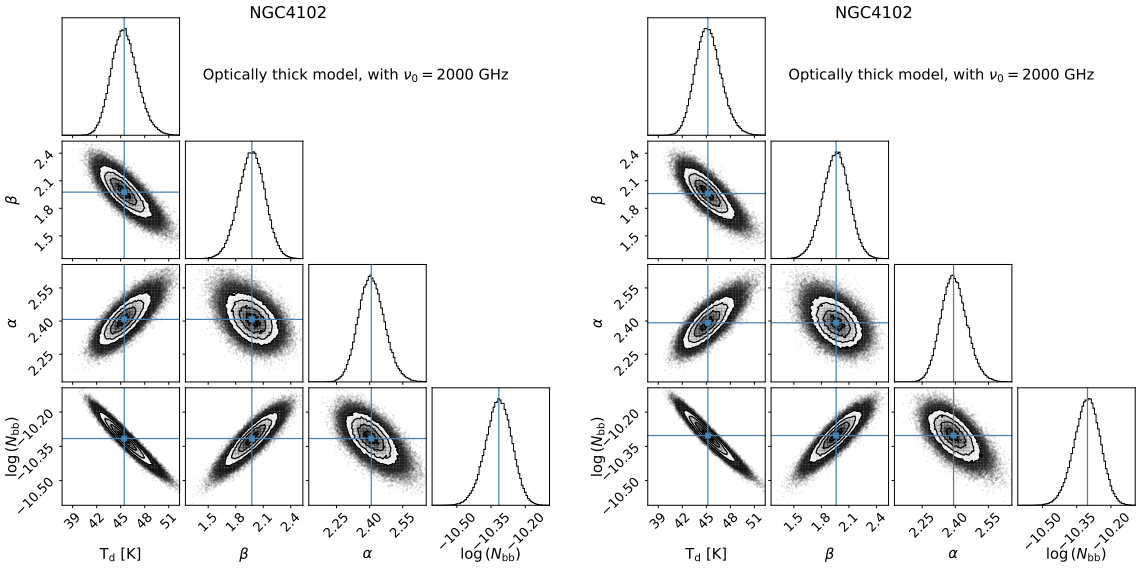

Figure D.22: The posterior probability distributions of the four parameters of our optically thick model, resulting from the MCMC fit of the model to the observed data. The highlights show the median values of the parameters. The left and right figures correspond to fits of models to fluxes originating from 25" and 27" diameter circular apertures, respectively. These apertures cover the regions we observed with the IRAM 30m telescope, at the H40α and H42α line frequencies, respectively. In this case, the ν_0 parameter was fixed at 2000 GHz.

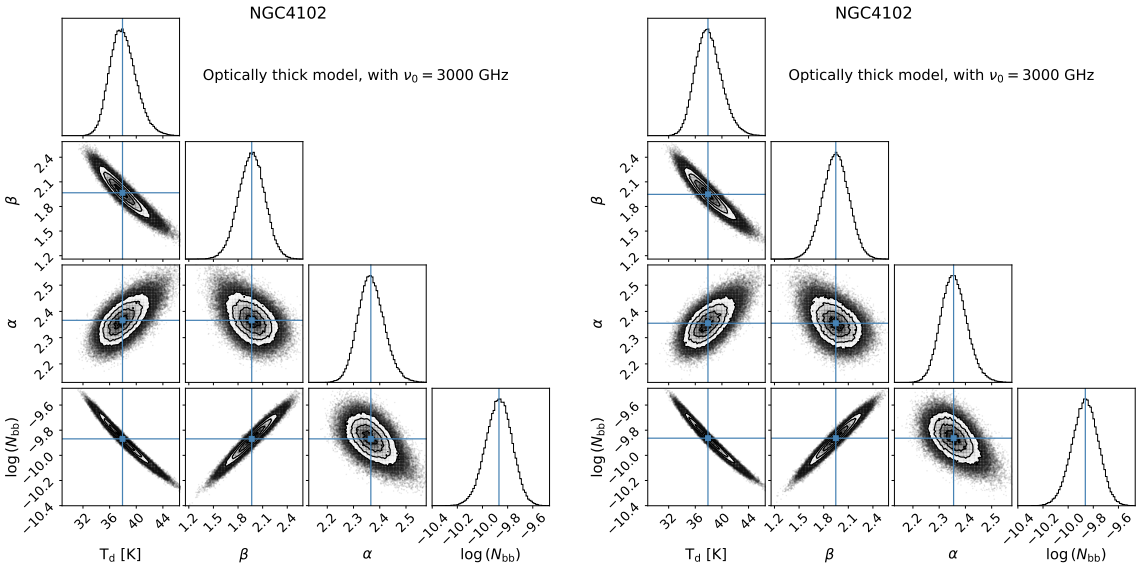

Figure D.23: The posterior probability distributions of the four parameters of our optically thick model, resulting from the MCMC fit of the model to the observed data. The highlights show the median values of the parameters. The left and right figures correspond to fits of models to fluxes originating from 25" and 27" diameter circular apertures, respectively. These apertures cover the regions we observed with the IRAM 30m telescope, at the H40α and H42α line frequencies, respectively. In this case, the ν_0 parameter was fixed at 3000 GHz.

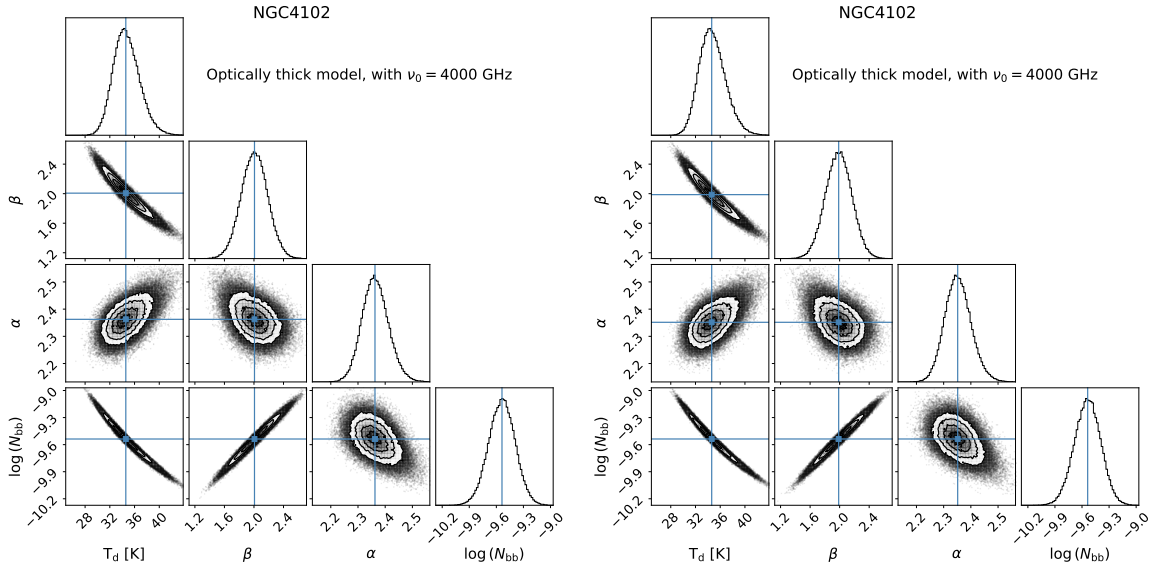

Figure D.24: The posterior probability distributions of the four parameters of our optically thick model, resulting from the MCMC fit of the model to the observed data. The highlights show the median values of the parameters. The left and right figures correspond to fits of models to fluxes originating from 25" and 27" diameter circular apertures, respectively. These apertures cover the regions we observed with the IRAM 30m telescope, at the H40α and H42α line frequencies, respectively. In this case, the ν_0 parameter was fixed at 4000 GHz.

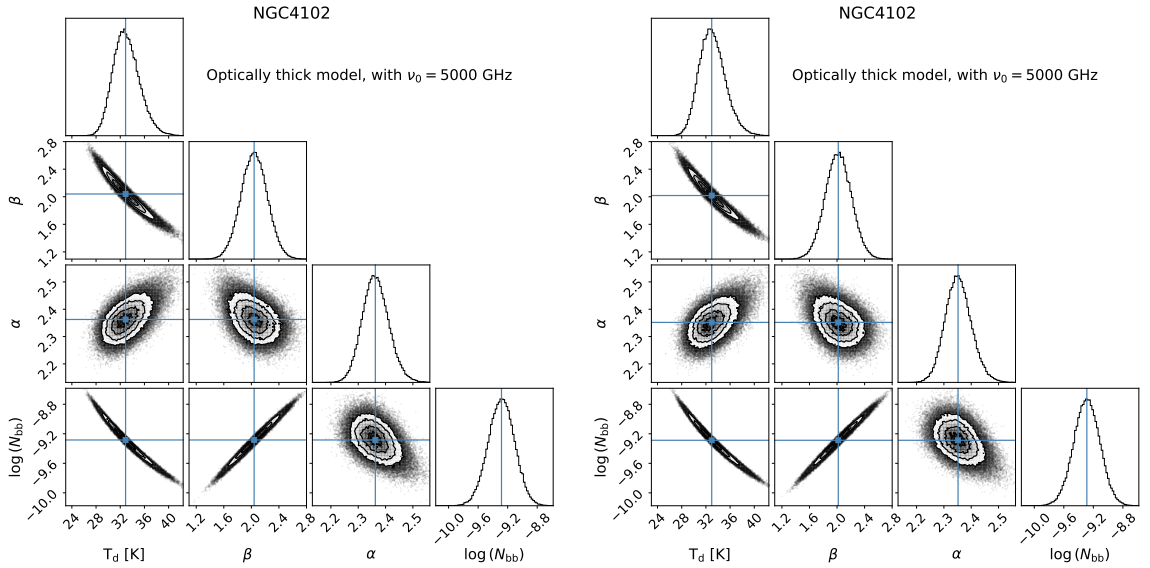

Figure D.25: The posterior probability distributions of the four parameters of our optically thick model, resulting from the MCMC fit of the model to the observed data. The highlights show the median values of the parameters. The left and right figures correspond to fits of models to fluxes originating from 25" and 27" diameter circular apertures, respectively. These apertures cover the regions we observed with the IRAM 30m telescope, at the H40α and H42α line frequencies, respectively. In this case, the ν_0 parameter was fixed at 5000 GHz.

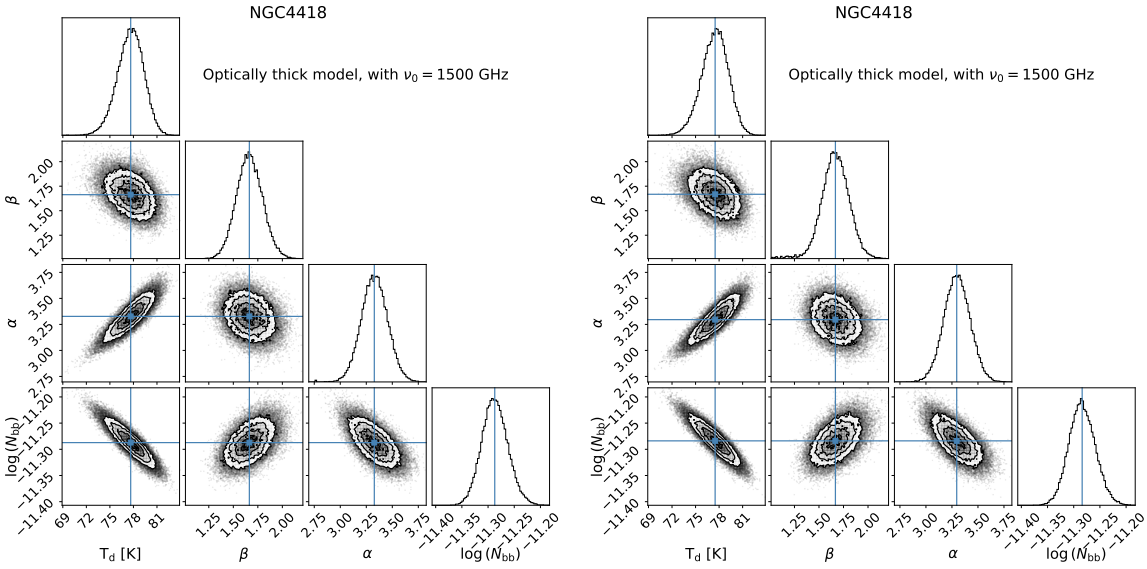

Figure D.26: The posterior probability distributions of the four parameters of our optically thick model, resulting from the MCMC fit of the model to the observed data. The highlights show the median values of the parameters. The left and right figures correspond to fits of models to fluxes originating from 25" and 27" diameter circular apertures, respectively. These apertures cover the regions we observed with the IRAM 30m telescope, at the H40α and H42α line frequencies, respectively. In this case, the ν_0 parameter was fixed at 1500 GHz.

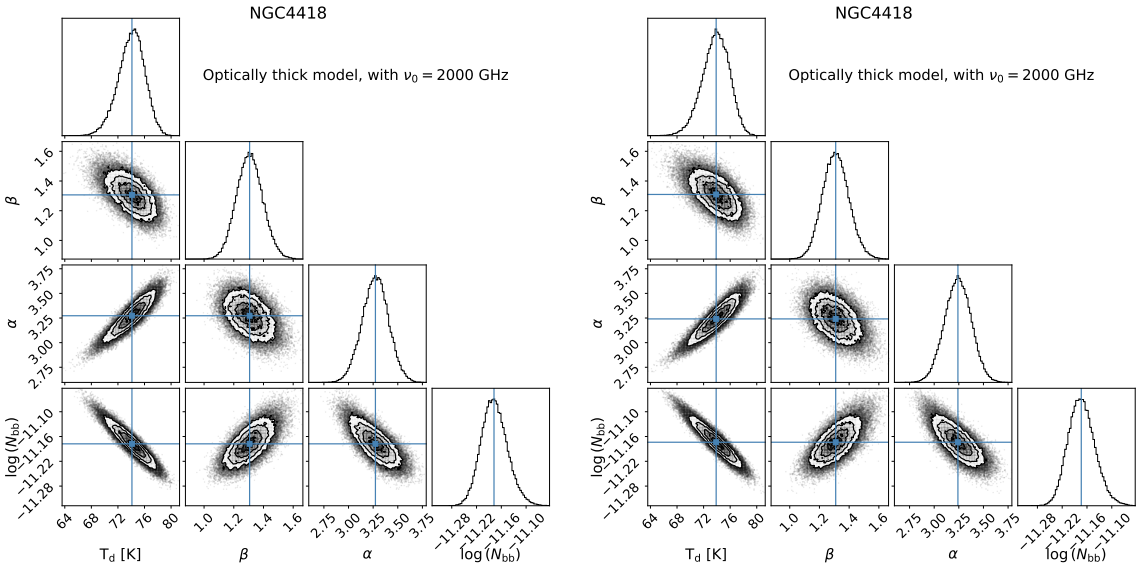

Figure D.27: The posterior probability distributions of the four parameters of our optically thick model, resulting from the MCMC fit of the model to the observed data. The highlights show the median values of the parameters. The left and right figures correspond to fits of models to fluxes originating from 25" and 27" diameter circular apertures, respectively. These apertures cover the regions we observed with the IRAM 30m telescope, at the H40α and H42α line frequencies, respectively. In this case, the ν_0 parameter was fixed at 2000 GHz.

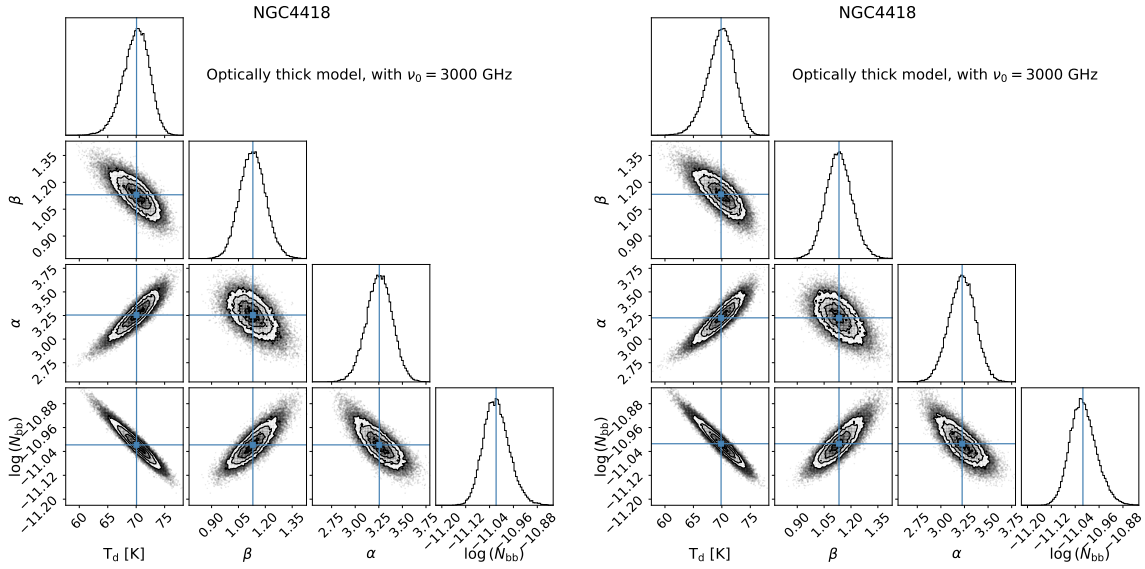

Figure D.28: The posterior probability distributions of the four parameters of our optically thick model, resulting from the MCMC fit of the model to the observed data. The highlights show the median values of the parameters. The left and right figures correspond to fits of models to fluxes originating from 25" and 27" diameter circular apertures, respectively. These apertures cover the regions we observed with the IRAM 30m telescope, at the H40α and H42α line frequencies, respectively. In this case, the ν_0 parameter was fixed at 3000 GHz.

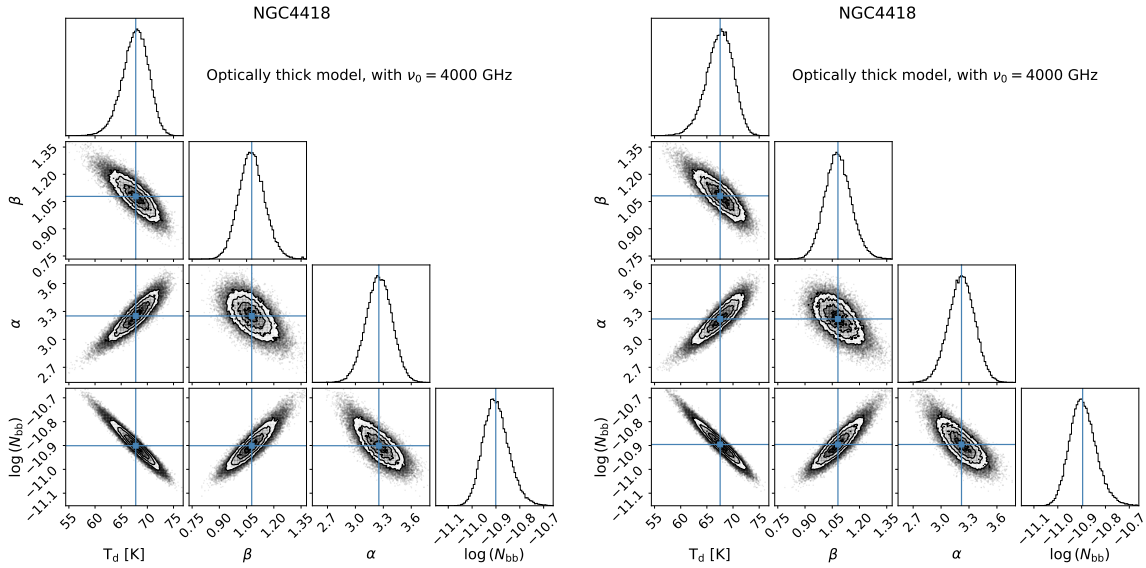

Figure D.29: The posterior probability distributions of the four parameters of our optically thick model, resulting from the MCMC fit of the model to the observed data. The highlights show the median values of the parameters. The left and right figures correspond to fits of models to fluxes originating from 25" and 27" diameter circular apertures, respectively. These apertures cover the regions we observed with the IRAM 30m telescope, at the H40α and H42α line frequencies, respectively. In this case, the ν_0 parameter was fixed at 4000 GHz.

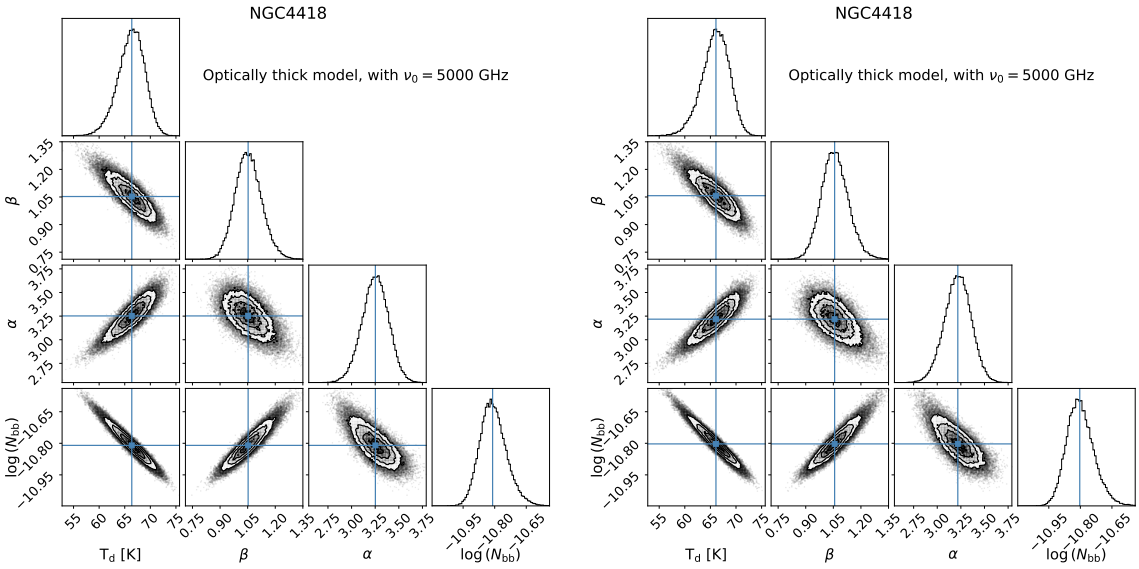

Figure D.30: The posterior probability distributions of the four parameters of our optically thick model, resulting from the MCMC fit of the model to the observed data. The highlights show the median values of the parameters. The left and right figures correspond to fits of models to fluxes originating from 25" and 27" diameter circular apertures, respectively. These apertures cover the regions we observed with the IRAM 30m telescope, at the H40α and H42α line frequencies, respectively. In this case, the ν_0 parameter was fixed at 5000 GHz.

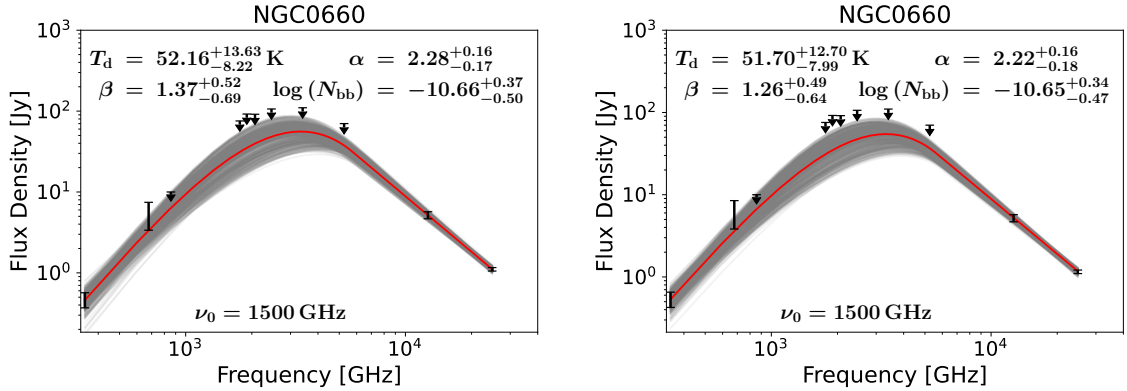

Figure D.31: The SED function resulting from the MCMC fit of the optically thick SED model to the continuum data. The best fit SED function is shown in red, while the 68% confidence level is shown in gray. The archival continuum data is shown with black symbols. The left and right figures show the fitting results using fluxes originating from 25" and 27" diameter circular apertures, respectively. These apertures cover the regions we observed with the IRAM 30m telescope, at the H40α and H42α line frequencies, respectively. The model parameters resulting from the fit are displayed on the plot. The ν_0 parameter was fixed at 1500 GHz.

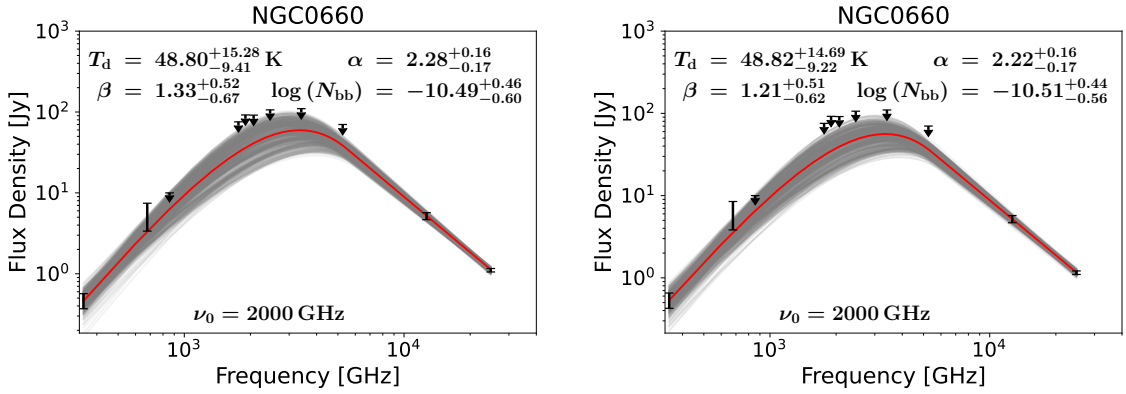

Figure D.32: The SED function resulting from the MCMC fit of the optically thick SED model to the continuum data. The best fit SED function is shown in red, while the 68% confidence level is shown in gray. The archival continuum data is shown with black symbols. The left and right figures show the fitting results using fluxes originating from 25" and 27" diameter circular apertures, respectively. These apertures cover the regions we observed with the IRAM 30m telescope, at the H40α and H42α line frequencies, respectively. The model parameters resulting from the fit are displayed on the plot. The ν_0 parameter was fixed at 2000 GHz.

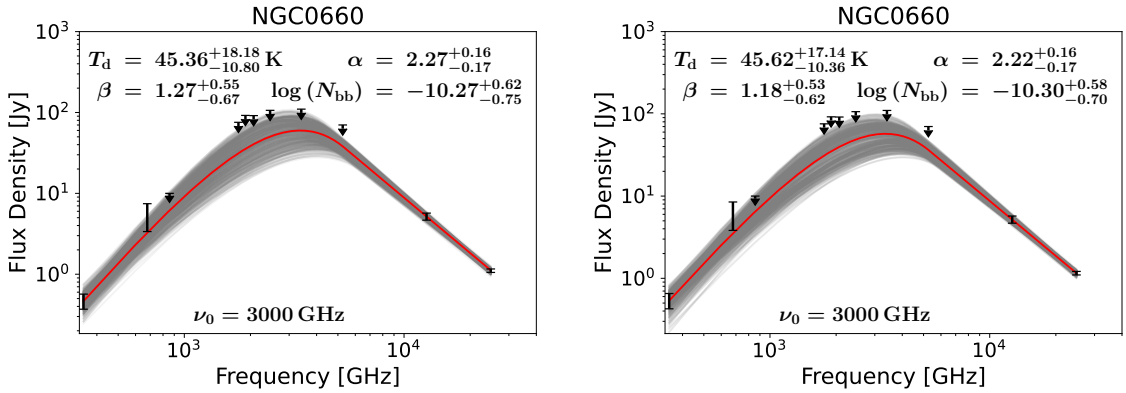

Figure D.33: The SED function resulting from the MCMC fit of the optically thick SED model to the continuum data. The best fit SED function is shown in red, while the 68% confidence level is shown in gray. The archival continuum data is shown with black symbols. The left and right figures show the fitting results using fluxes originating from 25" and 27" diameter circular apertures, respectively. These apertures cover the regions we observed with the IRAM 30m telescope, at the H40α and H42α line frequencies, respectively. The model parameters resulting from the fit are displayed on the plot. The ν_0 parameter was fixed at 3000 GHz.

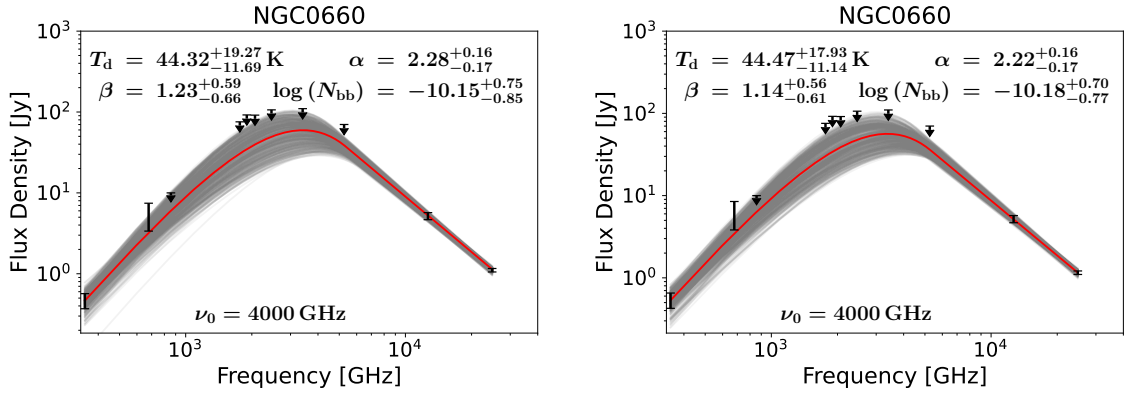

Figure D.34: The SED function resulting from the MCMC fit of the optically thick SED model to the continuum data. The best fit SED function is shown in red, while the 68% confidence level is shown in gray. The archival continuum data is shown with black symbols. The left and right figures show the fitting results using fluxes originating from 25" and 27" diameter circular apertures, respectively. These apertures cover the regions we observed with the IRAM 30m telescope, at the H40α and H42α line frequencies, respectively. The model parameters resulting from the fit are displayed on the plot. The ν_0 parameter was fixed at 4000 GHz.

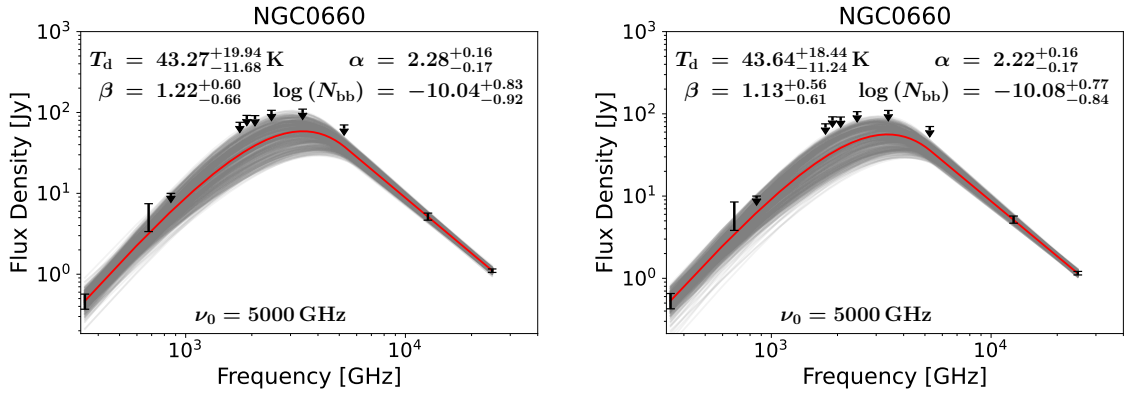

Figure D.35: The SED function resulting from the MCMC fit of the optically thick SED model to the continuum data. The best fit SED function is shown in red, while the 68% confidence level is shown in gray. The archival continuum data is shown with black symbols. The left and right figures show the fitting results using fluxes originating from 25" and 27" diameter circular apertures, respectively. These apertures cover the regions we observed with the IRAM 30m telescope, at the H40α and H42α line frequencies, respectively. The model parameters resulting from the fit are displayed on the plot. The ν_0 parameter was fixed at 5000 GHz.

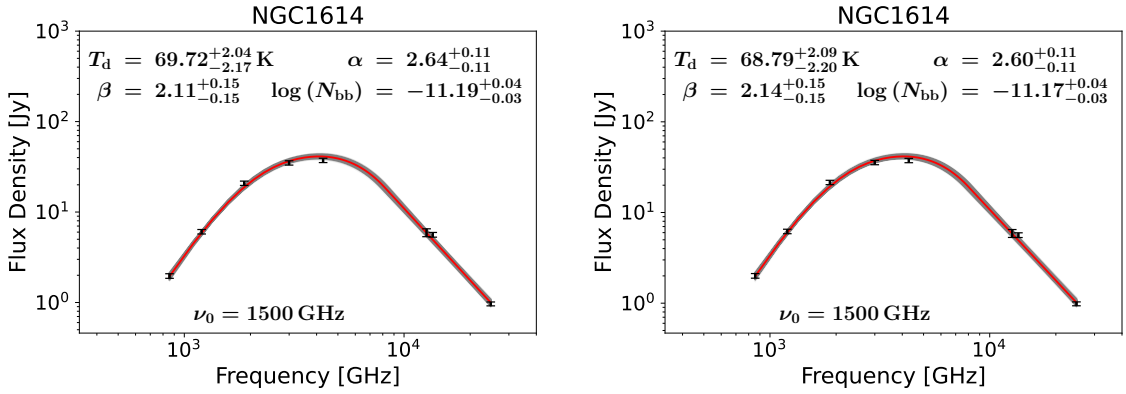

Figure D.36: The SED function resulting from the MCMC fit of the optically thick SED model to the continuum data. The best fit SED function is shown in red, while the 68% confidence level is shown in gray. The archival continuum data is shown with black symbols. The left and right figures show the fitting results using fluxes originating from 25" and 27" diameter circular apertures, respectively. These apertures cover the regions we observed with the IRAM 30m telescope, at the H40α and H42α line frequencies, respectively. The model parameters resulting from the fit are displayed on the plot. The ν_0 parameter was fixed at 1500 GHz.

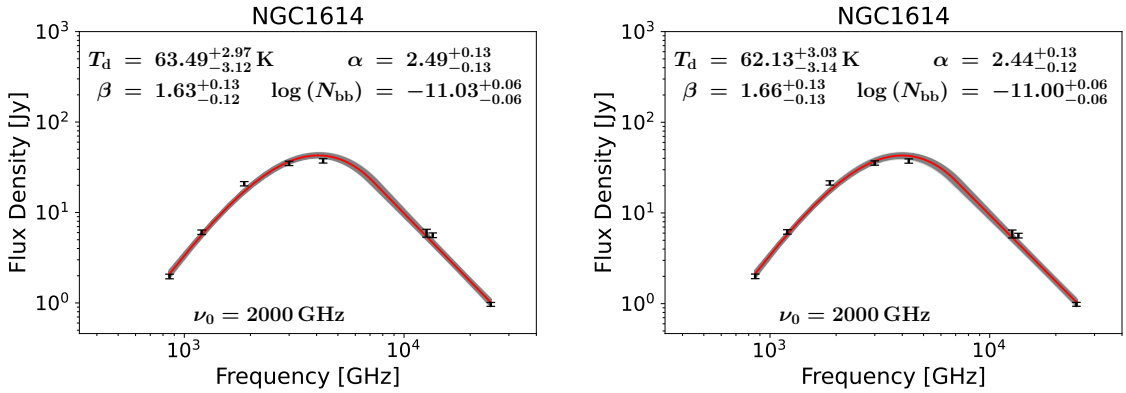

Figure D.37: The SED function resulting from the MCMC fit of the optically thick SED model to the continuum data. The best fit SED function is shown in red, while the 68% confidence level is shown in gray. The archival continuum data is shown with black symbols. The left and right figures show the fitting results using fluxes originating from 25" and 27" diameter circular apertures, respectively. These apertures cover the regions we observed with the IRAM 30m telescope, at the H40α and H42α line frequencies, respectively. The model parameters resulting from the fit are displayed on the plot. The ν_0 parameter was fixed at 2000 GHz.

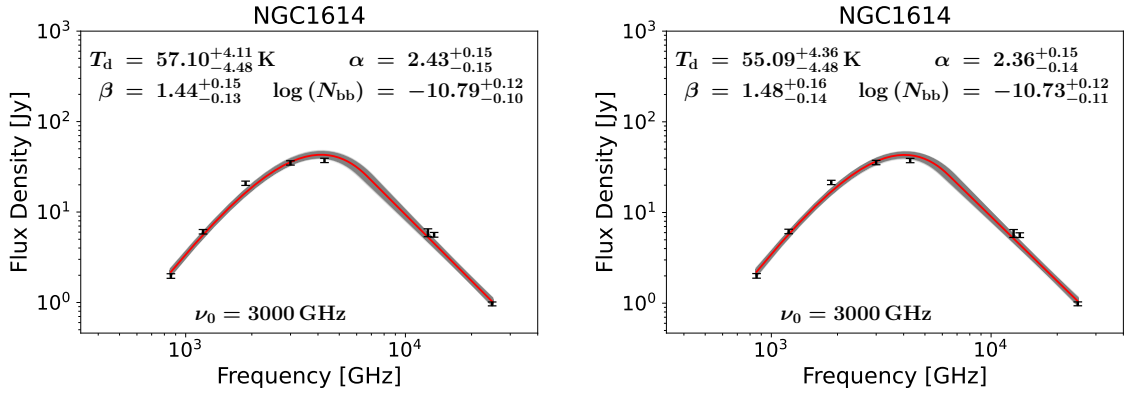

Figure D.38: The SED function resulting from the MCMC fit of the optically thick SED model to the continuum data. The best fit SED function is shown in red, while the 68% confidence level is shown in gray. The archival continuum data is shown with black symbols. The left and right figures show the fitting results using fluxes originating from 25" and 27" diameter circular apertures, respectively. These apertures cover the regions we observed with the IRAM 30m telescope, at the H40α and H42α line frequencies, respectively. The model parameters resulting from the fit are displayed on the plot. The ν_0 parameter was fixed at 3000 GHz.

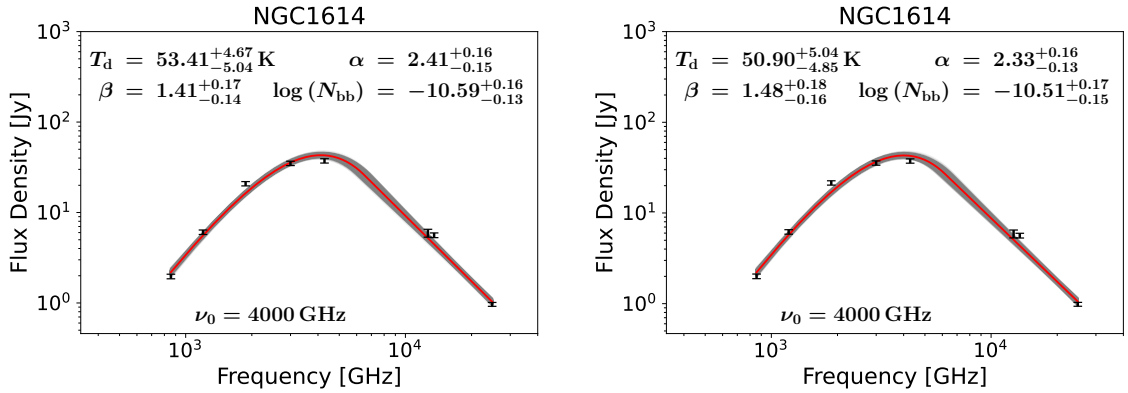

Figure D.39: The SED function resulting from the MCMC fit of the optically thick SED model to the continuum data. The best fit SED function is shown in red, while the 68% confidence level is shown in gray. The archival continuum data is shown with black symbols. The left and right figures show the fitting results using fluxes originating from 25" and 27" diameter circular apertures, respectively. These apertures cover the regions we observed with the IRAM 30m telescope, at the H40α and H42α line frequencies, respectively. The model parameters resulting from the fit are displayed on the plot. The ν_0 parameter was fixed at 4000 GHz.

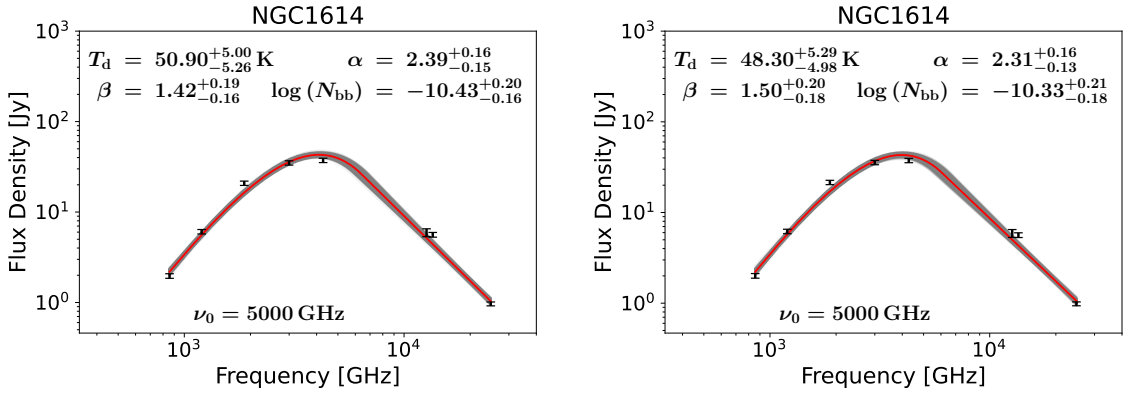

Figure D.40: The SED function resulting from the MCMC fit of the optically thick SED model to the continuum data. The best fit SED function is shown in red, while the 68% confidence level is shown in gray. The archival continuum data is shown with black symbols. The left and right figures show the fitting results using fluxes originating from 25" and 27" diameter circular apertures, respectively. These apertures cover the regions we observed with the IRAM 30m telescope, at the H40α and H42α line frequencies, respectively. The model parameters resulting from the fit are displayed on the plot. The ν_0 parameter was fixed at 5000 GHz.

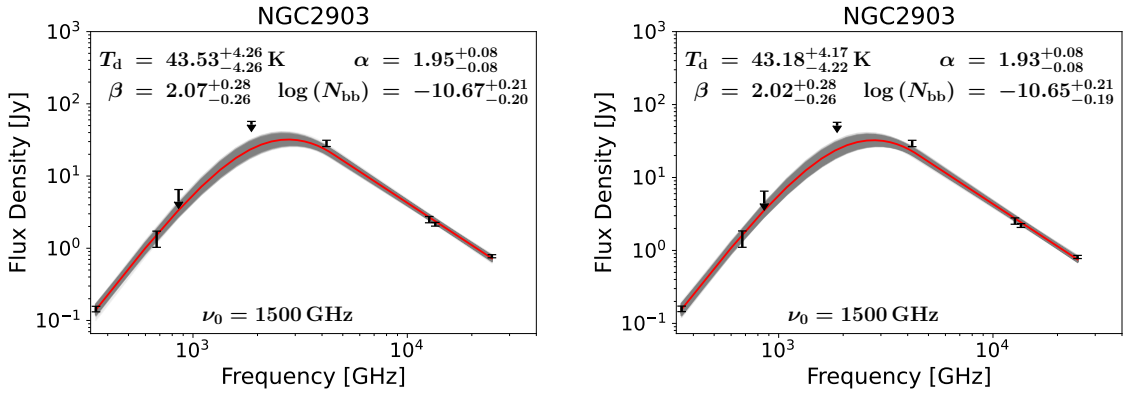

Figure D.41: The SED function resulting from the MCMC fit of the optically thick SED model to the continuum data. The best fit SED function is shown in red, while the 68% confidence level is shown in gray. The archival continuum data is shown with black symbols. The left and right figures show the fitting results using fluxes originating from 25" and 27" diameter circular apertures, respectively. These apertures cover the regions we observed with the IRAM 30m telescope, at the H40α and H42α line frequencies, respectively. The model parameters resulting from the fit are displayed on the plot. The ν_0 parameter was fixed at 1500 GHz.

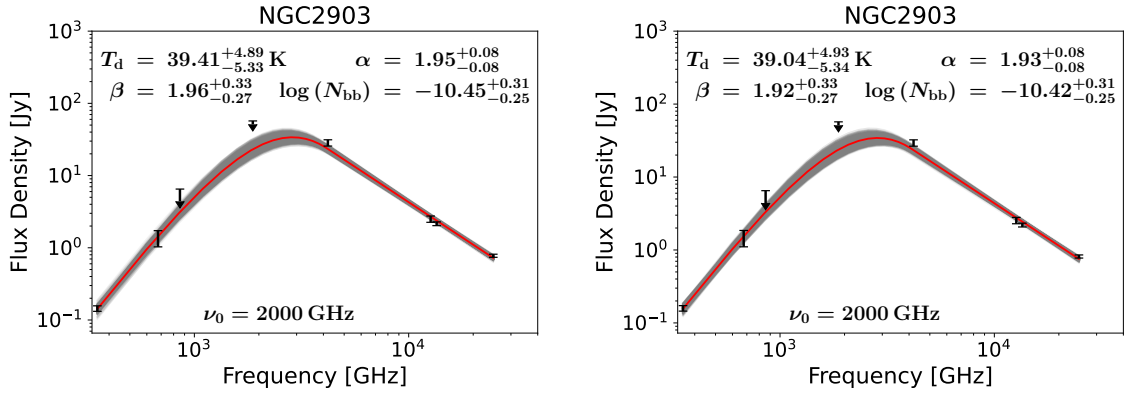

Figure D.42: The SED function resulting from the MCMC fit of the optically thick SED model to the continuum data. The best fit SED function is shown in red, while the 68% confidence level is shown in gray. The archival continuum data is shown with black symbols. The left and right figures show the fitting results using fluxes originating from 25" and 27" diameter circular apertures, respectively. These apertures cover the regions we observed with the IRAM 30m telescope, at the H40α and H42α line frequencies, respectively. The model parameters resulting from the fit are displayed on the plot. The ν_0 parameter was fixed at 2000 GHz.

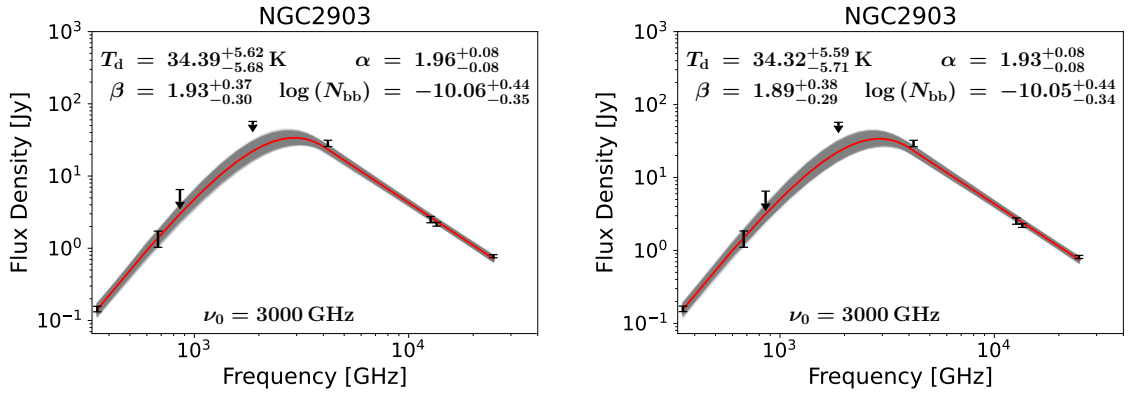

Figure D.43: The SED function resulting from the MCMC fit of the optically thick SED model to the continuum data. The best fit SED function is shown in red, while the 68% confidence level is shown in gray. The archival continuum data is shown with black symbols. The left and right figures show the fitting results using fluxes originating from 25" and 27" diameter circular apertures, respectively. These apertures cover the regions we observed with the IRAM 30m telescope, at the H40α and H42α line frequencies, respectively. The model parameters resulting from the fit are displayed on the plot. The ν_0 parameter was fixed at 3000 GHz.

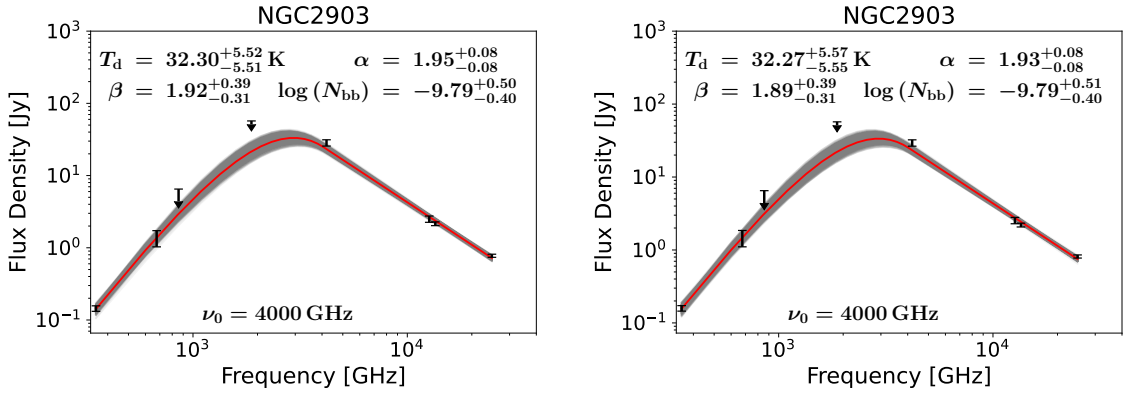

Figure D.44: The SED function resulting from the MCMC fit of the optically thick SED model to the continuum data. The best fit SED function is shown in red, while the 68% confidence level is shown in gray. The archival continuum data is shown with black symbols. The left and right figures show the fitting results using fluxes originating from 25" and 27" diameter circular apertures, respectively. These apertures cover the regions we observed with the IRAM 30m telescope, at the H40α and H42α line frequencies, respectively. The model parameters resulting from the fit are displayed on the plot. The ν_0 parameter was fixed at 4000 GHz.

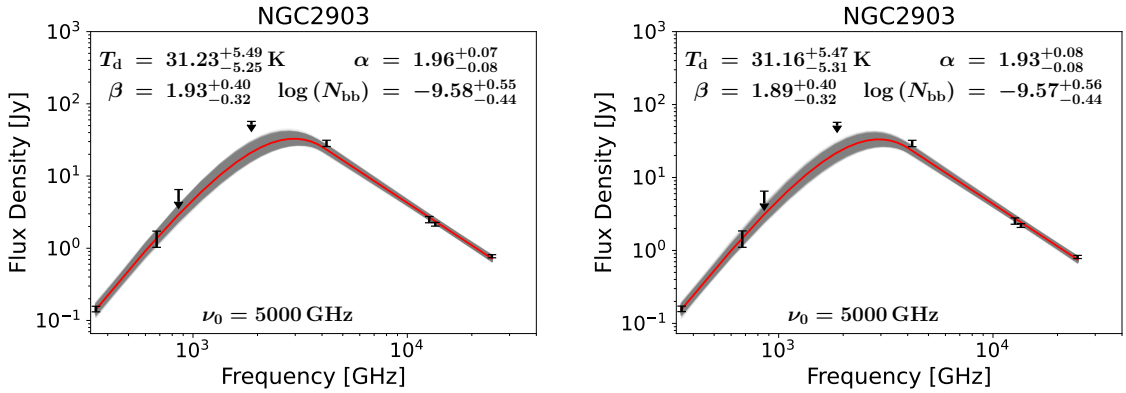

Figure D.45: The SED function resulting from the MCMC fit of the optically thick SED model to the continuum data. The best fit SED function is shown in red, while the 68% confidence level is shown in gray. The archival continuum data is shown with black symbols. The left and right figures show the fitting results using fluxes originating from 25" and 27" diameter circular apertures, respectively. These apertures cover the regions we observed with the IRAM 30m telescope, at the H40α and H42α line frequencies, respectively. The model parameters resulting from the fit are displayed on the plot. The ν_0 parameter was fixed at 5000 GHz.

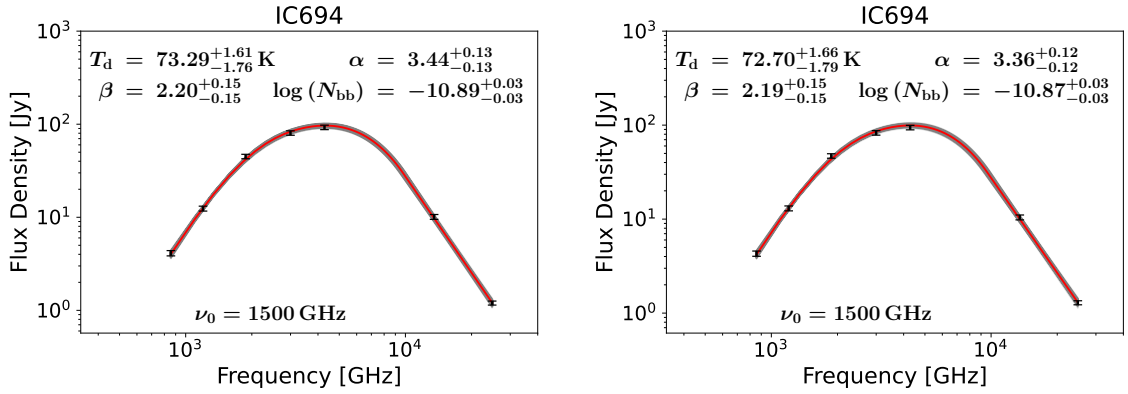

Figure D.46: The SED function resulting from the MCMC fit of the optically thick SED model to the continuum data. The best fit SED function is shown in red, while the 68% confidence level is shown in gray. The archival continuum data is shown with black symbols. The left and right figures show the fitting results using fluxes originating from 25" and 27" diameter circular apertures, respectively. These apertures cover the regions we observed with the IRAM 30m telescope, at the H40α and H42α line frequencies, respectively. The model parameters resulting from the fit are displayed on the plot. The ν_0 parameter was fixed at 1500 GHz.

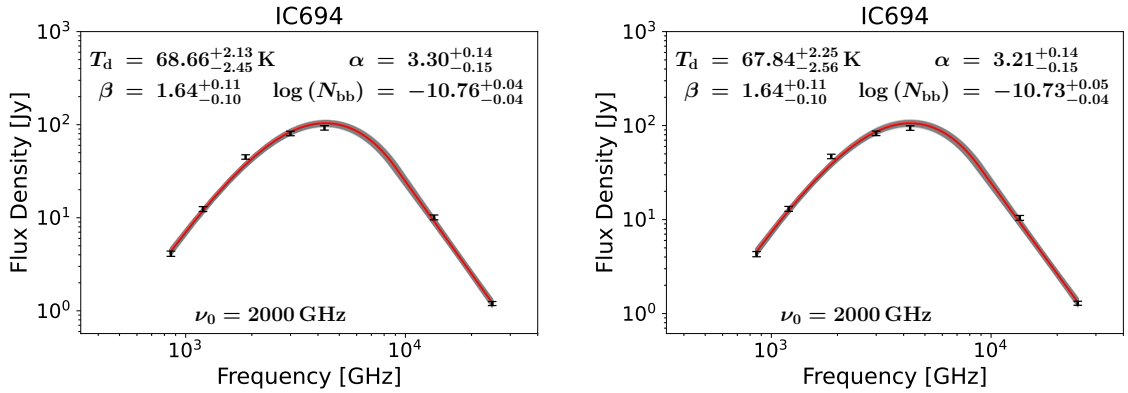

Figure D.47: The SED function resulting from the MCMC fit of the optically thick SED model to the continuum data. The best fit SED function is shown in red, while the 68% confidence level is shown in gray. The archival continuum data is shown with black symbols. The left and right figures show the fitting results using fluxes originating from 25" and 27" diameter circular apertures, respectively. These apertures cover the regions we observed with the IRAM 30m telescope, at the H40α and H42α line frequencies, respectively. The model parameters resulting from the fit are displayed on the plot. The ν_0 parameter was fixed at 2000 GHz.

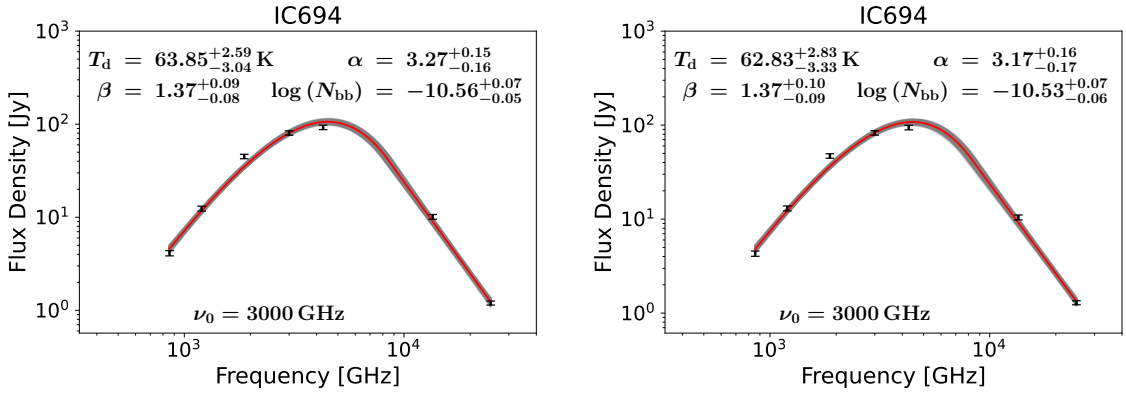

Figure D.48: The SED function resulting from the MCMC fit of the optically thick SED model to the continuum data. The best fit SED function is shown in red, while the 68% confidence level is shown in gray. The archival continuum data is shown with black symbols. The left and right figures show the fitting results using fluxes originating from 25" and 27" diameter circular apertures, respectively. These apertures cover the regions we observed with the IRAM 30m telescope, at the H40α and H42α line frequencies, respectively. The model parameters resulting from the fit are displayed on the plot. The ν_0 parameter was fixed at 3000 GHz.

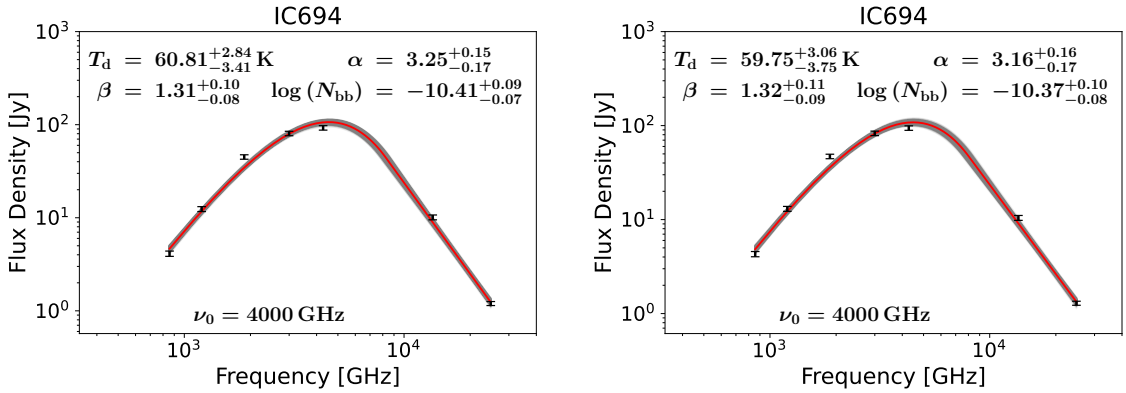

Figure D.49: The SED function resulting from the MCMC fit of the optically thick SED model to the continuum data. The best fit SED function is shown in red, while the 68% confidence level is shown in gray. The archival continuum data is shown with black symbols. The left and right figures show the fitting results using fluxes originating from 25" and 27" diameter circular apertures, respectively. These apertures cover the regions we observed with the IRAM 30m telescope, at the H40α and H42α line frequencies, respectively. The model parameters resulting from the fit are displayed on the plot. The ν_0 parameter was fixed at 4000 GHz.

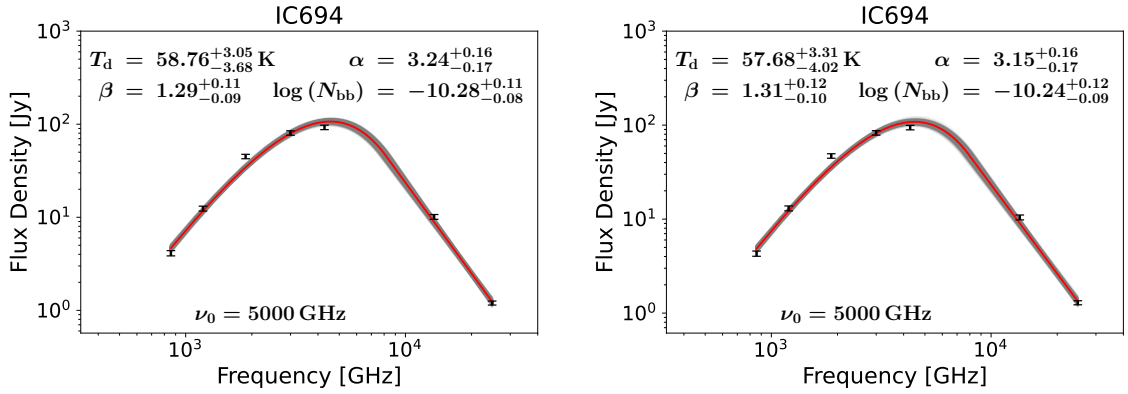

Figure D.50: The SED function resulting from the MCMC fit of the optically thick SED model to the continuum data. The best fit SED function is shown in red, while the 68% confidence level is shown in gray. The archival continuum data is shown with black symbols. The left and right figures show the fitting results using fluxes originating from 25" and 27" diameter circular apertures, respectively. These apertures cover the regions we observed with the IRAM 30m telescope, at the H40α and H42α line frequencies, respectively. The model parameters resulting from the fit are displayed on the plot. The ν_0 parameter was fixed at 5000 GHz.

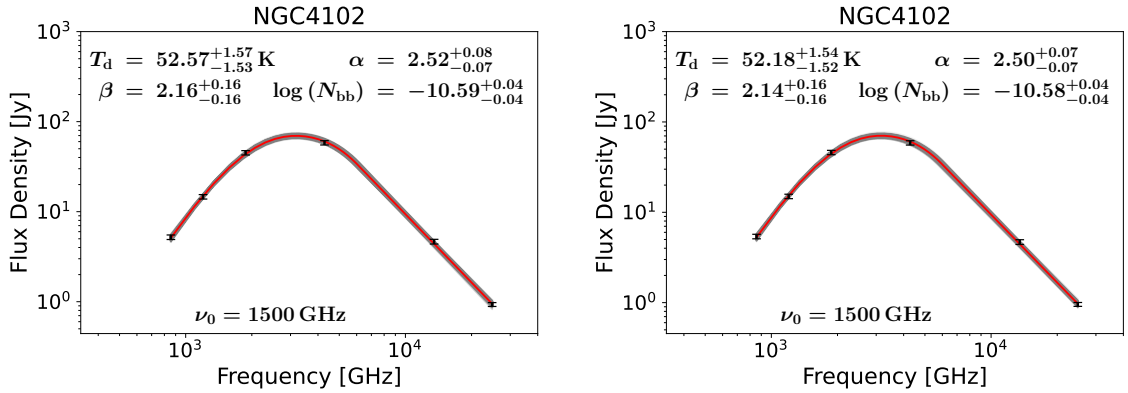

Figure D.51: The SED function resulting from the MCMC fit of the optically thick SED model to the continuum data. The best fit SED function is shown in red, while the 68% confidence level is shown in gray. The archival continuum data is shown with black symbols. The left and right figures show the fitting results using fluxes originating from 25" and 27" diameter circular apertures, respectively. These apertures cover the regions we observed with the IRAM 30m telescope, at the H40α and H42α line frequencies, respectively. The model parameters resulting from the fit are displayed on the plot. The ν_0 parameter was fixed at 1500 GHz.

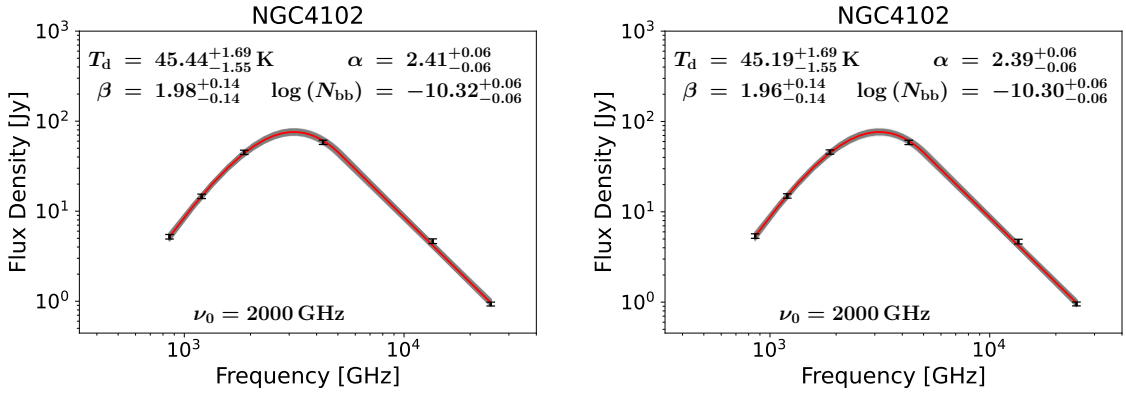

Figure D.52: The SED function resulting from the MCMC fit of the optically thick SED model to the continuum data. The best fit SED function is shown in red, while the 68% confidence level is shown in gray. The archival continuum data is shown with black symbols. The left and right figures show the fitting results using fluxes originating from 25" and 27" diameter circular apertures, respectively. These apertures cover the regions we observed with the IRAM 30m telescope, at the H40α and H42α line frequencies, respectively. The model parameters resulting from the fit are displayed on the plot. The ν_0 parameter was fixed at 2000 GHz.

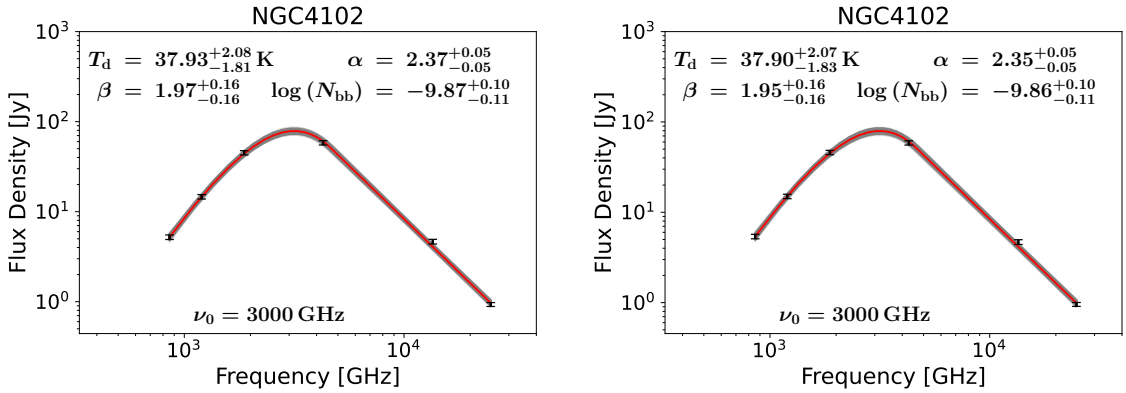

Figure D.53: The SED function resulting from the MCMC fit of the optically thick SED model to the continuum data. The best fit SED function is shown in red, while the 68% confidence level is shown in gray. The archival continuum data is shown with black symbols. The left and right figures show the fitting results using fluxes originating from 25" and 27" diameter circular apertures, respectively. These apertures cover the regions we observed with the IRAM 30m telescope, at the H40α and H42α line frequencies, respectively. The model parameters resulting from the fit are displayed on the plot. The ν_0 parameter was fixed at 3000 GHz.

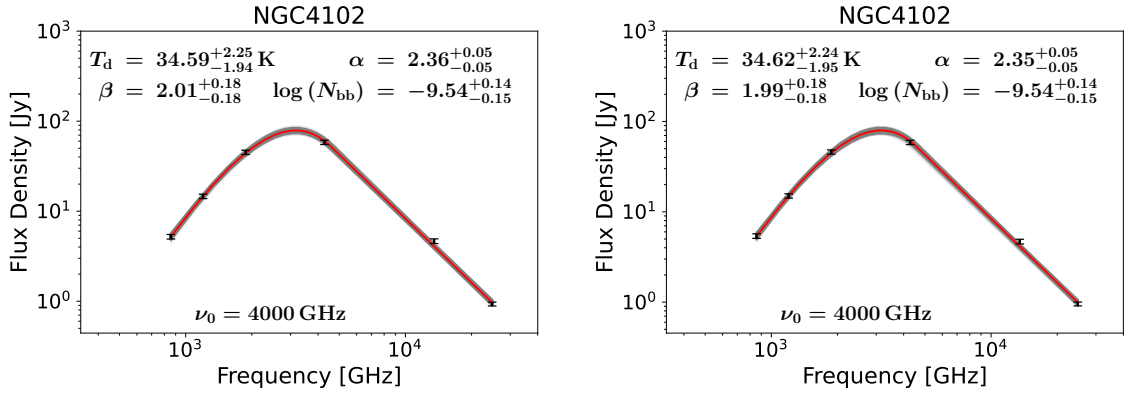

Figure D.54: The SED function resulting from the MCMC fit of the optically thick SED model to the continuum data. The best fit SED function is shown in red, while the 68% confidence level is shown in gray. The archival continuum data is shown with black symbols. The left and right figures show the fitting results using fluxes originating from 25" and 27" diameter circular apertures, respectively. These apertures cover the regions we observed with the IRAM 30m telescope, at the H40α and H42α line frequencies, respectively. The model parameters resulting from the fit are displayed on the plot. The ν_0 parameter was fixed at 4000 GHz.

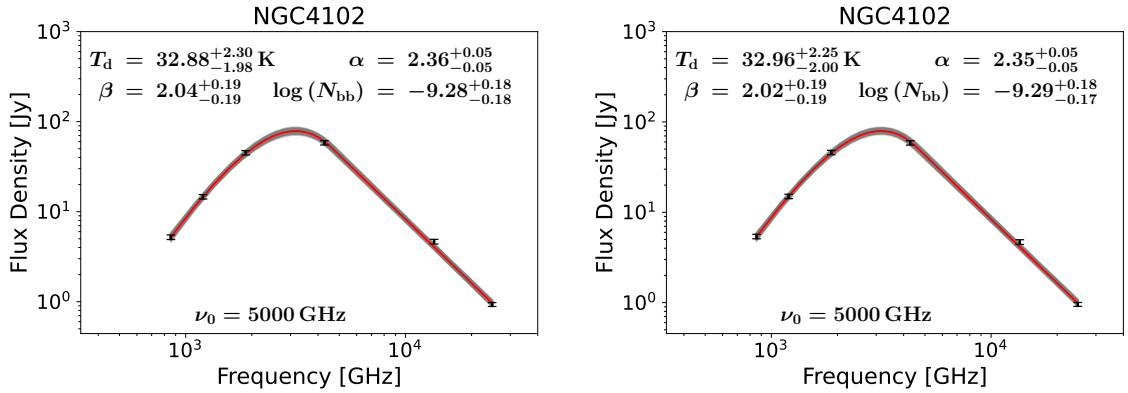

Figure D.55: The SED function resulting from the MCMC fit of the optically thick SED model to the continuum data. The best fit SED function is shown in red, while the 68% confidence level is shown in gray. The archival continuum data is shown with black symbols. The left and right figures show the fitting results using fluxes originating from 25" and 27" diameter circular apertures, respectively. These apertures cover the regions we observed with the IRAM 30m telescope, at the H40α and H42α line frequencies, respectively. The model parameters resulting from the fit are displayed on the plot. The ν_0 parameter was fixed at 5000 GHz.

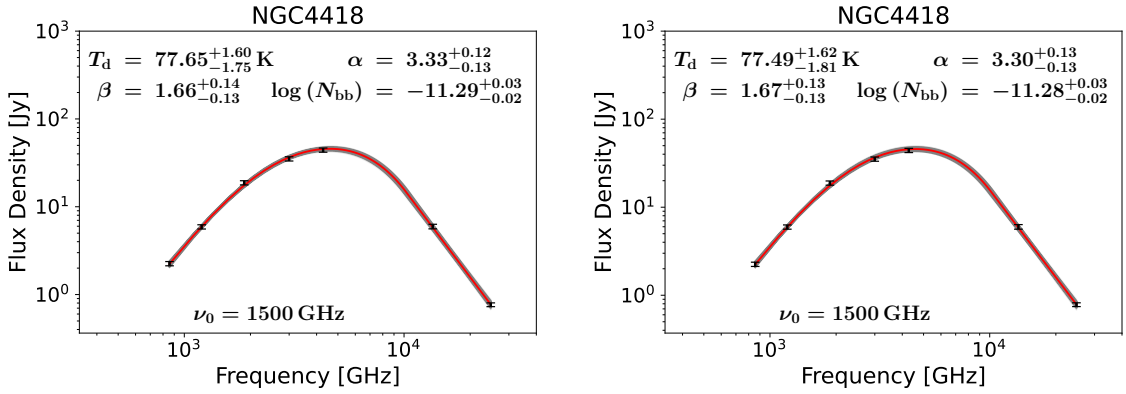

Figure D.56: The SED function resulting from the MCMC fit of the optically thick SED model to the continuum data. The best fit SED function is shown in red, while the 68% confidence level is shown in gray. The archival continuum data is shown with black symbols. The left and right figures show the fitting results using fluxes originating from 25" and 27" diameter circular apertures, respectively. These apertures cover the regions we observed with the IRAM 30m telescope, at the H40α and H42α line frequencies, respectively. The model parameters resulting from the fit are displayed on the plot. The ν_0 parameter was fixed at 1500 GHz.

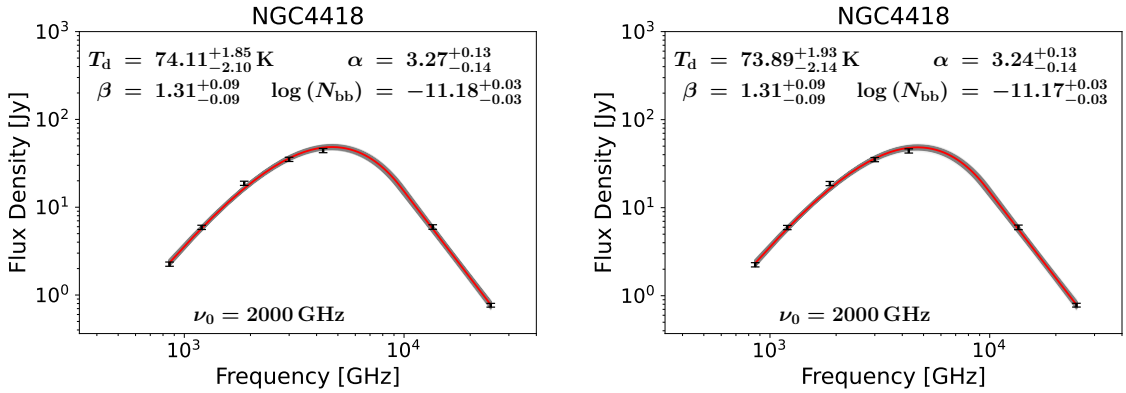

Figure D.57: The SED function resulting from the MCMC fit of the optically thick SED model to the continuum data. The best fit SED function is shown in red, while the 68% confidence level is shown in gray. The archival continuum data is shown with black symbols. The left and right figures show the fitting results using fluxes originating from 25" and 27" diameter circular apertures, respectively. These apertures cover the regions we observed with the IRAM 30m telescope, at the H40α and H42α line frequencies, respectively. The model parameters resulting from the fit are displayed on the plot. The ν_0 parameter was fixed at 2000 GHz.

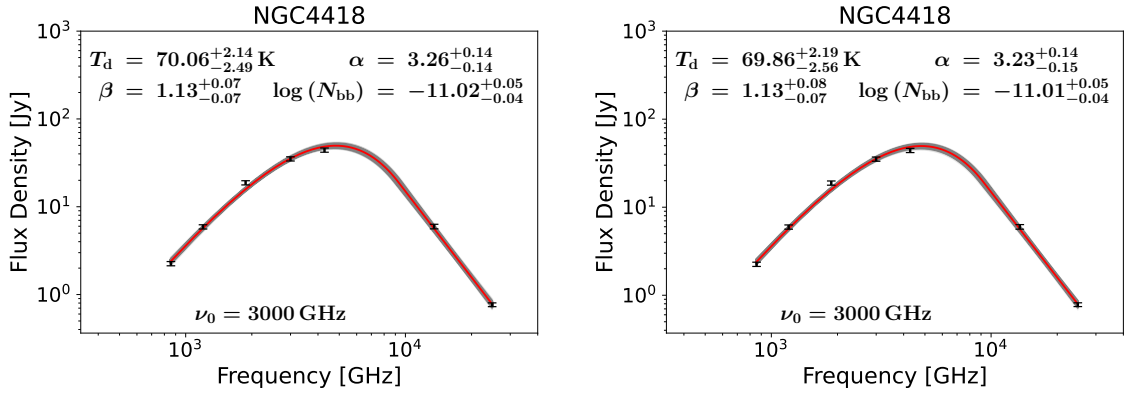

Figure D.58: The SED function resulting from the MCMC fit of the optically thick SED model to the continuum data. The best fit SED function is shown in red, while the 68% confidence level is shown in gray. The archival continuum data is shown with black symbols. The left and right figures show the fitting results using fluxes originating from 25" and 27" diameter circular apertures, respectively. These apertures cover the regions we observed with the IRAM 30m telescope, at the H40α and H42α line frequencies, respectively. The model parameters resulting from the fit are displayed on the plot. The ν_0 parameter was fixed at 3000 GHz.

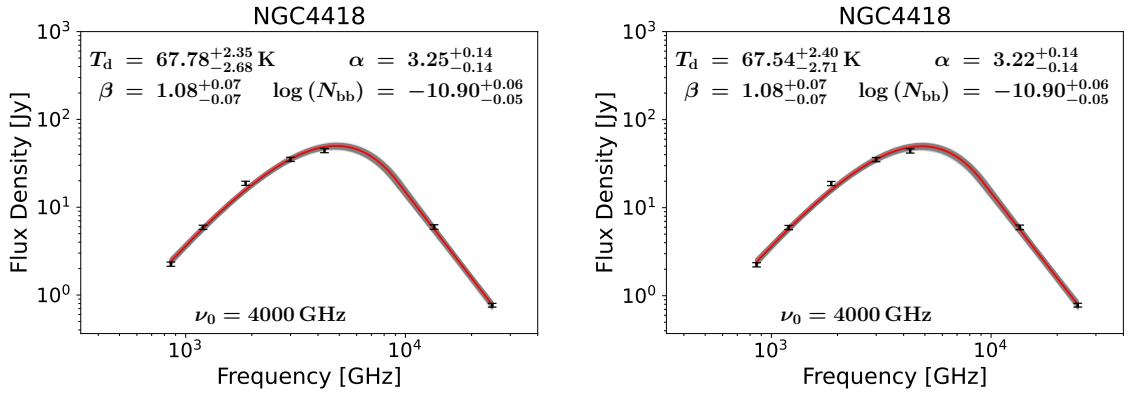

Figure D.59: The SED function resulting from the MCMC fit of the optically thick SED model to the continuum data. The best fit SED function is shown in red, while the 68% confidence level is shown in gray. The archival continuum data is shown with black symbols. The left and right figures show the fitting results using fluxes originating from 25" and 27" diameter circular apertures, respectively. These apertures cover the regions we observed with the IRAM 30m telescope, at the H40α and H42α line frequencies, respectively. The model parameters resulting from the fit are displayed on the plot. The ν_0 parameter was fixed at 4000 GHz.

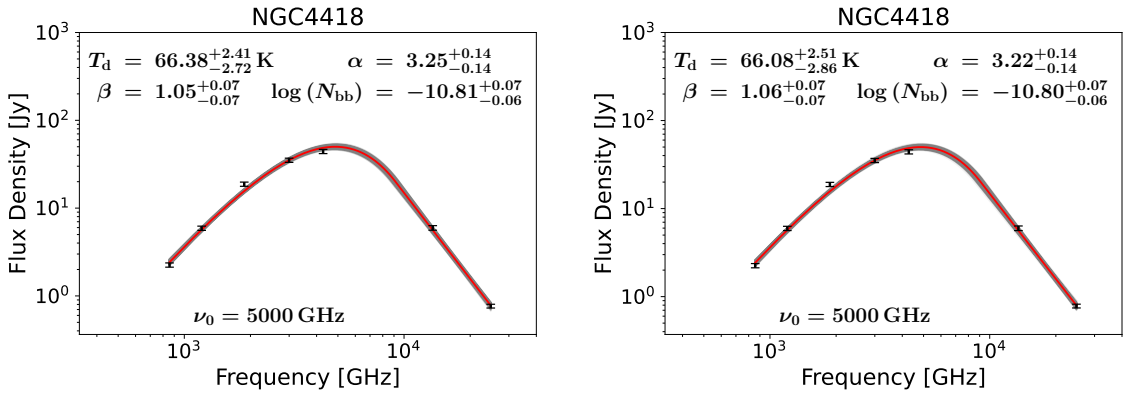

Figure D.60: The SED function resulting from the MCMC fit of the optically thick SED model to the continuum data. The best fit SED function is shown in red, while the 68% confidence level is shown in gray. The archival continuum data is shown with black symbols. The left and right figures show the fitting results using fluxes originating from 25" and 27" diameter circular apertures, respectively. These apertures cover the regions we observed with the IRAM 30m telescope, at the H40α and H42α line frequencies, respectively. The model parameters resulting from the fit are displayed on the plot. The ν_0 parameter was fixed at 5000 GHz.

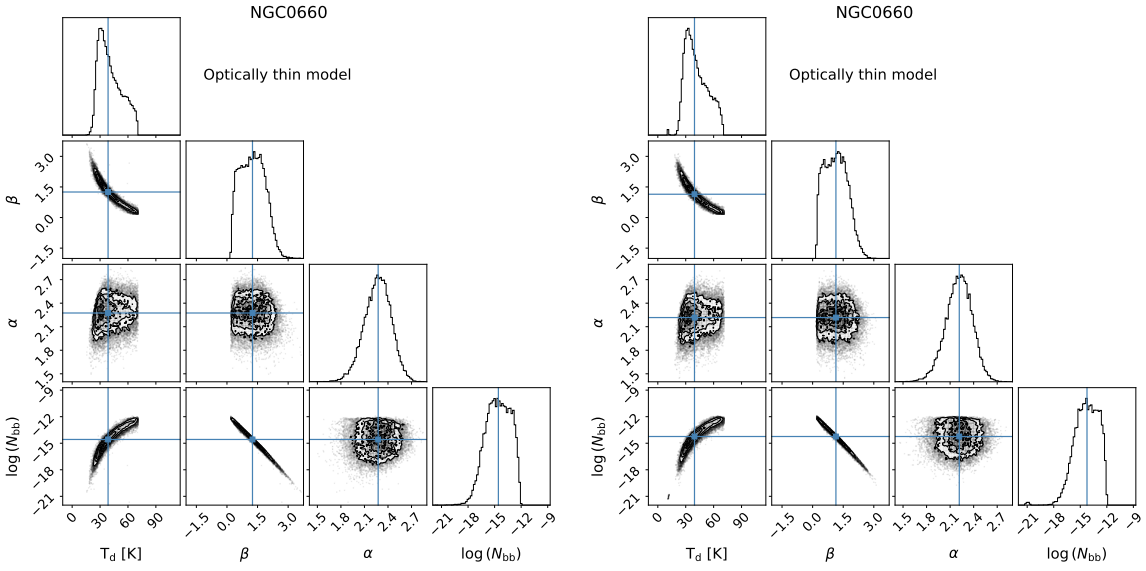

Figure D.61: The posterior probability distributions of the four parameters of our optically thin model, resulting from the MCMC fit of the model to the observed data. The highlights show the median values of the parameters. The left and right figures correspond to fits of models to fluxes originating from 25" and 27" diameter circular apertures, respectively. These apertures cover the regions we observed with the IRAM 30m telescope, at the H40α and H42α line frequencies, respectively.

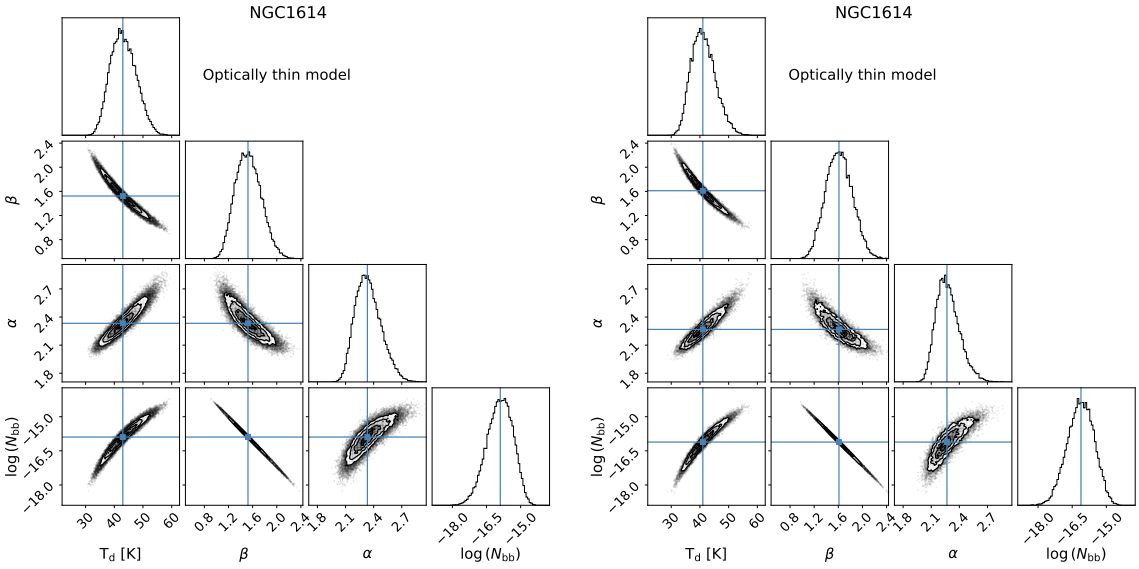

Figure D.62: The posterior probability distributions of the four parameters of our optically thin model, resulting from the MCMC fit of the model to the observed data. The highlights show the median values of the parameters. The left and right figures correspond to fits of models to fluxes originating from 25" and 27" diameter circular apertures, respectively. These apertures cover the regions we observed with the IRAM 30m telescope, at the H40α and H42α line frequencies, respectively.

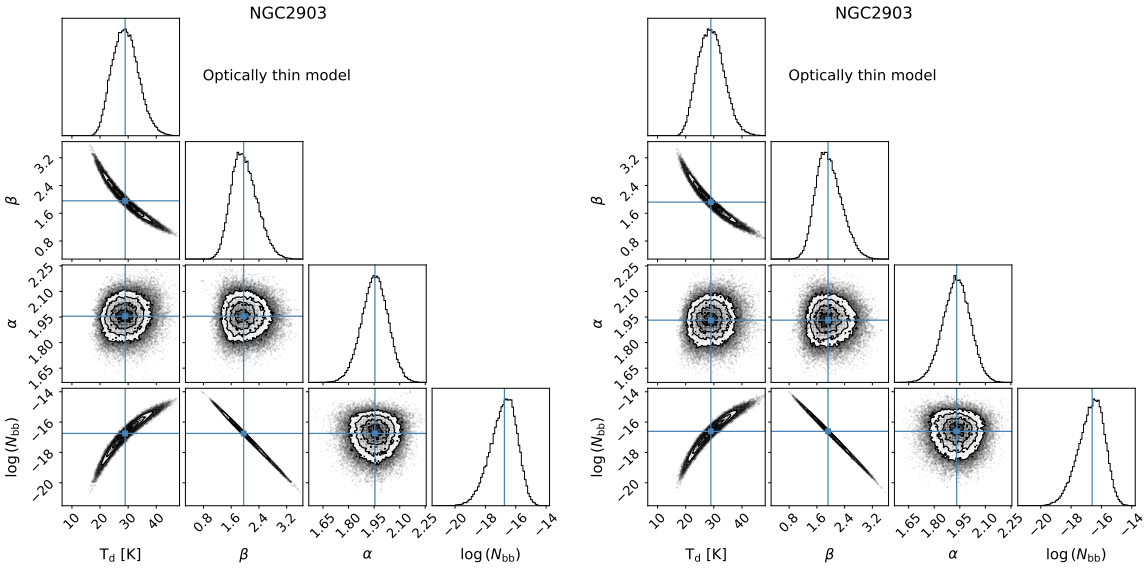

Figure D.63: The posterior probability distributions of the four parameters of our optically thin model, resulting from the MCMC fit of the model to the observed data. The highlights show the median values of the parameters. The left and right figures correspond to fits of models to fluxes originating from 25" and 27" diameter circular apertures, respectively. These apertures cover the regions we observed with the IRAM 30m telescope, at the H40α and H42α line frequencies, respectively.

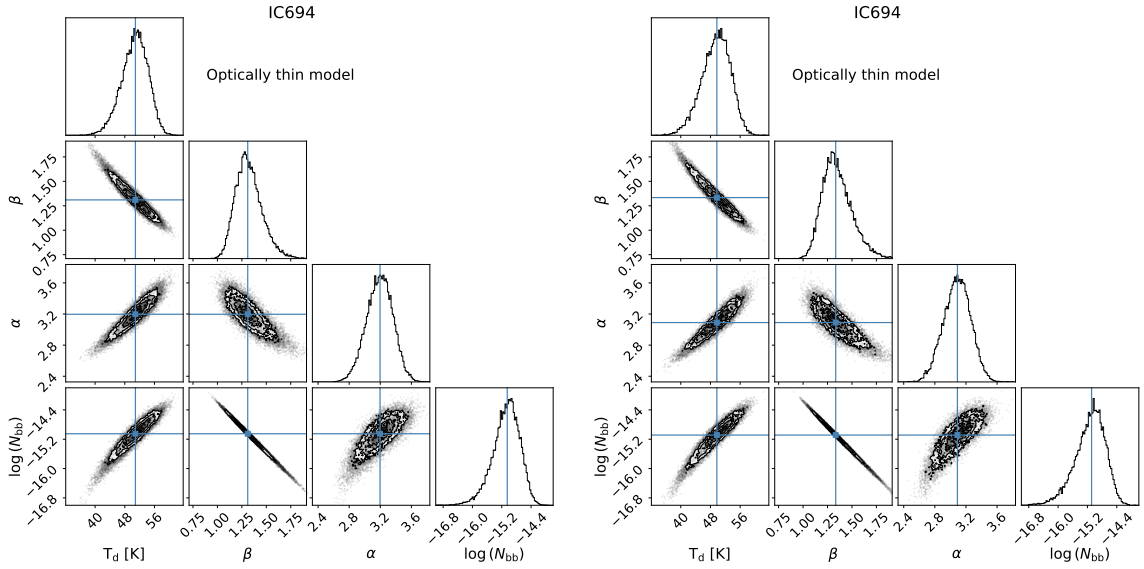

Figure D.64: The posterior probability distributions of the four parameters of our optically thin model, resulting from the MCMC fit of the model to the observed data. The highlights show the median values of the parameters. The left and right figures correspond to fits of models to fluxes originating from 25” and 27” diameter circular apertures, respectively. These apertures cover the regions we observed with the IRAM 30m telescope, at the H40α and H42α line frequencies, respectively.

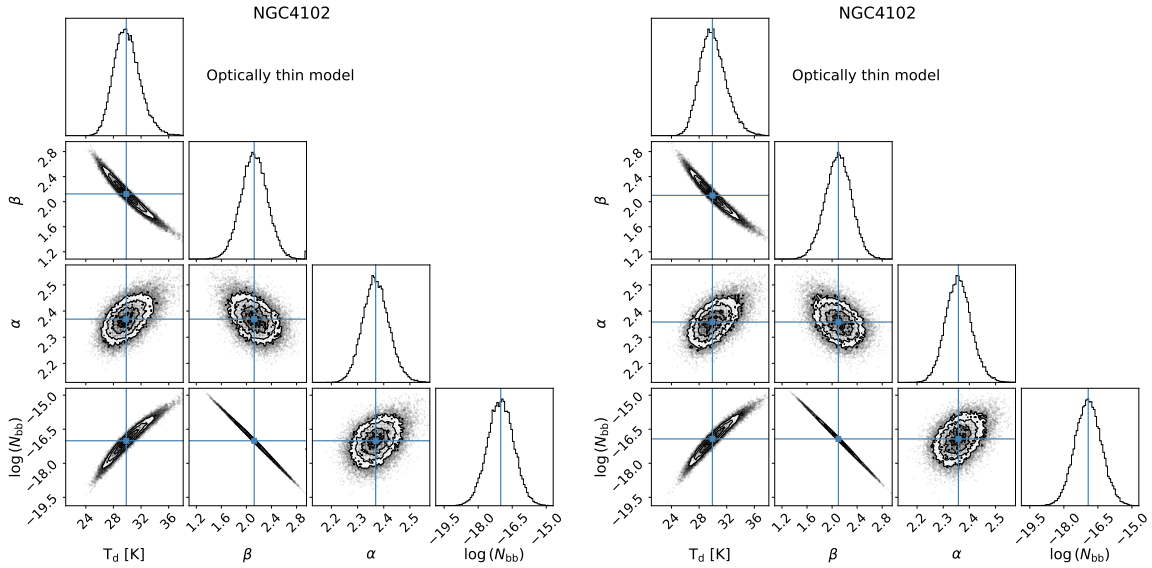

Figure D.65: The posterior probability distributions of the four parameters of our optically thin model, resulting from the MCMC fit of the model to the observed data. The highlights show the median values of the parameters. The left and right figures correspond to fits of models to fluxes originating from 25” and 27” diameter circular apertures, respectively. These apertures cover the regions we observed with the IRAM 30m telescope, at the H40α and H42α line frequencies, respectively.

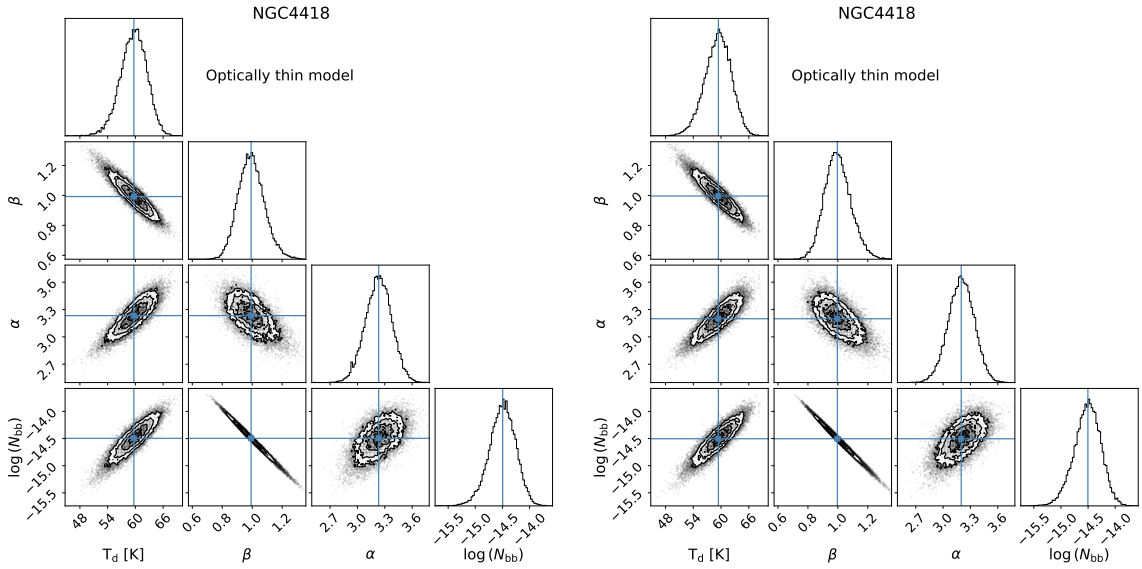

Figure D.66: The posterior probability distributions of the four parameters of our optically thin model, resulting from the MCMC fit of the model to the observed data. The highlights show the median values of the parameters. The left and right figures correspond to fits of models to fluxes originating from 25" and 27" diameter circular apertures, respectively. These apertures cover the regions we observed with the IRAM 30m telescope, at the H40α and H42α line frequencies, respectively.

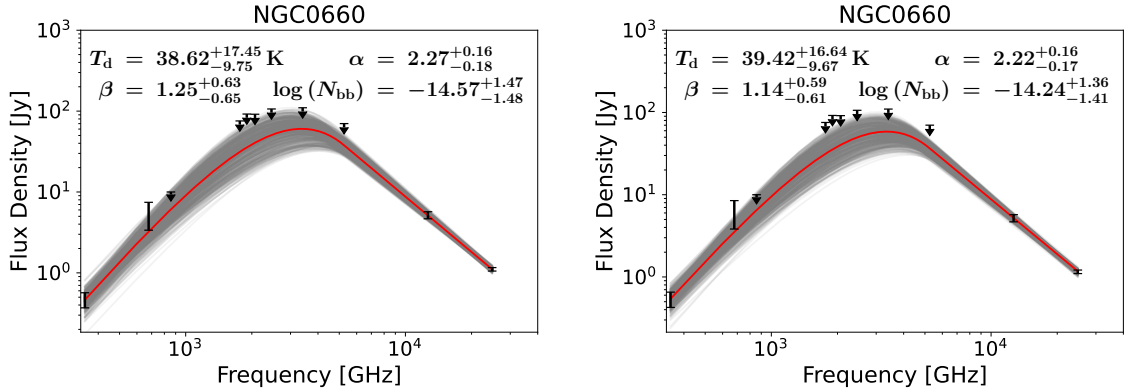

Figure D.67: The SED function resulting from the MCMC fit of the optically thin SED model to the continuum data. The best fit SED function is shown in red, while the 68% confidence level is shown in gray.The archival continuum data is shown with black symbols. The left and right figures show the fitting results using fluxes originating from 25" and 27" diameter circular apertures, respectively. These apertures cover the regions we observed with the IRAM 30m telescope, at the H40α and H42α line frequencies, respectively. The model parameters resulting from the fit are displayed on the plot.

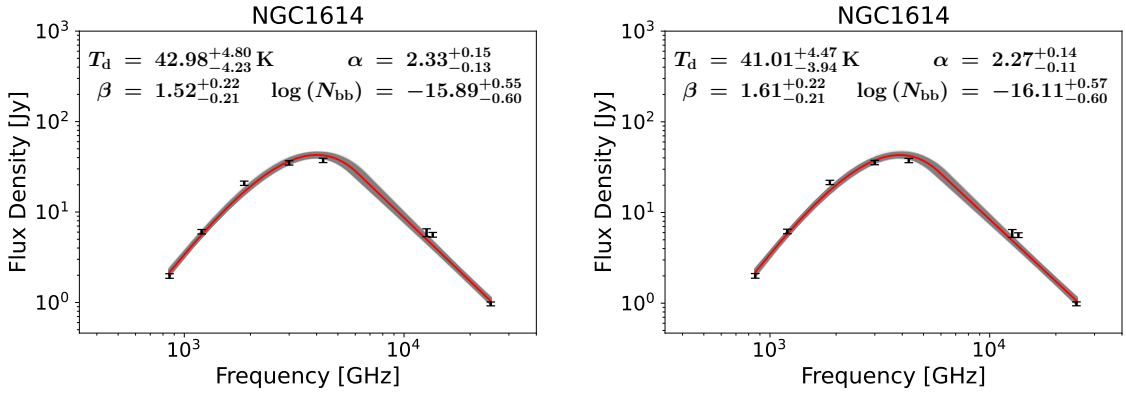

Figure D.68: The SED function resulting from the MCMC fit of the optically thin SED model to the continuum data. The best fit SED function is shown in red, while the 68% confidence level is shown in gray.The archival continuum data is shown with black symbols. The left and right figures show the fitting results using fluxes originating from 25" and 27" diameter circular apertures, respectively. These apertures cover the regions we observed with the IRAM 30m telescope, at the H40α and H42α line frequencies, respectively. The model parameters resulting from the fit are displayed on the plot.

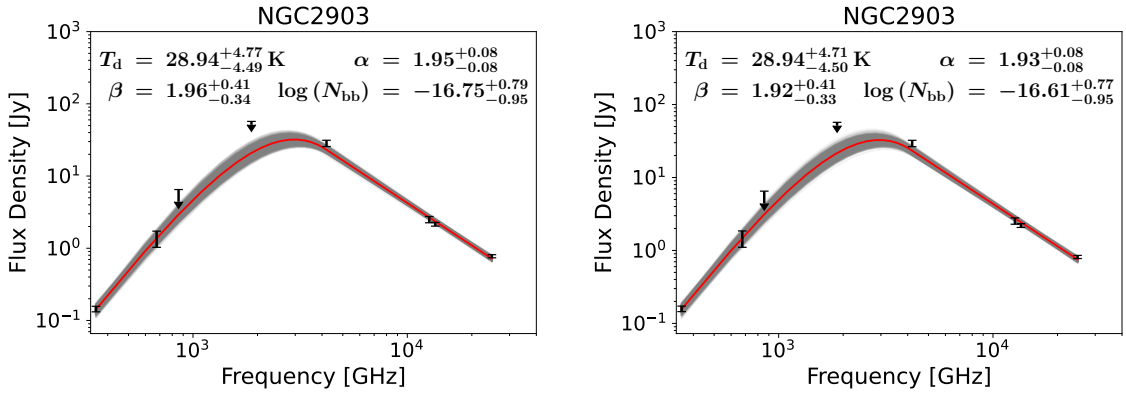

Figure D.69: The SED function resulting from the MCMC fit of the optically thin SED model to the continuum data. The best fit SED function is shown in red, while the 68% confidence level is shown in gray.The archival continuum data is shown with black symbols. The left and right figures show the fitting results using fluxes originating from 25" and 27" diameter circular apertures, respectively. These apertures cover the regions we observed with the IRAM 30m telescope, at the H40α and H42α line frequencies, respectively. The model parameters resulting from the fit are displayed on the plot.

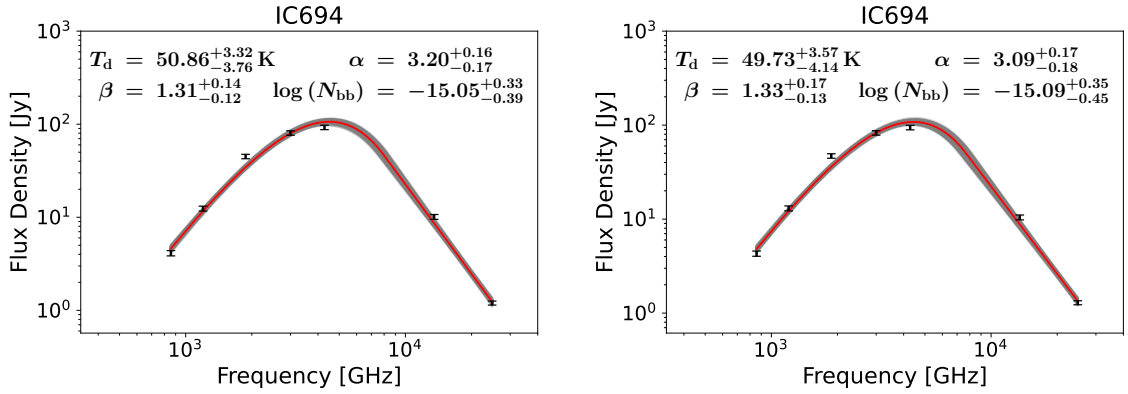

Figure D.70: The SED function resulting from the MCMC fit of the optically thin SED model to the continuum data. The best fit SED function is shown in red, while the 68% confidence level is shown in gray.The archival continuum data is shown with black symbols. The left and right figures show the fitting results using fluxes originating from 25" and 27" diameter circular apertures, respectively. These apertures cover the regions we observed with the IRAM 30m telescope, at the H40α and H42α line frequencies, respectively. The model parameters resulting from the fit are displayed on the plot.

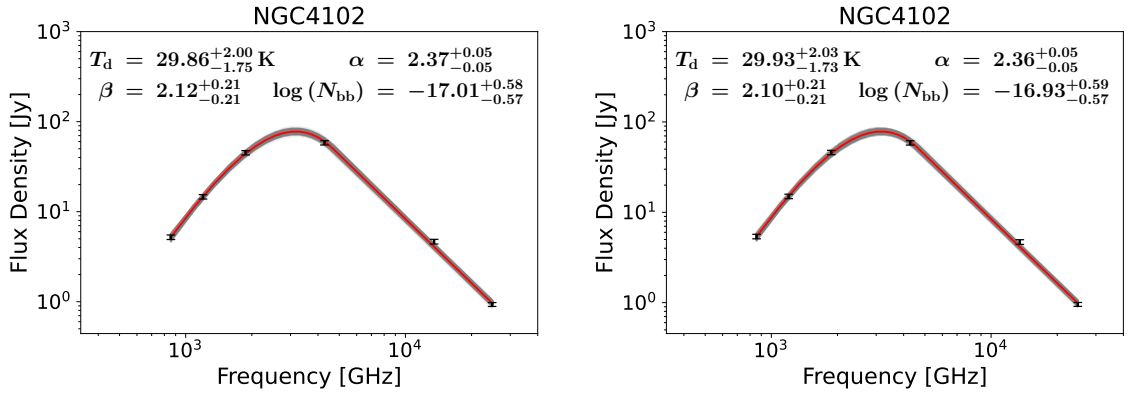

Figure D.71: The SED function resulting from the MCMC fit of the optically thin SED model to the continuum data. The best fit SED function is shown in red, while the 68% confidence level is shown in gray.The archival continuum data is shown with black symbols. The left and right figures show the fitting results using fluxes originating from 25" and 27" diameter circular apertures, respectively. These apertures cover the regions we observed with the IRAM 30m telescope, at the H40α and H42α line frequencies, respectively. The model parameters resulting from the fit are displayed on the plot.

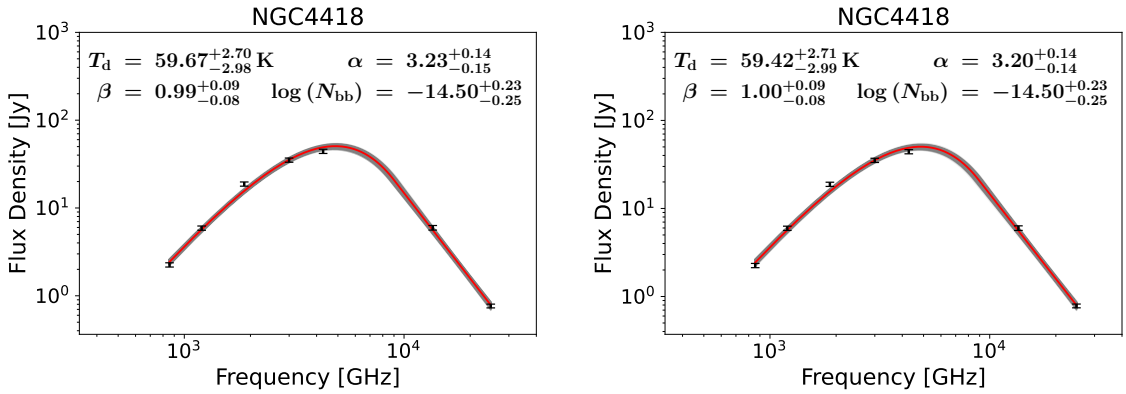

Figure D.72: The SED function resulting from the MCMC fit of the optically thin SED model to the continuum data. The best fit SED function is shown in red, while the 68% confidence level is shown in gray.The archival continuum data is shown with black symbols. The left and right figures show the fitting results using fluxes originating from 25" and 27" diameter circular apertures, respectively. These apertures cover the regions we observed with the IRAM 30m telescope, at the H40α and H42α line frequencies, respectively. The model parameters resulting from the fit are displayed on the plot.

Bibliography

Abbott B. P., et al., 2016, Phys. Rev. Lett., 116, 061102

Abbott B. P., et al., 2020, ApJL, 892, L3

Abdurro'uf Lin Y.-T., Hirashita H., Morishita T., Tacchella S., Akiyama M., Takeuchi T. T., Wu P.-F., 2022, ApJ, 926, 81

Adam R., et al., 2018, A&A, 609, A115

Afflerbach A., Churchwell E., Werner M. W., 1997, ApJ, 478, 190

Alexander R. D., Clarke C. J., Pringle J. E., 2006a, MNRAS, 369, 216

Alexander R. D., Clarke C. J., Pringle J. E., 2006b, MNRAS, 369, 229

Allen M. G., Dopita M. A., Tsvetanov Z. I., 1998, ApJ, 493, 571

Allen A., Li Z.-Y., Shu F. H., 2003, ApJ, 599, 363

Alloin D., et al., 1995, A&A, 293, 293

Alonso-Herrero A., Rieke G. H., Rieke M. J., Scoville N. Z., 2000, ApJ, 532, 845

Alonso-Herrero A., Ryder S. D., Knapen J. H., 2001a, MNRAS, 322, 757

Alonso-Herrero A., Ryder S. D., Knapen J. H., 2001b, MNRAS, 322, 757

Alonso-Herrero A., Ryder S. D., Knapen J. H., 2001c, MNRAS, 322, 757

Alonso-Herrero A., et al., 2009, ApJ, 697, 660

Anantharamaiah K. R., Goss W. M., 1990, in Gordon M. A., Sorochenko R. L., eds, Astrophysics and Space Science Library Vol. 163, IAU Colloq. 125: Radio Recombination Lines: 25 Years of Investigation. p. 267, doi:10.1007/978-94-009-0625-9˙26

Anantharamaiah K. R., Zhao J.-H., Goss W. M., Viallefond F., 1993, ApJ, 419, 585

Anantharamaiah K. R., Viallefond F., Mohan N. R., Goss W. M., Zhao J. H., 2000, ApJ, 537, 613

Anderson J. P., et al., 2016, A&A, 589, A110

Andrews S. M., Williams J. P., 2007, ApJ, 659, 705

Aniano G., Draine B. T., Gordon K. D., Sandstrom K., 2011, PASP, 123, 1218

Antonucci R., 1993, ARA&A, 31, 473

Argo M. K., van Bemmel I. M., Connolly S. D., Beswick R. J., 2015, MNRAS, 452, 1081

Armentrout W. P., Anderson L., Wenger T. V., Balser D., Bania T., 2018, in American Astronomical Society Meeting Abstracts #231. p. 445.04

Armus L., 2014, in American Astronomical Society Meeting Abstracts #223. p. 327.04

Armus L., et al., 2009, PASP, 121, 559

Asaki Y., et al., 2023, ApJ, 958, 86

Asplund M., Grevesse N., Jacques Sauval A., 2006, nphysa, 777, 1

Asplund M., Grevesse N., Sauval A. J., Scott P., 2009, ARA&A, 47, 481

Awaki H., Ueno S., Koyama K., Tsuru T., Iwasawa K., 1996, PASJ, 48, 409

Báez-Rubio A., Martín-Pintado J., Rico-Villas F., Jiménez-Serra I., 2018, ApJL, 867, L6

Bahcall N. A., Fan X., Cen R., 1997, ApJL, 485, L53

Baldry I. K., Glazebrook K., Brinkmann J., Ivezić Ž., Lupton R. H., Nichol R. C., Szalay A. S., 2004, ApJ, 600, 681

Baldry I. K., Balogh M. L., Bower R. G., Glazebrook K., Nichol R. C., Bamford S. P., Budavari T., 2006, MNRAS, 373, 469

Baldwin J. A., Phillips M. M., Terlevich R., 1981, PASP, 93, 5

Ballo L., Braito V., Della Ceca R., Maraschi L., Tavecchio F., Dadina M., 2004, ApJ, 600, 634

Balogh M. L., Baldry I. K., Nichol R., Miller C., Bower R., Glazebrook K., 2004, ApJL, 615, L101

Balser D. S., Rood R. T., Bania T. M., Anderson L. D., 2011, ApJ, 738, 27

Balzano V. A., 1983, ApJ, 268, 602

Barcos-Muñoz L., et al., 2015, ApJ, 799, 10

Barvainis R., 1987, ApJ, 320, 537

Beck S. C., Turner J. L., Ho P. T. P., Lacy J. H., Kelly D. M., 1996, ApJ, 457, 610

Beck S. C., Lacy J. H., Turner J. L., 2010, ApJ, 722, 1175

Belkus H., Van Bever J., Vanbeveren D., van Rensbergen W., 2003, A&A, 400, 429

Bell E. F., 2003, ApJ, 586, 794

Bell M. B., Seaquist E. R., 1978, ApJ, 223, 378

Beltrán M. T., Cesaroni R., Codella C., Testi L., Furuya R. S., Olmi L., 2006, Nature, 443, 427

Bendo G. J., Beswick R. J., D'Cruze M. J., Dickinson C., Fuller G. A., Muxlow T. W. B., 2015, MNRAS, 450, L80

Bendo G. J., Henkel C., D'Cruze M. J., Dickinson C., Fuller G. A., Karim A., 2016, MNRAS, 463, 252

Bendo G. J., Miura R. E., Espada D., Nakanishi K., Beswick R. J., D'Cruze M. J., Dickinson C., Fuller G. A., 2017, MNRAS, 472, 1239

Bergvall N., Zackrisson E., Andersson B. G., Arnberg D., Masegosa J., Östlin G., 2006, A&A, 448, 513

Best P. N., Röttgering H. J. A., Longair M. S., 2000, MNRAS, 311, 23

Biermann P. L., Strittmatter P. A., 1987, ApJ, 322, 643

Bigiel F., Leroy A. K., Blitz L., Bolatto A. D., da Cunha E., Rosolowsky E., Sandstrom K., Usero A., 2015, ApJ, 815, 103

Birnboim Y., Dekel A., 2003, MNRAS, 345, 349

Black D. C., Bodenheimer P., 1975, ApJ, 199, 619

Blain A. W., Smail I., Ivison R. J., Kneib J. P., Frayer D. T., 2002, physrep, 369, 111

Blain A. W., Barnard V. E., Chapman S. C., 2003, MNRAS, 338, 733

Boggs P. T., Rogers J. E., 1990, Contemporary mathematics, 112, 183

Bonato M., et al., 2018, MNRAS, 478, 1512

Bondi H., 1952, MNRAS, 112, 195

Bonnor W. B., 1956, MNRAS, 116, 351

Borthakur S., Heckman T. M., Leitherer C., Overzier R. A., 2014, Science, 346, 216

Boselli A., et al., 2010, PASP, 122, 261

Bothun G. D., Rogers C., 1992, AJ, 103, 1484

Boulangier J., Gobrecht D., Decin L., 2019, IAU Symposium, 343, 129

Brammer G. B., et al., 2009, ApJL, 706, L173

Brauher J. R., Dale D. A., George H., 2008, The Astrophysical Journal Supplement Series, 178, 280

Bresolin F., 2007, ApJ, 656, 186

Bresolin F., Schaerer D., González Delgado R. M., Stasińska G., 2005, A&A, 441, 981

Bresolin F., Gieren W., Kudritzki R.-P., Pietrzyński G., Urbaneja M. A., Carraro G., 2009, ApJ, 700, 309

Brinchmann J., Charlot S., White S. D. M., Tremonti C., Kauffmann G., Heckman T., Brinkmann J., 2004, MNRAS, 351, 1151

Bruzual G., Charlot S., 2003, MNRAS, 344, 1000

Bruzual A. G., Charlot S., 1993, ApJ, 405, 538

Buat V., 2002, Ap&SS, 281, 129

Buat V., et al., 2007, ApJS, 173, 404

Calabrò A., et al., 2019, A&A, 632, A98

Calderone G., Sbarrato T., Ghisellini G., 2012, MNRAS, 425, L41

Calzetti D., 2001, PASP, 113, 1449

Calzetti D., 2013, in Falcón-Barroso J., Knapen J. H., eds, , Secular Evolution of Galaxies. p. 419, doi:10.48550/arXiv.1208.2997

Calzetti D., Meurer G. R., Bohlin R. C., Garnett D. R., Kinney A. L., Leitherer C., Storchi-Bergmann T., 1997, AJ, 114, 1834

Calzetti D., Armus L., Bohlin R. C., Kinney A. L., Koornneef J., Storchi-Bergmann T., 2000, ApJ, 533, 682

Calzetti D., et al., 2005, ApJ, 633, 871

Calzetti D., et al., 2007, ApJ, 666, 870

Calzetti D., et al., 2010, ApJ, 714, 1256

Calzetti D., et al., 2015, ApJ, 811, 75

Campbell A., Terlevich R., Melnick J., 1986, MNRAS, 223, 811

Cappellari M., et al., 2012, Nature, 484, 485

Caputi K. I., et al., 2006, ApJ, 637, 727

Cardamone C., et al., 2009, MNRAS, 399, 1191

Carter M., et al., 2012, A&A, 538, A89

Casey C. M., 2012, MNRAS, 425, 3094

Cenarro A. J., Gorgas J., Vazdekis A., Cardiel N., Peletier R. F., 2003, MNRAS, 339, L12

Cerviño M., Mas-Hesse J. M., 1994, A&A, 284, 749

Cesaroni R., et al., 2017, A&A, 602, A59

Chabrier G., 2003, PASP, 115, 763

Chandar R., et al., 2023, ApJ, 943, 142

Chen H.-R. V., Keto E., Zhang Q., Sridharan T. K., Liu S.-Y., Su Y.-N., 2016, ApJ, 823, 125

Chen E., Yu S.-Y., Ho L. C., 2021, ApJ, 906, 19

Chevance M., et al., 2020, MNRAS, 493, 2872

Chini R., Kreysa E., Mezger P. G., Gemuend H. P., 1986, A&A, 157, L1

Chisholm J., Orlitová I., Schaerer D., Verhamme A., Worseck G., Izotov Y. I., Thuan T. X., Guseva N. G., 2017, A&A, 605, A67

Chou R. C. Y., et al., 2007, ApJ, 670, 116

Chu J. K., et al., 2017a, VizieR Online Data Catalog, p. J/ApJS/229/25

Chu J. K., et al., 2017b, ApJS, 229, 25

Churchwell E., 2002, ARA&A, 40, 27

Clark B. G., 1980, A&A, 89, 377

Clarke C. J., Gendrin A., Sotomayor M., 2001, MNRAS, 328, 485

Clements D. L., Dunne L., Eales S., 2010, MNRAS, 403, 274

Clements D. L., et al., 2018, MNRAS, 475, 2097

Coc A., Vangioni E., 2017, International Journal of Modern Physics E, 26, 1741002

Colaboration C., 2015, The Hertzsprung-Russell (H-R) diagram, https://chandra.harvard.edu/edu/formal/variable_stars/bg_info.html

Cole S., et al., 2005, MNRAS, 362, 505

Condon J. J., 1992, ARA&A, 30, 575

Condon J. J., Condon M. A., Gisler G., Puschell J. J., 1982, ApJ, 252, 102

Conroy C., 2013, ARA&A, 51, 393

Conroy C., van Dokkum P. G., 2012, ApJ, 760, 71

Cortese L., et al., 2014, MNRAS, 440, 942

Costagliola F., Aalto S., Sakamoto K., Martín S., Beswick R., Muller S., Klöckner H. R., 2013, A&A, 556, A66

Coupeaud A., et al., 2011, A&A, 535, A124

Crutcher R. M., 2005, in Cesaroni R., Felli M., Churchwell E., Walmsley M., eds, 2005 Vol. 227, Massive Star Birth: A Crossroads of Astrophysics. pp 98–107, doi:10.1017/S1743921305004412

Csengeri T., et al., 2018, A&A, 617, A89

Daddi E., et al., 2007, ApJ, 670, 156

Daflon S., Cunha K., 2004, ApJ, 617, 1115

Dale D. A., Helou G., 2002, ApJ, 576, 159

Dale D. A., et al., 2009, ApJ, 703, 517

Dall'Olio D., et al., 2019, A&A, 626, A36

Dame T. M., Hartmann D., Thaddeus P., 2001, ApJ, 547, 792

Davidge T. J., 2010, ApJ, 725, 1342

Davies J. I., et al., 2014, MNRAS, 438, 1922

De Looze I., Baes M., Bendo G. J., Cortese L., Fritz J., 2011, MNRAS, 416, 2712

De Looze I., et al., 2014, A&A, 568, A62

Deharveng L., Peña M., Caplan J., Costero R., 2000, MNRAS, 311, 329

Dekel A., et al., 2009, Nature, 457, 451

Delhaize J., et al., 2017, A&A, 602, A4

Della Ceca R., et al., 2002, ApJL, 581, L9

Désert F. X., et al., 2008, A&A, 481, 411

Di Francesco J., Johnstone D., Kirk H., MacKenzie T., Ledwosinska E., 2008, ApJS, 175, 277

Di Matteo P., Bournaud F., Martig M., Combes F., Melchior A. L., Semelin B., 2008, A&A, 492, 31

Dietrich J., et al., 2018, MNRAS, 480, 3562

Ding H., Deller A. T., Fonseca E., Stairs I. H., Stappers B., Lyne A., 2021, ApJL, 921, L19

Done C., Madejski G. M., Smith D. A., 1996, ApJL, 463, L63

Dopita M. A., Groves B. A., Sutherland R. S., Kewley L. J., 2003, ApJ, 583, 727

Downes D., Solomon P. M., 1998, ApJ, 507, 615

Doyon R., Joseph R. D., Wright G. S., 1994, ApJ, 421, 101

Draine B. T., 2006, ApJ, 636, 1114

Draine B. T., 2011, Physics of the Interstellar and Intergalactic Medium

Draine B. T., Fraisse A. A., 2009, ApJ, 696, 1

Draine B. T., Lee H. M., 1984, ApJ, 285, 89

Draine B. T., Li A., 2007a, ApJ, 657, 810

Draine B. T., Li A., 2007b, ApJ, 657, 810

Dufresne R. P., Del Zanna G., Mason H. E., 2023, MNRAS, 521, 4696

Duncan K., Conselice C. J., 2015, MNRAS, 451, 2030

Dunne L., Eales S. A., 2001, MNRAS, 327, 697

Dunne L., Eales S., Edmunds M., Ivison R., Alexander P., Clements D. L., 2000, MNRAS, 315, 115

Dupac X., et al., 2001, ApJ, 553, 604

Duric N., Bourneuf E., Gregory P. C., 1988, AJ, 96, 81

Dwek E., 1998, ApJ, 501, 643

Eales S. A., Wynn-Williams C. G., Duncan W. D., 1989, ApJ, 339, 859

Edelson R. A., Malkan M. A., 1986, ApJ, 308, 59

Eisenstein D. J., Hu W., 1998, ApJ, 496, 605

Eisenstein D. J., et al., 2005, ApJ, 633, 560

Elbaz D., et al., 2007, A&A, 468, 33

Elbaz D., et al., 2018, A&A, 616, A110

Eldridge J. J., Izzard R. G., Tout C. A., 2008, MNRAS, 384, 1109

Elvis M., Maccacaro T., Wilson A. S., Ward M. J., Penston M. V., Fosbury R. A. E., Perola G. C., 1978, MNRAS, 183, 129

English J., Norris R. P., Freeman K. C., Booth R. S., 2003, AJ, 125, 1134

Esteban C., García-Rojas J., Peimbert M., Peimbert A., Ruiz M. T., Rodríguez M., Carigi L., 2005, ApJL, 618, L95

Evans A. S., et al., 2003, AJ, 125, 2341

Evans Neal J. I., Kim K.-T., Wu J., Chao Z., Heyer M., Liu T., Nguyen-Lu'o'ng Q., Kauffmann J., 2020, ApJ, 894, 103

Faisst A. L., Capak P. L., Emami N., Tacchella S., Larson K. L., 2019, ApJ, 884, 133

Faucher-Giguère C.-A., Lidz A., Zaldarriaga M., Hernquist L., 2009, ApJ, 703, 1416

Ferguson A. M. N., Gallagher J. S., Wyse R. F. G., 1998, AJ, 116, 673

Field G. B., Goldsmith D. W., Habing H. J., 1969, ApJL, 155, L149

Figueira M., et al., 2022, A&A, 667, A29

Fioc M., Rocca-Volmerange B., 1997, A&A, 326, 950

Fioc M., Rocca-Volmerange B., 1999, arXiv e-prints, pp astro–ph/9912179

Flores Velázquez J. A., et al., 2021, MNRAS, 501, 4812

Foreman-Mackey D., Hogg D. W., Lang D., Goodman J., 2013, PASP, 125, 306

Franceschini A., 2000, arXiv e-prints, pp astro–ph/0009121

Gabor J. M., Davé R., Finlator K., Oppenheimer B. D., 2010, MNRAS, 407, 749

Gail H. P., 2009, in Boulanger F., Joblin C., Jones A., Madden S., eds, EAS Publications Series Vol. 35, EAS Publications Series. pp 173–194, doi:10.1051/eas/0935010

Galametz M., et al., 2012, MNRAS, 425, 763

Galliano F., 2022, Habilitation Thesis, p. 1

Galliano E., Alloin D., 2008, A&A, 487, 519

Galliano E., Pantin E., Alloin D., Lagage P. O., 2005, MNRAS, 363, L1

Galliano F., Galametz M., Jones A. P., 2018, ARA&A, 56, 673

Gao Y., Solomon P. M., 2004, ApJ, 606, 271

Gao F., et al., 2021, A&A, 654, A117

García-Burillo S., Usero A., Alonso-Herrero A., Graciá-Carpio J., Pereira-Santaella M., Colina L., Planesas P., Arribas S., 2012, A&A, 539, A8

García-Marín M., Colina L., Arribas S., Alonso-Herrero A., Mediavilla E., 2006, ApJ, 650, 850

Genzel R., et al., 1998, ApJ, 498, 579

Genzel R., et al., 2015, ApJ, 800, 20

Gioia I. M., Gregorini L., Klein U., 1982, A&A, 116, 164

Goddard Q. E., Bresolin F., Kennicutt R. C., Ryan-Weber E. V., Rosales-Ortega F. F., 2011, MNRAS, 412, 1246

Goldberg L., 1966, ApJ, 144, 1225

Goldberg L., 1968, Theoretical intensities of recombination lines.

González-Alfonso E., et al., 2012, A&A, 541, A4

González Delgado R. M., Cerviño M., Martins L. P., Leitherer C., Hauschildt P. H., 2005, MNRAS, 357, 945

González-Martín O., et al., 2011, A&A, 527, A142

Goodman J., Weare J., 2010, Communications in Applied Mathematics and Computational Science, 5, 65

Gordon M. A., 1989, ApJ, 337, 782

Gordon M. A., Sorochenko R. L., 2002, Radio Recombination Lines. Their Physics and Astronomical Applications. 2009 Vol. 282, doi:10.1007/978-0-387-09604-9,

Gordon K. D., Clayton G. C., Misselt K. A., Landolt A. U., Wolff M. J., 2003, ApJ, 594, 279

Gould R. J., Salpeter E. E., 1963, ApJ, 138, 393

Goulding A. D., Alexander D. M., 2009, MNRAS, 398, 1165

Grazian A., et al., 2016, A&A, 585, A48

Grazian A., et al., 2017, A&A, 602, A18

Griffin M. J., et al., 2010, A&A, 518, L3

Guzmán A. E., Sanhueza P., Zapata L., Garay G., Rodríguez L. F., 2020, ApJ, 904, 77

Haardt F., Madau P., 2012, ApJ, 746, 125

Habets G. M. H. J., Heintze J. R. W., 1981, A&AS, 46, 193

Hansen C. J., Kawaler S. D., 1994, Stellar Interiors. Physical Principles, Structure, and Evolution., doi:10.1007/978-1-4419-9110-2.

Hao C.-N., Kennicutt R. C., Johnson B. D., Calzetti D., Dale D. A., Moustakas J., 2011, ApJ, 741, 124

Harada N., Sakamoto K., Martín S., Watanabe Y., Aladro R., Riquelme D., Hirota A., 2019, ApJ, 884, 100

Hayward C. C., et al., 2014, MNRAS, 445, 1598

Heckman T. M., et al., 2011, ApJ, 730, 5

Heilbron J. L., 2013, Nature, 498, 27

Heiles C., Troland T. H., 2003, ApJ, 586, 1067

Heitsch F., Zweibel E. G., Slyz A. D., Devriendt J. E. G., 2004, Ap&SS, 292, 45

Henkel C., et al., 2018, A&A, 615, A155

Herbst E., van Dishoeck E. F., 2009, ARA&A, 47, 427

Herrero-Illana R., et al., 2014, ApJ, 786, 156

Herrero-Illana R., Alberdi A., Pérez-Torres M. Á., Alonso-Herrero A., González-Millán D., Pereira-Santaella M., 2017, MNRAS, 470, L112

Hertzsprung E., 1905, Zeitschrift Fur Wissenschaftliche Photographie, 3, 442

Hewitt A., Burbidge G., 1993, ApJS, 87, 451

Heywood I., Avison A., Williams C. J., 2011, arXiv e-prints, p. arXiv:1106.3516

Hirashita H., 1999, ApJL, 510, L99

Hirota T., Kim M. K., Kurono Y., Honma M., 2014, ApJL, 782, L28

Hitomi Collaboration et al., 2018, PASJ, 70, 12

Ho L. C., Filippenko A. V., Sargent W. L. W., 1997, ApJS, 112, 315

Hoare M. G., Kurtz S. E., Lizano S., Keto E., Hofner P., 2007, in Reipurth B., Jewitt D., Keil K., eds, Protostars and Planets V. p. 181 (arXiv:astro-ph/0603560), doi:10.48550/arXiv.astro-ph/0603560

Högbom J. A., 1974, A&AS, 15, 417

Holland W. S., et al., 1999, MNRAS, 303, 659

Holland W. S., et al., 2013, MNRAS, 430, 2513

Hollenbach D., Salpeter E. E., 1971, ApJ, 163, 155

Houck J. R., Schneider D. P., Danielson G. E., Beichman C. A., Lonsdale C. J., Neugebauer G., Soifer B. T., 1985, ApJL, 290, L5

Hughes T. M., et al., 2014, A&A, 565, A4

Hummel E., 1991, A&A, 251, 442

Hunt L. K., et al., 2015, A&A, 576, A33

Ilbert O., et al., 2015, A&A, 579, A2

Inoue A. K., Shimizu I., Iwata I., Tanaka M., 2014, MNRAS, 442, 1805

Inoue S., Dekel A., Mandelker N., Ceverino D., Bournaud F., Primack J., 2016, MNRAS, 456, 2052

Instrument M., Teams M. I. S., 2011, MIPS Instrument Handbook, doi:10.26131/IRSA488.

Ishibashi W., Courvoisier T. J. L., 2011, A&A, 525, A118

Iwata I., et al., 2009, ApJ, 692, 1287

Izotov Y. I., Guseva N. G., Thuan T. X., 2011, ApJ, 728, 161

Izotov Y. I., Schaerer D., Thuan T. X., Worseck G., Guseva N. G., Orlitová I., Verhamme A., 2016a, MNRAS, 461, 3683

Izotov Y. I., Orlitová I., Schaerer D., Thuan T. X., Verhamme A., Guseva N. G., Worseck G., 2016b, Nature, 529, 178

Jappsen A. K., Klessen R. S., 2004, A&A, 423, 1

Jarrett T. H., et al., 2011, ApJ, 735, 112

Jaskot A. E., Oey M. S., 2013, ApJ, 766, 91

Jeans J. H., 1928, Astronomy and cosmogony

Jermyn A. S., Steinhardt C. L., Tout C. A., 2018, MNRAS, 480, 4265

Jeřábková T., Hasani Zonoozi A., Kroupa P., Beccari G., Yan Z., Vazdekis A., Zhang Z. Y., 2018, A&A, 620, A39

Joblin C., Tielens A. G. G. M., eds, 2011, PAHs and the Universe: A Symposium to Celebrate the 25th Anniversary of the PAH Hypothesis EAS Publications Series Vol. 46

Jogee S., Scoville N., Kenney J. D. P., 2005, ApJ, 630, 837

Johnson D. J., Friedlander M. W., Katz J. I., 1993, ApJ, 407, 714

Johnson J. L., Greif T. H., Bromm V., Klessen R. S., Ippolito J., 2009, MNRAS, 399, 37

Joung M. R., Putman M. E., Bryan G. L., Fernández X., Peek J. E. G., 2012, ApJ, 759, 137

Juvela M., Ysard N., 2012, A&A, 539, A71

Kahn F. D., 1974, A&A, 37, 149

Karpov P. I., Martizzi D., Macias P., Ramirez-Ruiz E., Kolborg A. N., Naiman J. P., 2020, ApJ, 896, 66

Kellermann K. I., Sramek R., Schmidt M., Shaffer D. B., Green R., 1989, AJ, 98, 1195

Kemper F., Vriend W. J., Tielens A. G. G. M., 2005, ApJ, 633, 534

Kennicutt Robert C. J., 1998, ApJ, 498, 541

Kennicutt R. C., Evans N. J., 2012, ARA&A, 50, 531

Kennicutt Robert C. J., Edgar B. K., Hodge P. W., 1989, ApJ, 337, 761

Kennicutt Robert C. J., et al., 2009, ApJ, 703, 1672

Kereš D., Katz N., Weinberg D. H., Davé R., 2005, MNRAS, 363, 2

Kim S.-H., Martin P. G., 1996, ApJ, 462, 296

Kim W. J., Wyrowski F., Urquhart J. S., Menten K. M., Csengeri T., 2017, A&A, 602, A37

Kim W. J., Urquhart J. S., Wyrowski F., Menten K. M., Csengeri T., 2018, A&A, 616, A107

Kitamura Y., Momose M., Yokogawa S., Kawabe R., Tamura M., Ida S., 2002, ApJ, 581, 357

Klaas U., et al., 2001, A&A, 379, 823

Klein U., 1988, PhD thesis, Univ. Bonn

Klein U., Emerson D. T., 1981, A&A, 94, 29

Klein U., Fletcher A., 2015, Galactic and Intergalactic Magnetic Fields

Klein U., Lisenfeld U., Verley S., 2018, A&A, 611, A55

Kobayashi C., Taylor P., 2023, arXiv e-prints, p. arXiv:2302.07255

Kobulnicky H. A., Fryer C. L., 2007, ApJ, 670, 747

Kobulnicky H. A., Skillman E. D., Roy J.-R., Walsh J. R., Rosa M. R., 1997, ApJ, 477, 679

Kochanek C. S., 2011, ApJ, 743, 73

Kölligan A., Kuiper R., 2018, A&A, 620, A182

König S., Aalto S., Muller S., Gallagher J. S., Beswick R. J., Xu C. K., Evans A., 2016, A&A, 594, A70

Kotilainen J. K., Moorwood A. F. M., Ward M. J., Forbes D. A., 1996, A&A, 305, 107

Kramer M., et al., 2021, Phys. Rev. X, 11, 041050

Kroupa P., 2001, MNRAS, 322, 231

Kroupa P., 2002, Science, 295, 82

Krumholz M. R., Matzner C. D., 2009, ApJ, 703, 1352

Krumholz M. R., McKee C. F., Klein R. I., 2005, ApJL, 618, L33

Kuiper R., Klahr H., Beuther H., Henning T., 2011, ApJ, 732, 20

Lamastra A., Menci N., Fiore F., Santini P., 2013, A&A, 552, A44

Landy S. D., Szalay A. S., 1993, ApJ, 412, 64

Lanz L., et al., 2013, ApJ, 768, 90

Larson R. B., 1974, MNRAS, 169, 229

Lattanzio J., Forestini M., 1999, in Le Bertre T., Lebre A., Waelkens C., eds, Vol. 191, Asymptotic Giant Branch Stars. p. 31

Law C. J., Backer D., Yusef-Zadeh F., Maddalena R., 2009, ApJ, 695, 1070

Lawton B., et al., 2010, ApJ, 716, 453

Lee N., et al., 2017, MNRAS, 471, 2124

Leitet E., Bergvall N., Piskunov N., Andersson B. G., 2011, A&A, 532, A107

Leitet E., Bergvall N., Hayes M., Linné S., Zackrisson E., 2013, A&A, 553, A106

Leitherer C., et al., 1999, ApJS, 123, 3

Leitherer C., Ortiz Otálvaro P. A., Bresolin F., Kudritzki R.-P., Lo Faro B., Pauldrach A. W. A., Pettini M., Rix S. A., 2010, ApJS, 189, 309

Leitherer C., Ekström S., Meynet G., Schaerer D., Agienko K. B., Levesque E. M., 2014, ApJS, 212, 14

Leitherer C., Hernandez S., Lee J. C., Oey M. S., 2016, ApJ, 823, 64

Lenc E., Tingay S. J., 2009, AJ, 137, 537

Lequeux J., 2005, The Interstellar Medium, doi:10.1007/b137959.

Leroy A. K., Walter F., Brinks E., Bigiel F., de Blok W. J. G., Madore B., Thornley M. D., 2008, AJ, 136, 2782

Leroy A. K., et al., 2015, ApJ, 801, 25

Leroy A. K., et al., 2018, ApJ, 869, 126

Li A., Draine B. T., 2001, ApJL, 550, L213

Li J., Liu C., Zhang Z.-Y., Tian H., Fu X., Li J., Yan Z.-Q., 2023, Nature, 613, 460

Lian J., Bergemann M., Pillepich A., Zasowski G., Lane R. R., 2023, Nature Astronomy, 7, 951

Lípari S., Díaz R., Taniguchi Y., Terlevich R., Dottori H., Carranza G., 2000, AJ, 120, 645

Lisenfeld U., Isaak K. G., Hills R., 2000, MNRAS, 312, 433

Liu T., et al., 2017, ApJ, 849, 25

Liu T., et al., 2020a, MNRAS, 496, 2790

Liu S.-Y., Su Y.-N., Zinchenko I., Wang K.-S., Meyer D. M. A., Wang Y., Hsieh I. T., 2020b, ApJ, 904, 181

Lockman F. J., 1989, ApJS, 71, 469

Lonsdale C. J., Farrah D., Smith H. E., 2006, in Mason J. W., ed., , Astrophysics Update 2. p. 285, doi:10.1007/3-540-30313-8˙9

López-Sánchez Á. R., Esteban C., García-Rojas J., Peimbert M., Rodríguez M., 2007, ApJ, 656, 168

Louvet F., et al., 2016, A&A, 596, A88

Low C., Lynden-Bell D., 1976, MNRAS, 176, 367

Lu X., Li G.-X., Zhang Q., Lin Y., 2022, Nature Astronomy, 6, 837

Luisi M., Anderson L. D., Liu B., Balser D. S., Bania T. M., Wenger T. V., Haffner L., 2020, in American Astronomical Society Meeting Abstracts #236. p. 209.04

Ma X., Hopkins P. F., Wetzel A. R., Kirby E. N., Anglés-Alcázar D., Faucher-Giguère C.-A., Kereš D., Quataert E., 2017, MNRAS, 467, 2430

Ma X., Quataert E., Wetzel A., Hopkins P. F., Faucher-Giguère C.-A., Kereš D., 2020, MNRAS, 498, 2001

Madau P., Dickinson M., 2014, ARA&A, 52, 415

Magdis G. E., et al., 2012, ApJ, 760, 6

Magdis G. E., et al., 2017, A&A, 603, A93

Magnelli B., et al., 2014, A&A, 561, A86

Magnelli B., et al., 2015, A&A, 573, A45

Magrini L., Coccato L., Stanghellini L., Casasola V., Galli D., 2016, A&A, 588, A91

Mairs S., et al., 2021, AJ, 162, 191

Mancuso C., Lapi A., Shi J., Cai Z. Y., Gonzalez-Nuevo J., Béthermin M., Danese L., 2016, ApJ, 833, 152

Marconi A., Oliva E., van der Werf P. P., Maiolino R., Schreier E. J., Macchetto F., Moorwood A. F. M., 2000, A&A, 357, 24

Martín-Navarro I., et al., 2015, ApJL, 798, L4

Martin D. C., et al., 2005, ApJL, 619, L1

Martín S., Mauersberger R., Martín-Pintado J., Henkel C., García-Burillo S., 2006, ApJS, 164, 450

Martín S., et al., 2011, A&A, 527, A36

Martins F., Schaerer D., Hillier D. J., 2005, A&A, 436, 1049

Marvil J., Owen F., Eilek J., 2015, AJ, 149, 32

Massardi M., et al., 2008, MNRAS, 384, 775

Mathis J. S., Rumpl W., Nordsieck K. H., 1977, ApJ, 217, 425

Maud L. T., et al., 2018, A&A, 620, A31

Maud L. T., et al., 2019, A&A, 627, L6

Mauersberger R., 2003, in 1^{er} Congreso Nacional de Astrofísica Molecular: Una visión general del potencial de los grupos de química españoles anters los nuevos desafíos de la Astrofísica. p. 13

Maury A. J., et al., 2018, MNRAS, 477, 2760

McKee C. F., Ostriker J. P., 1977, ApJ, 218, 148

McKee C. F., Ostriker E. C., 2007, ARA&A, 45, 565

McMillan P. J., 2011, MNRAS, 414, 2446

McMullin J. P., Waters B., Schiebel D., Young W., Golap K., 2007, CASA Architecture and Applications. p. 127

McQuinn K. B. W., Skillman E. D., Cannon J. M., Dalcanton J. J., Dolphin A., Stark D., Weisz D., 2009, ApJ, 695, 561

McQuinn K. B. W., Skillman E. D., Heilman T. N., Mitchell N. P., Kelley T., 2018, MNRAS, 477, 3164

Mehta V., et al., 2023, ApJ, 952, 133

Meier D. S., et al., 2015, ApJ, 801, 63

Meixner M., et al., 2013, AJ, 146, 62

Meny C., Gromov V., Boudet N., Bernard J. P., Paradis D., Nayral C., 2007, A&A, 468, 171

Menzel D. H., 1968, Nature, 218, 756

Michiyama T., Iono D., Nakanishi K., Ueda J., Saito T., Yamashita T., Bolatto A., Yun M., 2020, arXiv e-prints, p. arXiv:2004.06123

Mihos J. C., Hernquist L., 1996, ApJ, 464, 641

Mills E. A. C., et al., 2021, arXiv e-prints, p. arXiv:2106.14970

Mirabel I. F., 2002, Ap&SS, 281, 375

Miyawaki R., Hayashi M., Hasegawa T., 2023, PASJ, 75, 225

Mollá M., García-Vargas M. L., Bressan A., 2009, MNRAS, 398, 451

Möller T., Endres C., Schilke P., 2017, A&A, 598, A7

Monreal-Ibero A., Vílchez J. M., Walsh J. R., Muñoz-Tuñón C., 2010, A&A, 517, A27

Moscadelli L., Cesaroni R., Beltrán M. T., Rivilla V. M., 2021, A&A, 650, A142

Motte F., Bontemps S., Louvet F., 2018, Annual Review of Astronomy and Astrophysics, 56, 41

Mouschovias T. C., 1987, in Morfill G. E., Scholer M., eds, NATO Advanced Study Institute (ASI) Series C Vol. 210, Physical Processes in Interstellar Clouds. pp 453–489

Murphy E. J., et al., 2011, ApJ, 737, 67

Murphy E. J., et al., 2015, ApJ, 813, 118

Muxlow T., Beswick R. J., Richards A. M. S., Thrall H. J., 2006, in Baan W., et al., eds, Proceedings of the 8th European VLBI Network Symposium. p. 31 (arXiv:astro-ph/0611951), doi:10.22323/1.036.0031

Nahar S. N., 2021, Atoms, 9, 73

Nakano T., 1989, ApJ, 345, 464

Nersesian A., et al., 2019, A&A, 624, A80

Nestor D. B., Shapley A. E., Kornei K. A., Steidel C. C., Siana B., 2013, ApJ, 765, 47

Netzer H., 2015, ARA&A, 53, 365

Noeske K. G., et al., 2007, ApJL, 660, L43

Nomoto K., Kobayashi C., Tominaga N., 2013, ARA&A, 51, 457

Norris R. P., Forbes D. A., 1995, ApJ, 446, 594

Nussbaumer H., Schmutz W., 1984, A&A, 138, 495

O'Connell R. W., 1999, ARA&A, 37, 603

Olsson E., Aalto S., Thomasson M., Beswick R., 2010, A&A, 513, A11

Osterbrock D. E., Ferland G. J., 2006, Astrophysics of gaseous nebulae and active galactic nuclei

Ostriker J. P., Peebles P. J. E., Yahil A., 1974, ApJL, 193, L1

Paladino R., Murgia M., Tarchi A., Moscadelli L., Comito C., 2008, A&A, 485, 679

Palla F., Stahler S. W., 1993, ApJ, 418, 414

Paspaliaris E. D., et al., 2021, A&A, 649, A137

Pastoriza M. G., 1967, The Observatory, 87, 225

Patrignani C., et al., 2016, Chinese Physics C, 40, 100001

Peebles P. J. E., 1980, The large-scale structure of the universe

Pellerin A., Robert C., 2007, MNRAS, 381, 228

Peng C. Y., Ho L. C., Filippenko A. V., Sargent W. L. W., 1998, in American Astronomical Society Meeting Abstracts. p. 06.07

Pérez-Beaupuits J. P., Spoon H. W. W., Spaans M., Smith J. D., 2011, A&A, 533, A56

Péroux C., Howk J. C., 2020, ARA&A, 58, 363

Phookun B., Anantharamaiah K. R., Goss W. M., 1998, MNRAS, 295, 156

Pierre Auger Collaboration et al., 2017, Science, 357, 1266

Pilbratt G. L., et al., 2010, A&A, 518, L1

Piqueras López J., Colina L., Arribas S., Alonso-Herrero A., 2013, A&A, 553, A85

Piqueras López J., Colina L., Arribas S., Pereira-Santaella M., Alonso-Herrero A., 2016, A&A, 590, A67

Plambeck R. L., Wright M. C. H., 2016, ApJ, 833, 219

Planck Collaboration et al., 2020, A&A, 641, A6

Poglitsch A., et al., 2010, A&A, 518, L2

Popesso P., et al., 2019, MNRAS, 483, 3213

Popper D. M., 1980, ARA&A, 18, 115

Popping G., Pérez I., Zurita A., 2010, A&A, 521, A8

Privon G., Rebolledo D., Popping G., Izumi T., 2023, ALMA Cycle 10 Proposer's Guide, doi:10.5281/zenodo.7822946. , https://doi.org/10.5281/zenodo.7822946

Purcell E. M., 1969, ApJ, 158, 433

Purser S. J. D., et al., 2016, MNRAS, 460, 1039

Puxley P. J., Brand P. W. J. L., Moore T. J. T., Mountain C. M., Nakai N., Yamashita T., 1989, ApJ, 345, 163

Puxley P. J., Brand P. W. J. L., Moore T. J. T., Mountain C. M., Nakai N., 1991, MNRAS, 248, 585

Puxley P. J., Mountain C. M., Brand P. W. J. L., Moore T. J. T., Nakai N., 1997, ApJ, 485, 143

Quireza C., Rood R. T., Balser D. S., Bania T. M., 2006a, ApJS, 165, 338

Quireza C., Rood R. T., Bania T. M., Balser D. S., Maciel W. J., 2006b, ApJ, 653, 1226

Ramachandran V., et al., 2019, A&A, 625, A104

Ramos Padilla A. F., Ashby M. L. N., Smith H. A., Martínez-Galarza J. R., Beverage A. G., Dietrich J., Higuera-G. M.-A., Weiner A. S., 2020, MNRAS, 499, 4325

Rawle T. D., et al., 2016, MNRAS, 459, 1626

Razoumov A. O., Sommer-Larsen J., 2010, ApJ, 710, 1239

Remijan A., et al., 2019, ALMA Technical Handbook ALMA Doc. 7.3, ver. 1.0, ISBN 978-3-923524-66-2

Rieke G. H., et al., 2004, ApJS, 154, 25

Rieke G. H., Alonso-Herrero A., Weiner B. J., Pérez-González P. G., Blaylock M., Donley J. L., Marcillac D., 2009, ApJ, 692, 556

Robert C., Pellerin A., Aloisi A., Leitherer C., Hoopes C., Heckman T. M., 2003, ApJS, 144, 21

Rodighiero G., et al., 2011, ApJL, 739, L40

Rodríguez-Rico C. A., Goss W. M., Turner J. L., Gómez Y., 2007, ApJ, 670, 295

Romeo A. B., Fathi K., 2016, MNRAS, 460, 2360

Rosen A. L., Krumholz M. R., 2020, AJ, 160, 78

Rosen A. L., Krumholz M. R., McKee C. F., Klein R. I., 2016, MNRAS, 463, 2553

Rosenberg M. J. F., et al., 2015, ApJ, 801, 72

Rowan-Robinson M., et al., 1991, Nature, 351, 719

Roy A. L., Goss W. M., Mohan N. R., Anantharamaiah K. R., 2005, A&A, 435, 831

Roy A. L., Oosterloo T., Goss W. M., Anantharamaiah K. R., 2010, A&A, 517, A82

Rubin V. C., Ford W. Kent J., 1970, ApJ, 159, 379

Rudolph A. L., Simpson J. P., Haas M. R., Erickson E. F., Fich M., 1997, ApJ, 489, 94

Russell H. N., 1919, Proceedings of the National Academy of Science, 5, 391

Sabatini G., et al., 2021, A&A, 652, A71

Saintonge A., et al., 2011, MNRAS, 415, 32

Sajina A., Scott D., Dennefeld M., Dole H., Lacy M., Lagache G., 2006, MNRAS, 369, 939

Sakai N., et al., 2017, MNRAS, 467, L76

Sakamoto K., Scoville N. Z., Yun M. S., Crosas M., Genzel R., Tacconi L. J., 1999, ApJ, 514, 68

Sakamoto K., et al., 2008, ApJ, 684, 957

Sakamoto K., Aalto S., Costagliola F., Martín S., Ohyama Y., Wiedner M. C., Wilner D. J., 2013, ApJ, 764, 42

Sakamoto K., Aalto S., Combes F., Evans A., Peck A., 2014, ApJ, 797, 90

Sakamoto K., Martín S., Wilner D. J., Aalto S., Evans A. S., Harada N., 2021, ApJ, 923, 240

Salak D., Tomiyasu Y., Nakai N., Kuno N., Miyamoto Y., Kaneko H., 2017, ApJ, 849, 90

Salim S., et al., 2007, ApJS, 173, 267

Salpeter E. E., 1955, ApJ, 121, 161

Sana H., et al., 2013, A&A, 550, A107

Sana H., et al., 2014, ApJS, 215, 15

Sánchez S. F., et al., 2014, A&A, 563, A49

Sandage A., Tammann G. A., 1981, Carnegie Inst. of Washington, p. 0

Sanders D. B., Mirabel I. F., 1996, ARA&A, 34, 749

Sanders D. B., Mazzarella J. M., Kim D. C., Surace J. A., Soifer B. T., 2003, AJ, 126, 1607

Sanders D., Mazzarella J., Kim D., Surace J., Soifer B., 2004, RBGS, p. 0

Schaerer D., 2003, A&A, 397, 527

Schaerer D., Contini T., Kunth D., Meynet G., 1997, ApJL, 481, L75

Schmidt M., 1959, ApJ, 129, 243

Schmitt H. R., Calzetti D., Armus L., Giavalisco M., Heckman T. M., Kennicutt R. C. J., Leitherer C., Meurer G. R., 2006, ApJ, 643, 173

Schreiber C., et al., 2015, A&A, 575, A74

Schuller F., et al., 2009, A&A, 504, 415

Schwab F. R., 1984, AJ, 89, 1076

Schweizer F., 1986, Science, 231, 227

Scoville N., Murchikova L., 2013, ApJ, 779, 75

Scoville N., Sheth K., Aussel H., Manohar S., ALMA Cycle 0 Teams 2013, ALMA Observations of Arp 220 and Dust Continuum Measurements of High-z Galaxies. p. 1

Scoville N., et al., 2014, ApJ, 783, 84

Scoville N., et al., 2015, ApJ, 800, 70

Scoville N., et al., 2017, ApJ, 836, 66

Seale J. P., Looney L. W., Wong T., Ott J., Klein U., Pineda J. L., 2012, ApJ, 751, 42

Seaquist E. R., Bell M. B., 1977, A&A, 60, L1

Seaquist E. R., Kerton C. R., Bell M. B., 1994, ApJ, 429, 612

Seaquist E. R., Carlstrom J. E., Bryant P. M., Bell M. B., 1996, ApJ, 465, 691

Seaton M. J., 1959, Physical Review, 113, 814

Seiffert M., Borys C., Scott D., Halpern M., 2007, MNRAS, 374, 409

Sérsic J. L., Pastoriza M., 1965, PASP, 77, 287

Sérsic J. L., Pastoriza M., 1967, PASP, 79, 152

Shapley A. E., Steidel C. C., Pettini M., Adelberger K. L., Erb D. K., 2006, ApJ, 651, 688

Shaver P. A., Churchwell E., Rots A. H., 1977, A&A, 55, 435

Shaver P. A., Churchwell E., Walmsley C. M., 1978, A&A, 64, 1

Shaver P. A., McGee R. X., Newton L. M., Danks A. C., Pottasch S. R., 1983, MNRAS, 204, 53

Sheth K., Vogel S. N., Regan M. W., Teuben P. J., Harris A. I., Thornley M. D., 2002a, AJ, 124, 2581

Sheth K., Vogel S. N., Regan M. W., Teuben P. J., Harris A. I., Thornley M. D., 2002b, AJ, 124, 2581

Shetty R., Kauffmann J., Schnee S., Goodman A. A., 2009, ApJ, 696, 676

Shields G. A., 1990, Annual Review of Astronomy and Astrophysics, 28, 525

Siana B., et al., 2010, ApJ, 723, 241

Smirnova K. I., Wiebe D. S., Moiseev A. V., 2017, Open Astronomy, 26, 88

Smith B. J., Harvey P. M., Colome C., Zhang C. Y., Difrancesco J., Pogge R. W., 1994, ApJ, 425, 91

Smith M. W. L., et al., 2012, ApJ, 756, 40

Sneppen A., Steinhardt C. L., Hensley H., Jermyn A. S., Mostafa B., Weaver J. R., 2022, ApJ, 931, 57

Soifer B. T., et al., 1984, ApJL, 278, L71

Soifer B. T., Boehmer L., Neugebauer G., Sanders D. B., 1989, AJ, 98, 766

Sorochenko R. L., Berulis J. J., 1969, Astrophys. Lett., 4, 173

Sorochenko R. L., Puzanov V. A., Salomonovich A. E., Shteinshleger V. B., 1969, Astrophys. Lett., 3, 7

Soto K. T., Martin C. L., 2010, ApJ, 716, 332

Speagle J. S., Steinhardt C. L., Capak P. L., Silverman J. D., 2014, ApJS, 214, 15

Spoon H. W. W., Koornneef J., Moorwood A. F. M., Lutz D., Tielens A. G. G. M., 2000, A&A, 357, 898

Spoon H. W. W., Moorwood A. F. M., Pontoppidan K. M., Cami J., Kregel M., Lutz D., Tielens A. G. G. M., 2003, A&A, 402, 499

Spoon H. W. W., Marshall J. A., Houck J. R., Elitzur M., Hao L., Armus L., Brandl B. R., Charmandaris V., 2007, ApJL, 654, L49

Stanway E. R., Eldridge J. J., Becker G. D., 2016, MNRAS, 456, 485

Steigman G., 2007, Annual Review of Nuclear and Particle Science, 57, 463

Stevens J. A., Amure M., Gear W. K., 2005, MNRAS, 357, 361

Storey P. J., Hummer D. G., 1995, MNRAS, 272, 41

Strateva I., et al., 2001, AJ, 122, 1861

Strickland D. K., Heckman T. M., Colbert E. J. M., Hoopes C. G., Weaver K. A., 2004, ApJ, 606, 829

Strömgren B., 1939, ApJ, 89, 526

Tabatabaei F. S., et al., 2017, ApJ, 836, 185

Tacconi L. J., et al., 2018, ApJ, 853, 179

Tacconi L. J., Genzel R., Sternberg A., 2020, ARA&A, 58, 157

Tachihara K., Gratier P., Sano H., Tsuge K., Miura R. E., Muraoka K., Fukui Y., 2018, PASJ, 70, S52

Tadaki K., et al., 2018, Nature, 560, 613

Tanaka K. E. I., Tan J. C., Zhang Y., 2017, ApJ, 835, 32

Tanaka K. E. I., et al., 2020, ApJL, 900, L2

Taniguchi Y., et al., 2012, ApJ, 753, 78

Taylor J. H., Fowler L. A., McCulloch P. M., 1979, Nature, 277, 437

Taylor E. N., et al., 2009, ApJ, 694, 1171

Thilker D. A., Braun R., Walterbos R. A. M., 2000, AJ, 120, 3070

Thornley M. D., Förster Schreiber N. M., Lutz D., Genzel R., Spoon H. W. W., Kunze D., Sternberg A., 2000, ApJ, 539, 641

Tielens A. G. G. M., 2022, Frontiers in Astronomy and Space Sciences, 9, 908217

Topping M. W., Shull J. M., 2015, ApJ, 800, 97

Tremblin P., et al., 2014, A&A, 568, A4

Treu T., Auger M. W., Koopmans L. V. E., Gavazzi R., Marshall P. J., Bolton A. S., 2010, ApJ, 709, 1195

Tsai C.-W., et al., 2015, ApJ, 805, 90

Tully R. B., Fisher J. R., Morrison P., 1988, Scientific American, 258, 104

Tully R. B., Shaya E. J., Karachentsev I. D., Courtois H. M., Kocevski D. D., Rizzi L., Peel A., 2008, ApJ, 676, 184

Tully R. B., Howlett C., Pomarède D., 2023, ApJ, 954, 169

Tunnard R., et al., 2015, ApJ, 800, 25

Turner J. L., Ho P. T. P., 1994, ApJ, 421, 122

Turner J. L., Ho P. T. P., Beck S., 1987, ApJ, 313, 644

Turner N. J., Fromang S., Gammie C., Klahr H., Lesur G., Wardle M., Bai X. N., 2014, in Beuther H., Klessen R. S., Dullemond C. P., Henning T., eds, Protostars and Planets VI. pp 411–432 (arXiv:1401.7306), doi:10.2458/azu˙uapress˙9780816531240-ch018

Urquhart J. S., et al., 2010, pasa, 27, 321

Urry C. M., Padovani P., 1995, PASP, 107, 803

Väisänen P., Rajpaul V., Zijlstra A. A., Reunanen J., Kotilainen J., 2012, MNRAS, 420, 2209

Vale Asari N., et al., 2020, MNRAS, 498, 4205

Veilleux S., 2006, nar, 50, 701

Veilleux S., 2008, nar, 52, 289

Veilleux S., et al., 2009, ApJS, 182, 628

Veron-Cetty M. P., Veron P., 1985, A&A, 145, 425

Virtanen P., et al., 2020, Nature Methods, 17, 261

Voyer E. N., et al., 2014, A&A, 569, A124

Waltman W. B., Waltman E. B., Schwartz P. R., Johnson K. J., Wilson W. J., 1973, ApJL, 185, L135

Wang B., Heckman T. M., 1996, ApJ, 457, 645

Wang J., Zhong Z., 2018, A&A, 619, L1

Wang M., Henkel C., Chin Y. N., Whiteoak J. B., Hunt Cunningham M., Mauersberger R., Muders D., 2004, A&A, 422, 883

Wang T.-M., et al., 2022, A&A, 660, A142

Wardziński G., Zdziarski A. A., 2000, MNRAS, 314, 183

Watkins L. L., van der Marel R. P., Sohn S. T., Evans N. W., 2019, ApJ, 873, 118

Weinberg D. H., Mortonson M. J., Eisenstein D. J., Hirata C., Riess A. G., Rozo E., 2013, physrep, 530, 87

Weiner B. J., et al., 2005, ApJ, 620, 595

Weingartner J. C., Draine B. T., 2001, ApJ, 548, 296

Weinmann S. M., Kauffmann G., van den Bosch F. C., Pasquali A., McIntosh D. H., Mo H., Yang X., Guo Y., 2009, MNRAS, 394, 1213

Weiß A., Kovács A., Güsten R., Menten K. M., Schuller F., Siringo G., Kreysa E., 2008, A&A, 490, 77

Weisskopf M. C., Tananbaum H. D., Van Speybroeck L. P., O'Dell S. L., 2000, in Truemper J. E., Aschenbach B., eds, Society of Photo-Optical Instrumentation Engineers (SPIE) Conference Series Vol. 4012, X-Ray Optics, Instruments, and Missions III. pp 2–16 (arXiv:astro-ph/0004127), doi:10.1117/12.391545

Werk J. K., Putman M. E., Meurer G. R., Santiago-Figueroa N., 2011, ApJ, 735, 71

Werner M. W., et al., 2004, ApJS, 154, 1

Westmoquette M. S., James B., Monreal-Ibero A., Walsh J. R., 2013, A&A, 550, A88

Wilkinson C. L., Pimbblet K. A., Stott J. P., Few C. G., Gibson B. K., 2018, MNRAS, 479, 758

Wille K., 1991, Reports on Progress in Physics, 54, 1005

Williams G. M., et al., 2022, MNRAS, 509, 748

Willick J. A., Courteau S., Faber S. M., Burstein D., Dekel A., Strauss M. A., 1997, ApJS, 109, 333

Willmer C. N. A., et al., 2006, ApJ, 647, 853

Wilson T. L., Pauls T., 1984, A&A, 138, 225

Wilson C. D., Rangwala N., Glenn J., Maloney P. R., Spinoglio L., Pereira-Santaella M., 2014, ApJL, 789, L36

Wolfire M. G., Cassinelli J. P., 1987, ApJ, 319, 850

Wright E. L., et al., 2010, AJ, 140, 1868

Wuyts S., et al., 2011, ApJ, 742, 96

Xu C. K., et al., 2015, ApJ, 799, 11

Yajima H., Choi J.-H., Nagamine K., 2011, MNRAS, 412, 411

Yang M., Greve T. R., Dowell C. D., Borys C., 2007, ApJ, 660, 1198

Ye T., 1992, MNRAS, 255, 32

Yen H.-W., et al., 2014, ApJ, 793, 1

Yong D., Carney B. W., Teixera de Almeida M. L., Pohl B. L., 2006, AJ, 131, 2256

Yorke H. W., Bodenheimer P., 1999, ApJ, 525, 330

Yorke H. W., Sonnhalter C., 2002, ApJ, 569, 846

Ysard N., et al., 2012, A&A, 542, A21

Yukita M., Swartz D. A., Tennant A. F., Soria R., Irwin J. A., 2012, ApJ, 758, 105

Zackrisson E., Rydberg C.-E., Schaerer D., Östlin G., Tuli M., 2011, ApJ, 740, 13

Zackrisson E., Inoue A. K., Jensen H., 2013, ApJ, 777, 39

Zaritsky D., Kennicutt Robert C. J., Huchra J. P., 1994, ApJ, 420, 87

Zeilik M., Gregory S., 1998, Introductory Astronomy and Astrophysics

Zenner S., Lenzen R., 1993, A&AS, 101, 363

Zhang F., Li L., Zhang Y., Kang X., Han Z., 2012, MNRAS, 421, 743

Zhang F., Li L., Kang X., Zhuang Y., Han Z., 2013, MNRAS, 433, 1039

Zhang Y., Tan J. C., Hosokawa T., 2014, ApJ, 788, 166

Zhang C., et al., 2022a, MNRAS, 510, 4998

Zhang Y., et al., 2022b, ApJ, 936, 68

Zhao J.-H., Anantharamaiah K. R., Goss W. M., Viallefond F., 1996, ApJ, 472, 54

Zhao J.-H., Anantharamaiah K. R., Goss W. M., Viallefond F., 1997, ApJ, 482, 186

Zhao B., Caselli P., Li Z.-Y., Krasnopolsky R., Shang H., Lam K. H., 2020, MNRAS, 492, 3375

Zhu F.-Y., Zhu Q.-F., Wang J.-Z., Zhang J.-S., 2019, ApJ, 881, 14

Zinnecker H., Yorke H. W., 2007, ARA&A, 45, 481

Zubko V., Dwek E., Arendt R. G., 2004, ApJS, 152, 211

Zweibel E. G., 2002, ApJ, 567, 962

Zwicky F., 1933, Helvetica Physica Acta, 6, 110

de Barros S., et al., 2016, A&A, 585, A51

de Grijs R., Anders P., Zackrisson E., Östlin G., 2013, MNRAS, 431, 2917

de Vaucouleurs G., de Vaucouleurs A., Corwin Herold G. J., Buta R. J., Paturel G., Fouque P., 1991a, Third Reference Catalogue of Bright Galaxies

de Vaucouleurs G., de Vaucouleurs A., Corwin Herold G. J., Buta R. J., Paturel G., Fouque P., 1991b, Third Reference Catalogue of Bright Galaxies

van Driel W., et al., 1995, AJ, 109, 942

van Terwisga S. E., Hacar A., 2023, A&A, 673, L2

van de Voort F., Schaye J., Booth C. M., Haas M. R., Dalla Vecchia C., 2011, MNRAS, 414, 2458

van 't Hoff M. L. R., Tobin J. J., Harsono D., van Dishoeck E. F., 2018, A&A, 615, A83

List of Figures

List of Tables

Acknowledgments

There have been many who have helped me over the years to bring this project to completion. It would be impossible to list them all, because in the endless, bottomless sea that is the flow of time, even a small push in the right direction can make a difference. That being said, I would first like to thank my parents, who have had faith in me even when my own was lost.

I would like to thank Benjamin for being an example of thoroughness and dedication and for his patience. I am very grateful to my supervisor, Frank, for his support throughout the years. Last but not least, I would like to thank Yujin for his advice and patience.

I am grateful to Cristina and Sabine for not letting me get overwhelmed by the bureaucracy and always finding a way to help me.

I would like to thank Andreas, Philipp and Uwe for their support and expertise, which made all the technical projects I worked on possible.

I am grateful for my friends, some still here with me, some far away and almost out of contact, know that I have not forgotten you. First, I'd like to acknowledge some of the people I have met and some of the friends I have made at the Institute, Sandra, Ana, Nathan, Christos, Ankur, Abel, David, Kevin and Maude. Their presence has made these years more enjoyable and has given me the strength to see them through to the end. I would also like to acknowledge friends from outside the Institute, Ronja, Gisela, Cosmin, and Anna, who have provided me with an outside perspective, and whose kind attitudes and understanding have been especially helpful in the final stages of the project.

I would like to acknowledge the financial support of the Sonderforschungsbereich 956, Teilprojekt A1, funded by the Deutsche Forschungsgemeinschaft.